Proceedings of the 19th Hellenic Nuclear Physics Society
Symposium 2010

Index table

Symposium Programme……...iv
Poster List……....vi
List of Participants……..viii

Radio-tracing techniques applied in a marine ecosystem, the case of a submarine groundwater source at southern Peloponnesus……1-6
D.L. Patiris, G. Eleftheriou, A. P. Karageorgis, D. Georgopoulos, V. Papadopoulos, K. Stamoulis, K.G. Ioannides, R. Vlastou, C. Tsabaris

^{128}Xe: Test for E(5) Symmetry through DDCM and GOSIA Analysis……7-12
T. Konstantinopoulos, A. Lagoyannis, S. Harissopulos, A. Dewald, C. Fransen, G. Frießner, M. Hackstein, J. Jolie, G. Pascovici, Th. Pissull, W. Rother, K.-O. Zell, G. Ilieh, H. Iwasakid, B. Melong, U. Jakobsson, R. Julin, P. Jones, S. Ketelhut, P. Nieminen, P. Peura, P. Rakhila, C. Scholey, J. Uusitalo, P.Greenlees, T. Grahn, D. L. Balabanski, P. Petkov

Theoretical study of the isomeric cross section of the ^{197}Au(n,2n) reaction……13-18
A. Tsinganis, M. Diakaki, M. Kokkoris, A. Lagoyannis, C. T. Papadopoulos, R. Vlastou

Analysis of the Binding Energies of the Λ- Particle in Hypernuclei with the RHVT Approach and the Gauss Potential 19-24
C.A. Efthimiou, M.E. Grypeos, C.G. Koutroulos, Th. Petridou

Neutrino scattering off the stable even-even Mo isotopes……25-30
K.G. Balasi and T.S. Kosmas

Neutral current neutrino-^{94}Mo scattering in the context of the QRPA method……31-36
K.G. Balasi and T.S. Kosmas

Approximate symmetries in the Interacting Boson Model……37-42
Dennis Bonatsos

β^--Decay Half-lives Using the ANN Model: Input for the R-Process……...43-48
N. J. Costiris, E. Mavrommatis

Inelastic cross sections of relativistic protons on Lead……..49-54
M. Zamania, S. Stoulos, M. Fragopoulou, M. Manolopoulou, N. A. Sosnin and M. Krivopustov

Nuclear muon capture rates by using relativistic muon wavefunctions……55- 62
I.S. Kardaras, V.N. Stavrou, I.G. Tsoulos and T.S. Kosmas

Non-Linear Derivative Interactions in Relativistic Hadrodynamics…….63-68
T. Gaitanos, M. Kaskulov

SUSYQM in nuclear structure: Bohr Hamiltonian
with mass depending on the deformation……..69-74
Dennis Bonatsos, P. E. Georgoudis, D. Lenis, N. Minkov, C. Quesne

Electron Capture in Nuclear Structure and Astrophysics……..75-82
P. Giannaka T.S. Kosmas and V. Tsaktsara

Influence of parasitic neutrons to the ^{176}Hf(n,2n)^{175}Hf
reaction cross section…….83-88
R. Vlastou, M. Kokkoris, M. Serris, M. Lambrou, L. Sofokleous, M. Diakaki, A.Tsinganis,
V. Loisou and A. Lagoyannis

Tomographic Image Reconstruction based on Artificial Neural
Network (ANN) Techniques…….89-94
M. Argyrou, P. Paschalis, D. Maintas, E. Stiliaris

^{8}B and hep solar neutrino detection by terrestrial experiments……..95-100
G. I. Karathanou V.Tsikoudi T.S. Kosmas

Attempted study of the ^{237}Np(n,2n)^{236}Np reaction
cross section at 9.5 MeV……..101-106
M. Diakaki, R. Vlastou, M. Kokkoris, C. T. Papadopoulos, A. Tsinganis,
C. A. Kalfas, A. Lagoyannis and G. Provatas

Constraints on the inner edge of neutron star crusts from relativistic
nuclear energy density functionals……107-112
Ch.C. Moustakidis, T. Nikšić, G.A. Lalazissis, D. Vretenar, and P. Ring

Application of RBS and NRA for the Investigation
of Corrosion Resistance of Nitrogen - Implanted Steel……..113-120
F. Noli, P. Misaelides, A Lagoyannis, J.-P. Rivière

Theoretically and under very special applied conditions a nuclear
fission reactor may explode as nuclear bomb……...121-130
Kondylakis J.C.

Probing the ^{17}F+p potential by means of elastic scattering
at near barrier energies……131-134
N. Patronis, A. Pakou, D. Pierroutsakou, A. M. Sanchez-Benitez, L. Acosta, N. Alamanos, A.
Boiano, G. Inglima, D. Filipescu, T. Glodariu, A. Guglielmetti, N. Keeley, M. La Commara, I. Martel,
C. Mazzocchi, M. Mazzocco, P. Molini, C. Parascandolo, M. Sandoli, C. Signorini, R. Silvestri,
F. Soramel, E. Stiliaris, M. Romoli, A. Trzcinska, K. Zerva, E. Vardaci

Investigation of the Transient Field at High Velocities
by magnetic-moment measurements in ^{74}Ge and ^{70}Zn……135-138
T.J. Mertzimekis

Isoscaling of mass A $\cong$ 40 reconstructed quasiprojectiles

from collisions in the Fermi energy regime……..139-144
S. Galanopoulos, G.A. Souliotis, A.L. Keksis, M. Veselsky, Z. Kohley,L.W. May, D.V. Shetty, S.N. Soisson, B.C. Stein, S. Wuenschel, S.J. Yennello

High sensitive depleted MOSFET-based neutron dosimetry……...145-154
M. Fragopoulou, V. Konstantakos, M Zamani, S. Siskos, T. Laopoulosand G.Sarrabayrouse

Gamma spectrometry technique for the determination of residence time in Submarine Groundwater Discharges……155-162
G. Eleftheriou, C. Tsabaris, D. Patiris, E. Androulakaki, M. Kokkoris, R. Vlastou

Application of Information and Complexity Measures to Neutron Stars Structure……163-168
K.Ch. Chatzisavvas, V.P. Psonis, C.P. Panos, and Ch.C. Moustakidis

Search for E(5) Symmetry in ^{102}Pd……169-174
S. F. Ashley, S. Harissopulos, T. Konstantinopoulos, G. de Angelis, A. Dewald, A. Fitzler, N. Marginean, M. Axiotis, D. L. Balabanski, D. Bazzacco, E. Farnea, A. Linnemann, R. Julin, G. Kalyva, D. R. Napoli, C. Rusu, B. Saha, A. Spyrou, C. Ud, R. Vlastou

Detailed calculations for muon capture rates within the quasi-particle RPA……175-180
I.S. Kardaras,V.N. Stavrou,I.G. Tsoulos and T.S. Kosmas

Towards applications of graded Paraparticle algebras……181-186
Konstantinos Kanakoglou, Alfredo Herrera-Aguilar

Nuclear response to supernova neutrino spectra……187-192
V. Tsakstara T.S. Kosmas and J. Sinatkas

Studying supernova neutrinos through nuclear structure calculations……193-200
V. Tsakstara T.S. Kosmas and J. Sinatkas

Elastic backscattering measurments for ^{6,7}Li+^{58}Ni, ^{6,7}Li+^{116,120}Sn, ^{6,7}Li+^{208}Pb at near barrier energies……...201-203
K. Zerva, A. Pakou, N. Patronis, P. Figuera, A. Musumarra, A. Di Pietro, M. Fisichella, T. Glodariu, M. La Commara, T. Glodariu, M. Mazzocco, M. G. Pellegriti, D. Pierroutsakou, A. Sanchez Benitez, V. Scuderi, E. Strano

Electron fluence determination per Monitor Unit of a linear accelerator used for radiation therapy……204-207
A. Makridou, C. Tziaka, M. Fragopoulou, S. Stoulos and M. Zamani

19^{o} SYMPOSIUM OF THE
Symposium Programme

HELLENIC NUCLEAR PHYSICS SOCIETY
28 - 29 May 2010, Thessaloniki, Greece

Organising Committee:

Zamani – Valasiadou M.
Savvidis E.
Massen S.
Lalazissis G.

Friday 28/5/2010

Session 1: Chairman: Α. Πάκου

9:30 - 9:50 **Approximate symmetries in the Interacting Boson Model**
D. Bonatsos *Institute of Nuclear Physics, NCSR Demokritos*

9:50 - 10:10 **Non-Linear Derivative Interactions in Relativistic Mean-Field Theory**
Th. Gaitanos *Universität Giessen, Department Institut für Theoretische Physik*

10:10 - 10:30 **Influence of parasitic neutrons to the ^{176}Hf(n,2n)^{175}Hf cross section**
R. Vlastou et al. *Department of Physics, National Technical University of Athens*

10:30 - 10:50 **Neutron-Rich Rare-Isotope Production in Peripheral Heavy-Ion Collisions in the Energy Range of 15 MeV/nucl**
G.A. Souliotis *Laboratory of Physical Chemistry, Department of Chemistry, National and Kapodistrian University of Athens, Athens*

Session 2: Chairman: Ρ. Βλαστού

Προσκεκλημένη Ομιλία
11:30 - 11:55 **Σύγχρονες εξελίξεις στην ΤΕΧΝΟΛΟΓΙΑ ΠΥΡΗΝΙΚΗΣ ΕΝΕΡΓΕΙΑΣ, ασφάλεια, περιβάλλον**
Μ. Αντωνόπουλος – Ντόμης *Aristotle University of Thessaloniki, Electrical and Computer Engineering*
11:55 - 12:10 **Large Volume Spherical Proportional Counter: The structure and the applications**
I. Savvidis et al. *University of Thessaloniki, School of Physics, Nuclear and Elementary Particle*

12:10 - 12:25 **Alpha-Capture reactions in inverse kinematics relevant to p-process nucleosynthesis**
A. Lagoyannis et al. *Institute of Nuclear Physics, NCSR Demokritos, Aghia Paraskevi, Athens, Greece*

12:25 - 12:40 **Study of the ^{197}Au(n,2n) reaction cross section**
A. Tsinganis et al. *Department of Physics, National Technical University of Athens*

12:40 - 12:55 **Study of neutron threshold reactions on Np and Cd isotopes**
M. Diakaki et al. *Department of Physics, National Technical University of Athens*

12:55 - 13:10 **FIssion Detector In AStrophysics (FIDIAS)**
M. Axiotis et al. *Institute of Nuclear Physics, NCSR Demokritos, GR-15310 Athens, Greece*

Session 3: Chairman: Α. Λαγογιάννης

14:20 - 14:35 **Approaching marine environment by radiotracers' methods, the study of a submarine groundwater discharge source at southern Peloponnesus**
D.L. Patiris et al. *Hellenic Centre for Marine Research, Institute of Oceanography, P.O. Box 712, GR-19013 Anavyssos, Greece*

14:35 - 14:50 **^{7}Be concentrations in the atmosphere at a year of solar minimum**
E. Kotsopoulou and A. Ioannidou *Department of Physics, Nuclear Physics & Elementary Particle Physics Division, Aristotle University of Thessaloniki, 54124, Thessaloniki, Greece*

14:50 - 15:05 **Aquatic Radioactivity Applications at HCMR using the Gamma Ray Spectrometry Method**
C. Tsabaris et al. *Hellenic Centre for Marine Research, Institute of Ocenography, Department of Physics*

15:05 - 15:20 **Gamma spectrometry technique for the determination of residence time in Submarine Groundwater Discharges**
G. Eleftheriou et al. *Hellenic Centre for Marine Research, Institute of Oceanography, 19013 Anavyssos, Greece*

15:20 - 15:35 **Activity size distribution of ^{7}Be under the influence of meteorological conditions**
Vasileiadis et al. *Department of Physics, Nuclear Physics & Elementary Particle Physics Division, Aristotle University of Thessaloniki, 54124, Thessaloniki*

Session 4: Chairman: Δ. Μπονάτσος

16:05 – 16:25 **Energy Density Functionals : Description of Nuclear Quantum Phase Transitions**
G. A. Lalazissis *Department of Physics, Aristotle University of Thessaloniki GR-54124 Thessaloniki , Greece*

16:25 - 16:40 **Parabosons, parfermions and graded Lie algebras**
K. Kanakoglou *University of Michoacan (UMSNH), Morelia, Michoacan, Mexico*

16:40 - 16:55 **Probing the Nuclear Symmetry Energy at high baryon densities in heavy ion collisions**
V. Prassa *Department of Theoretical Physics, Aristotle University of Thessaloniki, GR-54124*

16:55 - 17:10 **Analysis of Binding Energies of the Λ- particle in hypernuclei with the RHVT Approach and the Gauss Potential**
C.A. Efthimiou, M.E. Grypeos, C.G. Koutroulos, Th. Petridou *Department of Theoretical Physics, Aristotle University of Thessaloniki, Greece*

17:10 - 17:25 **Isotopic distributions in ^{40}Ar projectile fragmentation**
N. Nicolis *University of Ioannina, Department of Physics*

18:00 Γενική Συνέλευση της Ελληνικής Εταιρείας Πυρηνικής Φυσικής

Poster List of the 19th Symposium of the Hellenic Nuclear Physics Society

28-29 May 2010, Thessaloniki

Vertical profiles of caesium – 137 in 3 different regions of Eastern Mediterranean Sea
Nikolaos Evangeliou and Heleny Florou *NCSR 'Demokritos', Institute of Nuclear Technology-Radiation Protection, Environmental Radioactivity Laboratory, 15310, Agia Paraskevi, Athens, Greece*

Isoscaling of mass A reconstructed quasiprojectiles from collisions in the Fermi energy regime
S. Galanopoulos *Hellenic Military Academy*

Theoretically and applied consideration (under very special conditions) a nuclear fission reactor may nuclear explode as nuclear bomb
Joseph-Christos Kondylakis *Hellenic Centre for Marine Research*

An online database for electromagnetic moments data
Th. Mertzimekis *NCSR Demokritos, Institute of Nuclear Physics*

Probing the 17F+p potential my means of elastic scattering measurements at near barrier energies
N. Patronis *University of Ioannina, Physics Department/ Nuclear Physics Laboratory*

Radiological Risk Assessment in an Ecosystem Using ERICA Assessment Tool: Deficiencies and Improvements
A. E. Maroudi, H. Florou, M. J. Anagnostakis *NCSR 'Demokritos', Institute of Nuclear Technology-Radiation Protection, Environmental Radioactivity Laboratory, 15310, Agia Paraskevi, Athens, Greece*

Characterisation and Corrosion Behaviour of Nitrogen-Implanted Steel by Nuclear Reaction Analysis.
F. Noli, P. Misaelides, *Department of Chemistry, Aristotle University, GR-54124 Thessaloniki, Greece*
A Lagoyannis *Tandem Accelerator Laboratory, Nuclear Physics Institute, NCSR Demokritos, GR-15310 Aghia Paraskevi- Attiki,Greece*

Indirect measurements of inelastic cross sections of relativistic protons in Lead target
M. Zamania, S. Stoulosa, M. Fragopouloua, M. Manolopouloua *a Aristotle University of Thessaloniki, School of Physics, Thessaloniki 54 124, Greece*
M. Krivopustov *Joint Institute for Nuclear Research (JINR) Dubna, Russia, 141980*

Electron capture in nuclear structure and astrophysics
P. Giannaka, T.S. Kosmas *Theoretical Physics Section, University of Ioannina, GR 45110 Ioannina, Greece*

High sensitivity MOSFET-based neutron dosimetry
M. Fragopoulou, Konstantakos V., M Zamani, S. Siskos, T. Laopoulos *Aristotle University of Thessaloniki, Physics Department, 54124 Thessaloniki, Greece*
G. Sarrabayrouse *CNRS; LAAS; 7 avenue du colonel Roche, F-31077 Toulouse, France & Université de Toulouse; UPS, INSA, INP, ISAE; LAAS; F-31077 Toulouse, France*

Shannon Entropy of the (n,A) and (p,A) reactions
V.P. Psonis and S.E. Massen *Department of Theoretical Physics, Aristotle University of Thessaloniki*

List of Participants of the 19th Symposium of the Hellenic Nuclear Physics Society

28-29 May 2010, Thessaloniki

Antonopoulos-Domis Michail	domis@eng.auth.gr
Argyrou Maria	margyrou@phys.uoa.gr
Ashley Stephen	sfashley@inp.demokritos.gr
Axiotis Michail	axiotis@inp.demokritos.gr
Balasi Konstantia	dbalasi@hotmail.com
Barbagiannidis Prokopis	probarb@hotmail.com
Bonatsos Dionysios	bonat@inp.demokritos.gr
Boutova Katia	mkatia@chem.auth.gr
Costriris Nick	ncost@phys.uoa.gr
Clouvas Alexandros	clouvas@eng.auth.gr
Diakaki Maria	diakakim@gmail.com
Efthimiou Kostas	eleonid@central.ntua.gr
Eleftheriadis Christos	Christos.Eleftheriadis@cern.ch
Eleftheriou Georgios	gelefthe@.central.ntua.gr
Evangeliou Nikos	nevag@ipta.demokritos.gr
Foteinou Varvara	foteinou@inp.demokritos.gr
Fountas Panagiotis	
Fragopoulou Marianthi	fragom@auth.gr
Gaitanos Theodoros	Theodoros.Gaitanos@theo.physik.uni-giessen.de
Galanopoulos Stratos	stratos.galanopoulos@gmail.com
Georgou Giorgos	geogeorg@physics.auth.gr
Georgoudis Panagiotis	
Giannaka Panagiota	pgiannak@cc.uoi.gr
Gogou Dimitra	dgkogkou@physics.auth.gr
Grypaios Michalis	grypeos@auth.gr
Gyrinis Vasilis	vgkiri@physics.auth.gr
Harissopoulos Sotirios	sharisop@inp.demokritos.gr
Hasioti Vassiliki	me00041@cc.uoi.gr
Hatzipanagiotidis Dimitris	
Huszank Robert	huszank@inp.demokritos.gr
Ioannidou Alexandra	anta@auth.gr
Iosifidis Damianos	
Kalamakis Giorgos	gkalamak@physics.auth.gr
Karabagia Sofia	
Karanatsiou Anna	
Kardaras Ioannis	iokard@cc.uoi.gr
Katsioulas Ioannis	
Kokkoris Michalis	kokkoris@central.ntua.gr
Kanakoglou Konstantinos	kanakoglou@hotmail.com; kanakoglou@ifm.umich.mx
Kondylakis Joseph-Christos	
Konstantinopoulos Theodoros	theodorekon@inp.demokritos.gr
Kosmas Theocharis	hkosmas@uoi.gr
Kotsopoulou Evdokia	ekotsopo@physics.auth.gr
Kourlitis Evangelos	kourlitisV@hotmail.com
Koutroulos Christos	
Lagoyannis Anastasios	lagoya@inp.demokritos.gr
Lalazissis George	glalazis@auth.gr
Makridou Anna	anna.makridou@gmail.com
Margellos Nikolaos	nmargell@physics.auth.gr

Maroudi Katerina	katerinamar@hotmail.com
Mertzimekis Theo	tmertzi@inp.demokritos.gr
Massen Stelios	massen@physics.auth.gr
Moni Chrysanthi	
Mouratidis Pavlos	paulmour1@gmail.com
Moustakidis Charalampos	moustaki@auth.gr
Nicolis Nikolaos	nnicolis@cc.uoi.gr
Noli Fotini	noli@chem.auth.gr
Pakou Athina	apakou@cc.uoi.gr
Patiris Dionisis	dpatiris@ath.hcmr.gr; dionisispatiris@gmail.com
Patronis Nikolas	npatronis@cc.uoi.gr
Petridou Theodora	theopet@auth.gr
Provatas George	gprovatas@inp.demokritos.gr
Prasa Vaia	bpras@physics.auth.gr
Psonis Vasileios	bpson@auth.gr
Samaropoulos Ioannis	
Santorinaiou Nefeli-Domniki	
Savvidis Ilias	savvidis@physics.auth.gr
Souliotis Georgios	soulioti@chem.uoa.gr
Stiliaris Efstathios	stiliaris@phys.uoa.gr
Stoulos Stelios	stoulos@auth.gr
Takoudis Georgios	takoudis@nestoras.ee.auth.gr
Tokousbalidis Konstantinos	
Tsabaris Christos	tsabaris@ath.hcmr.gr
Tsakstara Vaitsa	vtsaksta@cc.uoi.gr
Tsaleggidou Maria	mariat@nikhef.nl
Tsinganis Andreas	tsiganis@mail.ntua.gr
Tzavellas Ilias	
Vasileiadis Alexandros	
Vitalis Kyriakos	
Vlastou Roza	vlastou@central.ntua.gr
Zamani Maria	zamani@physics.auth.gr
Zerva Konstantina	kzerva@cc.uoi.gr

Proceedings of the 19th Hellenic Nuclear Physics Society Symposium (2010)

Radio-tracing techniques applied in a marine ecosystem, the case of a submarine groundwater source at southern Peloponnesus.

D.L. Patiris[a], G. Eleftheriou[b], A. P. Karageorgis[a], D. Georgopoulos[a], V. Papadopoulos[a], K. Stamoulis[c], K.G. Ioannides[d], R. Vlastou[b], C. Tsabaris[a]

[a] *Institute of Oceanography, Hellenic Center for Marine Research, 190 13 Anavyssos, Greece*

[b] *Department of Physics, National Technical University of Athens, 157 80 Athens, Greece*

[c] *Archaeometry Center, University of Ioannina, 451 10 Ioannina, Greece*

[d] *Nuclear Physics Laboratory, Physics Department, University of Ioannina, 451 10 Ioannina, Greece*

Abstract

The submarine discharge of groundwater (SGD) into the coastal zone has been recognized as an important component of the hydrological cycle. Quantities of groundwater flowing toward coastal aquifers are leaded under the seafloor and due to geomorphologic causes may discharge into the coastal zone. At some locations the quantity of the water is large enough to establish these springs as valuable water sources. The estimation of the submarine groundwater flux is complicated by conventional methods. Instead, measurements of a variety of radioisotopes (^{222}Rn, ^{214}Pb, ^{226}Ra, ^{228}Ra, ^{40}K, ^{3}H) as tracers provide a means to obtain integrated flux estimations as well as residence time, the age of the water and a factor of ground-sea water mixing process. Results from the current study at Stoupa's (S. Peloponnesus) SGD source are presented revealing the importance of radio-tracing methods to the investigation of marine ecosystems.

Key words: Marine ecosystems, submarine groundwater discharge, radio-tracing techniques.

1. Introduction

Groundwater contains enhanced radon concentrations, in comparison with surface or sea water, due to radium presence and decay in aquifers soil and rocks. There are four isotopes of radium in subsoil as partners of the primordial natural radioactive series of uranium and thorium but the most abundant is radium ^{226}Ra. Radon ^{222}Rn is the first decay product of ^{226}Ra and is an inert gas. It is transported into groundwater by diffusion through the aquifer soil or by the decay of diluted ^{226}Ra inside the groundwater mass. Despite the potential hazard for the public health which follows the use of enhanced radon groundwater, radon may be served as a radio-tracer in multiple hydrological studies. As noble gas does not react chemically with aquifer solids or other substances into the water, it is entirely dissolved, it has a short half life (3.8 days) and can be measured directly [1].

Radon has been already utilized as tracer in many studies around the world concerning mainly the subsurface discharge of groundwater from coastal aquifers into the sea, usually called SGD [2]. In general, this discharge contains meteoric water from land drainage and possibly seawater which may enter from coastal aquifers. A more detailed definition of SGD has been reported [3] while many studies consider the phenomenon as an important pathway of dissolved matter transport to the ocean [4-6]. There are three main sources of SGD: i) coastal freshwater aquifers where SGD is driven by the hydraulic gradient between land and sea; ii) re-circulated seawater in which tides and/or internal waves cause a circulation of seawater though coastal sediments; and iii) a mixture of both i) and ii).

The detection and quantification of such sources is realized by direct measurements with e.g. seepage flux meter or by tracer techniques. The later are based on measurements of geochemical species which are naturally enriched in SGD relative to seawater. As groundwater is rich of radon, many studies use this noble radioactive gas to quantify the emanating water and to investigate the temporal and spatial distribution of SGD [5], [7-8]. Measurements of radon are conducted either by laboratory based methods like, e.g., liquid scintillation [9], or by stripping of radon from a water sample [10] and consecutive measurement in the laboratory. Although these methods are well established, cannot provide extended time-series. When the temporal behaviour of a source and the fluctuations of radon concentration are needed, in-situ methods prevail in advantages as the detection systems are immersed exactly on the point of interest monitoring continuously for several days. However such applications are scarce due to the instrumentation which needed for detection purposes. They require special, fully-integrated detection systems able to withstand many hardships (e.g. enhanced pressure and mechanical stress, chemical corrosion fatigue etc.) due to “unfriendly” acquiring conditions.

The Hellenic Centre for Marine Research (HCMR) has developed an autonomous underwater gamma-ray spectrometer named “KATERINA” [11]. As this study is still in progress (May 2010) the article presents some first results from the deployments (July 2009 to December 2009) of the system into the submarine source of Stoupa. Also, the age of the groundwater has been estimated comparing the activity concentration of tritium ^{3}H in groundwater with rain water. Finally, as it is described with details elsewhere [12], it is possible to estimate the residence time of the flowing water into the groundwater paths using the activity concentration of radium isotopes.

2. Study area and experimental set up.

The SGD site at Stoupa, named after the small town of Stoupa in SW Peloponnesus, is located ~500 m off the coast. Limestones and dolomites, and to a lesser ex-tent metamorphic rocks characterize the geological made-up of the coastal zone. The carbonate rocks are heavily karstified and almost completely permeable. The submarine springs have been first recorded in 1975, though local inhabitants are well-aware of their existence and claim that the springs have never stopped emanating water for at least the past 60 years. Although, the main spring discharges water from significant depth (~26 m), the strength of the outflow generates a gyre at the surface, which is clearly visible, particularly under calm weather conditions. Preliminary observations by scuba divers revealed a system of four locations of SGDs, two strong (in terms of discharge) ones and two smaller ones all

within a distance of less than 100 meters. The two strongest SGDs emanate directly from rocks, with very strong currents especially during winter.

Inside the main underwater spring, in a depth of 26m, a measuring station was immersed by a team of divers. Onto the station an underwater gamma-ray spectrometer was attached in combination with a passive aquatic listener (PAL), rotor flow meters and conductivity/temperature (CT) data loggers (see figure 1). The spectra were stored, after 12h of acquisition, in a special memory which is incorporated in the system and they were extracted after the recovery of the measuring station. The analysis of the spectra was performed with SPECTRW software. Radon progenies (^{214}Pb and ^{214}Bi) and potassium ^{40}K activity concentrations were quantitatively measured in Bq/m^3 using the appropriate marine efficiency parameters [13]. Also, a number of groundwater samples were collected by the divers. A small quantity (10ml) of groundwater, immediately after the collection, was ejected by syringes into plastic vials containing liquid scintillator. These samples were transported within 24h to the Archaeometry centre of University of Ioannina and were counted by means of a liquid scintillation counter (LSC) providing the activity concentration of radon ^{222}Rn itself. Moreover, to obtain the activity concentration of tritium ^{3}H, 100 ml of groundwater after standard preparation procedures (filtration, evaporation) were also measured by the LSC method.

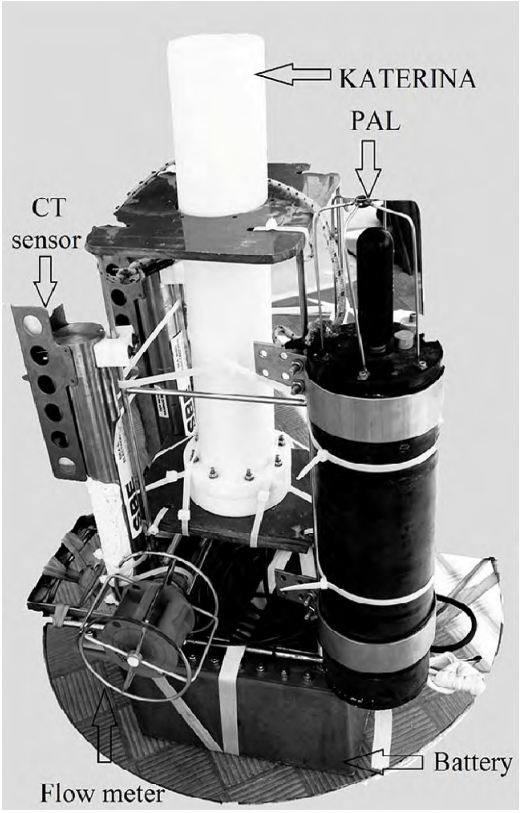

Figure 1. The station with several sensors including the underwater gamma-ray spectrometer KATERINA

3. Results and discussion.

3.1. Radon progenies and potassium time-series.

From the autumn to winter of 2009, a number of deployments of the measuring station took place, during a meteorological period with wet (rainfalls) and dry (no rainfalls) terms. Significant variations in the flow rate of the SGD were observed, which were reflected in the flux velocity measurements. In figure 2 indicative data concerning flux velocity and activity concentrations are plotted as time-series. During October and November of 2009 the activity concentration of radon progenies (^{214}Pb and ^{214}Bi) exhibits a strong correlation with flux velocity (flow rate). Although ^{214}Bi data are presented, ^{214}Pb was found in radioactive equilibrium with ^{214}Bi, and thus ^{214}Pb exhibits the same behaviour. In contrast, the activity concentration of ^{40}K was found inversely proportional to flux velocity. The above results have a physical interpretation. The emanating water may contain radon enhanced groundwater and seawater

which is rich in potassium and almost radon free. During the wet periods the amount of the groundwater into the emanating water is increased (against the re-circulated seawater), resulting greater flow rate/velocity and radon concentration. Conversely, during dry terms the amount of the groundwater is decreased causing lower levels of radon progenies activity concentrations and higher

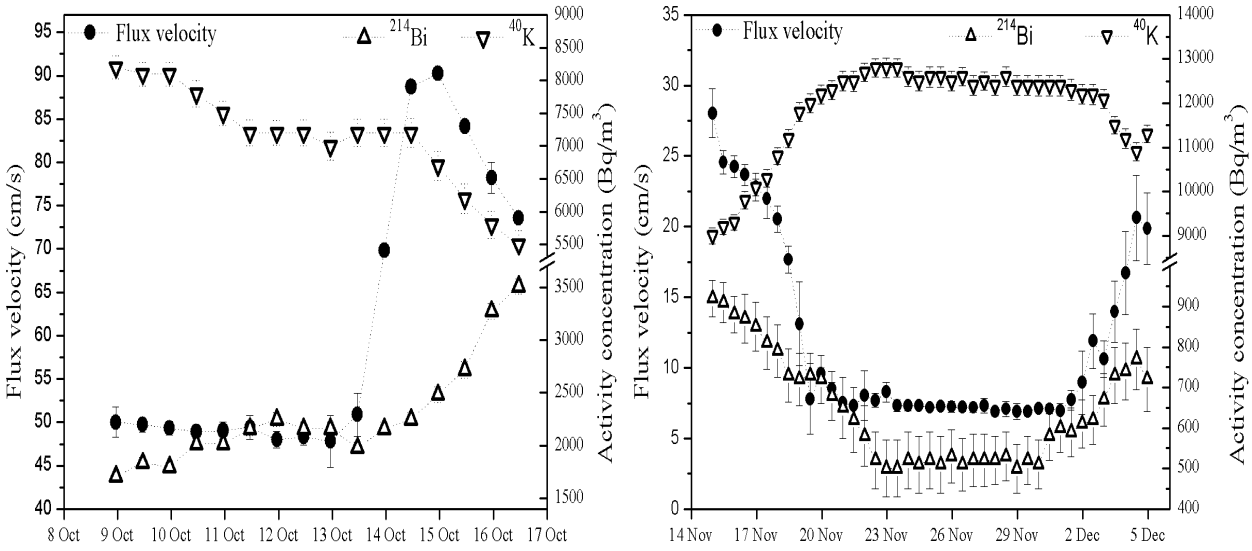

Figure 2: The activity concentration of radon progeny ^{214}Bi and potassium ^{40}K as time-series in respect with the velocity of the emanating groundwater. The radon progeny of ^{214}Pb was found in radioactive equilibrium with ^{214}Bi

levels of potassium. Also, till the current stage of the study, the radon measurements by LSC methods revealed no equilibrium between radon and its progenies. For instance, during the first deployment (late of July 2009) the activity concentration of radon was measured (by LSC) two times greater than its progenies (measured by KATERINA). As the water flows continuously, the time that a quantity of water remains in the vicinity (effective volume) of the underwater detector is not sufficient for a state of secular equilibrium between radon and its progenies to be reached.

3.2. Groundwater ageing using tritium concentrations.

Tritium is produced in the upper layers of the atmosphere from the interaction of cosmic rays (fast neutrons) with atmospheric nitrogen. It can combine with oxygen to form tritiated water (really heavy water) and following the water circle enters into the sub-soil aquifers from precipitation. Its half-live of 12.32y makes it an important tool to hydrology as age dating radio-tracer. In this study, the average value of activity concentration of tritium (in tritium units) containing in the groundwater of two submarine springs (SGD1 and SGD2) was compared with those into rainwater and terrestrial groundwater (Terr.1-5). As the study is still in progress, the so far results are depicted in figure 3. The main observation is the slight differences (less than the statistic error) of the measured activities of tritium from the sources in comparison with the levels of tritium in the rainwater (dot-line fig.3).

This fact is a strong indication of the small age of the groundwater which means that it remains into the aquifer for a short time period (less than six months according to detection limit) before emanates from a submarine or a terrestrial source. For accurate estimation of the groundwater age, pre-concentration of tritium from more massive samples via electrolysis has to be followed. Although the outcome was not estimated accurately, the fact that the age of the water does not outgo a period of approximately six months, may be turn into significant information for hydrologists.

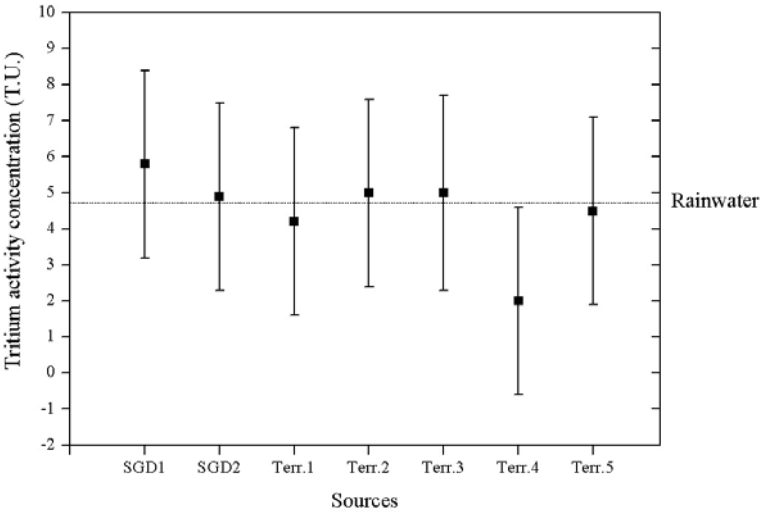

Figure 3. Activity concentration measurements (mean values) of tritium in groundwater emanating from submarine and terrestrial sources in comparison with the average tritium level of rain.

4. Conclusions

In this study was attempted the use of radio-tracing techniques in the investigation of a submarine groundwater source located near shore from Stoupa village / southern Peloponnesus. The underwater gamma-ray spectrometer KATERINA was utilized to record radon progenies (^{214}Pb and ^{214}Bi) and potassium (^{40}K) activity concentrations for long time periods providing results as time series. During the deployments of the winter of 2009, radon progenies activity concentrations revealed proportional fluctuations with the groundwater flux while potassium inversely proportional fluctuations. This fact indicates that an alternative method for flow rate estimations based on these radioisotopes could be developed. Also, using measurements of radon itself by means of a liquid scintillation counter, a non equilibrium state between radon and its progenies was revealed due to the fast moving of the water in the effective volume of the underwater spectrometer. The age of the ground water was estimated less than six months by the difference of tritium activity concentration in the groundwater and in the rainwater. Summarizing, in this study several radio-tracing techniques were used in combination with direct measurements of groundwater parameters (salinity, water flux, temperature etc). The so far results are promising for the development of new methods based on radioisotopes boosting the research of marine environment.

References

[1] D.Porcelli, Radioactiv. Environm. 13 (2008) 105-153.

[2] M.A. Charette, W.S. Moore and W.C. Burnett, Radioactiv. Environm. 13 (2008) 155-191.

[3] W.C. Burnett, H. Bokuniewicz, M. Huettel, W.S. Moore, and M. Taniguchi, Biochem. 66 (2003) 3-33.

[4] W.C. Burnett and H. Dulaiova, J. Environ. Radioactiv. 69 (2003) 21-35.

[5] W.C. Burnett , P.K. Aggarwal, A. Aureli, H. Bokuniewicz, J.E. Cable, M.A. Charette, E. Kontar, S. Krupa, K.M. Kulkarni, A. Loveless, W.S. Moore, J.A. Oberdorfer, J. Oliveira, N. Ozyurt, P. Povinec, A.M.G. Privitera, R. Rajar, R.T. Ramessur, J. Scholten, T. Stieglitz, M. Taniguchi, and J.V. Turner, Sci. Total Environ. 367 (2006) 498-543.

[6] W.S. Moore, Mar. Chem. 65 (1999) 111-125.

[7] W.C. Burnett and H. Dulaiova, Cont. Shelf. Res. 26 (2006) 862-873.

[8] W.C. Burnett, R. Peterson, W.S. Moore and J. Oliveira, Estuar. Coast. Shelf S. 76 (2008) 501-511.

[9] S. Purkl, and A. Eisenhauer, Mar. Chem. 87 (2004) 137-149.

[10] G.G. Mathieu, P.E. Biscaye, R.A. Lupton, and D.E. Hammond, Health Phys. 55 (1988) 989-992.

[11] C. Tsabaris, C. Bagatelas, Th. Dakladas, C.T. Papadopoulos, R. Vlastou, G.T. Chronis, Appl. Radiat. Isotopes 66 (2008) 1419-1426.

[12] G. Eleftheriou, C. Tsabaris, D. Patiris, E. Androulakaki,M. Kokkoris, R. Vlastou, Proc. 19th HNPS Symp.

[13] C. Bagatelas, C. Tsabaris, M. Kokkoris, C.T. Papadopoulos and R. Vlastou, Environ. Monit. Assess 165 (2009) 159-168.

^{128}Xe: Test for E(5) Symmetry through DDCM and GOSIA Analysis

T. Konstantinopoulos[a], A. Lagoyannis[a], S. Harissopulos[a], A. Dewald[b], C. Fransen[b], G. Frießner[b], M. Hackstein[b], J. Jolie[b], G. Pascovici[b], Th. Pissulla[b], W. Rother[b], K.-O. Zell[b], G. Ilie[h], H. Iwasaki[d], B. Melon[g], U. Jakobsson[c], R. Julin[c], P. Jones[c], S. Ketelhut[c], P. Nieminen[c], P. Peura[c], P. Rakhila[c], C. Scholey[c], J. Uusitalo[c], P. Greenlees[c], T. Grahn[e], D. L. Balabanski[f], P. Petkov[f]

[a] *Institute of Nuclear Physics, National Centre for Scientific Research "Demokritos", 15310 Aghia Paraskevi, Athens, Greece*
[b] *Institut för Kernphysic, Universität zu Köln, Zülpicherst, 77, D-50937 Köln, Germany*
[c] *Department of Physics, University of Jyväskylä, P.O. Box 35, 40014 Jyväskylä, Finland*
[d] *National Superconducting Cyclotron Laboratory, Michigan State University, East Lansing, Michigan 48824, USA*
[e] *Oliver Lodge Laboratory, University of Liverpool*
[f] *INRNE, Sofia, Bulgaria*
[g] *Dipartimento di Fisica, Universitü di Firenze and INFN Sezione di Firenze, Sesto Fiorentino (Firenze), I-50019*
[h] *Wright Nuclear Structure Laboratory, Yale University, New Haven, Connecticut 06520, USA*

Abstract

Lifetime measurements in ^{128}Xe have been undertaken at the JYFL accelerator facility using the novel Coulex-plunger in inverse kinematics technique [1], [2]. Excited states in ^{128}Xe were populated by the ^{nat}Fe(^{128}Xe, ^{128}Xe*) reaction at E(^{128}Xe)=525 MeV and the subsequent de-excitations were detected in the JUROGAM γ-ray array. Two independent analyses of the data were performed. Firstly the Differential Decay Curve Method (DDCM) [3] was applied to determine lifetimes of the excited states. Secondly, matrix elements and their corresponding B(E2) values, were extracted using the computer code GOSIA [4]. The results are presented and compared with the adopted values. Also, B(E2) values obtained from this work are compared to the values predicted by the E(5) critical-point symmetry, since ^{128}Xe has been proposed as a candidate for E(5) symmetry [5].

1. Motivation

The E(5) and X(5) critical point symmetries introduced by F. Iachello [6] describe systems that undergo shape-phase transitions. To date, X(5) symmetry is assumed to be well established [7] whereas this does not fully apply for the case of E(5) symmetry. Under these conditions, the confirmation of the E(5) symmetry in nuclear structure is still an open question motivating further experimental investigation. Among the E(5) candidates proposed, ^{128}Xe and ^{130}Xe have been underlined as two of the most promising ones. Their excitation spectra are indeed in good agreement with those predicted by the E(5) symmetry.

Preprint submitted to Elsevier *April 30, 2011*

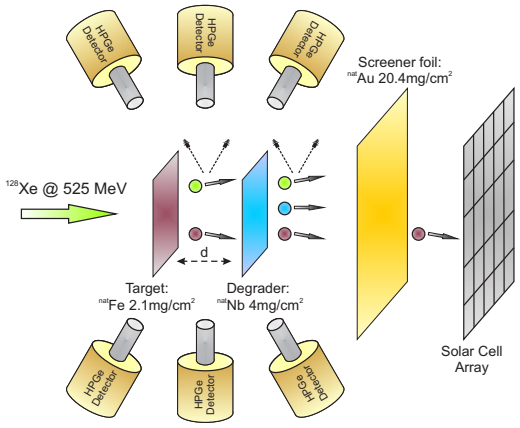

Figure 1: The experimental setup for the Coulex-Plunger technique is shown in the figure. The array of solar cells was placed at the endcap of the beamline covering an angular span between 8^o and 35^o around the beam axis. This allowed the detection of the Fe recoils which gave a clear trigger for the reaction.

A major problem in determining the lifetimes of these nuclei arises from the fact that they cannot be populated in a "standard" plunger experiment, i.e. in a heavy ion induced fusion-evaporation reaction. In addition, as they are in gaseous form they cannot be used as targets. A solution to this problem is Xe-induced Coulomb excitation. In this case, however, the analysis of the measured spectra is often not transparent. The combination of Coulomb excitation with the Recoil-Distance Doppler Shift method, known as Coulex-Plunger technique, has proved to be [8] a powerful experimental approach to determine lifetimes in the pico-second regime, enabling lifetime measurements of yrast as well as non-yrast collective states. The reduced transition probabilities of these states can provide a clear signature of the critical-point symmetry in a nucleus and as such they are of key importance in nuclear structure studies. Applying the Coulex-Plunger technique in inverse kinematics is, from an experimental point of view, a very challenging task not only because of various experimental problems but also because of its possible applicability to lifetime measurements with radioactive ion beams (RIB). On top of confirming the E(5) critical-point symmetry in ^{128}Xe and ^{130}Xe, the increasing interest in RIB worldwide was a strong motivation to perform the present feasibility study of the Coulex-Plunger technique in inverse kinematics.

2. Experimental Setup

The experimental setup is shown in Fig.1. The ^{128}Xe delivered by the Jyväskylä cyclotron with energy of 525 MeV passed through a $2.1 mg/cm^2$ Fe foil that served as target. The Coulomb-excited ^{128}Xe nuclei were subsequently retarded by a $4 mg/cm^2$ thick Nb foil. The Fe recoils were detected by an array of solar cells arranged at angles between 8^o and 35^o around the beam axis. The setup was surrounded by the JUROGAM array which consists of 45 high purity Ge detectors (HPGe) arranged in six different angles from 157.6^o to 72.05^o with respect to the beam. A screening Au foil was placed

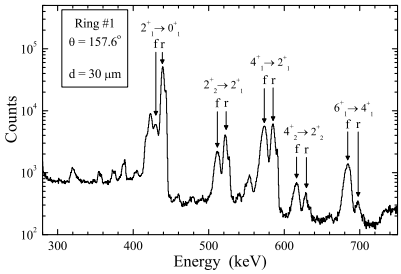

Figure 2: A typical RDDS spectrum is shown. Marked with "f" and "r" are the "flight" and "retarded" component accordingly of each of the five strongest transitions of the Coulomb excited ^{128}Xe. The spectrum is taken at an intermediate plunger distance of 30μm therefore both shifted and unshifted components are clearly visible.

in front of the solar cells. It was $20.4mg/cm^2$ thick in order to stop the Xe and Nb recoils allowing only the Fe nuclei to be detected by the solar cells. The latter recoils served as trigger for Coulomb excited events occurring in the target. This way, particle-γ coincidences between the Fe recoils and the γ-rays depopulating Coulomb-excited states of ^{128}Xe were recorded at 13 plunger distances ranging from 3 to 300 μm. A typical plunger spectrum is shown in Fig.2.

3. Differential Decay Curve Method and GOSIA analysis

The data were first sorted using the code "Grain" [9] and they were subsequently analyzed. Initially, the well known DDCM procedure for the γ-γ-coincidence as well as for the "singles" mode case was applied as described in [3] and [10]. Using this procedure lifetimes were extracted for the first 2^+, 4^+ and 6^+ levels as well as for the second 2^+ as can be seen in figure 3. It must me noted that an independent analysis of the data using the Bateman equations allowed the determination of the 3^+_1 lifetime [11].

As it was mentioned above, the Xe nuclei were excited through the very well known Coulomb interaction thus it is also possible to perform a full Coulomb excitation analysis of the data set by implementing the computer code GOSIA [4]. GOSIA is a least-squares search code, developed to analyze large sets of experimental data in order to determine the electromagnetic matrix elements involved in heavy-ion induced Coulomb excitation. As an input one gives the detector geometry (angles, distances etc.), the level scheme of the investigated nucleus along with any known experimental values such as branching ratios, the γ-yields measured in the experiment and an initial set of matrix elements which serve as a starting point for the minimization procedure. As an output GOSIA gives the full set of the matrix elements and the corresponding chi-square value which indicates the quality of the fit.

One should take notice that for the γ yields measured in the various Ge detectors, the Fe recoil angle needs to be defined. This is achieved in the off-line analysis of the data by using one solar cell at a time as a trigger for the filling of the γ-spectra. In figure

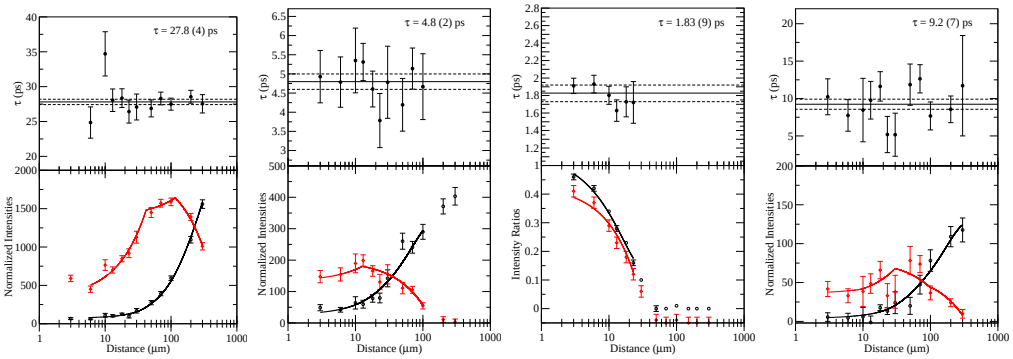

Figure 3: The lifetimes determined through the DDCM analysis for the 2_1^+, 4_1^+, 6_1^+ and 2_2^+ states are shown along with exemplary tauplots. The fitting of the decay curves and the extraction of lifetimes was done with the computer program NAPATAU [12].

4 the γ-yields determined by using three different solar cells as a trigger are shown along with the GOSIA fit.

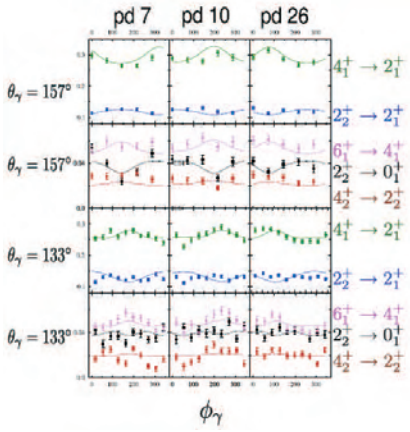

Figure 4: Measured (squares) and fitted (solid lines) γ-intensities for various transitions measured at θ_γ=133^o and θ_γ=157^o in coincidence with the solar cells 7, 10 and 26. Each of the three columns corresponds to the γ-yields measured in coincidence with one solar cell. This way the Fe recoil angle is fixed. The figure is taken from [13].

4. Results and comparison with the E(5) level scheme

The results derived from both analyses procedures, as described above, are summarized in table 1 together with the values given in literature for comparison. Transition strengths for all the involved transitions were calculated either by the lifetimes determined by the DDCM technique or directly from the matrix elements obtained from the

Level	Literature (KK01[14])	Literature (SCK93[15])	DDCM	GOSIA
2_1^+	30.7 (2)	27.0 (3)	28.8 (3)	28.1 (8)
4_1^+	5.0 (4)	5.0 (4)	5.0 (5)	5.0 (3)
6_1^+	1.6 (1)	1.6 (2)	1.8 (1)	1.97 (8)
2_2^+	8.2 (7)	8.4 (8)	8.7 (5)	7.1 (2)
4_2^+	-	3.6 (6)	-	2.1 (16)

Table 1: The lifetimes extracted from this measurement are shown in comparison with the values given in literature. The DDCM values are weighted averages of the lifetimes obtained from the γ-γ-coincident as well as the "singles" data. Good agreement is observed in most cases.

GOSIA analysis. In figure 5 the comparison of the derived experimental B(E2) values with the predictions of the E(5) critical point symmetry clearly shows that ^{128}Xe is not an E(5) nucleus.

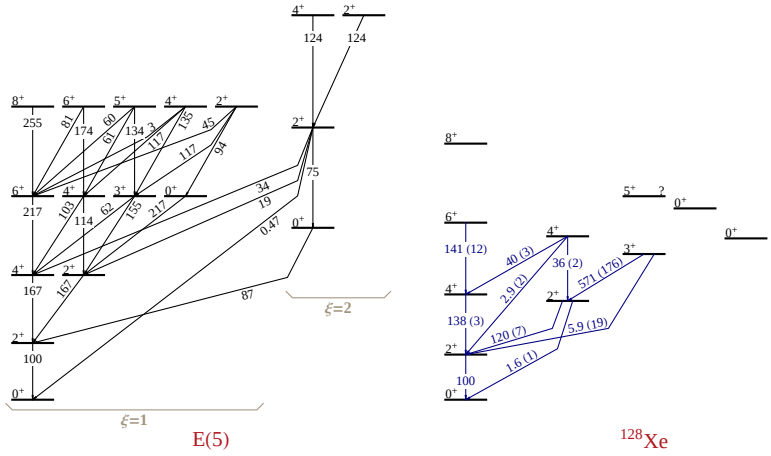

Figure 5: The derived transition strengths for ^{128}Xe are compared to the E(5) predictions. The B(E2) values are all normalized to the $2_1^+ \rightarrow 0_1^+$ transition. It can be seen that although ^{128}Xe does show E(5) features, deviations are apparent thus showing that it is not an E(5) nucleus.

5. Conclusions

Lifetimes of ^{128}Xe were extracted with the implementation of the proposed novel experimental technique named Coulex-Plunger in inverse kinematics. This technique enables a "direct" measurement of the effective lifetimes through the DDCM analysis

and an independent determination of the matrix elements of the involved transitions through a Coulomb excitation analysis of the data. The experimental setup is simple and efficient providing us with enough statistics even for the case of the γ-γ-coincidence analysis. Finally, by comparing the derived transition strengths with the ones predicted by the E(5) critical point symmetry it is clearly shown that ^{128}Xe is not an E(5) nucleus.

References

[1] T. Konstantinopoulos, A. Lagoyannis, S. Harissopulos, A. Dewald, W. Rother, G. Ilie, P. Jones, P. Rakhila, P. Greenlees, T. Grahn, R. Julin, D. Balabanski, ^{128}Xe lifetime measurement using the coulex-plunger technique in inverse kinematics, Vol. 1012, American Institute of Physics, 2008, p. 377.

[2] W. Rother, A. Dewald, G. Ilie, T. Pissulla, B. Melon, J. Jolie, G. Pascovici, H. Iwasaki, M. Hackstein, K. Zell, R. Julin, P. Jones, P. Greenlees, P. Rahkila, J. Uusitalo, C. Scholey, S. Harissopulos, A. Lagoyannis, T. Konstantinopoulos, T. Grahn, D. Balabanski, P. Petkov, Development of a new recoil distance technique using Coulomb excitation in inverse kinematics, Vol. 1090, American Institute of Physics, 2009, pp. 107–111.

[3] A. Dewald, S. Harissopulos, P. von Brentano, The differential plunger and the differential decay curve method for the analysis of recoil distance doppler-shift data, Zeitschrift fur Physik A Hadrons and Nuclei 334 (2) (1989) 163–175. doi:10.1007/BF01294217.

[4] T. Czosnyka, D. Cline, W. C.Y., Coulomb excitation data analysis code: GOSIA, Nuclear Structure Research Laboratory, University of Rochester (October 2007).

[5] R. M. Clark, M. Cromaz, M. A. Deleplanque, M. Descovich, R. M. Diamond, P. Fallon, I. Y. Lee, A. O. Macchiavelli, H. Mahmud, E. Rodriguez-Vieitez, F. S. Stephens, D. Ward, Searching for E(5) behavior in nuclei, Phys. Rev. C 69 (6) (2004) 064322. doi:10.1103/PhysRevC.69.064322.

[6] F. Iachello, Dynamic symmetries at the critical point, Phys. Rev. Lett. 85 (17) (2000) 3580–3583. doi:10.1103/PhysRevLett.85.3580.

[7] A. Dewald, O. Möller, B. Saha, K. Jessen, A. Fitzler, B. Melon, T. Pissulla, S. Heinze, J. Jolie, K. O. Zell, P. von Brentano, P. Petkov, S. Harissopulos, G. De Angelis, T. Martinez, D. R. Napoli, N. Marginean, M. Axiotis, C. Rusu, D. Tonev, A. Gadea, Y. H. Zhang, D. Bazzacco, S. Lunardi, C. A. Ur, R. Menegazzo, F. E., Test of the critical point symmetry X(5) in the mass A = 180 region, J. Phys. G: Nucl. Part. Phys. 31 (2005) 1427–1432. doi:doi:10.1088/0954-3899/31/10/008.

[8] R. Krücken, B. Albanna, C. Bialik, R. F. Casten, J. R. Cooper, A. Dewald, N. V. Zamfir, C. J. Barton, C. W. Beausang, M. A. Caprio, A. A. Hecht, T. Klug, J. R. Novak, N. Pietralla, P. von Brentano, B(E2) values in Nd^{150} and the critical point symmetry X(5), Phys. Rev. Lett. 88 (23) (2002) 232501. doi:10.1103/PhysRevLett.88.232501.

[9] P. Rahkila, Grain - a Java analysis framework for total data readout, Nuclear Instruments and Methods in Physics Research Section A: Accelerators, Spectrometers, Detectors and Associated Equipment 595 (3) (2008) 637–642. doi:DOI: 10.1016/j.nima.2008.08.039.

[10] G. Böhm, A. Dewald, P. Petkov, P. von Brentano, The differential decay curve method for the analysis of doppler shift timing experiments, Nuclear Instruments and Methods in Physics Research Section A: Accelerators, Spectrometers, Detectors and Associated Equipment 329 (1-2) (1993) 248 – 261. doi:DOI: 10.1016/0168-9002(93)90944-D.

[11] W. Rother, Development of a new recoil distance technique using Coulomb excitation in inverse kinematics, Master's thesis, Institut für Kernphysik der Universität zu Köln (2008).

[12] B. Saha, Program NAPATAU, Institute for Nuclear Physics, Cologne, unpublished.

[13] M. Hackstein, Determination of absolute transition probabilities and quadropole moments in ^{128}Xe, Master's thesis, Institut für Kernphysik der Universität zu Köln (June 2009).

[14] M. Kanbe, K. Kitao, Nuclear data sheets for A = 128, Nuclear Data Sheets 94 (2) (2001) 227 – 395. doi:DOI: 10.1006/ndsh.2001.0019.

[15] J. Srebrny, T. Czosnyka, W. Karczmarczyk, P. Napiorkowski, C. Droste, H.-J. Wollersheim, H. Emling, H. Grein, R. Kulessa, D. Cline, C. Fahlander, El, E2, E3 and M1 information from heavy ion Coulomb excitation, Nuclear Physics A 557 (1993) 663 – 672. doi:DOI: 10.1016/0375-9474(93)90578-L.

Theoretical study of the isomeric cross section of the ^{197}Au(n,2n) reaction

A. Tsinganis[a], M. Diakaki[a], M. Kokkoris[a], A. Lagoyannis[b], C. T. Papadopoulos[a], R. Vlastou[a]

[a] *Department of Physics, National Technical University of Athens, Greece*
[b] *Institute of Nuclear Physics, NCSR "Demokritos", Athens, Greece*

Abstract

In the present work, the ^{197}Au(n,2n) reaction cross section is studied within the framework of the Generalized Superfluid Model (GSM). The cross sections for the population of the second isomeric state (12^-) of ^{196}Au and the sum of the ground (2^-) and first isomeric state (5^-) population cross sections were independently studied in the 8 to 25 MeV region with the use of the STAPRE-F, EMPIRE and TALYS codes, which were also compared in their implementation of the GSM. The theoretical results are compared with previous work in the same mass region and the strong dependence on the level scheme of the nuclei involved was revealed.

1. Introduction

The presence of a high spin isomeric state in the residual nucleus of a neutron threshold reaction provides a sensitive test for existing nuclear models. The study of such reactions is a powerful tool for getting information on the structure of nuclei. In particular, the nuclei of the transitional region from well deformed to spherical nuclei near the Z=82 shell closure (Os-Pb region) present a very complex structure (γ-softening, triaxiality, shape coexistence) and for most of them an isomer with a high spin value with respect to the spin of the corresponding ground state has been reported. For the same element the energy of this isomer increases with increasing mass number A. Its existence is attributed to the coupling of high spin intruder states, and the systematic study of the excitation function of the formation of both the ground and the high spin isomeric state on the basis of a statistical model provides information on the energy and spin distribution of the level density of the nuclei involved [1] and on the changes in the structure of the low lying excited states of the corresponding nuclei.

In this context the ^{196}Au isotope presents an interesting isomeric pair: ground and isomeric states with spin values of 2^- and 12^- respectively (Fig. **??**). This 12^- isomer has been reported for other even A Au isotopes (^{198}Au, ^{200}Au) [2]. However, a survey of the literature revealed only a limited number of experimental data for the cross section of the ^{197}Au(n,2n)^{196}Au^{m2} reaction, especially near its threshold, where only one unpublished dataset [3] was found.

Thus, the purpose of this work was to perform theoretical statistical model calculations of the ^{197}Au(n,2n)^{196}Au^{m2} and the ^{197}Au(n,2n)^{196}Au^{g+m1} reaction cross sections in the 8 to 25 MeV incident neutron energy range. The results of the theoretical calculations were compared to the experimental data obtained in the first phase of this work and to all available experimental data in the above energy range to study the contribution of the spin distribution and the details of the level scheme of the residual nucleus to the formation of the isomeric state.

2. Theoretical Calculations

Theoretical cross section calculations in the energy region between 8 and 25 MeV were performed taking into account the compound and pre-compound nuclear processes, in the framework of the Hauser-Feshbach theory [4] and the exciton model [6] respectively. The level densities of the nuclei involved in the calculations were treated within the Generalized Superfluid Model (GSM) in its phenomenological version developed by

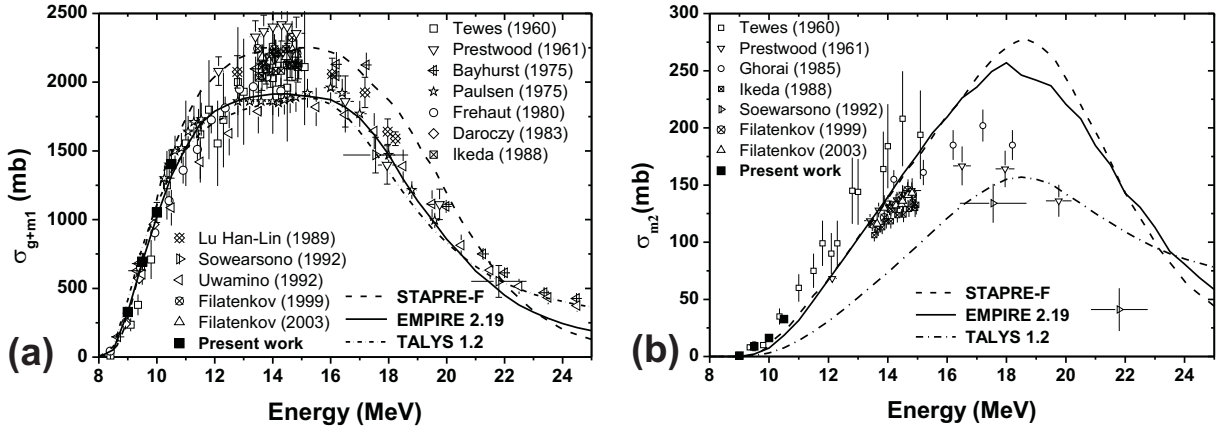

Figure 1: Experimental values and theoretical calculations for the population of the ground and first isomeric state of ^{196}Au (g+m1) (a) the second isomeric state of ^{196}Au (m2) (b). Several single-point datasets around 14 MeV omitted for clarity.

Ignatyuk et al [7, 8], which takes into account superconductive pairing correlations, shell effects and collective enhancement of the level density of the nucleus in a consistent way. It has already been successfully used in the past for theoretical cross section calculations in ^{191}Ir [9], which also lies in the transitional Os-Pb region. The calculations were carried out using three codes, STAPRE-F [10], EMPIRE 2.19 [11] and TALYS-1.2 [12].

The choices for the transmission coefficients, the preequilibrium and the level densities used for the calculations of the three codes were made in order to compare how the three codes implement the generalized superfluid model. The STAPRE-F code provides a local approach in which a consistent calculation is made using local model parameters established on the basis of various independent data, while EMPIRE and TALYS provide global approaches of the nuclear models included [15, 16].

The theoretical calculations obtained from the three codes for σ_{g+m1} and σ_{m2}, along with the data from this work and the previous measurements are presented in figure 1.

As can be seen, the results from all three codes fairly reproduce the trend of the experimental data for σ_{g+m1}. The theoretical curves appear to span the whole range of the experimental values in the 12-16 MeV region where large discrepancies in the data exist. This precludes a conclusion on the accuracy of the results in this region.

Concerning the cross section of the second isomeric state (Fig. 1b) the STAPRE-F and EMPIRE theoretical calculations seem to underestimate the near-threshold data up to about 13 MeV, while in the high-energy region they overestimate the cross sections by about 100 mb, despite the large discrepancies among the experimental data. The TALYS calculation underestimates the data in the whole energy range, a behavior also encountered in [15]. Furthermore, in all cases the cross section attains its maximum value at around 18 MeV, about 2 MeV higher than the experimental data suggests. This result will be discussed later. Nevertheless, all three codes reproduce the general trend of the experimental data.

Based on these observations, several tests were made, using the STAPRE-F code, to better reproduce the isomeric cross section results by changing the input parameters of the theoretical calculations. Particular attention was given to the value of $\tilde{\alpha}$ which is the level density parameter at high excitation energies and plays an important role in the calculations. These values were changed in a consistent way within their experimental uncertainties (i.e. $\pm$ 6 %) for $^{195-198}$Au isotopes and, subsequently, the systematics proposed in [13, p.103] were tested. Nevertheless, none of these attempts seemed to simultaneously improve the fit to the experimental data of σ_{m2}, σ_{g+m1} and the cross section values of the (n,3n) reaction. Changing the average experimental total radiation width and the moment of inertia of the ground state within their experimental uncertainties, the percentage of preequilibrium emission and the assumptions on the shape and symmetry of the Au isotopes also had limited effect.

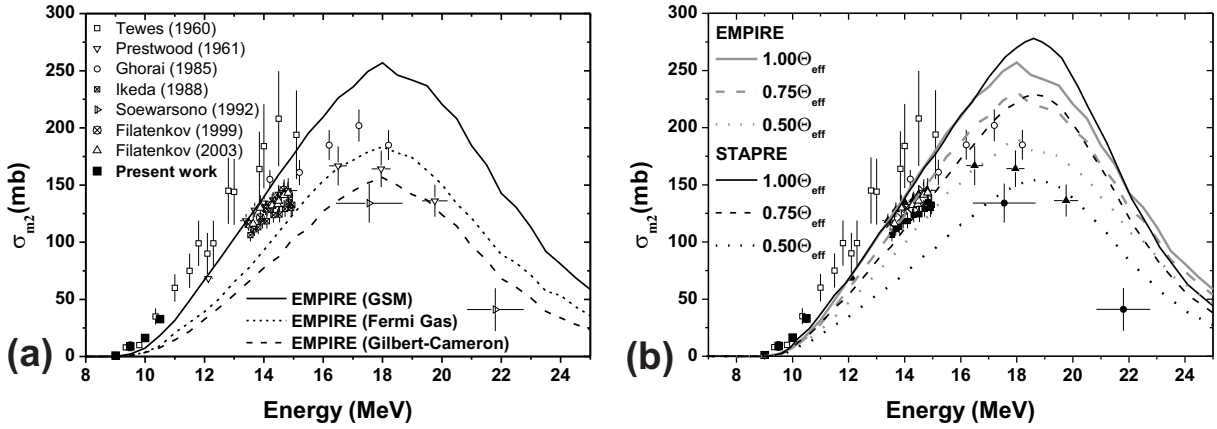

Figure 2: Theoretical calculations for σ_{m2} using the Fermi gas and Gilbert-Cameron level density models, compared to the result using the GSM (a) and theoretical calculations for σ_{m2} using values of the effective moment of inertia reduced by 25 and 50%. (b).

In order to understand and correct the shift of the σ_{m2} theoretical curve, the calculations were repeated using the Back Shifted Fermi Gas [17] and the Gilbert-Cameron level density models [18] with the EMPIRE code, leaving the rest of the input parameters as mentioned above. The results (Fig. 2) show that the shift of the isomeric cross section curve is independent on the model of the level density of the nuclei involved and also on the implementation of the GSM in the three codes used.

Generally, the population of the high spin isomers is highly dependent on the spin distribution of the continuum. The effect of this factor on the feeding of the 12^- isomer was examined in order to improve the theoretical predictions.

In previous cross section measurements of high spin isomers in nuclei belonging to the transitional region from the well deformed Os to the spherical Pb isotopes [9, 19–21] the need of the reduction of the effective moment of inertia was pointed out, in order to better reproduce the data of σ_{m2} and the isomeric ratio. Such systematics have been evaluated in the framework of the Back-Shifted Fermi Gas Model (BSFGM) for the mass dependence of the reduction of the effective moment of inertia with respect to the rigid body value [22] which have been proved quite satisfactory in an extended mass region, even in the heavy Hg and Au isotopes [19]. The same result has occurred in the framework of the GSM for the Ir isotopes as reported in [9]. The BSFGM and GSM have the same spin distribution shape and a similar systematic behavior of the spin cutoff parameter within the GSM would be expected. Calculations were carried out using Θ_{eff} values lowered by 25 and 50% using the STAPRE-F and EMPIRE codes, and the results are presented in Fig. 2. The reduction of the effective moment of inertia causes a significant decrease of the isomeric cross section but does not seem to improve the theoretical results with reference to the experimental data, since the theoretical calculations are already lower than the experimental data below 14 MeV. In the high energy region the theoretical predictions move closer to the experimental data but retain the maximum cross section value around 18 MeV.

After these results, the hypothesis of possible discrepancies in the level scheme was examined. In particular, the level schemes of ^{196}Au and ^{195}Au are expected to play a crucial role in the cross section value of the 12^- isomer and are discussed below.

The level scheme of ^{196}Au, especially the spins of levels lying above the 12^- isomer are very important for the feeding of this level [23, 24] in the whole neutron energy range. The possible existence of a rotational band built on the 12^- isomer and feeding it through gamma cascade would increase the calculated cross section, and lead to a better reproduction of σ_{m2} at incident neutron energies below 16 MeV. In a similar case, the existence of a rotational band built on the configuration of the 16^+ isomer of ^{178} Hf has been proposed in [24] in order to successfully reproduce, within the Hauser Feshbach theory, the cross section values of the

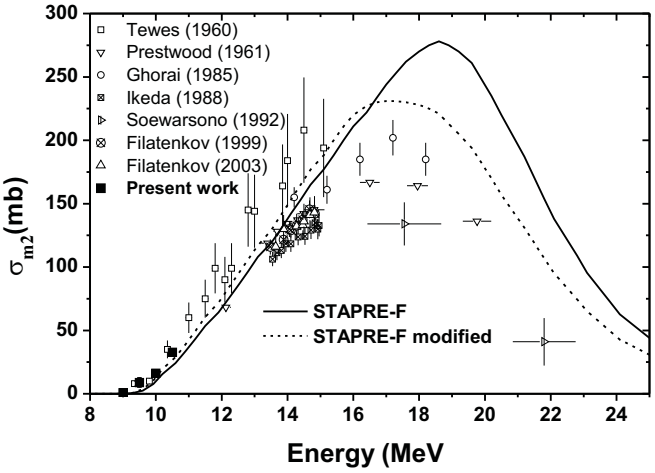

Figure 3: Theoretical calculations for σ_{m2} using a modified level scheme for ^{196}Au and ^{195}Au including hypothetical high-spin levels.

^{179} Hf(n,2n) reaction that leads to its formation and was experimentally observed some years later via the incomplete fusion ^{176}Yb(^{9}Be,α 3n) ^{178}Hf reaction [31]. The possible existence of a rotational band built on this intrinsic structure for doubly odd nuclei in this region is proposed in [25] and [26], and rotational bands based on high-j unique parity quasiparticle states (πh9/2, πh11/2, νi13/2) have been reported for Tl isotopes in [25] and other isotopes in the transitional region Os-Pb (references in [26]), as well as dipole bands in Pb and Hg isotopes [27–30].

The level scheme of ^{195}Au is also expected to play an important role in the neutron energy region above 16 MeV, where the (n,3n) channel becomes important and where the largest deviation from the experimental data occurs. An examination of the level scheme of ^{195}Au in comparison with the level schemes of neighboring odd Au isotopes ([32–34]) indicates a possible absence of high spin rotational band members from the documented levels. The introduction of such high spin states in the level scheme of ^{195}Au would lead to an increase of the de-excitation of the continuum of ^{196}Au towards these states, and thus a reduction of the theoretical σ_{m2} values above an incident neutron energy of 16 MeV.

Although the above assumptions on the level schemes of ^{196}Au and ^{195}Au seem physically likely, there is no possibility of embedding discrete levels in the continuum of the nuclei of interest via any of the three codes in order to further investigate this hypothesis and extract safe results.

The only test that could be performed was the addition of a few high spin levels in the discrete via the STAPRE-F code implementation. The result was an enhancement of σ_{m2} without altering the g+m1 and (n,3n) cross section values, simultaneously reducing the σ_{m2} by 10 % in the energy region above 16 MeV, as expected, and moved the maximum of the curve towards lower energies. The results of these two tests are shown in Fig. 3. Higher spins than those used in the tests, attributed to rotational bands, are expected to lie in the higher energy part of the continuum.

3. Conclusions

A theoretical study of the (n,2n) reaction cross section on ^{197}Au has been perofrmed in the energy range 8-25 MeV with the use of three different codes (STAPRE-F, EMPIRE 2.19 and TALYS-1.2) taking into account all available experimental data. The exciton model and Hauser-Feshbach theory were employed for the pre-compound and compound processes respectively. The Generalized Superfluid Model was chosen for the description of the level density of the nuclei involved. The σ_{g+m1} cross section was easily reproduced by the calculations, while for σ_{m2}, the theoretical results could only reproduce the general trend of the experimental data, with the distribution being shifted to higher energies. Several tests were performed to

improve the theoretical predictions. The results of these tests reveal the importance of the level scheme of the residual nuclei and indicate the possibility of incomplete documentation of high-spin levels in the level schemes of ^{196}Au and ^{195}Au. Furthemore, they highlight certain limitations of the nuclear codes used, particularly regarding the embedding of discrete states in the continuum, which is not currently possible and affects the reproduction of high-spin isomeric cross sections.

4. Acknowledgments

The present work was partially supported by the NTUA program for fundamental research PEVE-2008.

[1] Y. P. Gangrsky, N. N. Kolesnikov, V. G. Lukashik, and L. M. Melnikova, Physics of Atomic Nuclei **67**, 1227 (2004).

[2] E. Hagn and E. Zech, Nucl. Phys. A **373**, 256 (1982).

[3] H. A. Tewes, A. A. Caretto, A. E. Miller, and D. R. Nethaway, Tech. Rep. 6028 (USA, 1960) data retreived from EXFOR: www-nds.iaea.org/exfor.

[4] W. Hauser and H. Feshbach, Phys. Rev. **87**, 366 (1952).

[5] J. F. Ziegler, J. P. Biersack, and U. Littmark, *The Stopping and Range of Ions in Solids* (Pergamon Press, New York, 1985).

[6] J. J. Griffin, Phys. Rev. Lett. **17**, 478 (1966).

[7] A. V. Ignatyuk, K. Istekov, and G. N. Smirenkin, Sov. J. Nucl. Phys. **29**, 450 (1979).

[8] A. V. Ignatyuk, J. L. Weil, S. Raman, and S. Kahane, Phys. Rev. C **47**, 1504 (1993).

[9] N. Patronis, C. T. Papadopoulos, S. Galanopoulos, M. Kokkoris, G. Perdikakis, R. Vlastou, A. Lagoyannis, and S. Harissopulos, Phys. Rev. C **75**, 034607 (2007).

[10] M. Uhl and B. Strohmaier, *Computer Code for particle induced activation cross section and related quantities*, Tech. Rep. IRK-76/01 (Vienna, 1976).

[11] M. Herman, R. Capote, B. Carlson, P. Oblozinsky, M. Sin, A. Trakov, and V. Zerkin, *EMPIRE-II, Nuclear Reaction Model code, version 2.19*, Tech. Rep. (Vienna, 2005).

[12] O. Bersillon, F. Gunsing, E. Bauge, R. Jacqmin, and S. Leray, eds., *TALYS-1.0* (EDP Sciences, France, 2008).

[13] T. Belgya, O. Bersillon, R. Capote, T. Fukahori, G. Zhighang, S. Goriely, M. Herman, A. V. Ignatyuk, S. Kailas, A. Koning, P. Oblozinsky, V. Plujko, and P. Young, *Handbook for calculations of nuclear reaction data, RIPL-2*, Tech. Rep. IAEA-TECDOC-1506 (Vienna, 2006) available online at http://www.nds.iaea.org/RIPL-2/.

[14] H. Hofmann, J. Richert, J. Tepel, and H. Weidenmuller, Ann. Phys. **90**, 403 (1975).

[15] V. Avrigeanu, S. V. Chuvaev, R. Eichin, A. A. Filatenkov, R. A. Forrest, H. Freiesleben, M. Herman, A. J. Koning, and K. Seidel, Nucl. Phys. A **765**, 1 (2006).

[16] M. Avrigeanu, R. A. Forrest, F. L. Roman, and V. Avrigeanu, Tech. Rep. (Vancouver, BC, Canada, 1996).

[17] W. Dilg, W. Schantl, H. Vonach, and M. Uhl, Nucl. Phys. A **217**, 269 (1973).

[18] A. Gilbert and A. Cameron, Can. J. Phys. **43**, 1446 (1965).

[19] S. Sudar and S. M. Qaim, Phys. Rev. C **73**, 034613 (2006).

[20] M. Al-Abyad, S. Sudar, M. N. H. Comsan, and S. M. Qaim, Phys. Rev. C **73**, 064608 (2006).

[21] S. F. Mughabghab and C. Dunford, Phys. Rev. Lett. **81**, 4083 (1998).

[22] S. I. Al-Quraishi, S. M. Grimes, T. N. Massey, and D. A. Resler, Phys. Rev. C **67**, 015803 (2003).

[23] S. M. Qaim, A. Mushtaq and M. Uhl, Phys. Rev. C **38**, 645 (1988).

[24] M. B. Chadwick and P. G. . Young, Nuclear Science and Engineering **108**, 117 (1991).

[25] A. J. .Kreiner, M. Fenzl, S. Lunardi, and M. Mariscotti, Nuclear Physics A **282**, 243 (1977).

[26] A. J. Kreiner, Z. Physik A **288**, 373 (1978).

[27] E. F. Moore, M. P. Carpenter, Y. Liang, R. V. F. Janssens, I. Ahmad, I. G. Bearden, P. J. Daly, M. W. Drigert, B. Fornal, U. Garg, Z. W. Grabowski, H. L. Harrington, R. G. Henry, T. L. Khoo, T. Lauritsen, R. H. Mayer, D. Nisius, W. Reviol, and M. Sferrazza, Phys. Rev. C **51**, 115 (1995).

[28] H. Hubel, Prog. Part. Nucl. Phys. **38**, 89 (1997).

[29] N. Fotiades, S. Harissopulos, C. A. Kalfas, S. Kossionides, C. T. Papadopoulos, R. Vlastou, M. Serris, M. Meyer, N. Redon, R. Duffait, Y. L. Coz, L. Ducroux, F. Hannachi, I. Deloncle, B. Gall, M. G. Porquet, G. Schuck, F. Azaiez, J. Duprat, A. Korichi, J. F. Sharpey-Schafer, M. J. Joyce, C. W. Beausang, P. J. Dagnall, P. D. Forsyth, S. J. Gale, P. M. Jones, E. S. Paul, J. Simpson, R. M. Clark, K. Hauschild, and R. Wadsworth, J. Phys. G: Nucl. Part. Phys. **21**, 911 (1995).

[30] N. Fotiades, S. Harissopulos, C. A. Kalfas, S. Kossionides, C. T. Papadopoulos, R. Vlastou, M. Serris, J. F. Sharpey-Schafer, M. J. Joyce, C. W. Beausang, P. J. Dagnall, P. D. Forsyth, S. J. Gale, P. M. Jones, E. S. Paul, P. J. Twin, J. Simpson, D. M. Cullen, P. Fallon, M. A. Riley, R. M. Clark, K. Hauschild, and R. Wadsworth, Z. Phys. **A**, 354 (1996).

[31] S. M. Mullins, G. D. Dracoulis, A. P. Byrne, T. R. McGoram, S. Bayer, W. A. Seale, and F. G. Kondev, Phys. Lett. B **393**, 279 (1997).

[32] S. C. Wu and H. Niu, Nuclear Data Sheets **100**, 1 (2003).

[33] V. Vanin, N. Maidana, R. Castro, E. Achterberg, O. Capurro, and G. Marti, Nuclear Data Sheets **108**, 2393 (2007).

[34] E. Achterberg, O. A. Capurro, G. Marti, V. Vanin, and R. M. Castro, Nuclear Data Sheets **107**, 1 (2006).

ANALYSIS OF THE BINDING ENERGIES OF THE Λ- PARTICLE IN HYPERNUCLEI WITH THE RHVT APPROACH AND THE GAUSS POTENTIAL

C.A. Efthimiou, M.E. Grypeos, C.G. Koutroulos, Th. Petridou

Department of Theoretical Physics, Aristotle University of Thessaloniki, Greece

Abstract

An analysis is carried out mainly of the ground state binding energies of the Λ-particle in hypernuclei with values of the core mass number A_C between 15 and 207 (included) using, as far as possible, recent experimental data.The renormalized (non- relativistic) quantum mechanical hypervirial theorem (RHVT) technique is employed in the form of s- power series expansions and a Gauss single particle potential for the motion of a Λ- particle in hypernuclei is used. Not exact analytic solution is known for the Schrödinger eigenvalue problem in this case. Thus, the approximate analytic expressions (AAE) for the energy eigenvalues which are obtained with the RHVT approach and are quite useful as long as the involved dimensionless parameter s is sufficiently small, are compared only with the numerical solution. The potential parameters are determined by a least-squares fit in the framework of the rigid core model for the hypernuclei. A discussion is also made regarding the determination of the renormalization parameter χ.

1.Introduction

The Quantum mechanical hypervirial theorem (HVT) approach has been a very useful technique in dealing with various problems in Physics, Chemistry etc in which Quantum Mechanics provides the basic theoretical background. For pertinent reviews see refs [1,2].
This approach started originally with the work of Hirchfelder [3] and further elaborations and various applications followed (see e.g. ref.[4-8]).We mention in particular the use of this technique for the approximate treatment of problems such as the non relativistic motion of a particle in a potential V.

In more recent work [9-11] an investigation was carried out of the HVT approach in the form of approximate analytic expressions (AAE), originated from truncated expansions, when a small (compared to unity) dimensionless quantity s exists. Use was also made [12-13] of a renormalized HVT expansion (RHVT) for the energy eigenvalues of a particle moving in a single particle potential belonging to a fairly wide class of central potential wells, namely those of the form:

$$V(r) = -D\, f(r/R) \tag{1}$$

where $D>0$ is the potential depth, $R>0$ its "radius" and f $(f(0)=1)$ the potential form- factor which determines its shape and is assumed to be an appropriate analytic function of even powers of $x=r/R$ with $-d^2 f/dx^2\big|_{x=0} > 0$, that is they behave like an harmonic oscillator near the origin.

Typical examples are the Gaussian and the (reduced) Poeschl-Teller (PT) potentials:

$$V(r) = -D\, e^{-(r/R)^2} \quad \text{(a) and } V(r) = -D\cosh^{-2}(r/R) \quad \text{(b)} \tag{2}$$

In our first results we considered as an application to a physical problem the use of the derived AAE to estimate the binding energies of a Λ-particle in hypernuclei by assuming the PT single particle potential. The advantage in doing this, is that in certain cases (for the l=0, that is the s-states) there exist exact analytic expressions for this particle moving in this potential and a direct comparison of our AAE with them can be made to assess the accuracy of the latter. It should be clear, however, that the usefulness of the AAE refers mainly to the cases of the class of potentials (1) in which exact analytic results of the corresponding Schrödinger eigenvalues can not be found. It is the aim of the present work to use these AAE, mainly for the ground state a Λ- particle moving in hypernuclei pertaining to the well-known potential (2a), taken as a first approximation of the mean -field felt by the Λ in hypernuclei.

In the following section a summary of the formalism is outlined. For more details one is referred to refs [12,13]. In section 3 the detailed preliminary numerical results are displayed for the Λ energies in a number of

hypernuclei mainly for the ground state along with the corresponding experimental results used. The final section is devoted to final remarks and a comment.

2. Outline of the formalism

We consider first the more general class of even – power series central potentials:

$$V(r) = -D + \sum_{k=0}^{\infty} V_k \, \lambda^k \, r^{2k+2} \tag{3}$$

This potential takes the following form, by adding and subtracting the same harmonic oscillator potential Kr^2 (in a way analogous to that of ref [14,15] for the perturbed one dimensional oscillator):

$$V^R(r) = \left(-D + V_0^R \, r^2\right) + \left[\left(\sum_{k=1}^{\infty} V_k^R \, \lambda^k \, r^{2k+2}\right) - K r^2\right] \tag{4}$$

where: $V_0^R = V_0 + K$, $V_k^R = V_k$ for $k = 1, 2, 3, \ldots$

One introduces then the shifted energy eigenvalues

$$E'^R_{nl} = E^R_{nl} + D \tag{5}$$

and considers the corresponding radial Schrödinger equation and the corresponding equation for the relevant zeroth- order energy eigenvalues and eigenfunctions, (denoted by superscript (0)), and writes the expansions

$$E'^R_{n\ell} = \sum_{k=0}^{\infty} E^{R(k)} \lambda^k \tag{6}$$

$$\left\langle r^N \right\rangle^R_{n\ell} = \sum_{p=0}^{\infty} C_N^{R(p)} \lambda^p \tag{7}$$

On the basis of these expansions and the use of Hellmann-Feynmann theorem we end up after a rather lengthy algebra with the following recurrence relations which can be used to obtain the interested quantities:

$$\begin{aligned}(N+2) V_0 \, C_{N+2}^{R(k)} = \frac{\hbar^2}{2\mu} N \left[\frac{(N+1)(N-1)}{4} - \ell(\ell+1)\right] C_{N-2}^{R(k)} + (N+1) E^{R(0)} C_N^{R(k)} + \\ + \sum_{q=1}^{k} \left\{ (N+1) E^{R(q)} C_N^{R(k-q)} - (N+q+2) V_q C_{N+2q+2}^{R(k-q)} \right\}\end{aligned} \tag{8}$$

where:

$$C_0^{R(k)} = \delta_{k0} \text{ and } E^{R(q)} = \frac{1}{q} \sum_{m=1}^{q} m \, V_m C_{2m+2}^{R(q-m)} \, , \begin{cases} k = 0, 1, 2, 3, \ldots \\ q = 1, 2, 3, 4, \ldots \\ m = 1, 2, 3, 4, \ldots \end{cases} \tag{9}$$

We focus now our attention .to the class of potentials (1) mentioned in the introduction.
In this case we use the expression of the small (compared to unity) dimensionless quantity s :

$$s = \left(\hbar^2 / 2\mu D R^2\right)^{1/2} \tag{10}$$

We can write after a lengthy algebra the expression of the energy eigenvalues in the RHVT approach as a truncated expression:

$$\frac{E^R_{n\ell}}{D} = e^{R(0)}_{n\ell} + e^{R(1)}_{n\ell} \, s + e^{R(2)}_{n\ell} \, s^2 + e^{R(3)}_{n\ell} \, s^3 + O\left(s^4\right) \tag{11}$$

where

$$e^{R(0)}_{n\ell} = -1 \tag{12}$$

$$e^{R(1)}_{n\ell} = 2 \left|d_1\right|^{1/2} a_{n\ell} \, \chi^{1/2} \tag{13}$$

$$e_{n\ell}^{R(2)} = -\frac{d_2}{8|d_1|}\left[3 - 4\,\ell(\ell+1) + 12\,a_{n\ell}^2\,\chi\right] \tag{14}$$

$$e_{n\ell}^{R(3)} = \frac{a_{n\ell}\,\chi^{1/2}}{8|d_1|^{5/2}}\left\{\left(20\,d_1 d_3 - 17\,d_2^2\right)a_{n\ell}^2\,\chi + \left(25\,d_1 d_3 - \frac{67}{4}d_2^2\right) - 3\,\ell(\ell+1)\left(4\,d_1 d_3 - 3\,d_2^2\right)\right\} \tag{15}$$

and $a_{n\ell} = (2n + \ell + 3/2)$. The new renormalization parameter χ (which should depend, in general, on quantum numbers $n\ell$, that is $\chi = \chi_{n\ell}$) is related with the Killingbeck renormalization parameter K with the relation:

$$\chi = 1 + \frac{K}{\left(\frac{|d_1|D}{R^2}\right)} \tag{16}$$

and it is seen that this parameter enters formula (11) only as a factor of the state dependent number $a_{n\ell}^2$.

Finally, the numbers d_k are related to the derivatives of f and are defined as follows:

$$d_k = \frac{1}{(2k)!}\frac{d^{2k}}{dx^{2k}}f(x)\bigg|_{x=0}, \quad k = 0, 1, 2, 3, \ldots \tag{17}$$

It is seen that when $K = 0$ that is when $\chi = 1$ formula (11) becomes identical to the one in the HVT case [9-11]. Thus, depending on the value of χ formula (11) incorporates both the HVT and the RHVT results.

3.Results with the Gaussian single particle potential

In the case of the Gaussian potential, the numbers d_k given by expression (17) in the previous section reduce to the following: $d_k=(-1)^k/k!$ see refs. [16, 11]. The first of them are given in Table 1.

TABLE 1

d_k	**Gaussian**
d_0	1
d_1	-1
d_2	$1/2$
d_3	$-1/6$

Thus, the energy expressions for the ground state of the Λ (the 1s state) E^R_{00} and for the first excited state, the 1p state, E_{01}^R and also the absolute value of their difference: $\Delta_{ps} = |E_{01} - E_{00}|$ which enters the so- called Bertlmann and Martin inequalities (see e.g [17 – 19]) are easily followed from our general truncated expression (11) and are quite simple AAE .

Our detailed numerical results are displayed in Table 2, Table 3 and Table 4. In these tables we use the ground state experimental energy data for the determination of the potential parameters both for the 1s and 1p states. The same assumption was also made in refs [22, 23]. It should be also noted that, for the mass μ, the reduced mass of the Λ - core system was used.

We use, as far as possible, recent experimental data [20, 21] for the ground state energy of a Λ in a number of hypernuclei (displayed in Table 4), which are quite numerous, in order that we determine, by least squares fitting ,the potential parameters D and r_0 in the framework of the- rigid core model: $R=r_0A_c^{1/3}$. If we use the "almost exact" (that is apart from the usual numerical inaccuracies) numerical results (see Table 2) obtained with a pertinent subroutine, we find the following best fit values $D = 38.717\ MeV$, $r_0 = 1.01646\ fm$. The corresponding value of χ^2 (which we shall denote by F_{00} in order not to confuse that with the square of the renormalization parameter) is $F_{00} = 4.58342$.

Regarding the RHVT results, these depend on the assumed value of the renormalization parameter χ .

For purposes of a rough estimate we can follow the procedure discussed for the PT potential, taking into account that now the potential shape is different. In the case of Gauss potential an approximate value of χ^G is therefore $\chi^G = 1 - e^{-1} = 0.632121$, which is a little larger than the PT one. The best-fit values of the potential parameters obtained using a least squares –fitting of the ground state energies of the lambda particle to the corresponding experimental results are the following: $D = 38.981\ MeV$, $r_0 = 0.79150\ fm$ and $F_{00} = 4.53671$.

Table 2
Detailed numerical results for the 1s and 1p states with the Gauss potential.

Mass number of the core nucleus	**Numerical solution of the Schroedinger eigenvalue problem for the 1s state. Best fit values :** $D = 38.717\ MeV$. $r_0 = 1.01646\ fm$ $F_{00} = 4.58342$		**Numerical solution of the Schr. e.p. for the 1p state with the previous D and r_0.**	**The lowest energy level spacing**
A_C	**s (From Expr. (10))**	E_{00} **(MeV)**	E_{01} **(MeV)**	$\Delta_{ps} = \lvert E_{01} - E_{00} \rvert$ **(MeV)**
15	**0.278202**	**-12.420**	**-0.4838**	**11.936**
27	**0.224941**	**-16.465**	**-4.835**	**11.630**
31	**0.214232**	**-17.339**	**-5.935**	**11.404**
39	**0.197697**	**-18.726**	**-7.757**	**10.969**
50	**0.181391**	**-20.139**	**-9.690**	**10.449**
55	**0.175533**	**-20.658**	**-10.420**	**10.238**
88	**0.149482**	**-23.032**	**-13.830**	**9.202**
138	**0.128353**	**-25.039**	**-16.820**	**8.219**
207	**0.111967**	**-26.645**	**-19.270**	**7.375**

We recall also the remarks made for the determination of the renormalization parameter χ in ref [13], where the results were obtained with the PT potential.

In the first columns of Table 3, the results are displayed, for purposes of comparison, with the first two leading terms in the HVT (χ=1) approximation for the ground and the first excited state of the lambda particle in the hypernuclei, as well as the results of Δ_{ps}. It is easily seen that in this case, the formulae used are identical with those in the PT potential and the results with the Gauss potential are exactly the same as it is also immediately realized.

Regarding the RHVT case (displayed in the last columns of Table 3), we use the expression given in ref.[13]:

$$E_{n\ell}^R \cong D\left\{ -1 + 2\left| d_1 \right|^{1/2} a_{n\ell}\, \chi_{n\ell}^{1/2}\, s \right\} \tag{18}$$

where now $\chi_{n\ell}^{1/2} = \chi_{n\ell}^{1/2G}$ and we have:

$$\chi_{00}^{1/2G} \cong 1 - \frac{5}{8}s - \frac{25}{192}s^2 + O\left(s^3\right) \tag{19}$$

$$\chi_{01}^{1/2G} \cong 1 - \frac{7}{8}\,s - \frac{21}{64}s^2 + O\left(s^3\right). \tag{20}$$

This is equivalent to the HVT results in which the s^2 and s^3 terms are also included through the expressions of the renormalization parameters. The best-fit values of the potential parameters of the ground – state energy values (taken to be the same for the E_{01} as previously) are: $D = 38.587\ MeV$, $r_0 = 1.02392\ fm$ and $F_{00} = 4.65636$. It is seen that the AAE results of the RHVT case we are considering, are quite close to those obtained with the numerical subroutine for the determination of the energy eigenvalues of the ground state of the Λ in the hypernuclei. It is also seen that the behaviour of the Δ_{ps} is as expected. Furthermore, the values of this quantity are a little larger than the "almost exact" numerical ones for A_c <∐ 55 and less than those for Ac∐ >55. However, the absolute values of the corresponding differences are, in most cases, more pronounced than those obtained with the PT potential.

Table 3
Detailed numerical results based on simple approximate analytic expressions (AAE) and using the Gauss potential.

A_C	s	E_{00}^{HVT} (MeV)	E_{01}^{HVT} (MeV)	Δ_{ps}^{HVT} (MeV)	s	E_{00}^{RHVT} (MeV)	E_{01}^{RHVT} (MeV)	Δ_{ps}^{RHVT} (MeV)
15	0.21589	-12.399	2.796	15.195	0.27664	-12.419	0.527	12.946
27	0.17456	-16.672	-4.477	12.195	0.22368	-16.482	-4.587	11.895
31	0.16625	-17.640	-5.939	11.701	0.21303	-17.356	-5.759	11.597
39	0.15342	-18.994	-8.197	10.797	0.19657	-18.740	-7.664	11.076
50	0.14076	-20.330	-10.423	9.907	0.18037	-20.149	-9.651	10.498
55	0.13622	-20.810	-11.223	9.587	0.17455	-20.666	-10.391	10.275
88	0.11600	-22.944	-14.780	8.164	0.14864	-23.028	-13.845	9.183
138	0.09960	-24.675	-17.665	7.010	0.12763	-25.022	-16.844	8.178
207	0.08689	-26.018	-19.903	6.115	0.11134	-26.616	-19.286	7.330

Table 4
The experimental results of the binding energies along with the theoretical values of the energies of the Λ with the Gauss Potential for the s and the p states and of the quantities e_{00}, e_{01} (see table 5 of ref [13]) for various values A_C

A_C	$B^{exp} \pm \Delta B^{exp}$ (MeV)	E_{00} (MeV)	E_{00}^{RHVT} (MeV)	$e_{00} = E_{00}^{"ex"} - E_{00}^{RHVT}$ (MeV)	$e_{00}(\%)$	E_{01} (MeV)	E_{01}^{RHVT} (MeV)	$e_{01} = E_{01}^{"ex"} - E_{01}^{RHVT}$ (MeV)	$e_{01}(\%)$
15	12.42±0.05	-12.420	-12.419	-0.001	0.008	-0.4838	0.527	-1.011	208.929
27	16.6±0.2	-16.465	-16.482	0.017	-0.103	-4.835	-4.587	-0.248	5.129
31	17.5±0.5	-17.339	-17.356	0.017	-0.098	-5.935	-5.759	-0.176	2.965
39	18.70±1.1	-18.726	-18.740	0.014	-0.075	-7.757	-7.664	-0.093	1.199
50	19.97±0.13	-20.139	-20.149	0.010	-0.050	-9.690	-9.651	-0.039	0.402
55	21.15±1.5	-20.658	-20.666	0.008	-0.039	-10.420	-10.391	-0.029	0.278
88	23.11±0.1	-23.032	-23.028	-0.004	0.017	-13.830	-13.845	0.015	0.108
138	23.8±1.0	-25.039	-25.022	-0.017	0.068	-16.820	-16.844	0.024	0.143
207	26.5±0.5	-26.645	-26.616	-0.029	0.109	-19.270	-19.286	0.016	0.083

We mention, finally, that the differences between the values of the RHVT ground state energies of the Λ and the corresponding ones obtained numerically are quite small as are with the PT potential, although with the Gauss potential these differences are more pronounced. The differences are bigger in the E_{01} energies, as we can see from Tables 3 and 4 of this work (see also Table 4 and Table 5 of ref [13] and also the relevant comments there).

4. Final remarks and a comment

From the results with the Gauss potential displayed in the previous section it can be realized that the least - squares fit values F_{00} (both in the numerical and the RHVT cases) are a little smaller than the corresponding ones obtained with the PT potential (for which the numerical solution gives $F_{00} = 4,74393$ and the RHVT gives $F_{00} = 4,75062$) and in this sense the Gauss potential might be preferable in comparison with the PT one. It should be mentioned, however, that the RHVT results differ more from the "almost exact "numerical ones.
We mention also that the AAE used come from an appropriate truncation of the power series expansions. Another possibility would be to consider an HVT energy expression which has its finite terms (s^3 included) to coincide with the existing HVT ones plus an analytic expression, consisting only of higher s terms (which emerge by means e.g. of the binomial formula) which differ, however, from those of the original HVT expansion .We are currently investigating this possibility to see whether improvements can be obtained.

Acknowledgement

Thanks are due to Helen Grypeos for technical assistance.

References

1. (a) G. Marc and W.G. McMillan Advances in Chemical Physics58(1985)209,
(b) F.M. Fernandez and E.A.Castro, Hypervirial Theorems, Lecture notes in Chemistry,Vol.43 (Springer – Verlang) (1987).
2. S.M.McRae, E.R. Vrscay ,Journal of Mathematical Physics 33 (1992)3004
3. J.O.Hirschfelder Journal of Chemical Physics 33 (1960) 1462
4. R.J. Swenson and S.H. Danforth , J. Chem. Phys.57, (1972) 1734
5. J.P. Killingbeck, Phys.Lett. 65A , (1978) 87
6. M. Grant and C.S. Lai, Phys. Rev. A 20, (1979) 718
7. (a) C.S. Lai, J.Phys. A 16, (1983) L181, (b)) C.S. Lai and H.E. Lin, J. Phys. A 15, (1982) 1495
8. (a) M.R.M. Witwit, J.Phys. A 24, (1991) 5291, (b) M.R.M. Witwit, J.Phys. A 24, (1991) 4535, (c) M.R.M. Witwit, J.Phys. A 24, (1991) 3053
9. Th.E. Liolios and M.E. Grypeos International. Journal of Theoretical. Physics 36(1997)2051
10. M.E. Grypeos and Th.E.Liolios, Phys.Letters A 252 (1999) 125
11. M.E.Grypeos, C.G.Koutroulos,K.J. Oyewumi and Th. Petridou J.Phys.A: Math. Gen. 37 (2004) 7895
12. C.A.Efthimiou, M.E.Grypeos, C.G.Koutroulos,K.J. Oyewumi and Th. Petridou ,17th Symposium of HNPS. Ioannina, May 2008, page 107 of the proceedings, edited by A. Pakou, Th. Cosmas and N. Nicolis
13. C.A.Efthimiou, M.E.Grypeos, C.G.Koutroulos,K.J. Oyewumi and Th. Petridou, preprint (accepted for publication in Int. Jour. Modern Physics E (IJMPE))
14. J. Killingbeck J.Phys. A Math. Gen.14 (1981) 1005
15. E.J.Austin and J. Killingbeck J.Phys.A Math. Gen.15 (1982) L443
16. H.J.W Muller, J. Math. Phys. 11 (2) (1970) 355
17. W. Thirring, A course in Mathematical Physics 3. Quantum Mechanics of Atoms and Molecules (Springer, New York) (1979)
18. R.A. Bertlmann and A. Martin, Nucl. Phys. B168, (1980) 111
19. R.A. Bertlmann and A. Martin, Nucl. Phys. B182, (1981) 35
20. H. Bando, T Motoba, J.Zofka Int. J. of Modern Physics A 5 (1990) 4021
21. a) O. Hashimoto, H. Tamura Progress in Particle and Nuclear Physics 57 (2006) 564,
b) C. Samanta, P. Roy Chowdhury and D. N. Basu, J. Phys. G: Nucl. Part. Phys. **32,** (2006) 363
22. C.G. Koutroulos Z. Naturf. 45a (1990)14
23. C.G. Koutroulos J. Phys. G Nuclear Part. Phys. 17 (1991) 1069

Neutrino scattering off the stable even-even Mo isotopes

K.G. Balasi and T.S. Kosmas

Theoretical Physics Section, University of Ioannina, GR 45110 Ioannina, Greece

Abstract. A systematic study of neutrino-nucleus reaction rates at low and intermediate energies are presented and discussed, focusing on the even-even Mo isotopes. Contributions coming from both the vector and axial-vector components of the corresponding hadronic currents have been included. The response of these detectors to supernova neutrino is also studied, by exploiting the above results and utilizing the folding procedure assuming a two parameter Fermi-Dirac distribution for the supernova neutrino energy-spectra.

Keywords: Semi-leptonic electroweak interactions; Neutrino-nucleus reactions; Inelastic cross sections; Quasi-particle random phase approximation
PACS: 23.40.Bw;25.30.Pt;21.60.Jz;26.30.+k

INTRODUCTION

Neutrino physics has gained a large interest both from the experimental and the theoretical point of view. Neutrino-nucleus interaction of charged and neutral current reactions is a highly valuable source for detecting neutrino flavor and exploring the structure of electro-weak interactions [1]. Both weak neutral-current (NC) and charged-current (CC) scattering have stimulated detailed analysis in the intermediate-energy region, using a variety of methods including the quasi-particle random phase approximation (QRPA), random phase approximation (RPA), Fermi gas (FG) and shell model calculations, [2]. For detailed reviews of neutrino physics and recent experimental results the reader is referred to Ref. [3].

In the present work, we devote a special effort in performing realistic calculations for the dependence on the scattering angle and initial neutrino-energy of the differential and integrated cross sections of the reactions $^{92}Mo(\nu,\nu')^{92}Mo^*$, $^{94}Mo(\nu,\nu')^{94}Mo^*$, $^{96}Mo(\nu,\nu')^{96}Mo^*$, $^{98}Mo(\nu,\nu')^{98}Mo^*$ and $^{100}Mo(\nu,\nu')^{100}Mo^*$. Molybdenum has attracted much attention concerning the fact that it is a structural metal at elevated temperatures. Two thirds of the element consists of the even isotopes ^{92,94,96,98,100}Mo. Study of the neutrino scattering cross sections off these nuclei substantially provides the quantitative nuclear data requisite to many engineering applications to a precision not easily achieved in elemental studies. To this aim we investigate the nuclear response of this isotope to supernova neutrino spectra and explore its role as a supernova neutrino detector.

TABLE 1. Adjusted single-particle energies together with the Woods-Saxon energies in units of MeV for neutron (ν) and proton (π) orbitals respectively. Blank voids indicate that the unadjusted values are used.

orbital	^{92}Mo		^{94}Mo		^{96}Mo		^{98}Mo		^{100}Mo	
	E_{adj}	E_{WS}	E_{adj}	E_{WS}	E_{adj}	E_{WS}	E_{adj}	E_{WS}	E_{adj}	E_{WS}
$\nu 1d_{5/2}$							-5.17	-7.37	-5.17	-7.30
$\nu 0g_{9/2}$	-12.28	-12.08								
$\nu 2s_{1/2}$	-6.58	-5.82	-6.35	-5.76	-5.90	-5.70	-5.84	-5.64	-5.64	-5.59
$\nu 1d_{3/2}$			-6.29	-4.86	-6.01	-4.84	-4.23	-4.83	-4.23	-4.81
$\nu 0g_{7/2}$	-6.08	-5.78	-6.19	-5.82	-5.81	-5.85	-4.80	-5.88	-4.60	-5.91
$\nu 0h_{11/2}$							-4.03	-3.53	-4.30	-3.50
$\pi 1p_{3/2}$			-7.27	-8.66	-8.18	-9.51			-10.73	-11.20
$\pi 1p_{1/2}$	-6.29	-5.92	-6.29	-6.84	-7.17	-7.72	-9.45	-8.64	-9.46	-9.47
$\pi 0f_{5/2}$			-6.90	-8.74	-7.79	-9.69	-10.23	-10.63	-10.23	-11.54
$\pi 0g_{9/2}$	-5.46	-4.64					-9.40	-7.43	-9.40	-8.31

THE QUASI-PARTICLE RANDOM PHASE APPROXIMATION

The appropriate transition densities in order to calculate the cross-sections are determined within the quasi-particle random phase approximation, QRPA method. In this approach, a QRPA excitation has the following form:

$$|\omega\rangle = Q^{\dagger}_{\omega}|QRPA\rangle \tag{1}$$

and a pair of quasiparticles is created by the operator:

$$Q^{\dagger}_{\omega} = \sum_{a\leq b}\left[X^{\omega}_{ab}A^{\dagger}_{ab}(JM) - Y^{\omega}_{ab}\tilde{A}_{ab}(JM)\right] \tag{2}$$

where subscript $\omega = nJ^{\pi}$ and the two-body operators are:

$$A^{\dagger}_{(JM)} = N_{ab}(J)[a^{\dagger}_{a}a^{\dagger}_{b}]_{JM}, \tag{3}$$

and

$$\tilde{A}^{\dagger}_{(JM)} = (-1)^{J+M}A_{ab}(J-M) = -N_{ab}(J)[\tilde{a}_{a}\tilde{a}_{b}]_{JM}. \tag{4}$$

The QRPA equations are given in a matrix form:

$$\begin{pmatrix} \mathscr{A} & \mathscr{B} \\ -\mathscr{B}^{*} & -\mathscr{A}^{*} \end{pmatrix}\begin{pmatrix} X^{\omega} \\ Y^{\omega} \end{pmatrix} = \omega\begin{pmatrix} X^{\omega} \\ Y^{\omega} \end{pmatrix} \tag{5}$$

where E_{ω} the excitation energy of the $|J^{\pi}_{m}\rangle$ nuclear state. The QRPA matrices, A and B, are defined through the following nuclear matrix elements:

$$A_{ab,cd}(J) = \left\langle BCS\right|\left[A_{ab}(J),H,A^{\dagger}_{cd}(J)\right]\left|BCS\right\rangle, \tag{6}$$

$$B_{ab,cd}(J) = -\left\langle BCS\right|\left[A_{ab}(J), H, \tilde{A}_{cd}(J)\right]\left|BCS\right\rangle. \quad (7)$$

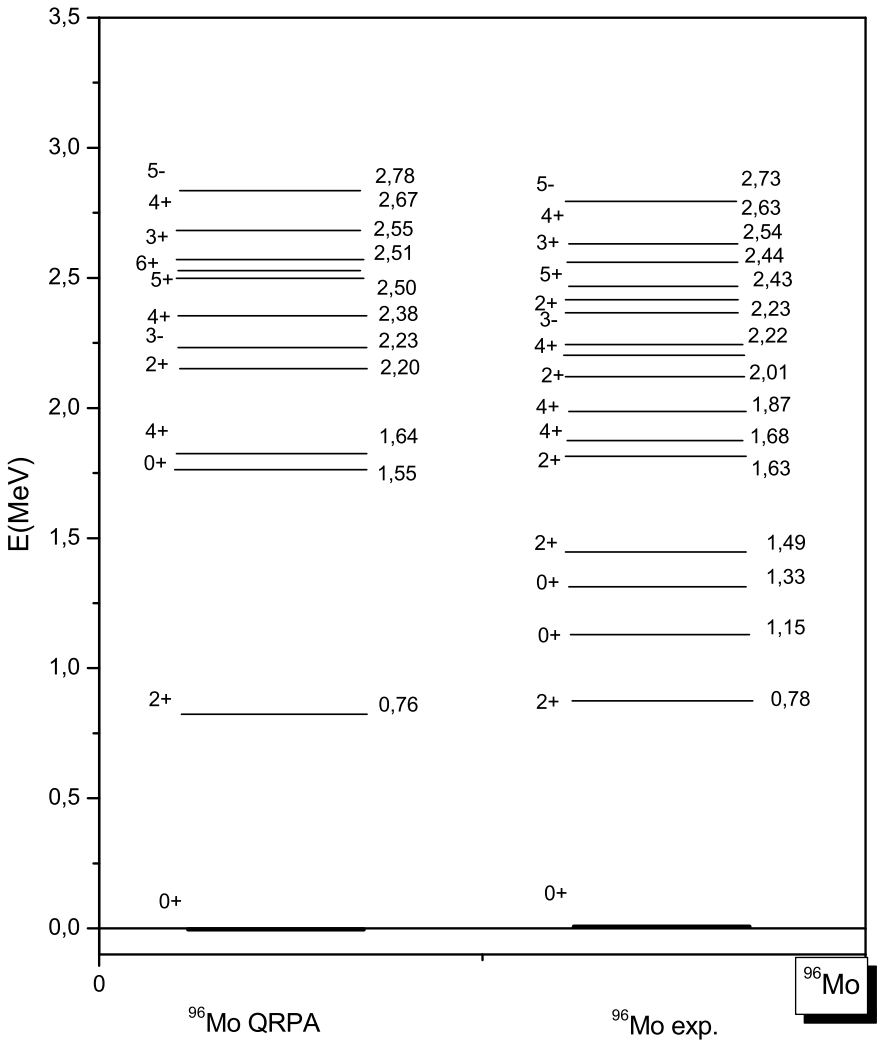

FIGURE 1. Comparison of experimental(left) and theoretical (right)low-energy spectra of ^{96}Mo nucleus. The theoretical results are obtained by using the QRPA method.

RESULTS

In this work we have performed realistic state-by-state calculations for inelastic and elastic neutrino-nucleus scattering off the even-even Mo isotopes. Calculations were performed for all nuclei under consideration but as the results for the different isotopes

are similarly we use in the following ^{96}Mo as a representative case to illustrate the more detailed characteristics.

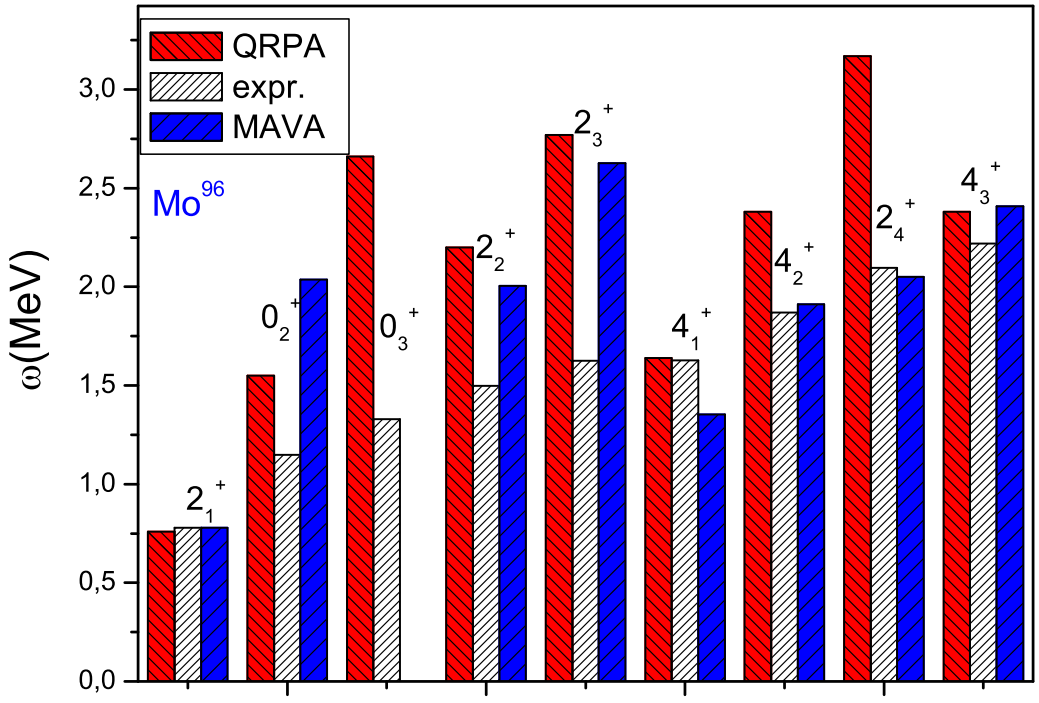

FIGURE 2. Excitation energies for the multipole states $J^\pi = 0^+$, $J^\pi = 2^+$ and $J^\pi = 4^+$ of the ^{96}Mo nucleus. Our theoretical results are compared with the experimental results as well as theoretical results obtained by the MAVA method.

In the QRPA calculations a valence space containing the $3\bar{h}\omega$ and the $4\bar{h}\omega$ harmonic oscillator shells plus the $0h_{11/2}$ was used for both protons and neutrons. The single-particle energies were first calculated from the Coulomb-corrected Woods-Saxon potential with the Bohr-Mottelson parametrization [4]. The quality of the obtained results could be refined by slightly adjusting the proton and neutron single-particle energies in the vicinity of the respective Fermi surfaces. The adjustments for all nuclei under consideration are presented in Table 1. In the present calculations the Bonn one-boson-exchange potential [5] was used as the two-body interaction. BCS calculations were subsequently performed separately for neutrons and protons. The monopole matrix elements were renormalized by adjusting the proton and neutron pairing strengths (g^p_pair and g^n_{pair} respectively) in such a way that the lowest one-quasiparticle energy was approximately equal to the experimental pairing gap, calculated by using the three-point formulae. The QRPA wave functions and energies were then obtained by diagonalizing the QRPA equations (5) for each multipolarity J^π. The particle-particle strength (g_{pp}) and the particle-hole strength (g_{ph}) were adjusted for each multipole in order to reproduce the low-lying experimental energy spectrum of the even-even nucleus under consideration [6, 7, 8, 9, 10, 11]. The calculated energy spectra together with experimental

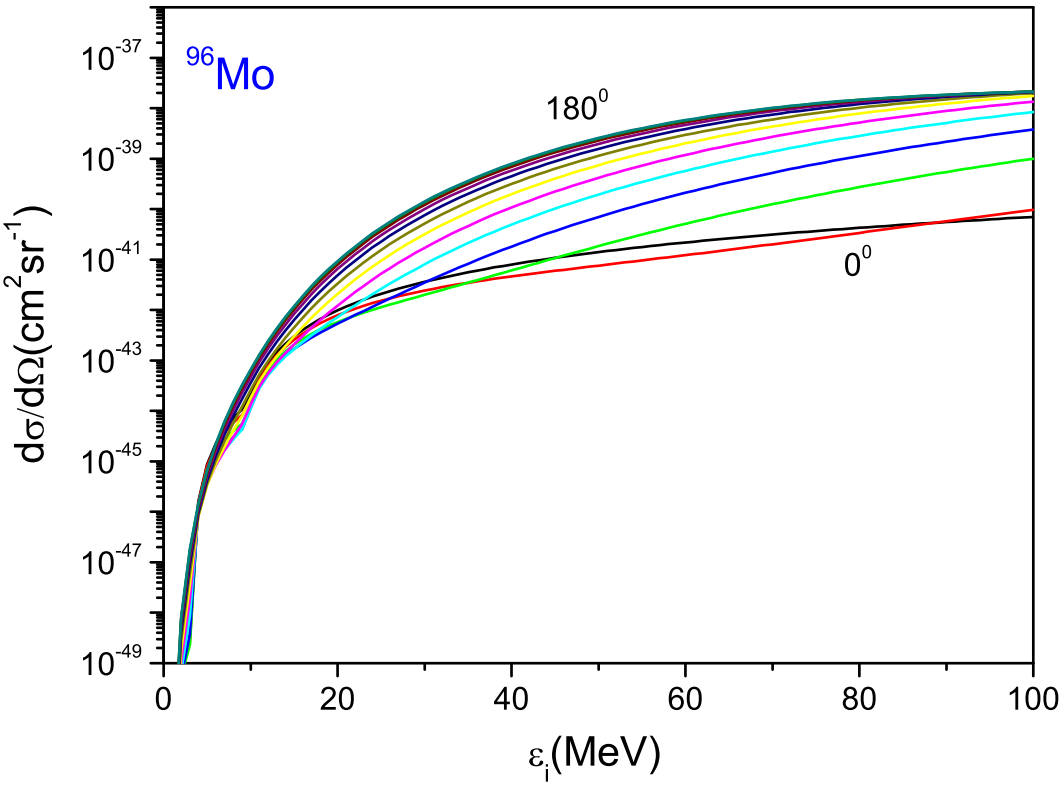

FIGURE 3. Comparison of experimental(left) and theoretical (right)low-energy spectra of ^{96}Mo nucleus. The theoretical results are obtained by using the QRPA method.

data [12] for ^{96}Mo is shown in Fig. 1. As can be seen from the figure we have a rather good agreement with experimental data.

In Fig. 2 we show the excitation energies of the multipole states $J^\pi = 0^+$, $J^\pi = 2^+$ and $J^\pi = 4^+$ by using the QRPA method. In the low energy spectra our results are in good comparison with the experimental ones. It is additionally useful to study the angular dependence of the cross sections. In Fig. 3 the differential cross sections for various scattering angle θ (step $\Delta\theta = 15^o$) of the reaction $^{96}Mo(\nu,\nu')^{96}Mo^*$ are shown. In general, our results show a smooth dependance of the $d\sigma/d\omega$ with initial neutrino energy. As can be seen for low neutrino energies up to $\simeq \varepsilon_i = 10-12$ MeV, the region of the discrete energy spectrum of ^{96}Mo, i.e. the differential cross section decreases as the scattering angle increases but for higher energies the cross section increases with the scattering angle [13, 14].

SUMMARY AND CONCLUSIONS

In the present paper we employed the quasiparticle random-phase approximation (QRPA) to study the neutral-current neutrino-nucleus inelastic and elastic scattering cross sections of the even-even Mo isotopes. The lowlying energy spectrum was reproduced. For both Fermi and Gamow-Teller like contributions we calculated the angular dependence of the cross sections from $\theta = 0$ to $\theta = \pi$. We concluded that the differential cross section decreases as the scattering angle increases but for higher energies the cross section increases with the scattering angle. For energies greater than $\varepsilon_i \geq 15$ MeV the total cross section comes from the axial vector component of the operator.

ACKNOWLEDGMENTS

This research was supported by the ΠΕΝΕΔ No 03ΕΔ807 project of the General Secretariat for Research and Technology of the Hellenic Ministry of Development.

REFERENCES

1. T.S. Kosmas and E. Oset, *Phys. Rev.* **C 53**, 1409–1415 (1996).
2. K. Langanke, *Rev. Mod. Phys.* **75**, (2003).
3. P. Lipari, *Introduction to Neutrino Physics, CERN Yellow Report* 2003-003 (2003).
4. A. Bohr and B.R. Mottelson, *Nuclear Structure vol I*, Benjamin, New York, 1969.
5. K. Holinde, *Phys. Rep.* **68** 121 (1981).
6. K.G. Balasi, T.S. Kosmas, P.C. Divari and V.C. Chasioti, *Proc. of the Carp. Sum. Sch. of Phy.* **554-557** (2007).
7. K.G. Balasi, T.S. Kosmas, P.C. Divari and V.Ch. Chasioti, *AIP Conf. Proc.* **972** 554 (2008).
8. K.G. Balasi, T.S. Kosmas, P.C. Divari and H.Ejiri, *J. Phys. Conf. Ser.* **203** 012101 (2010).
9. K.G. Balasi, T.S. Kosmas, P.C. Divari, *AIP Conf. Proc.* **1180** 1 (2009).
10. K.G. Balasi, T.S. Kosmas, P.C. Divari, *Prog. Part. Nucl. Phys.* **64** 414 (2010).
11. K.G. Balasi, T.S. Kosmas, E. Ydrefords, *Nucl. Phys. A* **submited** (2011).
12. D. Abriola and A.A. Sonzogni, *Nucl. Data Sheets* **109** 2501 (2008).
13. V.Ch. Chasioti and T.S. Kosmas *Nucl. Phys. A* **829** 234 (2009).
14. T.S. Kosmas, *Nucl Phys. A*, **683**, 443 (2001).

Neutral current neutrino-^{94}Mo scattering in the context of the QRPA method

K.G. Balasi and T.S. Kosmas

Theoretical Physics Section, University of Ioannina, GR 45110 Ioannina, Greece

Abstract.
A systematic investigation of neutrino-nucleus reaction rates at low and intermediate energies of the stable ^{94}Mo isotope is performed. Differential and integrated cross sections for neutrino inelastic scattering off the aforementioned target are calculated for neutrino energies $\varepsilon_i \preceq 100$ MeV. The nuclear wave functions for the initial and final nuclear states are constructed in the context of the quasi-particle random phase approximation (QRPA). The reliability of our method is tested by checking the reproducibility of the low-lying energy spectrum of the isotope under investigation.

Keywords: Semi-leptonic electroweak interactions; Neutrino-nucleus reactions; Inelastic cross sections; Quasi-particle random phase approximation
PACS: 23.40.Bw;25.30.Pt;21.60.Jz;26.30.+k

INTRODUCTION

The interaction of neutrinos with nuclei both of charged and neutral current reactions, is a highly valuable source for detecting neutrino flavor and exploring the structure of electro-weak interactions [1, 2, 3, 4]. The determination of neutrino nucleus cross sections is of primary importance and to this aim various nuclear structure models have been employed for the description of the nuclear transition matrix elements. Among them the quasi-particle random phase approximation(QRPA) is offering reliable neutrino-nucleus reactions cross sections needed for current neutrino-detection experiments and star evolution modeling. Its main advantage lies in the ability to provide calculations based on a very large valence space.

Recently, an advantageous numerical approach has been developed for calculating the reduced matrix elements of neutrino induced nuclear transitions [5]. In the present work, we use this method to investigate inelastic neutrino scattering for neutral current reactions from stable ^{94}Mo isotope at low and intermediate neutrino energies.

The starting point of our calculations is the Walecka-Donnelly formalism which describes in a unified way electromagnetic and weak semi-leptonic processes in nuclei, by taking advantage of the multipole decomposition of the relevant hadronic current density operators. This formalism has recently been improved, by constructing compact analytical expressions for all nuclear matrix elements of the basic multipole expansion operators entering these cross sections The QRPA method employed for the construction of these nuclear states permits the evaluation of the individual contributions of the various incoherent (inelastic) neutrino induced nuclear transitions of the studied isotope [6].

THE NEUTRINO-NUCLEUS FORMALISM

We consider neutral current neutrino-nucleus interactions in which a low and intermediate energy neutrino (or antineutrino) is scattered elastically or inelastically from a nucleus (A,Z), via exchange of neutral Z^0 bosons with the nucleus as

$$\nu_e + (A,Z) \longrightarrow \nu_e' + (A,Z)^* \tag{1}$$

where ν_e ($\overline{\nu}_e$) denote neutrinos (anti-neutrinos) of any flavor.

In the coherent channel, the nucleus remains in its ground state while in the incoherent the nucleus is excited. The neutrino-induced reactions leave the final nucleus in an excited state below or above particle-emission threshold.

The initial nucleus is assumed to be spherically symmetric and to reside in its ground state with angular momentum and parity $J_p = 0^+$. In our J-projected nuclear structure calculations, the initial and final nuclear states have well-defined spins and parities, $|J^\pi_m\rangle$ (the index m counts the multipole state from low to high energies).

Then the differential cross section(according to the energy and the direction of the outgoing neutrino) is written as

$$\left(\frac{\mathrm{d}^2\sigma_{i\to f}}{\mathrm{d}\Omega \mathrm{d}\omega}\right)_{\nu/\overline{\nu}} = \frac{G_F^2}{\pi}\frac{|\mathbf{k}_f|\,\varepsilon_f}{(2J_i+1)}\left(\sum_{J=0}^{\infty}\sigma_{CL}^J + \sum_{J=1}^{\infty}\sigma_T^J\right) \tag{2}$$

where $\omega = \varepsilon_i - \varepsilon_f$ is the excitation energy of the nucleus and ε_i, denotes the energy of the incoming neutrino while ε_f ($\mathbf{k}_f$) represent the energy (momentum) of the outgoing lepton. The contributions σ_{CL}^J, for the Coulomb and Longitudinal components, and σ_T^J, for the transverse components, are written as

$$\begin{aligned}\sigma_{CL}^J &= (1+\cos\Phi)\left|\langle J_f||\widehat{\mathscr{M}_J}(q)||J_i\rangle\right|^2 + \left(1+\cos\Phi-2b\sin^2\Phi\right)\left|\langle J_f||\widehat{\mathscr{L}_J}(q)||J_i\rangle\right|^2 \\ &+ \left[\frac{\omega}{q}(1+\cos\Phi)\right]2\Re e\langle J_f||\widehat{\mathscr{L}_J}(q)||J_i\rangle\langle J_f||\widehat{\mathscr{M}_J}(q)||J_i\rangle^* \end{aligned} \tag{3}$$

$$\begin{aligned}\sigma_T^J &= \left(1-\cos\Phi+b\sin^2\Phi\right)\left[\left|\langle J_f||\widehat{\mathscr{T}_J^{mag}}(q)||J_i\rangle\right|^2 + \left|\langle J_f||\widehat{\mathscr{T}_J^{el}}(q)||J_i\rangle\right|^2\right] \\ &\mp \frac{(\varepsilon_i+\varepsilon_f)}{q}(1-\cos\Phi)2\Re e\langle J_f||\widehat{\mathscr{T}_J^{mag}}(q)||J_i\rangle\langle J_f||\widehat{\mathscr{T}_J^{el}}(q)||J_i\rangle^* \end{aligned} \tag{4}$$

where Φ is the lepton scattering angle and $b = \varepsilon_i\varepsilon_f/q^2$, In our convention ($\hbar = c = 1$) it holds $|\mathbf{k}_f| = \varepsilon_f$. The summations in Eq. (2) contain the contributions of the well known operators Coulomb $\widehat{\mathscr{M}_J}$, longitudinal $\widehat{\mathscr{L}_J}$, transverse electric $\widehat{\mathscr{T}_J^{el}}$ and transverse magnetic $\widehat{\mathscr{T}_J^{mag}}$ multipole operators as defined in [6].

The magnitude of the three momentum transfer q is given by

$$q = |\mathbf{q}| = \left[\omega^2 + 2\varepsilon_i\varepsilon_f(1-\cos\Phi)\right]^{\frac{1}{2}} \tag{5}$$

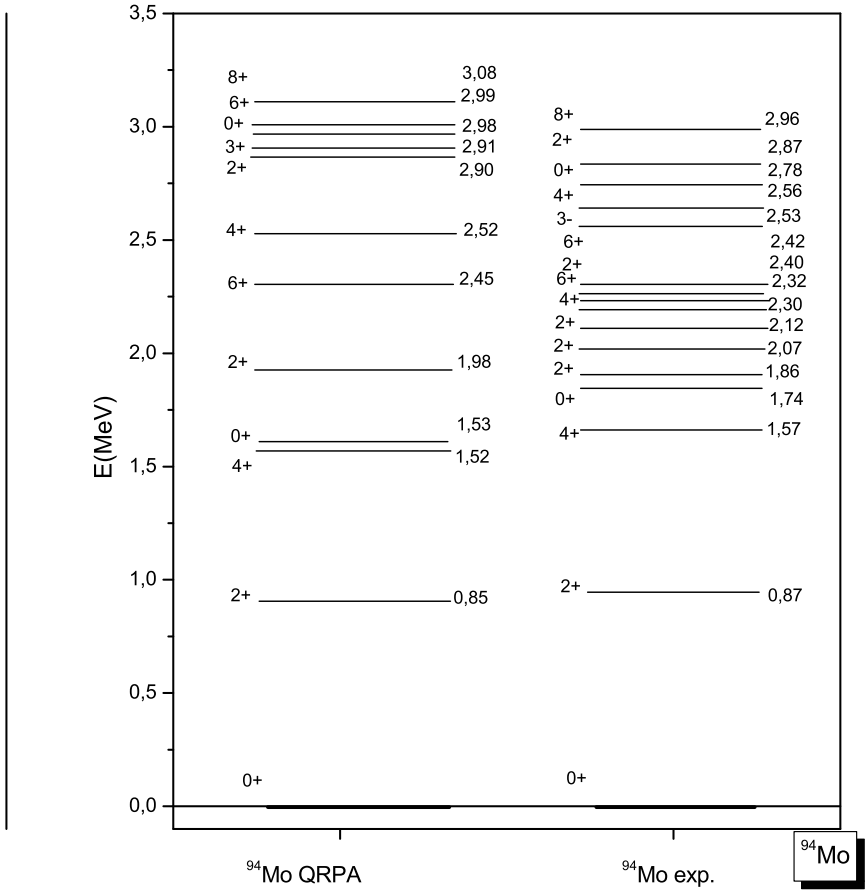

FIGURE 1. Comparison of experimental(left) and theoretical (right)low-energy spectra of ^{94}Mo nucleus. The theoretical results are obtained by using the QRPA method.

RESULTS

In this work we have performed realistic state-by-state calculations for inelastic and elastic neutrino-nucleus scattering off the stable ^{94}Mo isotope. Our calculations were performed in five steps: First the wave functions of the initial (the 0^+ ground state of the even-even nucleus) and the final states were calculated within the QRPA. The obtained wave functions were subsequently used to evaluate the required reduced one-body transition densities. Then, the double-differential cross section was calculated for each scattering angle (θ), neutrino energy (E_ν) and final state. In the next step, the differential cross section as a function of the scattering angle and neutrino energy was obtained by summing over all the (discrete) final states. Then, numerical integration techniques were used to calculate the total cross section $\sigma(E_\nu)$ as a function of neutrino energy. In the last step the averaged cross section $\langle\sigma\rangle$ was finally obtained by folding the cross section $\sigma(E_\nu)$ with a two-parameter Fermi-Dirac distribution appropriate for

TABLE 1. Pairing gaps and the corresponding pairing strength parameters

Nucleus	Δ_{np}	Δ_{pp}	g_{ph}	g_{pp}
^{94}Mo	0.979	1.510	1.040	0.972

supernova neutrinos.

For the construction of the wavefunctions of the initial and final nuclear states we used the QRPA method. Both Fermi and Gamow-Teller like contributions of the polar vector and axial vector have been considered. A Coulomb corrected Woods-Saxon potential was used as field interaction and as two body residual interaction the Bonn-C meson exchange potential was utilized. Our model space consists of the following eleven active single particle levels: $0f^{7/2}$, $1p^{3/2}$, $1d^{1/2}$, $0f^{5/2}$, $0g^{9/2}$, $1d^{5/2}$, $2s^{1/2}$, $1d^{3/2}$, $0g^{7/2}$, $0h^{11/2}$, $0h^{9/2}$(up to $4\bar{h}\omega$ major harmonic oscillator shells).

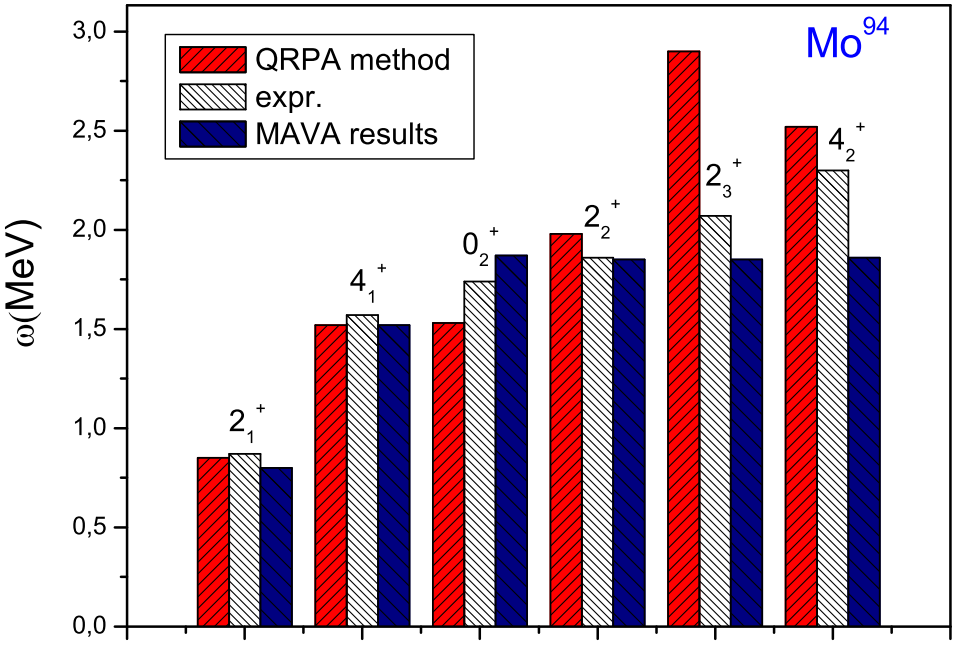

FIGURE 2. Excitation energies for the multipole states $J^\pi = 2_1^+$, $J^\pi = 4_1^+$ and $J^\pi = 6_1^+$ of the ^{94}Mo nucleus. Our theoretical results are compared with the experimental results as well as theoretical results obtained by the MAVA method

At the BCS level, the values of the pairing parameters for protons (g^p_{pair}) and neutrons (g^n_{pair}) which reproduce the pairing gaps in the usual way [7] was found to be $g^p_{pair} = 0.972$ and $g^n_{pair} = 1.040$. By solving the QRPA equations the strength parameters for the particle-hole channel, g_{ph} and the particle-particle channel,g_{pp} were fixed so as the

lowest lying excitation energies to be reproduced. The above parameters get values in the ranges shown in Table 1. The evaluation of these strength parameters was obtained separately for each set of multiple states. By using the above parameters we produced the low-lying energy spectrum, shown in Figure 1, where this spectrum was compared to that given by experiment.

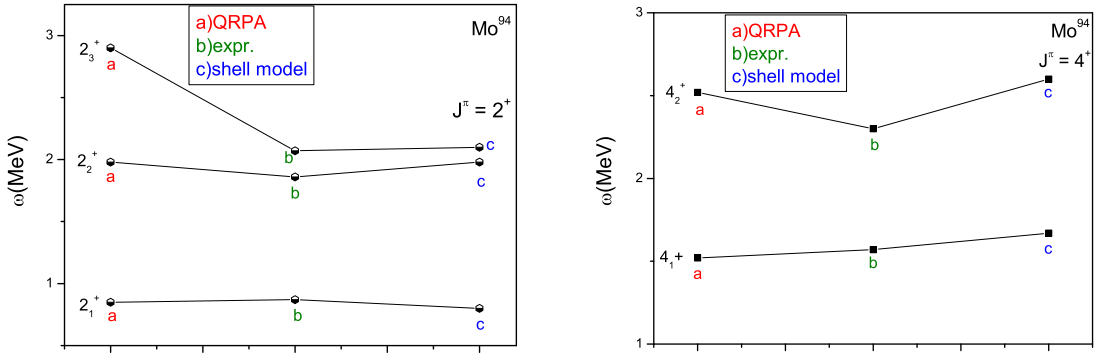

FIGURE 3. Excitation energies for the multipole states $J^\pi = 2^+$ and $J^\pi = 4^+$ of the ^{94}Mo isotope. Our theoretical results are compared with the experimental results and results obtained by using the shell model method.

In Figure 2 we show the excitation energies of the multipole states $J^\pi = 2_1^+$, $J^\pi = 4_1^+$ and $J^\pi = 6_1^+$ by using the QRPA method. In the low energy spectra our results are in good comparison with the experimental ones. In Figure 3 the excitation energies of the $J^\pi = 2^+$ and $J^\pi = 4^+$ states are illustrated. The obtained results are compared to the experimental results and those obtained by using the shell model method.

In the next step of our research we proceeded with the calculation of the cross sections.The primary results refer to the double differential cross sections of Eq.(2). Total differential cross sections were evaluated by summing over partial rates for various sets of multipole states included in our truncated model space up to $J^\pi = 8^+$. For integrated (total) cross-sections we used numerical integration techniques(Gauss method) to integrate the aforementioned differential cross sections [8]. From our results, shown in Table 2, one could conclude that the total cross sections are large at low energies. For higher neutrino energies,($\varepsilon_i > 80$ MeV) the total cross sections are dramatically decreased [9, 10, 11, 12, 13, 14].

SUMMARY AND CONCLUSIONS

In the present paper we employed the quasiparticle random-phase approximation (QRPA) to study the neutral-current neutrino-nucleus inelastic and elastic scattering cross sections. Our present results refer to the stable ^{94}Mo isotope. The obtained energy spectra show a good agreement with experimental data.

The results for the contribution of the separate multipole sets of excited states have shown that for low-energy neutrino-scattering off ^{94}Mo the cross sections are dominated by transitions to 1^+ states.

TABLE 2. Total cross sections (in $10^{-40} cm^2$) for the neutral-current neutrino-nucleus reactions, $^{94}Mo(\nu,\nu')^{94}Mo^*$, calculated with QRPA method.

Initial Neutrino Energy $\varepsilon_i(MeV)$	Total reaction Cross Sections $^{94}Mo(\nu,\nu')^{94}Mo^*$
5	1.35(-2)
10	2.47(-2)
15	2.32(-1)
20	1.197(+0)
25	1.12(+1)
30	8.16(+1)
35	1.60(+1)
40	2.74(+2)
45	4.23(+2)
50	6.06(+2)
55	8.13(+3)
60	1.04(+3)
65	1.27(+4)
70	3.85(+4)
75	4.88(+4)
80	5.90(+4)
85	6.83(+4)
90	7.62(+4)
95	8.22(+4)
100	8.63(+4)

ACKNOWLEDGMENTS

This research was supported by the ΠΕΝΕΔ No 03ΕΔ807 project of the General Secretariat for Research and Technology of the Hellenic Ministry of Development.

REFERENCES

1. K. Langanke, *Rev. Mod. Phys.* **75**, (2003).
2. H. Ejiri, *Phys. Rep.* **338**, 265–351 (2000), and references therein.
3. W.C. Haxton, *Phys.Rev.Lett.* **60**, 768 (1988).
4. J.N. Bahcall and R.K. Ulrich, *Rev. Mod. Phys.* **60** (1988) 297.
5. V.Ch. Chasioti and T.S. Kosmas *Nucl. Phys. A* **829** (2009) 234.
6. T.S. Kosmas and E. Oset, *Phys. Rev.* **C 53**, 1409–1415 (1996).
7. T.S. Kosmas, *Nucl Phys. A*, **683**, 443 (2001).
8. E. Kolbe and T.S. Kosmas,*Springer Trac. Mod. Phys.* **163**, 199–225 (2000).
9. K.G. Balasi, T.S. Kosmas, P.C. Divari and V.C. Chasioti, *Proc. of the Carp. Sum. Sch. of Phy.* **554-557** (2007).
10. K.G. Balasi, T.S. Kosmas, P.C. Divari and V.Ch. Chasioti, *AIP Conf. Proc.* **972** (2008) 554.
11. K.G. Balasi, T.S. Kosmas, P.C. Divari and H.Ejiri, *J. Phys. Conf. Ser.* **203** (2010) 012101.
12. K.G. Balasi, T.S. Kosmas, P.C. Divari, *AIP Conf. Proc.* **1180** (2009) 1.
13. K.G. Balasi, T.S. Kosmas, P.C. Divari, *Prog. Part. Nucl. Phys.* **64** (2010) 414.
14. K.G. Balasi, T.S. Kosmas, E. Ydrefords, *Nucl. Phys. A* **submited** (2011) .

Approximate symmetries in the Interacting Boson Model

Dennis Bonatsos

Institute of Nuclear Physics, N.C.S.R. "Demokritos", GR-15310 Aghia Paraskevi, Attiki, Greece

Abstract

Dynamical symmetries have played a central role for many years in the study of nuclear structure. Recently, the concepts of Partial Dynamical Symmetry (PDS) and Quasi-Dynamical Symmetry (QDS) have been introduced. We shall discuss examples of PDS and QDS appearing in the large boson number limit of the Interacting Boson Model.

Dynamical symmetries have been used in nuclear structure for several years. A well known example is provided by the Interacting Boson Model, having an overal U(6) symmetry, within which the dynamical symmetries U(5), SU(3), and O(6) occur. These dynamical symmetries are traditionally placed at the corners of the symmetry triangle of IBM, depicted in Fig. 3.

More recently, two new kinds of symmetries have been considered, the Partial Dynamical Symmetries (PDS) [1–3] and the Quasi-Dynamical Symmetries (QDS) [4–8].

There are three kinds of Partial Dynamical Symmetries [1–3]:
i) Type I, where some of the states preserve all the relevant symmetry.
ii) Type II, in which all the states preserve part of the dynamical symmetry.
iii) Type III, where some of the states preserve part of the symmetry.
We will show [9] that signs of a yet unknown PDS seem to appear near the critical line [10,11] of the IBM.

On the other hand, Quasi-Dynamical Symmetries [4–8] are defined as the situations in which dynamical symmetries persist despite strong symmetry-breaking interactions. We will show [12] that such a QDS appears to be providing an explanation for the existence of the Alhassid–Whelan arc of regularity [13,14] among chaotic regions within the symmetry triangle of the IBM.

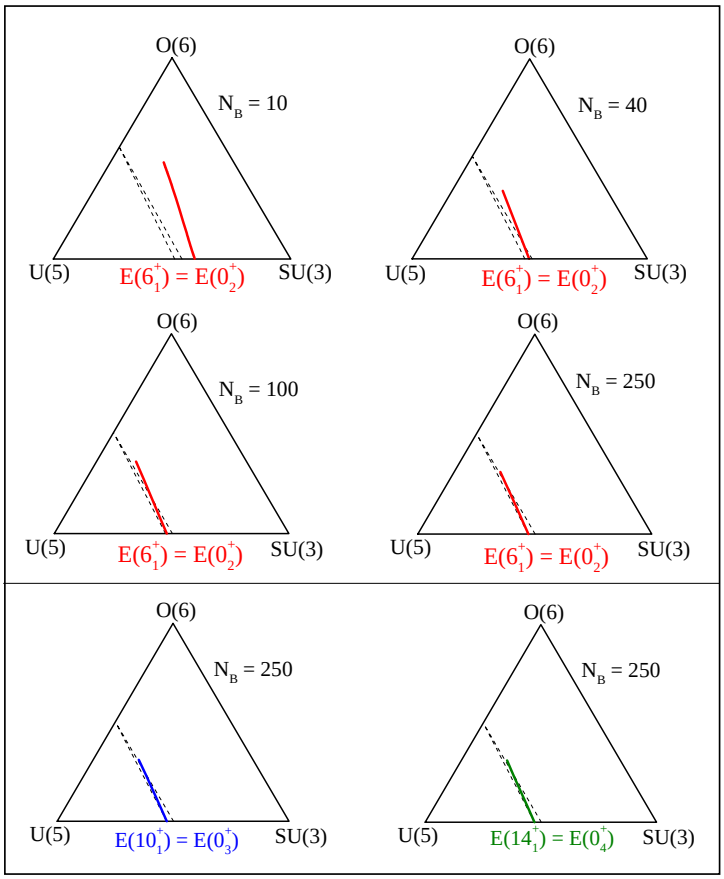

Fig. 1. (Top) Line of degeneracy between the 0_2^+ and 6_1^+ levels (solid line) for N_B = 10, 40, 100, and 250 in the IBA triangle. (Bottom) Line of degeneracy between the 0_3^+ and 10_1^+ levels (solid line) for $N_B = 250$ (left) and between the 0_4^+ and 14_1^+ levels (solid line) for $N_B = 250$ (right) in the IBA triangle. The dashed lines denote the critical region in the IBA obtained in the large N_B limit from the intrinsic state formalism. Taken from Ref. [9].

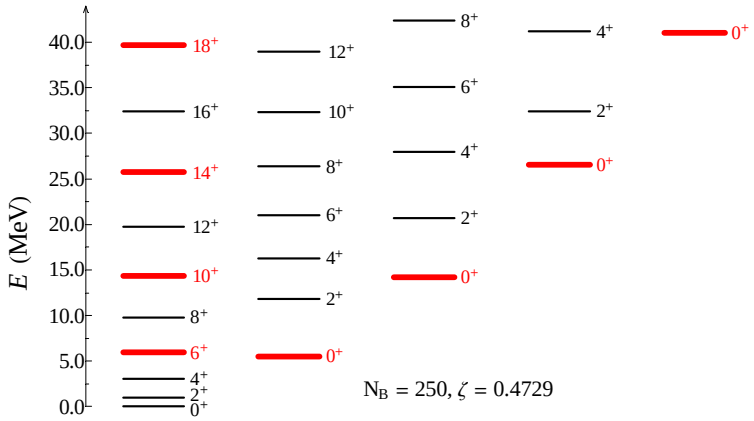

Fig. 2. Energies of low-lying states (normalized to $E(2_1^+)$=1) of the Hamiltonian of Eq. (1) with χ=$-\sqrt{7}/2$, ζ=0.4729, and N_B=250. The parameter ζ was chosen to reproduce the approximate degeneracy of $E(0_2^+)$ and $E(6_1^+)$. Taken from Ref. [9].

We focus attention on the IBM, especially at large boson numbers. We use an IBA Hamiltonian of the form

$$H(\zeta,\chi) = c\left[(1-\zeta)\hat{n}_d - \frac{\zeta}{4N_B}\hat{Q}^\chi\cdot\hat{Q}^\chi\right], \qquad (1)$$

where $\hat{n}_d = d^\dagger\cdot\tilde{d}$, $\hat{Q}^\chi = (s^\dagger\tilde{d} + d^\dagger s) + \chi(d^\dagger\tilde{d})^{(2)}$, N_B is the number of valence bosons, and c is a scaling factor. Calculations in this work have been performed with the code IBAR [15], which has recently been developed to handle large boson numbers.

As seen in Fig. 1, certain lines representing degeneracies of pairs of levels [(6_1, 0_2^+), (10_1, 0_3^+), (14_1, 0_4^+)] approach the critical region as the boson number is increased. In Fig. 2 one can see that these are degeneracies between members of the ground state band (gsb) and the 0^+ states studied in Refs. [16,17].

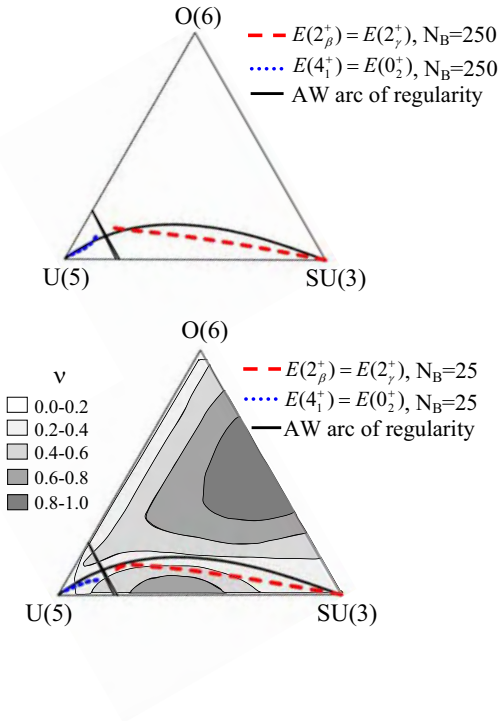

Fig. 3. IBA symmetry triangle in the parametrization of Eq. (2) with the three dynamical symmetries and the Alhassid–Whelan arc of regularity. The shape coexistence region between spherical and deformed phases, shown by slanted lines near the U(5) vertex, encloses a first order phase transition terminating in a point of second order transition on the U(5)-O(6) leg. The loci of the degeneracies $E(2^+_\beta)$=$E(2^+_\gamma)$ (dashed line on the right, corresponding to the QDS discussed in the text) and $E(4^+_1)$=$E(0^+_2)$ (dotted line on the left) are shown for N_B=250 (top) and N_B = 25 (bottom). In the bottom part, the ν-diagram, based on Ref. [14] is shown. Taken from Ref. [12].

One can see empirically that these states approximately satisfy [17] the expression $J(J+2) = 12n(n+3)$, where J indicates the angular momentum of

the gsb members, while n enumerates the 0^+ states. These degeneracies maybe indicate the existence of some underlying symmetry, which is yet unknown. Locating this symmetry could help in clarifying the nature of the X(5) critical point symmetry, which remains unknown to date.

Now we turn attention to the QDS concept. A puzzle which has been around for nearly 20 years is the existence of the Alhassid–Whelan arc of regularity [13,14], a region of increased regularity within the symmetry triangle of the IBM, amidst chaotic regions, as shown in Fig. 3. In these studies a different parametrization (using the parameters η, χ) of the IBM Hamiltonian of Eq. (2) has been used, reading [13,14]

$$H(\eta,\chi) = c\left[\eta\hat{n}_d + \frac{\eta-1}{N_B}\hat{Q}^\chi\cdot\hat{Q}^\chi\right], \qquad (2)$$

where the symbols have the same meaning as in Eq. (1).

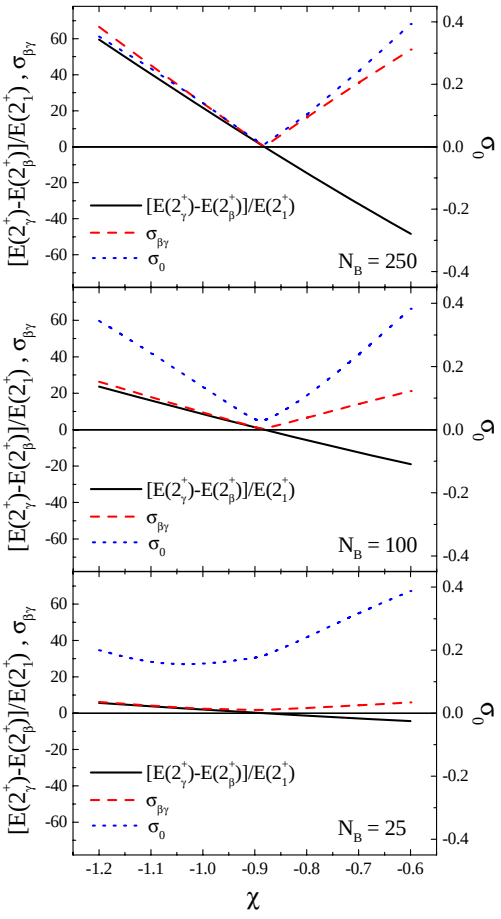

Fig. 4. The energy difference $E(2^+_\gamma) - E(2^+_\beta)$ (normalized to $E(2^+_1)$) and the quality measures $\sigma_{\beta\gamma}$ [Eq. (3), up to L_{max}=10] and σ_0 [Eq. (4), up to i_{max}=9], are shown for η=0.632, varying χ, and boson numbers N_B=25, 100, 250. Taken from Ref. [12].

We shall show that an underlying SU(3) QDS is responsible for the existence of the arc. In order to do so, we shall use some measures of SU(3), like the

amount of the degeneracy breaking between the β_1 and γ_1 bands [12]

$$\sigma_{\beta\gamma} = \sqrt{\frac{\sum_2^{L_{max}} [E(L_\beta^+) - E(L_\gamma^+)]^2}{\frac{L_{max}}{2} - 1}}, \tag{3}$$

where $L_\beta^+ = L_\gamma^+$ and all energies are normalized to $E(2_1^+)$. In order to examine to which degree the 0^+ states occurring in an IBM calculation obey the SU(3) rules, we shall also use the relevant rms deviation of the 0^+ states from the positions predicted by the second order Casimir operator of SU(3) [12],

$$\sigma_0 = \sqrt{\frac{\sum_3^{i_{max}} [E(0_i^+)^{th} - E(0_i^+)^{\mathrm{SU(3)}}]^2}{i_{max} - 3}}. \tag{4}$$

with all energies normalized to $E(0_2^+)$ and considering the lowest nine 0^+ states (i.e., i_{max}=9).

As depicted in Fig. 4, one can see numerically that both measures of SU(3) behaviour exhibit at large boson numbers strong minima at the point where the degeneracy $2_\gamma^+ = 2_\beta^+$ occurs. This indicates that the spectra acquire an SU(3) structure if this degeneracy is imposed. In Ref. [9] one can see that the SU(3) degeneracies appear also at higher bands, well beyond the gsb.

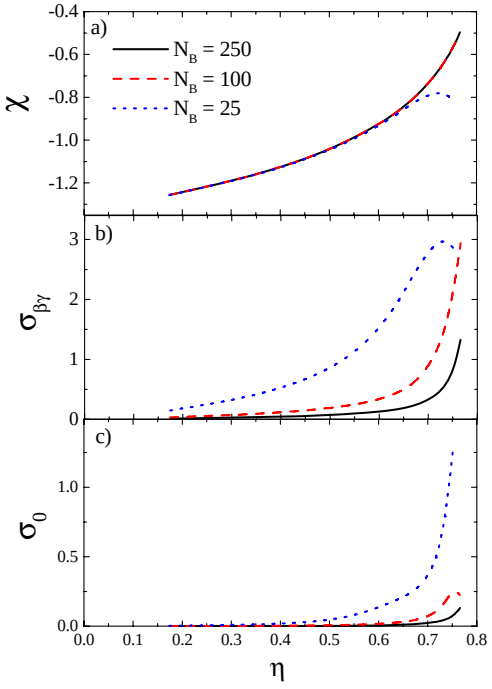

Fig. 5. The $|\chi|$ parameter values providing the degeneracy $E(2_\beta^+)$=$E(2_\gamma^+)$ and the quality measures $\sigma_{\beta\gamma}$ [Eq. (3), up to L_{max}=10] and σ_0 [Eq. (4), up to i_{max}=9], are shown for different values of η and N_B=25, 100, 250. Taken from Ref. [9].

The track of this degeneracy within the symmetry triangle of the IBM shown in Fig. 3, nearly coincides with the Alhassid–Whelan arc of regularity, suggest-

ing an underlying SU(3) symmetry as the reason behind the existence of the branch of the arc between the SU(3) vertex and the critical line. In Fig. 5 one can see that the SU(3) measures remain close to their SU(3) values far beyond the SU(3) point, thus providing an example of a SU(3) QDS. A similar line, based on the degeneracy $E(4_1^+) = E(0_2^+)$, can be obtained between the U(5) vertex and the critical line, but the relevant minima there are rather shallow, in sharp contrast with the deep minima of Fig. 4. 42

In conclusion, we have shown some examples of PDS and QDS appearing in the framework of the IBM. Further searches for approximate symmetries in nuclear structure models appear to be promising.

References

[1] Y. Alhassid and A. Leviatan, *J. Phys. A: Math. Gen.* **25** (1992) L1265.

[2] A. Leviatan, *Phys. Rev. Lett.* **77** (1996) 818.

[3] A. Leviatan and P. Van Isacker, *Phys. Rev. Lett.* **89** (2002) 222501.

[4] D. J. Rowe, *Phys. Rev. Lett.* **93** (2004) 122502.

[5] D. J. Rowe, P. S. Turner, and G. Rosensteel, *Phys. Rev. Lett.* **93** (2004) 232502.

[6] D. J. Rowe, *Nucl. Phys. A* **745** (2004) 47.

[7] P. S. Turner and D. J. Rowe, *Nucl. Phys. A* **756** (2005) 333.

[8] G. Rosensteel and D. J. Rowe, *Nucl. Phys. A* **759** (2005) 92.

[9] D. Bonatsos, E.A. McCutchan, R.F. Casten, and R.J. Casperson, *Phys. Rev. Lett.* **100** (2008) 142501.

[10] F. Iachello, N. V. Zamfir, and R. F. Casten, *Phys. Rev. Lett.* **81** (1998) 1191.

[11] E. A. McCutchan, D. Bonatsos, and N. V. Zamfir, *Phys. Rev. C* **74** (2006) 034306.

[12] D. Bonatsos, E. A. McCutchan, and R. F. Casten, *Phys. Rev. Lett.* **104** (2010) 022502.

[13] Y. Alhassid and N. Whelan, *Phys. Rev. Lett.* **67** (1991) 816.

[14] N. Whelan and Y. Alhassid, *Nucl. Phys. A* **556** (1993) 42.

[15] R. J. Casperson, Ph.D. thesis, Yale University (2010).

[16] D. Bonatsos, E.A. McCutchan, and R.F. Casten, *Phys. Rev. Lett.* **101** (2008) 022501.

[17] D. Bonatsos, E.A. McCutchan, R.F. Casten, R.J. Casperson, V. Werner, and E. Williams, *Phys. Rev. C* **80** (2009) 034311.

β^--Decay Half-lives Using the ANN Model: Input for the R-Process

N. J. Costiris*, E. Mavrommatis

Department of Physics, Section of Nuclear & Particle Physics, University of Athens, 15771 Athens, Greece

K. A. Gernoth

School of Physics & Astronomy, Schuster Building, The University of Manchester, Manchester, M13 9PL, United Kingdom

J. W. Clark

McDonnell Center for the Space Sciences and Department of Physics, Washington University, St. Louis, Missouri 63130, USA

Abstract

Full understanding of nucleosynthesis via the r-process continues to be a major challenge for nuclear astrophysics. Apart from issues within astrophysical modeling, there remain significant uncertainties in the nuclear physics input, notably involving the β-decay halflives of neutron-rich nuclei. Both the element distribution on the r-process path and the time scale of the r-process are highly sensitive to β^- lifetimes. Since the majority of nuclides that lie on the r-process path will not be experimentally accessible in the foreseeable future, it is important to provide accurate predictions from reliable models. Toward this end, a statistical global model of the β^--decay halflife systematics has been developed to estimate the lifetimes of nuclides relevant to the r-process, in the form of a fully-connected, multilayer feedforward Artificial Neural Network (ANN) trained to predict the halflives of ground states that decay 100% by the β^- mode. In predictive performance, the model can match or even surpass that of conventional models of β-decay systematics. Results are presented for nuclides situated on the r-ladders $N = 50$, 82 and 126 where abundances peak, as well as for others that affect abundances between peaks. Also reported are results for halflives of interesting neutron-rich nuclides on or towards the r-process path that have been recently measured. Comparison with results from experiment and conventional models is favorable.

*Speaker, Url: www.pythaim.phys.uoa.gr

Email addresses: ncost@phys.uoa.gr (N. J. Costiris), emavrom@phys.uoa.gr (E. Mavrommatis), klaus.a.gernoth@manchester.ac.uk (K. A. Gernoth), jwc@wuphys.wustl.edu (J. W. Clark)

1. Introduction

Nucleosynthesis through the r-process produces more than half of the heavy elements beyond iron. Command of the quantitative details of this process is one of the most exciting and challenging goals of modern nuclear astrophysics [1, 2]. Its astrophysical site as well as the necessary nuclear physics input are yet to be unambiguously identified. A knowledge of β^--decay halflives T_{β^-} of heavy neutron-rich nuclides are of primary importance for a full understanding of the r-process, since they play a crucial role in determination of the time scale for matter flow and of the abundances of heavier nuclei. In the classical waiting-point approximation, T_{β^-} values are particularly important for the r-ladder isotones $N = 50$, 82, and 126 where abundances peak. In the latter dynamical r-process models T_{β^-} of all nuclides are involved.

In recent years, significant progress has been made experimentally toward determination of β^- halflives of r-process nuclides, and there are ambitious plans for further measurements at existing and new-generation facilities such as FAIR/GSI, FRIB/NSCL, and RIBF/RIKEN [1]. Still, the majority of the neutron-rich nuclides involved will remain inaccessible in the near future. Thus, continued progress rests on reliable predictions from models of nuclear systematics, based on fundamental theory or otherwise. A number of useful approaches to modeling β^- lifetimes have been proposed and applied to different regions of the nuclear chart. These include the shell-model calculation of Ref. [3] and models based on the proton-neutron Quasiparticle Random-Phase Approximation (*pn*QRPA). Important among the latter are the hybrid model by Möller et al., which combines the *pn*QRPA model with the statistical Gross Theory of *ff* decay (*pn*QRPA+*ff*GT) [4], the model by Borzov et al. in which the continuum QRPA is based on a self-consistent density-functional description of the ground-state properties (DF3+CQRPA) [5], and the relativistic *pn*QRPA model of Ref. [6] (*pn*RQRPA+*ff*). Although there is continuing improvement, the predictive power of these "theory-thick" models is rather limited far from stability. This being the case,"theory-thin," data-driven statistical modeling based on artificial neural networks (ANNs) and other adaptive techniques of statistical inference presents a potentially effective alternative for global modeling of β^--decay lifetimes, as it does for other nuclear properties. Here we apply our recently developed ANN statistical global model of T_{β^-} systematics [7] to nuclides relevant to the r-process. The essentials of this model are sketched in Sec. 2. Results are presented and discussed in Sect. 3, with concluding remarks in Sec. 4. (Further details can be found in Ref. [8].)

2. The Model

The fully-connected feedforward Artificial Neural Network (ANN) of Ref. [7] with architecture symbolized by [3-5-5-5-5-1—116] has been employed to generate T_{β^-} values for r-process nuclides. Based on existing lifetime data, this network has been taught with the Levenberg-Marquardt backpropagation optimization algorithm, supplemented

by a combination of two well-established techniques, namely Bayesian regularization and cross-validation to avoid overfitting effects. The activation functions of the processing units (model neurons) of the network are taken to be of hyperbolic-tangent sigmoid form in the four intermediate (hidden) layers, a saturated linear function being chosen for the single neuron of the output layer. Inputs to the network consist of the proton and neutron numbers Z and N of the parent nucleus, together with an extra parity input coding the δ-parameter, defined as the mean of the parities of Z and N. Implementation of this parity unit helps to soften the discrepancies in performance induced by pairing gaps. The experimental data used in our β^--decay modeling have been taken from the Nubase2003 evaluation of nuclear and decay properties [9]. We restrict attention to the ground states of parent nuclei that decay 100% by the β^- mode. Additionally, we apply a cut-off at 10^6 s. Without detriment to the prediction of β^- halflives, this creates a more homogeneous collection of nuclides, which facilitates training of the network. We arrive at a data set called NuSet-B consisting of 838 nuclides, which is divided randomly into three subsets, with 503 nuclides (60%) used for training the network (learning set) and 167 (20%) used to assess the training procedure (validation set), the residual 168 (20%) being reserved to evaluate the accuracy of prediction (test set). In direct comparison with the experimental data, the ANN performance measured by the root-mean-square error $\sigma_{\rm rms}$ attains the values 0.53 (learning), 0.60 (validation) and 0.65 (test).

3. Results and Discussion

We now present some results for β^--decay halflives of nuclides relevant to the r-process, obtained by implementation of the ANN model described in the preceding section. As mentioned in the introduction, knowledge of T_{β^-} values for nuclides with $N = 50$, 82 and 126 plays a key role in understanding the process. Fig. 1 displays results for these isotones in interesting Z regions, together with the available experimental results [9, 10] and T_{β^-} values given by the *pn*QRPA+*ff*GT [4], DF3+CQRPA [5], and shell-model calculations [3]. In most cases our values are smaller than those provided by the *pn*QRPA+*ff*GT model, which would imply a corresponding speedup of the r-process. Information on β^- decay of other neutron-rich nuclides is also important for studies of r-process nucleosynthesis. Accordingly, Fig. 1 presents halflife results from our model for known and unknown nuclides of the isotopic chain of Ir, in comparison with the available experimental values [9, 14] and results from the *pn*QRPA+*ff*GT [4] and DF3+CQRPA [5] calculations. The predictive performance of the ANN model can be further assessed in terms of recently measured β^--decay lifetimes of neutron-rich nuclides [8-12]. The corresponding halflife results are included in Table 1, along with those given by the *pn*QRPA+*ff*GT [4] and DF3+CQRPA [5] models. For these nuclides, the $\sigma_{\rm rms}$ for the ANN and *pn*QRPA+*ff*GT models are 0.45 and 0.77, respectively.

4. Conclusion and Prospects

Our data-driven, theory-thin, statistical global model of β^--decay halflives, and its successors, can provide a robust tool that complements the conventional r-process clock and matter-flow studies. We plan further statistical modeling of nuclear properties relevant to the r-process, including masses and neutron-capture cross sections, based on existing artificial neural network (ANN) techniques and support vector machine (SVM) approaches [15]. Refinement of current treatments will be sought through committee-machine strategies, in which different ANNs are built to process input patterns and vote on the proper output.

5. Acknowledgments

The authors thank I. N. Borzov and T. Marketin for communicating with theoretical data and for helpful discussions. This research has been supported in part by the University of Athens under Grant No. 70/4/3309.

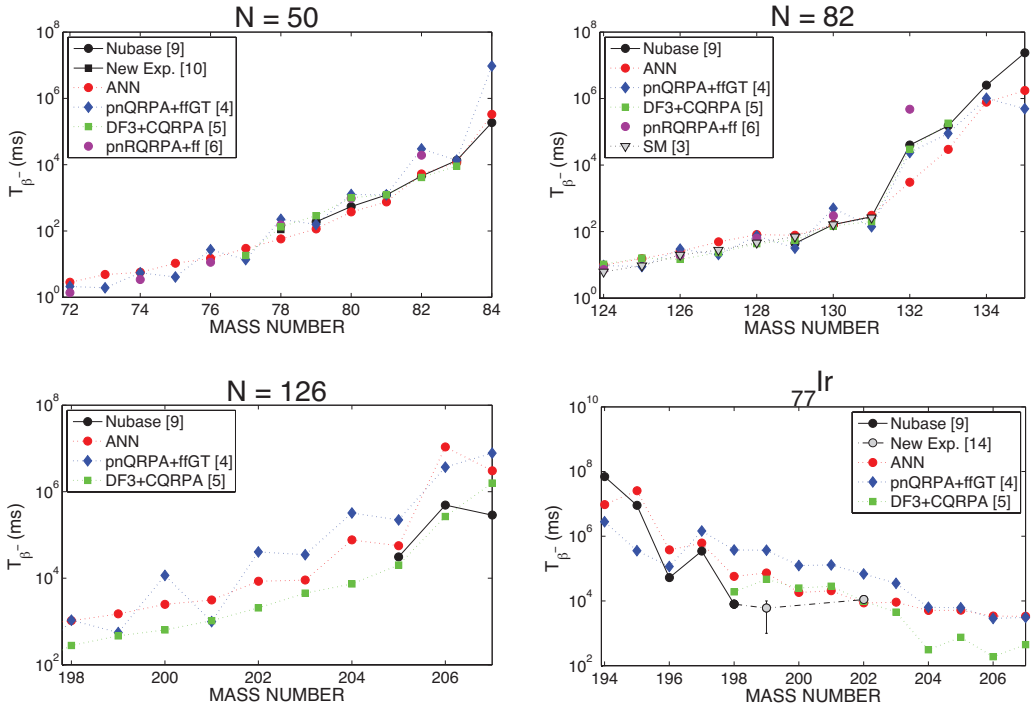

Figure 1: β^--decay halflives given by the ANN model for the r-ladder isotonic chains at $N = 50$, 82 and 126 and for the isotopic chain of Ir, in comparison with experimental and theoretical data.

	$T_{\beta^-}(ms)$			
Nucleus	**Exp. Data**	**ANN Model**	***pn*QRPA+*ff*GT**	**DF3+CQRPA**
a.) $N = 50$ **- P. T. Hosmer et al. (NSCL, MSU) 2005 [10]**				
^{78}Ni	110^{+100}_{-60}	57	224	108
b.) $N \simeq 66$ **- J. Pereira et al. (NSCL, MSU) 2009 [11]**				
^{105}Y	$160 \pm 15^{+85}_{-60}$	58	46	-
^{106}Zr	$260 \pm 20^{+35}_{-30}$	106	322	-
^{107}Zr	$150 \pm 5^{+40}_{-30}$	75	177	-
^{111}Mo	$200 \pm 10^{+40}_{-35}$	145	808	146
c.) $N \simeq 82$ **- F. Montes et al. (NSCL, MSU) 2006 [12]**				
^{115}Tc	73^{+32}_{-22}	84	71	134
^{116}Ru	204^{+32}_{-29}	188	540	193
^{117}Ru	142^{+18}_{-17}	129	163	127
^{118}Ru	123^{+48}_{-35}	69	212	95
^{119}Rh	171 ± 18	209	108	146
^{120}Rh	136^{+14}_{-13}	196	83	-
^{121}Rh	151^{+67}_{-58}	91	62	87
^{121}Pd	285 ± 24	334	1275	262
^{122}Pd	175 ± 16	227	951	184
^{123}Pd	174^{+38}_{-34}	149	397	143
^{124}Pd	38^{+38}_{-19}	124	289	105
d.) $N \simeq 82$ **- K.-L. Kratz et al. (ISOLDE, CERN) 2005 [13]**				
^{133}Cd	57 ± 10	57	185	47
^{138}Sn	150 ± 60	113	336	240
e.) $N \simeq 126$ **- T. Kurtukian-Nieto et al. (FRS, GSI) 2009 [14]**				
^{194}Re	$1^{+0.5}_{-0.5}$ (s)	20.8 (s)	70.8 (s)	2.1 (s)
^{195}Re	6^{+1}_{-1} (s)	23.9 (s)	3.3 (s)	8.5 (s)
^{196}Re	3^{+1}_{-2} (s)	8.8 (s)	3.6 (s)	1.4 (s)
^{199}Os	5^{+4}_{-2} (s)	13.6(s)	106.8 (s)	6.6 (s)
^{200}Os	6^{+4}_{-3} (s)	21.7 (s)	187.1 (s)	6.9 (s)
^{199}Ir	6^{+5}_{-4} (s)	73 (s)	370.6 (s)	46.7 (s)
^{202}Ir	11^{+3}_{-3} (s)	8.6 (s)	68.4 (s)	9.8 (s)
	$\sigma^{Log_{10}T_{\beta^-}}_{\rm rms}$	**0.45**	**0.77**	**-**

Table 1: β^--decay halflives of newly measured r-process nuclides beyond Nubase as given by the ANN model, in comparison with experimental values and results from the *pn*QRPA+ffGT [4] and DF3+CQRPA [5] calculations.

References

[1] The Frontiers of Nuclear Science: "A Long Range Plan for the New Decade" (DOE/NSF Nuclear Science Advisory Committee, December 2007); NuPECC: "Long Range Plan 2010, Perspectives of Nuclear Physics in Europe", edited by G. Rosner et al., NuPECC Report (NuPECC, December 2010).

[2] M. Arnould, S. Gorielly and K. Takahashi, Phys. Repts. **450** (2007) 97; K.-L. Kratz , K. Farouqi, and B. Pfeiffer, Prog. Part. Nucl. Phys. **59** (2007) 147.

[3] J. J. Cuenca-Garcia et al., Eur. Phys. J. **A34** (2007) 99.

[4] P. Möller, B. Pfeiffer and K.-L. Kratz, Phys. Rev. **C67** (2003) 055802.

[5] I. N. Borzov, Phys. Rev. **C67** (2003) 025802; Private communication (2010).

[6] T. Marketin, D. Vretenar and P. Ring, Phys. Rev. **C75** (2007) 024304; Private communication (2010).

[7] N. J. Costiris, E. Mavrommatis, K. A. Gernoth and J. W. Clark, Phys. Rev. **C80** (2009) 044332.

[8] N. J. Costiris, E. Mavrommatis, K. A. Gernoth and J. W. Clark, in submission to Phys. Rev. **C**.

[9] G. Audi, O. Bersillon, J. Blachot and A.H. Wapstra, Nucl.Phys. **A729** (2003) 3.

[10] P. T. Hosmer, H. Schatz, A. Aprahamian, O. Arndt et al., Phys. Rev. Lett. **94** (2005) 112501.

[11] J. Pereira, S. Hennrich, A. Aprahamian, O. Arndt, A. Becerril et al., Phys. Rev. **C79** (2009) 35806.

[12] F. Montes, A. Estrade, P. T. Hosmer, S. N. Liddick, P. F. Mantica et al., Phys. Rev. **C73** (2006) 035801.

[13] K.-L. Kratz, B. Pfeiffer, O. Arndt, S. Hennrich, A. Wöhr, et al., Eur. Phys. J. **A25** (2005) 633.

[14] T. Kurtukian-Nieto, J. Benlliure, K.-H. Schmidt, L. Audouin et al., Nucl. Phys. **A827** (2009) 587c.

[15] J. W. Clark and H. Li, Int. J. Mod. Phys. **B20** (2006) 5015.

Inelastic cross sections of relativistic protons on Lead

M. Zamani[a*], S. Stoulos[a], M. Fragopoulou[a], M. Manolopoulou[a], N. A. Sosnin[b] and M. Krivopustov[b]

[a]*Aristotle University of Thessaloniki, School of Physics, Thessaloniki 54 124, Greece*
[b]*Institute for Nuclear Research, 141980 Dubna, Russia*

Abstract

The inelastic cross section of relativistic protons in Lead was determined indirectly by measuring the neutron distribution along a Lead spallation neutron source. The spallation neutron source was irradiated by 1, 1.5 and 2 GeV protons. The experimental results were taken using passive methods. A fitting procedure has been applied to the experimental data and the results have been compared with analytical calculation of the produced hadrons' spatial distribution based on High Energy Physics concepts. Using the beam attenuation coefficient the inelastic cross section of protons in Pb was estimated.

PACS: 25.40.Sc, 25.40.Ep, 29.25.Dz

1. Introduction

The spallation neutron sources are sub-critical neutron systems, driven by an accelerator (ADS). The accelerator bombards a target with high-energy particles mainly protons. Spallation reactions have been thoroughly investigated using energetic proton beams [1-4]. Spallation experiments have been performed also in Dubna using a large cylindrical Pb target surrounded by a paraffin moderator. In order to use slow neutrons for transmutation purposes the moderator has been used to shift the hard spallation neutron spectrum to lower neutron energies [5-7]. In order to perform transmutation experiments using a spallation neutron source, calculation and measurements of produced neutron spectra by the spallation source are necessary. For the calculation of the produced neutrons the inelastic cross section of the projectile particles with the target material is needed to be known. Lead is one of the most common materials used in spallation sources. Several measurements have been made to estimate the inelastic cross section of protons with energy from few hundreds MeVs up to few GeVs in Pb [4, 8-15]. In the current work a measurement of the inelastic cross sections of 1.0, 1.5 and

* Corresponding author. Postal address Aristotle University of Thessaloniki, School of Physics, Thessaloniki 54 124, Greece, Tel: +302310998176, Fax: +302310998176
E-mail address : zamani@physics.auth.gr

2.0 GeV protons in Pb targets was performed. Neutron and proton distributions along the spallation source were performed using Solid State Nuclear Track Detectors (SSNTDs) and activation methods. The inelastic cross sections were determined from neutron and proton spatial distributions along the target applying a fitting procedure based on High energy Physics concept.

2. Experimental

The inelastic cross section of protons in Pb was determined by irradiation of a thick spallation target. The experimental set-up, “Gamma-2”, consists of a cylindrical Pb target, with 40 cm length and 8 cm in diameter covered with a paraffin moderator 6 cm in thickness. The target irradiated by 1, 1.5 and 2 GeV proton beams, produce a fast neutron spectrum with a significant thermal-epithermal neutron component [5]. The experiments have been performed at the Nuclotron accelerator, at High Energy Laboratory, JINR Dubna, Russia. The neutron distribution was studied along the paraffin moderator by using Solid State Nuclear Track Detectors (SSNTDs). Fast neutrons were also measured by proton recoil tracks on the detector CR-39 itself (neutron elastic scattering on H of the detector). The neutron energy region detected by proton recoils is between 0.3-3 MeV due to limitations in the proton registration efficiency [16 - 17]. Neutron distribution along the target at the paraffin surface was determined also by using activation detectors. Natural Cd foils (mass ~ 2 g, purity 99.9%, thickness1mm) were also used as activation detector. The ^{nat}Cd effectively captures neutrons below 1 eV because of the high capture cross section of ^{113}Cd while it can be used for neutron detection above 1 eV via the ^{114}Cd(n,γ)^{115}Cd reaction. Moreover, ^{nat}Cd has a significant cross section to ^{nat}Cd(p,x)^{111}In reaction in the energy range of few MeV up to practically 400 MeV, responded well to the emitted proton spectrum [18-19].

3. Results and Discussion

Typical spatial distributions of fast neutrons and protons, as it was measured by SSNTDs and activation detectors at the same positions for proton beam energy of 1.0 GeV, is presented in figure 1. The neutron spatial distribution has the same behavior for all studied proton beam energies peaked at 10 cm upstream the target. Then a decrease is observed due to the beam attenuation. Protons generated by the target have energies high enough to pass through the moderator. Some of them are products of neutron

interactions in moderator. Their energies ranged between 10 to 100 MeV presented a peak around 50 MeV, as it was calculated by Monte Carlo code DCM-DEM [18].

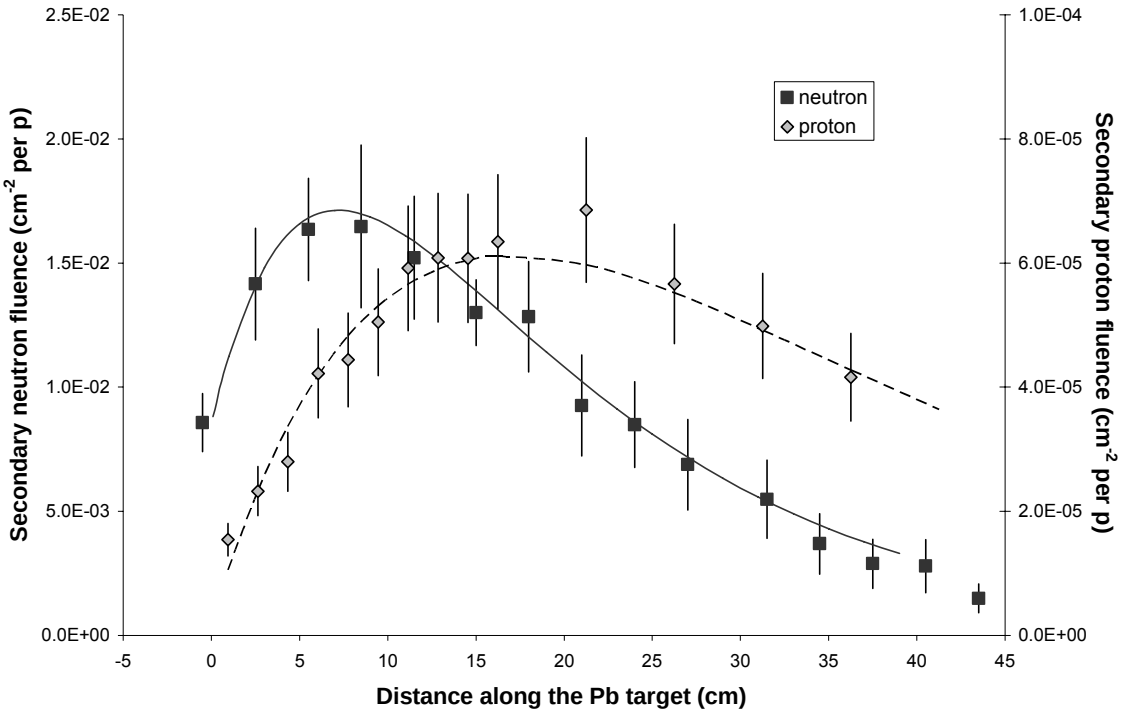

Fig.1. Spatial neutron and proton distributions along the target for incoming proton beam energy of 1 GeV. The lines referred to the fitting process using equation (1).

The hadron fluencies per incident proton (ρ, cm^{-2} per incoming proton) were fitted based on the consideration that two competitive effects take place inside the Pb target. An exponential increase of the secondary particle production at the head of the target, due to internuclear cascade (build up effect) and the exponential decrease of the proton beam intensity along the target (attenuation effect). The following equation was used [19]:

$$\rho = C\,(1-ae^{-bx})\,e^{-dx} \qquad (1)$$

where C is a parameter in units neutrons cm^{-2}.$proton^{-1}$. The first part of the equation was setting to describe the build up effect with the build up parameter a and the build up coefficient b. The second part represents the beam attenuation along the target as it was observed over the moderator surface with the attenuation coefficient d (cm^{-1}). The attenuation coefficient d is related to interaction length of primary protons in Pb. In fact secondary particle production continues along the target but the energy of the

particles is low reducing so further particle production. In a heavy target protons and neutrons of low energies can induce fission reactions which in case of a Pb target have very low cross section and can be neglected. So the fall along the target can be attributed basically to the beam attenuation. Such considerations are valid for target dimensions relatively large comparing to the range of protons hitting the heavy target, as in case of Pb target used for the present study. It have to be taken into account that the results of this work correspond to inelastic cross sections as they have taken from measurements at large angles relative to the beam and so the elastic component is not included.

Using the determined interaction length λ, the inelastic cross section of protons in Pb can be estimated by the relation between the interaction length and the inelastic cross section, $\sigma = A/N\lambda\rho$. A is the Pb atomic number, N is the Avogadro's number and ρ is the Pb target density ($gr.cm^{-3}$) [20]. The values of the inelastic cross sections are presented in Table 1, for beam energies applied to those experiments.

Table 1. Inelastic cross section estimations for various incoming proton beam energies.

Proton energy (GeV)	Fast neutron (SSNTDs)	Proton (Cd-activation)	Mean Value
1.0	2.09 ± 0.33	1.67 ± 0.21	1.79 ± 0.18
1.5	1.61 ± 0.18	1.61 ± 0.15	1.61 ± 0.12
2.0	1.70 ± 0.12	1.55 ± 0.18	1.65 ± 0.10

It is interesting to focus the attention on the point that inelastic cross sections can equally be determined by measuring the beam attenuation via neutrons or via protons at the paraffin surface. Independently of the particle-tracker used for the calculation of beam attenuation along the target the inelastic cross sections are in good agreement with the inelastic cross sections of protons in Pb at the same energy region, as it is presented in the literature [4, 8-15,19].

Conclusion

The use of protons in cross section experiments has the advantage of the possibility to have monoenergetic beams of well known energy and energy spread. Moreover it is in theory possible to determine the inelastic cross section accurately by absorbing out the low energy secondary. For relativistic proton at energy range between 1 to 2 GeV the inelastic-total cross section in Pb presented to be quite constant within the measurement uncertainty with value 1.68 ± 0.09 b. The method can be applied also

in other heavy targets under the restriction that target dimensions are small relative to the range of proton incident beam in the target.

Acknowledgment
The authors are grateful to Professor A.I. Malakhov and the staff of the Laboratory of High Energies, JINR Dubna, for their continuous support to our work. Special gratitude is due to Professor A.D. Kovalenko and the operation staff of the NUCLOTRON accelerator for providing high intensity beams during irradiations.

References

[1] L. Pienkowski et al., Phys. Rev. C 56 (1997) 1909.
[2] D. Hilscher et al., Nucl. Instrum. Meth. Phys. Res. A 414 (1998) 100.
[3] B. Lott et al., Nucl. Instrum. Meth. Phys. Res. A 414 (1998) 117.
[4] A. Letourneau et al., Nucl. Instrum. Meth. Phys. Res. B 170 (2000) 299.
[5] J. S. Wan et al., Nucl. Instum. Meth. Phys. Res. A 463 (2001) 634.
[6] J. Adam et al., Radiochim. Acta 90 (2002) 431.
[7] W. Westmeier, et al., Radiochim. Acta. 93(2005) 65
[8] G. P. Millburn, et al., Phys. Rev 95 (1954) 1268
[9] F.F. Chen, et al., Phys. Rev 99 (1955) 857
[10] R. Goloskie and K. strauch, Nuclear Physics A 92(1962) 474
[11] C.M. Herbach et al. Nucl. Instr. Method A 562 (2006) 729
[12] P.U. Renberg, et al., Nuclear Physics A 183(1972) 81
[13] F.S. Dietrich et al. J. Nucl. Sci. Techn. 2 (2002) 269
[14] K. Amos et al. Phys. Rev. C65 (2002) 064618
[15] A. Auce et al. Phys. Rev. C71 (2005) 064606
[16] M. Zamani and E. Savvidis, Rad. Prot. Dos. 63 (1996) 299
[17] J.R. Harvey et al., Radiat. Prot. Dos. 77 (1998) 267
[18] M. Manolopoulou, et al., Nucl. Instr. and Meth. Phys. Res. A 586 (2008) 239
[19] G. S. Bauer, Nucl. Instrum. Meth. Phys. Res. A 463 (2001) 505.
[20]. A.H.Sullivan, A Guide to Radiation and Radioactivity Levels near High Energy Particle Accelerators, Nuclear Technology Publishing, England, (1992).

Nuclear muon capture rates by using relativistic muon wavefunctions.

I.S. Kardaras [a],V.N. Stavrou [b],I.G. Tsoulos [c] and T.S. Kosmas [a]

[a] *Theoretical Physics Section, University of Ioannina, GR 45110 Ioannina, Greece*

[b] *Theoretical Physics Section, University of Ioannina, GR 45110 Ioannina, Greece, Division of Academic Studies, Hellenic Navy NCO School, GR 12400*

[c] *Department of Computer Science, University of Ioannina, GR 45110 Ioannina, Greece*

1 Introduction.

The numerical solutions of ordinary and partial differential equations (ODEs and PDEs) among others are of special importance for quantum mechanics problems. The wavefunctions of elementary particles in nuclei and the binding energies are calculated by the Schrödinger and Dirac equations. The last two decades or so, a large number of numerical algorithms have been employed to solve the eigen value problem. Such numerical methods the Artificial Neural Networks (ANN), genetic algorithms, direct diagonalization, and the finite elements method (FEM) among others. ANN and FEM were presented as the most reliable algorithms (e.g. MERLIN) to solve non-homogeneous ODEs and PDEs [1,3,2].

We apply the genetic algorithm in order to solve the Dirac equation of muonic atoms. For the case of ^{208}Pb the muon binding energy $E_b \sim -10.54MeV$ and the muon wavefunction using the ANN method [1] are in good agreement with our calculations obtained by a genetic algorithm. The calculation of the wavefunctions can be used to estimate the total muonic capture rates. For these purpose, we make use of the Fermi's golden rule and the semi-empirical Primakoff's method [4] and highlight the limitation of the method.

2 Dirac equation

In this paragraph, we solve the Dirac equation for muonic atoms. In our investigation we consinder both the large and small component [5,6]. The Dirac

Equation in a central force system is described by the following equation

$$E\psi = [-i\gamma_5\sigma_r(\frac{\partial}{\partial r} + \frac{1}{r} - \frac{\beta}{dr}K) + V(r) + m_i\beta]\psi \tag{1}$$

where γ_i are the well known Dirac matrices and

$$\sigma_r = \begin{pmatrix} \sigma \cdot r & 0 \\ 0 & \sigma \cdot r \end{pmatrix} \; ; \; K = \begin{pmatrix} \sigma \cdot l + 1 & 0 \\ 0 & \sigma \cdot l + 1 \end{pmatrix} \tag{2}$$

where μ_i is the reduced mass, s are the Pauli matrices, l is the orbital angular momentum. For the case $l = 0$ (s-$state$), the two components of Dirac's equation could be given by

$$\frac{d}{dr}f(r) + \frac{1}{r}f(r) = \frac{1}{\hbar}(\mu c^2 - E + V(r))g(r) \tag{3}$$

$$\frac{d}{dr}g(r) - \frac{1}{r}g(r) = \frac{1}{\hbar}(\mu c^2 + E - V(r))f(r) \tag{4}$$

where $f(r)$ and $g(r)$ are the small and large components of the reduced radial wavefunction of the muon bound respectively. The total energy is calculated by

$$E = \frac{\mu c^2 \int_0^\infty [g^2(r) + f^2(r)]dr + \int_0^\infty V(r)[g^2(r) - f^2(r)]dr}{\int_0^\infty [g^2(r) - f^2(r)]dr} \tag{5}$$

and the extended nuclear Coulomb field, for example the one originating from the point-nucleon charge distribution $\rho(r)$ is given by

$$V(\mathbf{r}) = -\mathbf{e^2} \int_{-\infty}^{\infty} \frac{\rho(\mathbf{r'})}{|\mathbf{r} - \mathbf{r'}|}\mathbf{d^3r'} \tag{6}$$

The nuclear charge density $\rho(r)$ can be estimated using the following models [7]:
1) Two parameter Fermi model

$$\rho(r) = \frac{\rho(r_0)}{1 + e^{\frac{r-c}{z}}} \tag{7}$$

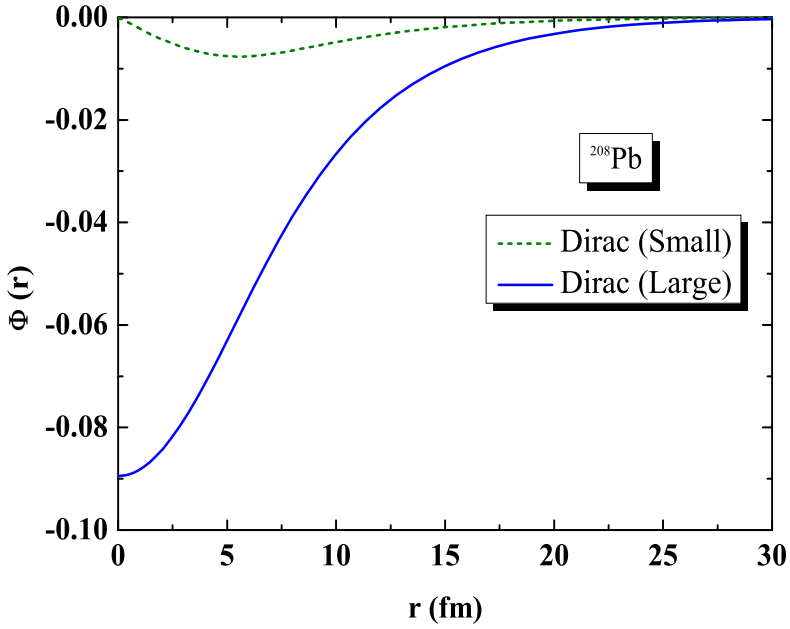

Fig. 1. The large, small component of Dirac spinor solution for muon bound in ^{208}Pb.

where c, z are the radius and thickness parameter respectively.
2) Fourier-Bessel model

$$\rho(r) = \begin{cases} \sum_n \alpha_n j_0(n\pi r/R) & \text{for } r \leq R \\ 0 & \text{for } r \geq R \end{cases} \tag{8}$$

where $j_0(qr)$ denotes the Bessel function of order zero.
3) Sum of Gaussians

$$\rho(r) = \sum_n A_n (e^{-[(r-R_n)/\gamma]^2} + e^{-[(r+R_n)/\gamma]^2}) \tag{9}$$

where the coefficients are defined in Ref. [7].

We use the following parametrized solutions for the small and large component of Dirac equation

$$f(r) = re^{-\beta r} N(r, \mathbf{u_f}, \mathbf{v_f}, \mathbf{w_f}) \tag{10}$$

$$g(r) = re^{-\beta r} N(r, \mathbf{u_g}, \mathbf{v_g}, \mathbf{w_g}) \tag{11}$$

with $\beta > 0$ and the parameters $\mathbf{u_g}$, $\mathbf{v_g}$, $\mathbf{w_g}$ being ANN parameters. $N(r, \mathbf{u_g}, \mathbf{v_g}, \mathbf{w_g})$ is feed-forward artificial neural network

The following error function has to be minimized for estimating the binding energy

$$\frac{\sum_{i=1}^{n}[\frac{df(r_i)}{dr} + \frac{f(r_i)}{r_i} - \frac{\mu c^2 - E + V(r_i)}{\hbar c} g(r_i)]^2 + [\frac{dg(r_i)}{dr} - \frac{g(r_i)}{r_i} - \frac{\mu c^2 + E - V(r_i)}{\hbar c} f(r_i)]^2}{\int_0^\infty [g^2(r) + f^2(r)] dr} \quad (12)$$

The minimization has been achived using a genetic algorithm. Genetic algorithms are biologically inspired global optimization methods that are based on the so called genetic operations of natural selection, reproduction and mutation. These techniques have been used with success in many scientific fields such as combinatorial problems [8], neural network training [9,10], electromagnetics [11], design of water distribution networks [12] etc. The main advantages of genetic algorithms are: a) they can be implement easily, b) they can be parallelized and c) they do not require the computation of derivatives of any order. The main steps of the used genetic algorithm are shortly described as follows:

- Step 1 (**initialization**):
  - Generate N uniformly distributed random points (chromosomes) and store them to the set S.
  - Set iter=0
- Step 2 (**evaluation**): Evaluate the function value of each chromosome.
- Step 3 (**termination check**): If termination criteria are hold terminate. The termination criteria of the used algorithm are based on asymptotic considerations. At every generation denoted by iter, the variance $\sigma^{(\text{iter})}$ of the best located value is recorded. If there is not any improvement for a number of generations, it is highly possible that the global minimum is already found and hence the algorithm should terminate.
- Step 4 (**genetic operations**):
  - **Selection**: Select $m \leq N$ parents from S. The selection is performed using the tournament selection technique.
  - **Crossover**: Create m new points (offsprings) from the previously selected parents.
  - **Mutation**: Mutate the offsprings produced in the crossover step with probability p_m.
- Step 5 (**replacement**): Replace the m worst chromosomes in the population with the previously generated offsprings.
- Step 6 (**local technique**): Create using the local technique procedure a trial point $\tilde{x}$. If $f(\tilde{x}) \leq f(x_h)$ where x_h is the current worst point in S, then replace x_h by $\tilde{x}$.
- Step 7:

- A local search procedure is applied to the best located chromosome x_l every $K_{\rm ls}$ generations, where $K_{\rm ls}$ is a user defined constant that denotes how frequent the local search procedure has to be applied.
- **Set** iter=iter+1
- **goto** step 2

In this article the modified genetic algorithm was used with a population of 200 chromosomes. The maximum number of generations allowed was set to 20 and the mutation rate was set to 5%. The binding energy ϵ_b could be given by $\epsilon_b = E - \mu c^2$.

3 Results for muon capture

The capture of a muon bound in the field of a nucleus (A, Z) can be represented by the following nuclear process

$$\mu^- + (A, Z) \rightarrow (A, Z-1) + \nu_\mu \tag{13}$$

The total muon capture rates could be estimated by the following relation [4]

$$\lambda_{\mu c} = G^2 \frac{\nu}{2\pi\hbar^2 c} \left(\frac{m_{\mu_\mu} c^2 \alpha}{\hbar c} \right)^3 \frac{Z_{eff}^4}{Z} \left[Z - F_\sigma(A, Z) \right] \tag{14}$$

where α is the fine structure constant, $F_\sigma(A, Z)$ is the correlation function and the effective atomic number Z_{eff} is given by

$$\left\langle \Phi_\mu^{1s} \right\rangle^2 = \frac{\int |\Phi_\mu|^2 \rho(\mathbf{r}) d^3\mathbf{r}}{\int \rho(\mathbf{r}) d^3\mathbf{r}} = \frac{\alpha^2 m_\mu^3}{\pi} \frac{Z_{eff}^4}{Z} \tag{15}$$

where Φ_μ^{1s} is the muon wavefunction for the 1s state (see Fig. 1.) It is worth mentioning that the effective atomic number is less than the atomic number Z because a large part of the muon wavefunction is inside the nucleus.

The correlation function $F_\sigma(A, Z)$ can be estimated by microscopic methods and Primakoff's semi-empirical method. The Primakoff's semi-empirical method is an approximation which works for light nuclei as is presented in table 1. For heavy nuclei, $F_\sigma(A, Z)$ gets four times larger value than the microscopic method.

Table 1
The correlation function for light and heavy nuclei for two different models.

$Nuclei$	$Microscopic\ method$	$Primakoff\ method$
(A, Z)	$F_\sigma(A, Z)$	$F_\sigma(A, Z)$
(4, 2)	-1.72	-1.68
(208, 82)	-17.80	-78.18

4 Summary and Conclusions

In summary, in the present work we have used a genetic algorithm in order to calculate the muon wavefunction and the corresponding binding energy of the μ^- in a ^{208}Pb muonic atom. More specifically, we have solved the Dirac's equation and concluded that the estimated binding energy and the bound muon wavefunctions (small and large component for the $1s$ state) are in very good agreement with those obtained by solving this equation by utilizing artificial neural network (ANN) techqniques [1]. Lastly, we have discussed and point out the frame of the muonic capture process by using the semi-empirical Primakoff's method.

5 ACKNOWLEDGMENTS

The authors would like to thank Prof I.E. Lagaris for valuable discussions.

References

[1] T.S. Kosmas and I.E. Lagaris, J. Phys. G 28 (2002) 2907.

[2] I.E. Lagaris, A. Likas and D.I. Fotiadis, Comput. Phys. Commun. **104** (1997) 1-14.

[3] I.E. Lagaris, A. Likas and D.I. Fotiadis, Comput. Phys. Commun. **103** (1997) 112.

[4] H. Primakoff, Rev. Mod.Phys. **31** 802 (1959).

[5] N.T. Zinner, K. Langanke and P. Vogel, Phys. Rev. C **74** 024326 (2006).

[6] R. Kitano, M. Koike and Y. Okada Phys. Rev. D **66** 096002 (2002).

[7] H. de Vries, C.W. de Jager and C. de Vries, At. Data and Nucl. Data Tables **36**, (1987) 495.

[8] J.J. Grefenstette, R. Gopal, B. J. Rosmaita, D. Van Gucht, Genetic Algorithms for the Traveling Salesman Problem, In: Proceedings of the 1st International Conference on Genetic Algorithms, pp. 160 - 168, Lawrence Erlbaum Associates, 1985.

[9] G. F. Miller, P. M. Todd, S. U. Hegde, Designing neural networks using genetic algorithms, In: Proceedings of the third international conference on Genetic algorithms, George Mason University, United States, pp. 379 - 384, Morgan Kaufmann, 1989.

[10] D. Whitley, T. Starkweather, C. Bogart, Genetic algorithms and neural networks: Optimizing connections and connectivity, Parallel Computing **14**, pp. 347-361, 1990.

[11] R.L. Haupt, An introduction to genetic algorithms for electromagnetics, Antennas and Propagation Magazine **37**, pp. 7-15, 1995.

[12] D. A. Savic, G. A. Walters, Genetic Algorithms for Least-Cost Design of Water Distribution Networks, Journal of Water Resources Planning and Management **123**, pp. 67-77, 1997.

[13] I.G. Tsoulos, Modifications of real code genetic algorithm for global optimization, Applied Mathematics and Computation 203, pp. 598-607, 2008.

Non-Linear Derivative Interactions in Relativistic Hadrodynamics

T. Gaitanos, M. Kaskulov

Institut für Theoretische Physik, Universität Giessen, Heinrich-Buff-Ring 16, 35392 Giessen, Germany

Abstract

The Lagrangian of Relativistic Hadrodynamics (RHD) is extended by introducing non-linear derivative (NLD) operators into the interactions between the nucleon with the meson fields. As the novel feature of the NLD model, the nucleon selfenergy depends on both, on energy and density. Our approach contains a single cut-o parameter, which determines the density dependence of the nuclear equation of state (EoS) and the energy dependence of the nucleon-nucleus optical potential. The NLD formalism is compatible with results from microscopic nuclear matter calculations as well as with Dirac phenomenology.

Keywords: relativistic hadrodynamics, non-linear derivative model, nuclear matter, Schrödinger equivalent optical potential
PACS: 21.65.-f, 21.65.Mn, 25.40.Cm

1. Introduction

Relativistic mean-field (RMF) models have been widely established as a successful tool for the theoretical description of di erent nuclear systems such as nuclear matter, finite nuclei and heavy-ion collisions [1]. The major advantage of RMF models has been a correct description of the saturation mechanism and simultaneously an explanation of the strong spin-orbit force. An energy dependence of the Schrödinger equivalent optical potential is naturally included in RMF as a consequence of a relativistic description, but it is not consistent with Dirac phenomenology [2].

We have developed a manifestly covariant model, which generates both, the correct density and, in particular, momentum dependence of the selfenergies in an unified framework. The proposed model is simple in realization and respects all the underlying symmetries of the RHD Lagrangian. The main idea was to extend the original Lagrangian of RHD [3] by including *non-linear* derivative interactions of meson fields with nucleons. In contrast to conventional RHD, the NLD Lagrangian contains all higher order derivatives of the Dirac field. Therefore the standard canonical formalism had to be generalized [4]. Although the complex structure of the canonical equations (Euler-Lagrange equations of motion, Noether-Theorem), the NLD model gives field equations with very simple structure in nuclear matter. As an important result, both the equation of state (EoS) (density dependence) and the optical potential (energy dependence) are quantitatively well reproduced with a single parameter. Furthermore, the results are comparable with microscopic Dirac-Brueckner-Hartree-Fock (DBHF) models.

2. NLD Formalism

The basis of the NLD formalism [4] builds the Lagrangian density of RHD [3]. It describes the interaction of nucleons through the exchange of virtual meson fields (Lorentz-scalar, σ, and Lorentz-vector meson fields ω^μ)

$$\mathcal{L} = \mathcal{L}_{Dirac} + \mathcal{L}_{mes} + \mathcal{L}_{int} \ . \tag{1}$$

The Lagrangian in Eq. (1) consists of the free Lagrangians for the nucleon field Ψ and for the meson fields σ and ω^μ. In standard RHD the interaction Lagrangian $\mathcal{L}_{int}$ contains meson fields which couple to the Dirac spinors via the Lorentz-density operators $\overline{\Psi}\Psi\sigma$ and $\overline{\Psi}\gamma^\mu\Psi\omega_\mu$ with given coupling constants g_σ and g_ω, respectively. Such interactions give rather successful saturation properties of nuclear matter, but they don't describe the energy dependence of the mean-field correctly. For this reason we have generalized the standard RHD by introducing non-linear derivative operators into the interaction Lagrangian density

$$\mathcal{L}_{int} = \frac{g_\sigma}{2}\left[\overline{\Psi}\ \overleftarrow{\mathcal{D}}\ \Psi\sigma + \sigma\overline{\Psi}\ \overrightarrow{\mathcal{D}}\ \Psi\right] - \frac{g_\omega}{2}\left[\overline{\Psi}\ \overleftarrow{\mathcal{D}}\ \gamma^\mu\Psi\omega_\mu + \omega_\mu\overline{\Psi}\gamma^\mu\ \overrightarrow{\mathcal{D}}\ \Psi\right] \ . \tag{2}$$

The interaction between the spinor fields $\overline{\Psi}$, Ψ and the meson fields has a similar functional form as in standard RHD [3]. However, now new operators $\mathcal{D}$ acting on the nucleon fields appear

$$\overrightarrow{\mathcal{D}} := \exp\left(\frac{-v^\beta i\ \overrightarrow{\partial}_\beta + m}{\Lambda}\right) \ , \quad \overleftarrow{\mathcal{D}} := \exp\left(\frac{i\ \overleftarrow{\partial}_\beta\ v^\beta + m}{\Lambda}\right) \ . \tag{3}$$

In Eq. (3) v^μ is a dimensionless auxiliary 4-vector. Λ is a cut-o parameter which has been adjusted to the saturation properties of nuclear matter, and m is the nucleon mass. In the limiting case of $\Lambda \to \infty$ the standard RMF or Walecka model is retained.

The NLD Lagrangian $\mathcal{L}$ is a functional of not only Ψ, $\overline{\Psi}$ and their first derivatives, but it depends on all higher order covariant derivatives of the spinor fields Ψ and $\overline{\Psi}$. For such a generalized functional the Euler-Lagrange equations take the form [4]

$$\frac{\partial\mathcal{L}}{\partial\varphi} - \partial_\alpha\frac{\partial\mathcal{L}}{\partial(\partial_\alpha\varphi)} + \partial_\alpha\partial_\beta\frac{\partial\mathcal{L}}{\partial(\partial_\alpha\partial_\beta\varphi)} + \cdots + (-)^n\partial_{\alpha_1}\partial_{\alpha_2}\cdots\partial_{\alpha_n}\frac{\partial\mathcal{L}}{\partial(\partial_{\alpha_1}\partial_{\alpha_2}\cdots\partial_{\alpha_n}\varphi)} = 0 \ , \tag{4}$$

where φ stands for the NLD degrees of freedom (Dirac Spinor Ψ and meson fields σ and ω).

Contrary to the standard expressions for the Euler-Lagrange equation, now infinite series of terms proportional to higher order derivatives of the Dirac field appear. They can be evaluated by a Taylor expansion of the non-linear derivative operators (3). As shown in [4], all infinite series can be resumed and all the equations simplify considerably. Applying the usual RMF approximation to infinite nuclear matter, the standard Dirac equation is obtained

$$\left[\gamma_\mu(i\partial^\mu - \Sigma^\mu) - (m - \Sigma_s)\right]\Psi = 0 \ , \tag{5}$$

with selfenergies given by

$$\Sigma_v = g_\omega \omega_0 e^{-\frac{E-m}{\Lambda}} \ , \ \Sigma_s = g_\sigma \sigma e^{-\frac{E-m}{\Lambda}} \ . \tag{6}$$

The relation between the particle momentum p and the particle energy E is obtained from the in-medium mass-shell condition

$$E(p) = \sqrt{p^2 + m^{*2}} + \Sigma_v \tag{7}$$

with the in-medium (or e ective) Dirac mass given by $m^* = m - \Sigma_s$. Note, that the selfenergies and thus the e ective mass m^* explicitly depend on particle momentum. For the limiting case when $\Lambda \to \infty$, the exponential factors are equal to unity and the equations are reduced to the ones from the Walecka model. The NLD selfenergies contain a non-linear energy dependence, as also expected from Dirac Phenomenology [2]. In nuclear matter the NLD equations of motion for ω and σ simplify to standard meson field equations

$$m_\omega^2 \omega^0 = g_\omega \rho_0 \ , \ m_\sigma^2 \sigma = g_\sigma \rho_s \ . \tag{8}$$

with the corresponding density sources $\rho_s = \langle \overline{\Psi} e^{-\frac{E-m}{\Lambda}} \Psi \rangle$ and $\rho_0 = \langle \overline{\Psi} \gamma^0 e^{-\frac{E-m}{\Lambda}} \Psi \rangle$. Note, that the density ρ_0 is not related to the conserved nucleon density ρ_B. It has to be derived from a generalized Noether-theorem [4] and reads

$$J^0 \equiv \rho_B = \langle \overline{\Psi} \gamma^0 \Psi \rangle + \frac{g_\omega}{\Lambda} \langle \overline{\Psi} \gamma^0 e^{-\frac{E-m}{\Lambda}} \Psi \rangle \omega_0 - \frac{g_\sigma}{\Lambda} \langle \overline{\Psi} e^{-\frac{E-m}{\Lambda}} \Psi \rangle \sigma \quad . \tag{9}$$

The NLD model contains no free parameters except Λ, since in the limiting cases the conventional Walecka model is retained. The original meson-nucleon couplings can be taken from any linear Walecka model, e.g., [3], as it has been done here. The cut-o parameter Λ is of natural size, i.e., of typical hadronic mass scale in this problem. In the following, $\Lambda = 0.770$ GeV is chosen [4].

3. Results and Discussion

We have applied both the NLD approach and the linear Walecka model to infinite nuclear matter at various baryon densities and nucleon energies relative to nuclear matter at rest.

According Eqs. (6) the cut-o parameter Λ generates a highly non-linear density dependence for nuclear matter at rest, which arises from the exponential terms. This non-linear density dependence a ects considerably the equation of state (EoS), i.e., the binding energy per nucleon as function of nucleon density. This is demonstrated in Fig. 1 for nuclear matter and also pure neutron matter (for neutron matter the isovector ρ-meson was included). First of all, the conventional linear Walecka model (dashed curve) leads to an EoS with high sti ness. This results to a very high value for the compression modulus. The NLD model weakens the sti ness of the EoS for nuclear and pure neutron matter to a large extent. The agreement of the NLD-EoS with the underlying DB theory is successful indicating that saturation nuclear matter properties, e.g., binding energy per nucleon

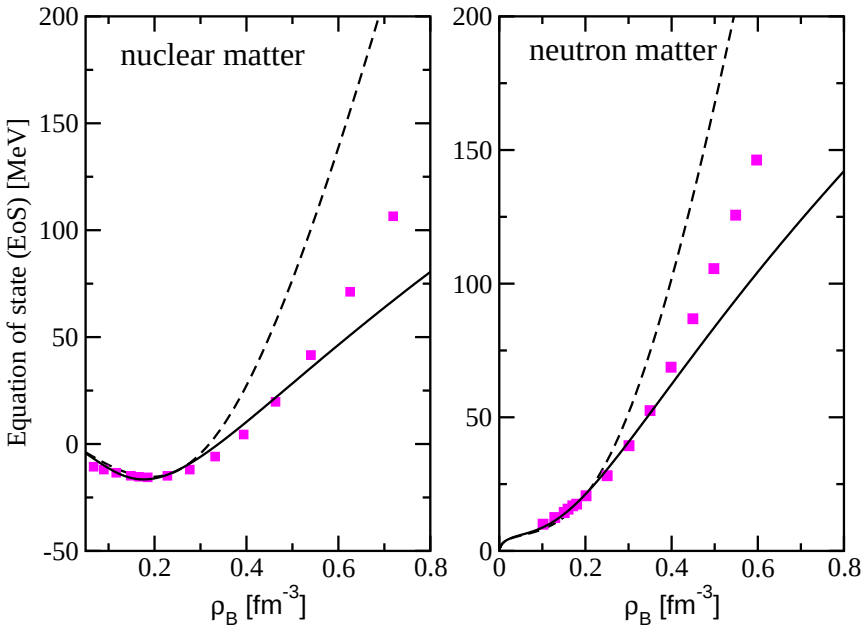

Figure 1: Equation of state for nuclear (left panel) and pure neutron matter (right panel). Dashed: linear Walecka model, solid: NLD model, lled squares: DBHF model [5].

and compression modulus at saturation density, are fairly well reproduced by the NLD approach. Similar e ects are observed for the density dependence of the e ective mass (not shown here). At saturation density a value of $m^* \approx 0.65m$ is obtained, which is again very close to DBHF predictions. Therefore, it turns out that conventional RMF models without any explicit introduction of selfinteractions of the meson fields are able to describe nuclear matter properties, if non-linear derivatives are accounted for in the underlying meson-nucleon interaction Lagrangian.

A novel feature of the NLD model is the prediction of an energy (or momentum) dependence of the nuclear mean-field with only one parameter. Dirac Phenomenology on elastic proton-nucleus scattering predicts a non-linear energy dependence of the Schrödinger equivalent optical potential, which cannot be reproduced in standard linear Walecka models nor in their extensions to non-linear meson field terms. The question arises if the NLD model can reproduce this feature with the same parameter Λ as used for the density dependence.

For this purpose, we consider the situation of a nucleon with particular momentum p (or kinetic energy E_{kin}) relative to nuclear matter at rest. The kinetic energy for an incident free nucleon with mass m and momentum p is usually defined as $E_{kin} = \sqrt{p^2 + m^2} - m$. In the nuclear medium one has to determine the kinetic energy relative to the potential deep [5]

$$E_{kin} = E - m = \sqrt{p^2 + m^{*2}} + \Sigma_v - m \quad . \tag{10}$$

The energy dependence of the nuclear mean-field is empirically determined by Dirac phenomenology in elastic nucleon-nucleus scattering [2]. The key quantity in empirical studies is the Schrödinger equivalent optical potential U_{opt}, which serves as a convenient

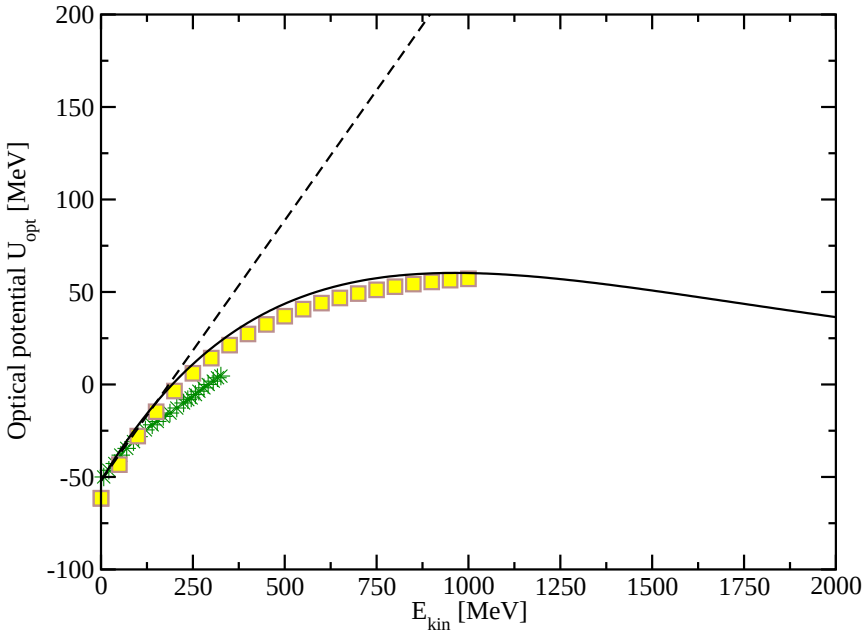

Figure 2: Energy dependence of the Schrodinger equivalent proton-nucleus optical potential at saturation density $\rho_{sat} = 0.16\ fm^{-3}$. Theoretical calculations in the linear Walecka model (dashed) and NLD approach (solid) are compared to Dirac phenomenology (lled squares) [2].

means to describe the in-medium interaction of a nucleon with momentum p relative to nuclear matter at rest. It is obtained by a non-relativistic reduction of the Dirac equation and reads

$$U_{\rm opt} = \frac{E}{m}\Sigma_v - \Sigma_s + \frac{1}{2m}\left(\Sigma_s^2 - \Sigma_v^2\right) \ . \tag{11}$$

It is fully determined by the Lorentz-scalar and Lorentz-vector components of the nucleon selfenergy. The optical potential rises linearly with energy, if the selfenergies do not depend explicitely on momentum. This is the case of the linear Walecka model, as can be seen in Fig. 2 (dashed curve). The DBHF model (filled stars), on the other hand, reproduces the empirical behavior of the optical potential only at low energies, since the parameters of the underlying free NN-interaction are fitted to low energy scattering data [5]. The NLD model (solid curve) with its non-linear energy dependence weakens strongly the linear sti ness of the original Walecka model, and the empirical energy dependence of the optical potential can be reproduced fairly well without the introduction of any further parameters.

4. Summary and Outlook

In summary, we presented the NLD formalism, which constitutes a generalization of standard RHD by imposing on a mean-field level highly non-linear e ects in baryon density and simultaneously in single-particle energy. In contrast to conventional RMF models, the NLD approach contains a single cut-o parameter of natural hadronic scale, which drives the density *and simultaneously* the energy dependence of the mean-field.

We applied the NLD approach to nuclear matter and nucleon scattering with nuclear matter at rest. Astonishing were the non-linear density dependence of the vector field without the introduction of any additional self-interaction terms in the original Lagrangian of the linear Walecka model. These non-linear effects lead to a softening of the equation of state for nuclear and pure neutron matter at high densities. It was possible to describe quantitatively well the empirically known saturation properties. The results were also comparable to predictions of microscopic DBHF calculations over a wide density range. The NLD approach lead furthermore to a momentum dependence of the selfenergies. As a novel feature of NLD, the energy dependence of the Schrödinger equivalent optical potential was reproduced fairly well by utilizing the same parameter.

The application of the NLD formalism to heavy-ion collisions in the spirit of a covariant transport theory based on the present Lagrangian would be a great challenge for the future in studying hadronic matter under extreme conditions with the ultimative goal of exploring the equation of state at supra-normal densities, as they are planned at the new FAIR facility at GSI.

Acknowledgements

Supported by the Deutsche Forschungsgemeinschaft and SFB/TR 16, Subnuclear Structure of Matter

References

[1] B. Serot and J.D. Walecka, Int. J. Mod. Phys. **E6** (1997) 631.

[2] E.D. Cooper, et al., Phys. Rev. **C47** (1993) 297.

[3] H.P. Duerr, Phys. Rev. **103** (1956) 469;
J.D. Walecka, Ann. Phys. (N.Y.) **83** (1974) 497

[4] T. Gaitanos, M. Kaskulov, U. Mosel, Nucl. Phys. **A828** (2009) 9

[5] B. ter Haar and R. Malfliet, Phys. Rev. **C36** (1987) 1611;
B. ter Haar and R. Malfliet, Phys. Rep. **149** (1987) 207.

SUSYQM in nuclear structure: Bohr Hamiltonian with mass depending on the deformation

Dennis Bonatsos [a], P. E. Georgoudis [a], D. Lenis [a], N. Minkov [b], C. Quesne [c]

[a] *Institute of Nuclear Physics, N.C.S.R. "Demokritos", GR-15310 Aghia Paraskevi, Attiki, Greece*

[b] *Institute of Nuclear Research and Nuclear Energy, Bulgarian Academy of Sciences, 72 Tzarigrad Road, 1784 Sofia, Bulgaria*

[c] *Physique Nucléaire Théorique et Physique Mathématique, Université Libre de Bruxelles, Campus de la Plaine CP229, Boulevard du Triomphe, B-1050 Brussels, Belgium*

Abstract

A well known problem of the Bohr Hamiltonian for the description of nuclear collective motion is that the nuclear moment of inertia increases with deformation too fast. We show that this can be avoided by allowing the nuclear mass to depend on the deformation. The resulting Hamiltonian is solved exactly, using techniques of Supersymmetric Quantum Mechanics.

1 Introduction

Deformation is not only a structural feature defined by the orientation of an organized nuclear system as a whole. It is also a reflection of mass differences between neighboring, almost spherical droplets of nuclear matter.

The liquid drop is pictured in the Bohr Hamiltonian [1,2]. An antithesis of this picture views the orientation of the nuclear system that causes its rotational spectra and the behavior of its moments of inertia. They are predicted to increase proportionally to β^2 [3], where β is the collective variable corresponding to the axial deformation, while experimentally a much more moderate increase is observed.

What follows is the presentation of an effort to confront this antithesis. Motivation is based mainly in the classical limit of Interacting Boson Model (IBM) [4,5], where the momentum gets dressed with terms of deformation and thus, reveals the entrance of deformed algebras. It is also based on the argumentation developed

in [6], for the experiment-based path to a non-constant mass coefficient in the Bohr Hamiltonian. The resulting method is dictated by the "Quesne and Tkachuk equivalence" [7], which manifests that under certain circumstances, deformed canonical commutation relations are equivalent to a position dependent mass and also to a curved space.

2 The Quesne and Tkachuk equivalence and Position Dependent Mass Bohr Hamiltonian

A mathematicaly self-consistent way to obtain deformed operators is that of the deformed algebras, where the usual canonical quantization is modified by the presence of a so called deformation function. Quesne and Tkachuk [7] showed that if this deformation is a function of the position, that is

$$[\mathbf{x}, \mathbf{p}] = i\hbar f(\mathbf{x}), \tag{1}$$

then the following equivalence holds (the Quesne and Tkachuk equivalence)

$$f^2(\mathbf{x}) = \frac{1}{M(\mathbf{x})} = \frac{1}{g(\mathbf{x})}, \tag{2}$$

where $1/M(\mathbf{x})$ is an inverted position dependent mass and $1/g(\mathbf{x})$ is an inverted diagonalized metric. The consequence of the first part of this equivalence is that a deformed momentum operator of the type $\sqrt{f(\mathbf{x})}\mathbf{p}\sqrt{f(\mathbf{x})}$, is equivalent with the consideration of an effective mass $M(\mathbf{x}) = \frac{1}{(f(\mathbf{x}))^2}$. Following [7] the resulting Hamiltonian is of the form

$$H = -\frac{\hbar^2}{2m_0}\sqrt{f(\mathbf{x})}\nabla f(\mathbf{x})\nabla\sqrt{f(\mathbf{x})} + V_{eff}(\mathbf{x}), \tag{3}$$

with

$$V_{eff}(\mathbf{x}) = V(\mathbf{x}) + \frac{\hbar^2}{2m_0}\left[\frac{1}{2}(1-\delta-\lambda)f(\mathbf{x})\nabla^2 f(\mathbf{x}) + \left(\frac{1}{2}-\delta\right)\left(\frac{1}{2}-\lambda\right)(\nabla f(\mathbf{x}))^2\right]. \tag{4}$$

The parameters δ,λ (von Roos parameters) manifest the mass dependence of the position and are analyzed in [7]. The application of the Position Dependent Mass (PDM) framework in the case of the Bohr Hamiltonian is presented in [8], for a mass dependent on the β variable. First, a mass dependence of the form

$$B(\beta) = \frac{B_0}{(f(\beta))^2}, \tag{5}$$

where B_0 is a constant, is assumed. As the dependence is a scalar one, it permits us to follow the usual Pauli–Podolsky prescription. The PDM Bohr Hamiltonian is

$$\left[-\frac{1}{2}\frac{\sqrt{f}}{\beta^4}\frac{\partial}{\partial\beta}\beta^4 f\frac{\partial}{\partial\beta}\sqrt{f} - \frac{f^2}{2\beta^2\sin 3\gamma}\frac{\partial}{\partial\gamma}\sin 3\gamma\frac{\partial}{\partial\gamma} + \frac{f^2}{8\beta^2}\sum_{k=1,2,3}\frac{Q_k^2}{\sin^2\left(\gamma-\frac{2}{3}\pi k\right)} + v_{eff}\right]\Psi = \epsilon\Psi, \quad (6)$$

where reduced energies $\epsilon = B_0E/\hbar^2$ and reduced potentials $v = B_0V/\hbar^2$ have been used, and

$$v_{eff} = v(\beta,\gamma) + \frac{1}{4}(1-\delta-\lambda)f\nabla^2 f + \frac{1}{2}\left(\frac{1}{2}-\delta\right)\left(\frac{1}{2}-\lambda\right)(\nabla f)^2. \quad (7)$$

3 The deformed radial equation for the γ-unstable Davidson potential

The solution of the above Bohr-like equation can be reached for certain classes of potentials using techniques developed in the context of supersymmetric quantum mechanics (SUSYQM) [9, 10]. In order to achieve separation of variables, we assumed that the potential $v(\beta,\gamma)$ depends only on the variable β, i.e. $v(\beta,\gamma) = u(\beta)$ [11]. Such a choice is appropriate for the γ-unstable case. For the radial potential we used the Davidson potential [12]

$$u(\beta) = \beta^2 + \frac{\beta_0^4}{\beta^2}, \quad (8)$$

which belongs to such a class. The radial equation takes its deformed version

$$HR = -\frac{1}{2}\left(\sqrt{f}\frac{d}{d\beta}\sqrt{f}\right)^2 R + u_{eff}R = \epsilon R, \quad (9)$$

with

$$u_{eff} = v_{eff} + \frac{f^2+\beta f f'}{\beta^2} + \frac{f^2}{2\beta^2}\Lambda, \quad (10)$$

where $\Lambda = \tau(\tau+3)$, with τ being the seniority quantum number.

4 SUSY QM, Shape Invariance and the deformation function

Following the general method used in SUSYQM [9], one should first factorize the Hamiltonian in terms of generalized ladder operators. In order to obtain exact solutions, someone extents this factorization to a whole hierarchy of Hamiltonians

with an integrability condition, the shape invariance. Shape invariance states that all the members of the hierarchy must retain the same functional dependence of the potential.

The deformation function is unknown. Its definition in Eq. (10) must respect the shape invariance condition, *i.e.*, bring the Davidson behavior to the u_{eff}. The choice

$$f(\beta) = 1 + a\beta^2, \tag{11}$$

gives the Davidson behavior to the effective potential,

$$u_{eff} = \beta^2 + a^2\beta^2 \left[\frac{5}{2}(1-\delta-\lambda) + 2\left(\frac{1}{2}-\delta\right)\left(\frac{1}{2}-\lambda\right) + 3 + \frac{\Lambda}{2}\right] + \frac{1}{\beta^2}\left(1 + \frac{1}{2}\Lambda + \beta_0^4\right) + a\left[\frac{5}{2}(1-\delta-\lambda) + 4 + \Lambda\right]. \tag{12}$$

The parameter a is called the deformation parameter. The mass is position dependent for non-zero values of a. Therefore the values of β_0 and a show first the magnitude of the deformation, and second the position dependence of the mass. For tiny changes of β_0, the parameter a varies in the Davidson behavior and this variation reflects the position dependence of the mass during the transition, as well as the deformation as an effect of mass differences. In Sec. 5 this situation is clarified. From Eq. (6) it is clear that in the present case the moments of inertia are not proportional to $\beta^2 \sin^2(\gamma - 2\pi k/3)$, but to $(\beta^2/f^2(\beta)) \sin^2(\gamma - 2\pi k/3)$. The function $\beta^2/f^2(\beta)$ is shown in Fig. 1 for different values of the parameter a. It is clear that the increase of the moment of inertia is slowed down by the function $f(\beta)$, as it is expected as nuclear deformation sets in [3].

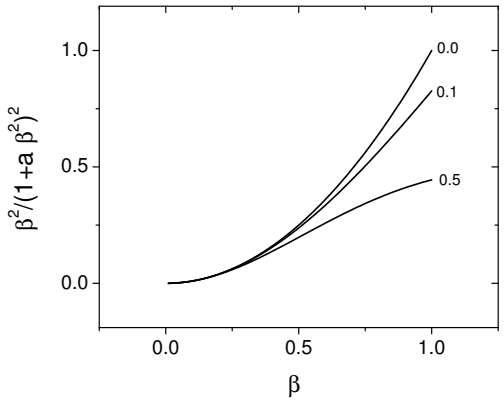

Fig. 1. The function $\beta^2/f^2(\beta) = \beta^2/(1+a\beta^2)^2$, to which moments of inertia are proportional as seen from Eq. (6), plotted as a function of the nuclear deformation β for different values of the parameter a. See Sec. 4 for further discussion.

It is obvious now that the superpotential of the effective potential should be the one corresponding to the Davidson potential, which is known [10]. Therefore the ladder

operators of the first member of the hierarchy should take the form [8]

$$B_0^{\pm} = \mp\frac{1}{\sqrt{2}}\left(\sqrt{f}\frac{d}{d\beta}\sqrt{f}\right) + \frac{1}{\sqrt{2}}\left(c_0\beta + \bar{c}_0\frac{1}{\beta}\right), \tag{13}$$

From these equations the eigenvalues and eigenfunctions are obtained in [8].

5 Numerical results

As a first testground of the present method we have used the Xe isotopes shown in Table 1. Their choice is justified in [8]. It is worth considering here the values of the parameters in each nucleus.
i) ^{134}Xe and ^{132}Xe are almost pure vibrators. Therefore no need for deformation dependence of the mass exists, the least square fitting leading to $a = 0$. Furthermore, no β_0 term is needed in the potential, the fitting therefore leading to $\beta_0 = 0$, *i.e.*, to pure harmonic behaviour.
ii) In the next two isotopes (^{130}Xe and ^{128}Xe) the need to depart from the pure harmonic oscillator becomes clear, the fitting leading therefore to nonzero β_0 values. However, there is still no need of dependence of the mass on the deformation, the

Table 1
Comparison of theoretical predictions of the γ-unstable Bohr Hamiltonian with β-dependent mass (with $\delta = \lambda = 0$) to experimental data [13] of Xe isotopes. The $R_{4/2} = E(4_1^+)/E(2_1^+)$ ratios (indicated as $4/2$ in the table), as well as the quasi-β_1 and quasi-γ_1 bandheads, normalized to the 2_1^+ state and labelled by $R_{0/2} = E(0_\beta^+)/E(2_1^+)$ and $R_{2/2} = E(2_\gamma^+)/E(2_1^+)$ respectively (indicated as $0/2$ and $2/2$ in the table), are shown. n indicates the total number of levels involved in the fit and σ is the rms quality measure.

	$4/2$ exp	$4/2$ th	$0/2$ exp	$0/2$ th	$2/2$ exp	$2/2$ th	β_0	a	n	σ
^{118}Xe	2.40	2.32	2.5	2.6	2.8	2.3	1.27	0.103	19	0.319
^{120}Xe	2.47	2.36	2.8	3.4	2.7	2.4	1.51	0.063	23	0.524
^{122}Xe	2.50	2.40	3.5	3.3	2.5	2.4	1.57	0.096	16	0.638
^{124}Xe	2.48	2.36	3.6	3.5	2.4	2.4	1.55	0.051	21	0.554
^{126}Xe	2.42	2.33	3.4	3.1	2.3	2.3	1.42	0.064	16	0.584
^{128}Xe	2.33	2.27	3.6	3.5	2.2	2.3	1.42	0.000	12	0.431
^{130}Xe	2.25	2.21	3.3	3.1	2.1	2.2	1.27	0.000	11	0.347
^{132}Xe	2.16	2.00	2.8	2.0	1.9	2.0	0.00	0.000	7	0.467
^{134}Xe	2.04	2.00	1.9	2.0	1.9	2.0	0.00	0.000	7	0.685

fitting still leading to $a = 0$. Even if we have a finite value for the β_0, the mass is not yet position dependent. But in ^{126}Xe, for the same value of β_0 as in ^{128}Xe, the mass is position dependent. These three nuclei (^{130}Xe, ^{128}Xe, and ^{126}Xe) seem to be good candidates for the examination of the behavior of the mass during the phase transition from a spherical to a γ-unstable behavior.
iii) Beyond ^{126}Xe, both the β_0 term in the potential and the deformation dependence of the mass become necessary, leading to nonzero values of both β_0 and a.

6 Conclusion

Based on the classical limit of the IBM and on the approach of a non constant mass coefficient in the Bohr Hamiltonian, a PDM Bohr Hamiltonian is obtained. Its application to γ-unstable nuclei gives encouranging results. Furthermore, the mass behaviour during the transition from the spherical to the γ-unstable case seems to be promising, indicating a dependence relationship between deformation and mass.

References

[1] A. Bohr, Mat. Fys. Medd. K. Dan. Vidensk. Selsk. 26 (1952) 14.

[2] J. M. Eisenberg, W. Greiner, Nuclear Theory, Vol.I: Nuclear Models, North-Holland, Amsterdam, 1975.

[3] P. Ring, P. Schuck, The Nuclear Many-Body Problem, Springer, Berlin, 1980.

[4] F. Iachello, A. Arima, The Interacting Boson Model, Cambridge University Press, Cambridge, 1987.

[5] O. S. van Roosmalen, Ph.D. thesis, U. Groningen, 1982.

[6] R. V. Jolos, P. von Brentano, Phys. Rev. C 79 (2009) 044310.

[7] C. Quesne, V. M. Tkachuk, J. Phys. A: Math. Gen. 37 (2004) 4267.

[8] D.Bonatsos, P.E Georgoudis, D.Lenis,N. Minkov,and C.Quesne, Phys. Lett. B 683 (2010) 264.

[9] F. Cooper, A. Khare, U. Sukhatme, Supersymmetry in Quantum Mechanics, World Scientific, Singapore, 2001.

[10] B. Bagchi, A. Banerjee, C. Quesne, V. M. Tkachuk, J. Phys. A: Math. Gen. 38 (2005) 2929.

[11] L. Wilets, M. Jean, Phys. Rev. 102 (1956) 788.

[12] P. M. Davidson, Proc. R. Soc. London Ser. A 135 (1932) 459.

[13] Nuclear Data Sheets, as of December 2005.

Electron Capture in Nuclear Structure and Astrophysics

P. Giannaka [a] T.S. Kosmas [a] and V. Tsaktsara [a]

[a] *Theoretical Physics Section, University of Ioannina, GR 45110 Ioannina, Greece*

Abstract

Electron capture on nucleons and nuclei, is one of the most important weak interaction processes in the dynamics and evolution of massive stars. Especially on nuclei of the Fe mass region the role of e^- capture is crucial in the phase of stellar core collapse. Furthermore, a realistic treatment of electron capture on heavy nuclei provides significant information in the hydrodynamics of core collapse and bounce. In this work, we exploit the advantages of a recently published numerical approach to perform nuclear structure calculations of the electron capture in Fe group nuclear isotopes. As a first concrete example, which is simultaneously o ering a good test of our method, we choose the reaction $^{56}Fe(e^-,\nu_e)^{56}Mn^*$ that plays a decisive role in core collapse supernovae. We also improve the previous formalism by constructing compact analytical expressions for the required reduced matrix elements of all basic multipole operators in isospin representation. Such a compact formalism o ers the advantage of performing state-by-state calculations of the transition rates for semi-leptonic nuclear processes through advantageous computer codes written in isospin representation.

1 Introduction

In the unified description of semi-leptonic electro-weak processes in nuclei developed by Walecka and Donnelly [1 3]), the calculation of the transition rates relies on a multipole decomposition of the hadronic current-density matrix elements leading to a set of eight independent irreducible tensor operators. These operators contain spherical Bessel functions, j_l, combined with spherical harmonics, Y^L_M, or vector spherical harmonics, $\mathbf{Y}^{(L,1)J}_M$ as

$$M^J_M(q\mathbf{r}) \;=\; \delta_{LJ} j_L(qr) Y^L_M(r), \tag{1}$$

$$\mathbf{M}^{(L1)J}_M(q\mathbf{r}) \;=\; j_L(qr)\mathbf{Y}^{(L1)J}_M(r)\,. \tag{2}$$

Preprint submitted to Elsevier *2 May 2011*

where

$$\mathbf{Y}_M^{(L,1)J}(r) \;=\; \sum_{M_L,q} \langle L m_L 1 q | J M \rangle Y^L_{M_L}(r) e_q \tag{3}$$

The parameters $q^\mu = (q_0, \mathbf{q}), \qquad q = |\mathbf{q}|$ are determined from the kinematics of the process in question. The standard multipole expansion of the polar-vector (hadronic) current (J_λ) density matrix elements leads to the operators: Coulomb (M^{coul}_{JM}), longitudinal (L_{JM}), transverse electric (T^{el}_{JM}) and transverse magnetic (T^{mag}_{JM}) [1]. Correspondingly, the axial-vector current component, J^5_λ, leads to the operators M^{Coul5}_{JM}, L^5_{JM}, T^{el5}_{JM} and T^{mag5}_{JM}. In the context of the conserved vector current (CVC) theory assumed by many authors, the longitudinal component is linearly dependent on the Coulomb one, $L_{JM}(q) = (q_0/q) M^{Coul}_{JM}(q)$, and then the number of independent operators emerging out of the decomposition procedure is reduced to seven [1 3]. Then, the matrix elements of these seven basic operators involve momentum dependent form factors, $F_X(q^2_\mu)$ where X=1, 2, A, P,and in the Walecka-Donnelly method [1] seven new operators are defined.

In Ref. [3] we suppressed isospin labels from the multipole operators and we concentrated on the proton-neutron representation applied in the QRPA method.

2 The Donnelly–Walecka decomposition method

2.1 Proton-Neutron representation formalism

The latter operators are denoted as $T^{JM}_i(q\mathbf{r})$, $i = 1, 2, ..., 7$ and are given by the expressions

$$T^{JM}_1 \;\equiv\; M^J_M(q\mathbf{r}) \;=\; \delta_{LJ}\, j_L(\rho) Y^L_M(r), \tag{4}$$

$$T^{JM}_2 \;\equiv\; \mathbf{\Sigma}^J_M(q\mathbf{r}) \;=\; \mathbf{M}^{JJ}_M \cdot \boldsymbol{\sigma}, \tag{5}$$

$$T^{JM}_3 \;\equiv\; \mathbf{\Sigma'}^J_M(q\mathbf{r}) \;=\; -i \left[\frac{1}{q} \nabla \times \mathbf{M}^{JJ}_M(q\mathbf{r})\right] \cdot \boldsymbol{\sigma}, \tag{6}$$

$$T^{JM}_4 \;\equiv\; \mathbf{\Sigma''}^J_M(q\mathbf{r}) \;=\; \left[\frac{1}{q} \nabla M^J_M(q\mathbf{r})\right] \cdot \boldsymbol{\sigma}, \tag{7}$$

$$T^{JM}_5 \;\equiv\; \mathbf{\Delta}^J_M(q\mathbf{r}) \;=\; \mathbf{M}^{JJ}_M(q\mathbf{r}) \cdot \frac{1}{q} \nabla, \tag{8}$$

$$T_6^{JM} \equiv \Delta'^{J}_{M}(q\mathbf{r}) = -i\Big[\frac{1}{q}\nabla \times \mathbf{M}^{JJ}_{M}(q\mathbf{r})\Big] \cdot \frac{1}{q}\nabla, \tag{9}$$

$$T_7^{JM} \equiv \Omega^{J}_{M}(q\mathbf{r}) = M^{J}_{M}(q\mathbf{r})\boldsymbol{\sigma} \cdot \frac{1}{q}\nabla. \tag{10}$$

(in addition to the unified notation T_i^{JM}, we keep also the common notation [1,3]).

In the present work, we first construct explicit analytic expressions for the reduced matrix elements of the basic tensor operators by using harmonic oscillator wave functions [4] in the isospin representation.

These expressions allow the systematic calculation of all basic multipole matrix elements by separating out the geometrical coefficients from the kinematical parameters (energy, momentum, scattering angle) of the studied reaction.

One of the main goals of this effort is to construct an advantageous code for calculating electron-capture cross sections in various currently interesting nuclear isotopes on the basis of the present formalism and within the context of the quasi-particle random phase approximation (QRPA) [3]

2.2 Tensor Multipole operators

Most physical observables in semi-leptonic electro-weak processes in nuclei, are reliably expressed in terms of reduced matrix elements of the above basic one-body operators between two single particle orbits $|n(l1/2)j\rangle \equiv |j\rangle$, i.e. matrix elements of the form

$$\langle n_1(l_1 1/2)j_1||T_i^J||n_2(l_2 1/2)j_2\rangle \equiv \langle j_1||T_i^J||j_2\rangle, \quad i = 1, 2, ...7. \tag{11}$$

Due to the fundamental importance of such reduced nuclear matrix elements in Ref. [3] we constructed compact analytic expressions for their evaluation.

The above eight types of irreducible tensor multipole operators [Eqs. (14)-(21)] are acting on the nuclear Hilbert space and have rank J. The components of the polar vector $(\rho(\mathbf{r}), \mathbf{J}(\mathbf{r}))$ and axial vector $(\rho(\mathbf{r})^5, \mathbf{J}(\mathbf{r})^5)$ currents are defined e.g. in Ref. [2].

The multipole operators are written in terms of the seven basic operators, $T_i^{JM}(q\mathbf{r})$, $i = 1, 2, ..., 7$ (the exact expressions are given in the Appendix of Ref. [5]) For the definition of the form factors $F(q_\mu^2)$ (assuming CVC theory) see Ref. [3]

Using Eqs. (**??**), (**??**) and (**??**), one can straightforwardly deduce a general closed analytic formula for the reduced matrix elements $\langle j_1||T_i^J||j_2\rangle$ of the seven basic operators Eqs. (4)-(2.1) as

$$\langle j_1||T^J||j_2\rangle \;=\; e^{-y}y^{\beta/2}\sum_{\mu=0}^{n_{max}}\mathcal{P}_\mu^J\,y^\mu\,, \qquad y=(qb/2)^2 \tag{12}$$

In the summation of Eq. (12) the upper index n_{max} represent the maximum h.o. quanta included in the model space chosen.

$$n_{max}=(N_1+N_2-\beta)/2\,. \tag{13}$$

2.3 Formalism in Isospin representation

In the isospin representation the eight basic multipole operators are written as follows. The four components of the polar vector current are

$$M^{coul}_{JM;TM_T} \;=\; \int d\mathbf{r}M^J_M(q\mathbf{r})\rho(\mathbf{r})_{TM_T}, \tag{14}$$

$$L_{JM;TM_T} \;=\; i\int d\mathbf{r}\left(\frac{1}{q}\nabla M^J_M(q\mathbf{r})\right)\cdot\mathbf{J}(\mathbf{r})_{TM_T}, \tag{15}$$

$$T^{el}_{JM;TM_T} \;=\; \int d\mathbf{r}\left(\frac{1}{q}\nabla\times\mathbf{M}^{JJ}_M(q\mathbf{r})\right)\cdot\mathbf{J}(\mathbf{r})_{TM_T}, \tag{16}$$

$$T^{mag}_{JM;TM_T} \;=\; \int d\mathbf{r}\mathbf{M}^{JJ}_M(q\mathbf{r})\cdot\mathbf{J}(\mathbf{r})_{TM_T}. \tag{17}$$

The four components of the axial vector current are

$$M^5_{JM;TM_T} \;=\; \int d\mathbf{r}M^J_M(q\mathbf{r})\rho(\mathbf{r})^5_{TM_T}, \tag{18}$$

$$L^5_{JM;TM_T} \;=\; i\int d\mathbf{r}\left(\frac{1}{q}\nabla M^J_M(q\mathbf{r})\right)\cdot\mathbf{J}(\mathbf{r})^5_{TM_T}, \tag{19}$$

$$T^{el5}_{JM;TM_T} \;=\; \int d\mathbf{r}\left(\frac{1}{q}\nabla\times\mathbf{M}^{JJ}_M(q\mathbf{r})\right)\cdot\mathbf{J}(\mathbf{r})^5_{TM_T}, \tag{20}$$

$$T^{mag5}_{JM;TM_T} \;=\; \int d\mathbf{r}\mathbf{M}^{JJ}_M(q\mathbf{r})\cdot\mathbf{J}(\mathbf{r})^5_{TM_T}. \tag{21}$$

2.4 Nuclear level multipole operators

At nuclear level the multipole operators which contain the nucleon form factors $F_X(q_\mu^2)$ are given by the expressions

$$M^{coul}_{JM;TM_T} = \sum_{i=1,A} F_V^\alpha M_J(\mathbf{q}_i) \tag{22}$$

$$L_{JM;TM_T} = \sum_{i=1,A} \left(\frac{F_V^\alpha}{2M} \frac{1}{[J]} \left((J+1)^{1/2} \mathbf{M}_{J+1,J}(\mathbf{q}_i) + J^{1/2} \mathbf{M}_{J-1,J}(\mathbf{q}_i) \right) \cdot (\overrightarrow{\boldsymbol{\nabla}}_i - \overleftarrow{\boldsymbol{\nabla}}_i) \right.$$
$$\left. - \frac{F_V^\alpha + F_M^\alpha}{2M} \frac{i}{[J]} \left((J+1)^{1/2} \mathbf{M}_{J+1,J}(\mathbf{q}_i) + J^{1/2} \mathbf{M}_{J-1,J}(\mathbf{q}_i) \right) \cdot \boldsymbol{\sigma} \times \overrightarrow{\boldsymbol{\nabla}}_i \right) \tag{23}$$

$$T^{el}_{JM;TM_T} = \sum_{i=1,A} \left(\frac{F_V^\alpha}{2M} \frac{1}{[J]} \left((J+1)^{1/2} \mathbf{M}_{J-1,J}(\mathbf{q}_i) - J^{1/2} \mathbf{M}_{J+1,J}(\mathbf{q}_i) \right) \cdot (\overrightarrow{\boldsymbol{\nabla}}_i - \overleftarrow{\boldsymbol{\nabla}}_i) \right.$$
$$\left. - \frac{F_V^\alpha + F_M^\alpha}{2M} \frac{i}{[J]} \left(J+1)^{1/2} \mathbf{M}_{J-1,J}(\mathbf{q}_i) - J^{1/2} \mathbf{M}_{J+1,J}(\mathbf{q}_i) \right) \cdot \boldsymbol{\sigma} \times \overrightarrow{\boldsymbol{\nabla}}_i \right) \tag{24}$$

$$T^{mag}_{JM;TM_T} = \sum_{i=1,A} \left(-\frac{iF_V^\alpha}{2M} \mathbf{M}_{J,J}(\mathbf{q}_i) \cdot (\overrightarrow{\boldsymbol{\nabla}}_i - \overleftarrow{\boldsymbol{\nabla}}_i) - \frac{F_V^\alpha + F_M^\alpha}{2M} \mathbf{M}_{J,J}(\mathbf{q}_i) \boldsymbol{\sigma} \times \overrightarrow{\boldsymbol{\nabla}}_i \right) \tag{25}$$

$$M^5_{JM;TM_T} = \sum_{i=1,A} \left(-\frac{iF_A^\alpha}{2M} M_J(\mathbf{q}_i) \boldsymbol{\sigma} \cdot (\overrightarrow{\boldsymbol{\nabla}}_i - \overleftarrow{\boldsymbol{\nabla}}_i) - \frac{i\omega}{2M} F_P^\alpha M_J(\mathbf{q}_i) \boldsymbol{\sigma} \cdot \overrightarrow{\boldsymbol{\nabla}}_i \right) \tag{26}$$

$$L^5_{JM;TM_T} = \sum_{i=1,A} F_A^\alpha \frac{i}{[J]} \left((J+1)^{1/2} \mathbf{M}_{J+1,J}(\mathbf{q}_i) + J^{1/2} \mathbf{M}_{J-1,J}(\mathbf{q}_i) \right) \cdot \boldsymbol{\sigma} \tag{27}$$

$$T^{el5}_{JM;TM_T} = \sum_{i=1,A} F_V^\alpha \frac{i}{[J]} \left(J+1)^{1/2} \mathbf{M}_{J-1,J}(\mathbf{q}_i) - J^{1/2} \mathbf{M}_{J+1,J}(\mathbf{q}_i) \right) \cdot \boldsymbol{\sigma} \tag{28}$$

$$T^{mag5}_{JM;TM_T} = \sum_{i=1,A} F_A^\alpha \mathbf{M}_{J,J}(\mathbf{q}_i) \boldsymbol{\sigma} \tag{29}$$

where A is the mass number of the studied nucleus and nabla operators are acting to the right and left respectively. The isospin dependence of the oper-

ators (14)-(21) is included in the operator $I_T^{M_T}$ which is written as [1]

$$I_T^{M_T} = \begin{cases} 1, & T=0,\ M_T=0 \\ \tau_0=\tau_3, & T=1,\ M_T=0 \\ \tau_\pm = \mp\frac{1}{\sqrt{2}}(\tau_1 \pm \tau_2), & T=1,\ M_T=\pm 1 \end{cases} \tag{30}$$

The exact form of $I_T^{M_T}$, i.e. the values of the quantum numbers of T and M_T, is determined from the specific reaction studied (charged or neutral current type reaction).

3 e^-–Capture in stellar evolution

3.1 Electron Capture in ^{56}Fe

In the present work we perform detailed calculations of the electron capture process in the iron group nuclei. As a first concrete example we study the reaction

$$e^- + ^{56}Fe \rightarrow ^{56}Mn + v_e \tag{31}$$

The required nuclear matrix elements are calculated in the context of the quasi-particle RPA. In Tables 1 and 2 we list the values of the model parameters through which we construct the wave functions for the initial (ground) and final $|J^\pi\rangle$ states.

b (fm)	g_{pair}^n	g_{pair}^p	S_n	S_p	Δ_p^{exp}	Δ_p^{th}	Δ_n^{exp}	Δ_n^{th}
1.996	0.945	0.890	11.197	10.183	1.568	1.579	1.362	1.359

Table 1. Parameters for the interaction of proton pairs, g_{pair}^p, and neutrons pairs, g_{pair}^n. They are fixed in such a way that the corresponding experimental

gaps, Δ_p^{exp} and Δ_n^{exp}, to be reproduced.

State	Strength parameters		*Low-lying Energies (MeV)*	
J^π	g_{ph}	g_{pp}	E^{exp}	E^{theor}
0^+	0.442	0.853	0.004	0.000
1^+	1.183	1.191	3.120	3.120
2^+	0.550	1.171	0.847	0.847
4^+	0.801	1.195	2.085	2.085
0^-	1.119	1.138	3.610	3.610
3^-	0.800	0.918	3.077	3.076
5^-	1.000	0.807	5.122	5.122

Table 2. Strength parameters for the particle-particle (g_{pp}) and particle-hole (g_{ph}) interaction for various multipolarities and the corresponding low-lying energies of the ^{56}Fe spectrum.

A detailed description for the adjustment of the QRPA pamameters

$$g_{pair}^{p,n}, g_{ph}^{p,n} and g_{pp}^{p,n}$$

is done in Ref. [4,5].

3.2 QRPA matrix elements calculations

This is an extension of the numerical approach, which, by using harmonic oscillator basis in the proton-neutron representation, analytical expressions for all basic multipole RME have been obtained. They are expressed in terms of elementary functions, i.e. products of an exponential times a simple polynomial with constant coe cients.

The model space chosen in our QRPA includes the harmonic oscillator levels $0d_{5/2}, 1s_{1/2}$, $0d_{3/2}$, $0f_{7/2}$, $1p_{1/2}$,$1p_{3/2}$, $0f_{5/2}$, $0g_{9/2}$, $1d_{5/2}$, $0g_{7/2}$, $1d_{3/2}$, $2s_{1/2}$, $0h_{9/2}$, $0h_{11/2}$. Our method has been checked in the reproducibility of the low-lying (up to about 5 MeV) spectrum of the ^{56}Fe isotope by using: (i) at the BCS level the pairing parameters for proton-pairs, g_{pair}^p and neutron-pairs, g_{pair}^n [4], and (ii) at the QRPA level the fitting parameters for the strength of the residual interaction, i.e. the g_{ph}, for the particle-hole, and the g_{pp}, for the particle-particle channel, respectively [4,3].

The reliability of the present calculations, could be acquired by the comparison of our electron capture cross sections with those evaluated in other processes, e.g the charged current neutrino nucleus reaction, $^{56}Fe(\nu_e, e^-)^{56}Co$ which is the particle conjugate process reaction of the electron capture.

4 Summary

During the presupernova and collapse phase, electron captures on nuclei, and in the late stage also on free protons, plays an important role, as does nuclear β-decay during silicon burning. Electron captures are made possible by the increasing density in the star's center, accompanied by an increase of the chemical potential (Fermi energy) of the degenerate electron gas. Electron captures reduce the electron-to-baryon ratio Y_e of the matter composition which has important consequences for the subsequent evolution.

In this work, we are going to use a numerical approach constructed recently based on analytical expressions for all basic multipole reduced matrix elements, to perform systematic studies electron capture on nuclear isotopes in the mass range of Fe. The nuclear wave functions would be obtained by using the quasi-particle RPA.

References

[1] T.W. Donnelly and R.D. Peccei, Phys. Rep. **50** (1979) 1.

[2] N.T. Zinner, K. Langanke, P. Vogel, Phys. Rev. **C 74** 74 (2006) 024326.

[3] V.C. Chasioti, T.S. Kosmas, Nucl. Phys. **A 829** (2009) 234.

[4] T.S. Kosmas, Nucl. Phys. **A 683** (2001) 443.

[5] V. Tsakstara and T.S. Kosmas, Phys. Rev. C, in press

Influence of parasitic neutrons to the ^{176}Hf(n,2n)^{175}Hf reaction cross section

R. Vlastou[1], M. Kokkoris[1], M. Serris[1], M. Lambrou[1], L. Sofokleous[1], M. Diakaki[1], A.Tsinganis[1], V. Loisou[1] and A. Lagoyannis[2]

[1]National Technical University of Athens, Department of Physics, Athens, Greece
[2]Institute of Nuclear Physics, NCSR "Demokritos", Aghia Paraskevi, Athens, Greece

Abstract

Cross sections for ^{176}Hf(n,2n)^{175}Hf reaction have been measured at the VdG Tandem accelerator of NCSR \Demokritos", in the neutron energy region from 8.80 to 11.02 MeV, using the activation technique. In order to account for the contamination of the ^{176}Hf(n,2n)^{175}Hf by the ^{174}Hf(n,γ)^{175}Hf reaction activated by the presence of parasitic neutrons, an experimental method has been developed based on the influence of the parasitic neutrons in the case of the (n,2n) and (n,γ) reactions on ^{197}Au. The results were found to be consistent with the energy spectrum of the neutron beam which has been studied by means of the multiple foil activation analysis technique as well as by a liquid scintillator BC501A detector and subsequent deconvolution of its recoil energy spectra.

Introduction

Studies of neutron induced reactions are of considerable significance, both for their importance to fundamental research in Nuclear Physics and Astrophysics and for practical applications in nuclear technology, medicine and industry. In the energy region up to 20 MeV, many reaction channels, which may proceed via different reaction mechanisms, are open and therefore can be simultaneously studied both experimentally and theoretically. In particular, neutron induced reactions on Hf are important since Hf is used for reactor control rods in nuclear submarines due to its high thermal neutron absorption cross section. In addition, neutron induced reactions on W and Ta in reactor materials could lead to long lived isomeric states of Hf isotopes with rather harmful γ-ray production. In the case of the ^{176}Hf(n,2n)^{175}Hf reaction, experimental data are available only at ~14MeV with many discrepancies among them.
Measurements of neutrons on natural Hf for the determination of the ^{176}Hf(n,2n)^{175}Hf cross section, are influenced by the presence of parasitic neutrons which accompany the main neutron beam and activate the ^{174}Hf(n,γ)^{175}Hf reaction. In order to account for this contamination of the ^{175}Hf production, a method has been developed, based on the investigation of the parasitic neutrons in the case of the (n,2n) and (n,γ) reactions on ^{197}Au. These two reactions produce different daughter nuclei ^{196}Au and ^{198}Au, respectively, thus allowing the comparison between the useful neutrons which activate the threshold (n,2n) reaction and the parasitic ones which activate the (n,γ) reaction.

Experimental Procedure

Cross section measurements of (n,2n) threshold reactions on high purity natural Hf have been performed in the energy range 8.80 -11.02 MeV, at the 5 MV Tandem T11/25 accelerator laboratory of NCSR "Demokritos", by using the activation method. Quasi-monoenergetic neutron beams were produced via the $^{2}H(d,n)^{3}He$ reaction at a flux of the order of $\sim 10^{6}$ n/(cm^2 sec). Thin metallic targets of high purity natural Hf with masses ~0.95 g were used, stacked between two Al foils and placed at 0 degrees with respect to the beam direction and at distances which varied from 7 to 12cm from the end of the deuterium gas cell. The absolute flux of the beam was obtained with respect to the $^{27}Al(n,\alpha)^{24}Na$ reference reaction, while its variation was monitored by a BF_3 detector placed at a distance of 3 m from the neutron source. The average effective flux on each sample was obtained by taking the mean values for the front and back Al foils. The induced activity of product radionuclides and reference foils was measured with HPGe detectors of 80% and 56% efficiency. The characteristic γ-rays were corrected for self absorption in the target, summing effects of cascading transitions and counting geometry.

The neutron beam however, is not purely monoenergetic due to parasitic neutrons mainly originating from the deuteron break up reactions. In order to study the influence of the parasitic neutrons on the main neutron beam, an investigation of the energy dependence of the neutron flux has been carried out [1] by using two experimental methods: deconvolution of recoil energy spectra taken with a liquid scintillator BC501A detector, with the DIFBAS code [2], as well as via the multiple foil activation technique in combination with the SULSA [3] unfolding code. The results from the two methods seem to be in fair agreement, indicating that around nominal neutron energies E_n = 7 MeV, parasitic neutrons start to appear and above E_n = 9 MeV, they contribute considerably to the neutron flux. The tail of parasitic neutrons is important in the region 2-3 MeV, mainly due to the deuteron break-up process above E_d = 4.5 MeV [4].

Natural Hf consists of 6 isotopes $^{174, 176, 177, 178, 179, 180}$ Hf and three of them produce long lived residual nuclei which can thus be studied by using the neutron activation technique. The $^{174}Hf(n,2n)^{173}Hf$, $^{176}Hf(n,2n)^{175}Hf$ and $^{174}Hf(n,\gamma)^{175}Hf$ are the three reactions which can be studied with the activation mehod. The $^{174}Hf(n,2n)^{173}Hf$ reaction cross section has already been investigated [5], while the data for the $^{176}Hf(n,2n)^{175}Hf$ reaction is contaminated by the $^{174}Hf(n,\gamma)^{175}Hf$ reaction and needs more consideration. The cross section of the $^{176}Hf(n,2n)^{175}Hf$ reaction can be determined via the 343.4 keV characteristic γ-ray from the deexcitation of the ^{175}Hf. It is a threshold reaction (Ethr=8.2MeV) and opens with neutrons of energy above ~9MeV, while the contaminant reaction $^{174}Hf(n,\gamma)^{175}Hf$ has no threshold and opens with parasitic low energy neutrons. In order to account for this contamination of the ^{175}Hf production, the effect of parasitic neutrons has been studied in the case of the (n,2n) and (n,γ) reactions on ^{197}Au. These two reactions produce different daughter nuclei ^{196}Au and ^{198}Au, respectively, thus allowing the comparison between the useful neutrons which activate the threshold (n,2n) reaction and the parasitic ones which activate the (n,γ) reaction. Furthermore, the cross sections of the $^{174}Hf(n,\gamma)^{175}HF$ and $^{197}Au(n,\gamma)^{198}Au$ reactions, have similar behavior with respect to neutron energy. The technique implemented to perform these corrections is described below.

The correction technique

At the end of the irradiation of the ^{197}Au target, the number of the produced nuclei, is given by the relations:

$$N^{196} = \sigma_{2n} N^{197} \Phi_{2n} f(t)_{2n} \quad (1)$$

$$N^{198} = \sigma_{\gamma} N^{197} \Phi_{\gamma} f(t)_{\gamma} \quad (2)$$

where N^{196} and N^{198} are the numbers of the produced nuclei of ^{196}Au and ^{198}Au respectively, N^{197} is the number of the target nuclei, σ_{2n} and σ_{γ} are the cross sections of the ^{197}Au(n, 2n)^{196}Au and ^{197}Au(n, γ)^{198}Au reactions, respectively, Φ is the neutron flux and f(t) is the correction factor which represents the fluctuations of the neutron beam.

The fraction of the produced nuclei which are decaying during the irradiation is expressed by the formula :

$$f_c(t) = \frac{\int_0^{t_B} f(t) e^{\lambda t} dt}{\int_0^{t_B} f(t)} e^{-\lambda t_B} \quad (3)$$

where t_B is the irradiation time and λ is the decay probability for the reaction c. Considering that f(t) remains constant with time we are lead to the relation :

$$f(t) = \frac{\lambda (1 - e^{-\lambda t_B})}{t_B} \quad (4)$$

Finally from the relations (1), (2) and (4) we end up to the expression :

$$\Lambda = \frac{\overline{\sigma_{\gamma} \Phi_{\gamma}}}{\Phi_{2n}} = \frac{\sigma_{2n} N^{198} \lambda^{196} (1 - e^{-\lambda^{196} t_B})}{N^{196} \lambda^{198} (1 - e^{-\lambda^{198} t_B})} \quad (5)$$

with the mean values representing the average cross section and neutron flux with respect to the whole neutron energy spectrum which activates the (n,γ) reaction on ^{197}Au. The experimental ratio Λ has been deduced for all the measurements carried out from 8 to 10.5 MeV and is presented in Figure 1.

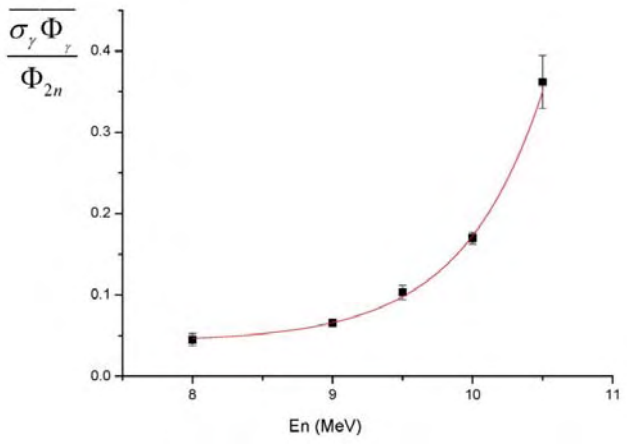

Fig.1. The ratio Λ with respect to the nominal neutron beam energy.

From this figure correction factors, have been extracted for each energy with respect to the 8 MeV value of Λ, energy which corresponds to the threshold where the ^{176}Hf(n,2n)^{175}Hf reaction is closed and the production of the 343.4 keV γ-ray derives only from the contaminant (n,γ) reaction. Assuming that these correction factors representing the effect of the contamination of (n,2n) by the (n,γ) reaction, are the same for both Hf and Au, they have been used to extract the corrected values of ^{176}Hf(n,2n)^{175}Hf cross sections, as described below.

For energy E_l=8MeV lower than the threshold energy of the ^{176}Hf(n,2n)^{175}Hf reaction and for energy E_h higher than the threshold energy of the ^{176}Hf(n,2n)^{175}Hf reaction, the number of the parasitic events from the ^{174}Hf(n,γ)^{175}Hf reaction is given respectively by the relations:

$$C_l^\gamma = \overline{\sigma_{Hf}^{\gamma l}} N_\tau^l \overline{\Phi_l^\gamma} f_c^l \varepsilon_\gamma^l I_\gamma K_\gamma e^{-\lambda t_w^l} (1 - e^{-\lambda t_m^l}) \quad (6)$$

and

$$C_h^\gamma = \overline{\sigma_{Hf}^{\gamma h}} N_\tau^h \overline{\Phi_h^\gamma} f_c^h \varepsilon_\gamma^h I_\gamma K_\gamma e^{-\lambda t_w^h} (1 - e^{-\lambda t_m^h}) \quad (7)$$

where N_τ is the number of the target nuclei, ε_γ is the peak efficiency of the measured γ-ray and I_γ its transition probability, K_γ is the correction factor of the activity to account for self absorption of the sample, t_w is the waiting time between the end of the irradiation and the start of the measurement and t_m is the measurement time.

Dividing relations (6) and (7) by parts and multiplying and dividing the numerator and the denominator with the flux Φ, we end up to the expression:

$$C_h^\gamma = C_l^a \frac{\frac{\overline{\sigma_{Hf}^{\gamma h}} \overline{\Phi^\gamma}}{\Phi_{2n}^h} \Phi_{2n}^h N_\tau^h f_c^h \varepsilon_\gamma^h I_\gamma K_\gamma e^{-\lambda t_w^h} (1 - e^{-\lambda t_m^h})}{\frac{\overline{\sigma_{Hf}^{\gamma l}} \overline{\Phi^\gamma}}{\Phi_{2n}^l} \Phi_{2n}^l N_\tau^l f_c^l \varepsilon_\gamma^l I_\gamma K_\gamma e^{-\lambda t_w^l} (1 - e^{-\lambda t_m^l})} \quad (8)$$

The values of the fractions $\frac{\overline{\sigma_{Hf}^{\gamma} \Phi^\gamma}}{\Phi_{2n}}$ in the previous expression, for each energy, are taken from Figure 3, assuming that is the same for the (n,2n) and (n,γ) reactions on both Hf and Au.

Results

The measured cross sections of the ^{176}Hf(n,2n)^{175}Hf reaction at the neutron energies of 8.8, 9, 9.975, 10.51 and 11.023 MeV are presented in Table 1 and in Figure 2. The black squares represent the values of the ^{176}Hf(n,2n)^{175}Hf cross section and include the contribution of the ^{174}Hf(n,γ)^{175}Hf reaction, while the red circles represent the corrected values, determined by the technique described above. It should be emphasized that these are preliminary results and that the errors represent only the statistical part and not the systematic errors of this method.

Table 1
Cross section Values of the ^{176}HF(n,2n)^{175}HF reaction

Neutron Energy (MeV)	Cross Sections including (n,γ) contamination (barn)	Corrected Cross Sections (barn)
8.8	0.48 ± 0.04	0.45 ± 0.04
9.0	0.76 ± 0.03	0.73 ± 0.03
10.0	1.00 ± 0.08	0.92 ± 0.08
10.5	1.92 ± 0.13	1.75 ± 0.13
11.0	2.42 ± 0.22	2.04 ± 0.24

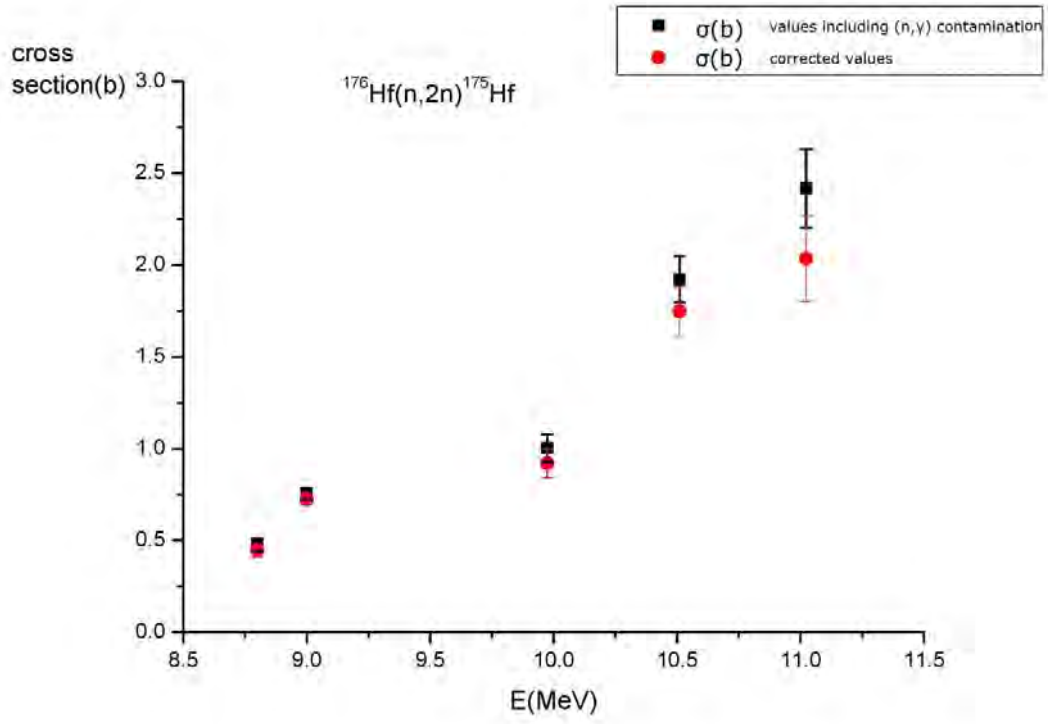

Fig. 2. Cross section Values of the ^{176}Hf(n,2n)^{175}Hf reaction

From the results in Table 1 and in Figure 2, it is apparent that the divergence between the corrected and the uncorrected cross section values increases with neutron energy. This result is consistent with the fact that the amount of the parasitic neutrons in the beam increases with increasing energy of neutron beam.

References

1. R.Vlastou et. al.,.Characterization of the neutron flux distribution at the Athens Tandem Accelerator NCSR "Demokritos", Nucl.Instr.Meth.Phys.Res.B(2011), in press
2. M.Tichy, PTB Laboratory Report PTB-7.2-1993-1, Braunschweig,1993.
3. S.Sudar, A solution for the neutron spectrum unfolding problem without using an input spectrum, INDC (HUN)-0261, IAEA, Vienna, 1989.
4. H.W.Lefevre et al. Phys.Rev. 128(1962)1328.
5. M.Serris et. al., Study of the (n,2n) cross section measurement of the ^{174}Hf isotope. Nucl. Instr. Meth. Phys. Res.B261(2007)941.

Tomographic Image Reconstruction based on Artificial Neural Network (ANN) Techniques

M. Argyrou[a], P. Paschalis[a], D. Maintas[c], E. Stiliaris [1a,b]

[a]*National and Kapodistrian University of Athens, Department of Physics, Ilissia Campus, GR–15771 Athens*
[b]*Institute of Accelerating Systems and Applications (IASA), P.O. Box 17214, GR–10024 Athens*
[c]*Institute of Isotopic Studies, Medical Center of Athens, Distomou 5-7, GR–15125 Marousi, Athens*

Abstract

A new approach for tomographic image reconstruction from projections using Artificial Neural Network (ANN) techniques is presented in this work. The design of the proposed reconstruction system is based on a simple but efficient network architecture, which best utilizes all available input information. Due to the computational complexity, which grows quadratically with the image size, the training phase of the system is characterized by relatively large CPU times. The trained network, on the contrary, is able to provide all necessary information in a quick and efficient way giving results comparable to other time consuming iterative reconstruction algorithms. The performance of the network studied with a large number of software phantoms is directly compared to the well known Algebraic Reconstruction Technique (ART). For a given image and projections size, the role of the hidden layers in the network architecture is examined and the quality dependence of the reconstructed image on the size of the geometrical patterns used in the training phase is also investigated.

1. Introduction

1.1. The Tomographic Problem

In the emission and absorbtion tomography, an image can be simply represented by a square matrix whose elements are proportional to the intensity of each pixel. Once this matrix is known, the projections in various angles θ, that is the sum of all cell contributions (Figure 1) along a certain ray R_i can be easily calculated. In tomography, we would rather interested in solving the inverse problem, that is to reconstruct the square matrix from its projections at different directions. By using the radiation emitted by an object, after the injection of radiopharmaceutical, we are able to obtain sectional (planar) images of the object. These projection data are then feeded into a reconstruction algorithm. The intensity of each ray R_i at a given angle can be calculated from the projection matrix P_{ij} and the reconstructed matrix Q_j. The projection matrix carries the information of how much the j^{th} element of the matrix Q contributes to the i^{th} ray. Let

[1]Corresponding author: stiliaris@phys.uoa.gr

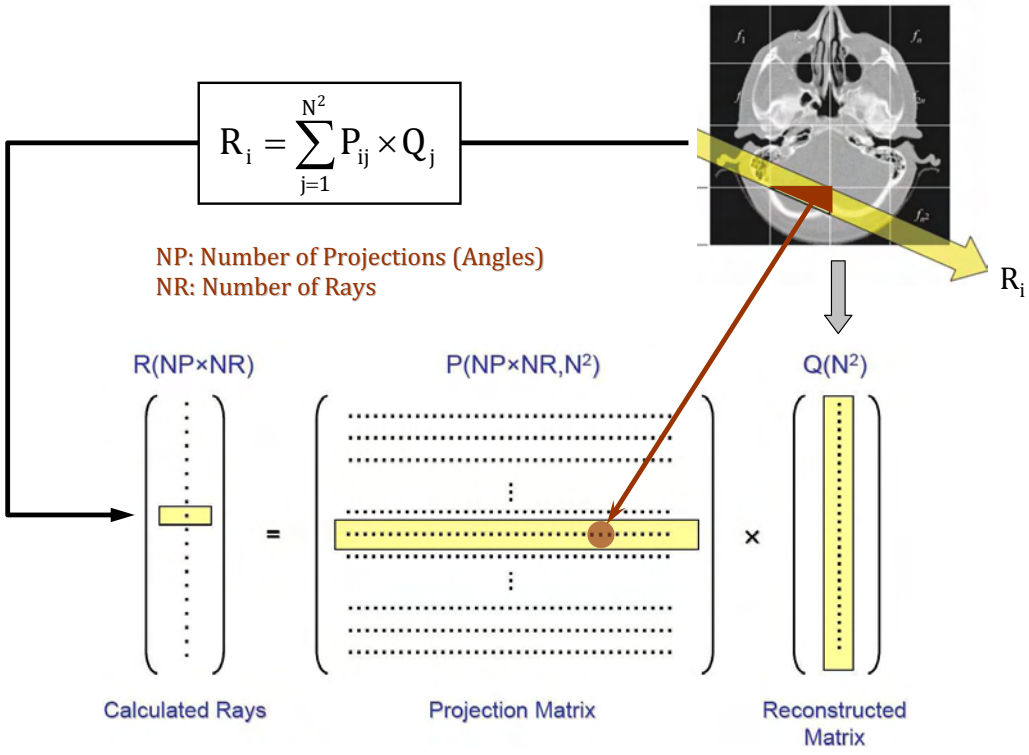

Figure 1: Reconstruction of an $N \times N$ square matrix from its $NP \times NR$ projections.

$N \times N$ be the dimension of the square matrix, NP the number of projections (angles) and NR the number of constant width rays per each projection; then the following expression holds:

$$R_i = \sum_{j=1}^{N^2} P_{ij} \times Q_j \quad \{i = 1 \cdots NP \times NR,\ j = 1 \cdots N^2\} \tag{1}$$

1.2. Image Reconstruction Methods

In order to reconstruct an image, several solutions are proposed [1]. One of them is the use of analytic algorithms. The reconstruction can be achieved by two dimensional Fourier analysis or by the filtered back-projection. In the later, the square matrix elements are exactly calculated by solving a system with N^2 unknown and $NP \times NR$ known parameters. However, a large number of projections are required in order to obtain an exact and satisfying solution.

In the iterative procedures, random values to the square matrix elements are given initially. The projections of the matrix in different angles are calculated and the matrix elements are corrected in such a way that the calculated projections best match the measured ones. Thus, after the k^{th} iteration the Q matrix elements are corrected as follows:

$$Q_j^k = Q_j^{k-1} + P_{ij} \frac{R_i^{meas} - R_i^{calc}}{N} \tag{2}$$

These methods, based on back-projected correction procedure, are known as Algebraic Reconstruction Techniques (ART). In a Newton-Raphson approach, an improved version of the above, the contribution of the nearest pixels and rays to the projection angles is taken into account [2]. The obtained reconstruction results are characterized by a good quality. In Figure 2 we present an example of reconstruction of a software phantom using ART. The evolution of the quantity $\chi^2 = \sum_{i=1}^{NP\times NR}(R_i^{meas} - R_i^{calc})^2$ with the number of iterations is also depicted in the same figure. The improvement of the reconstruction quality is demonstrated by the decrease of χ^2 after a sufficient number of iterations.

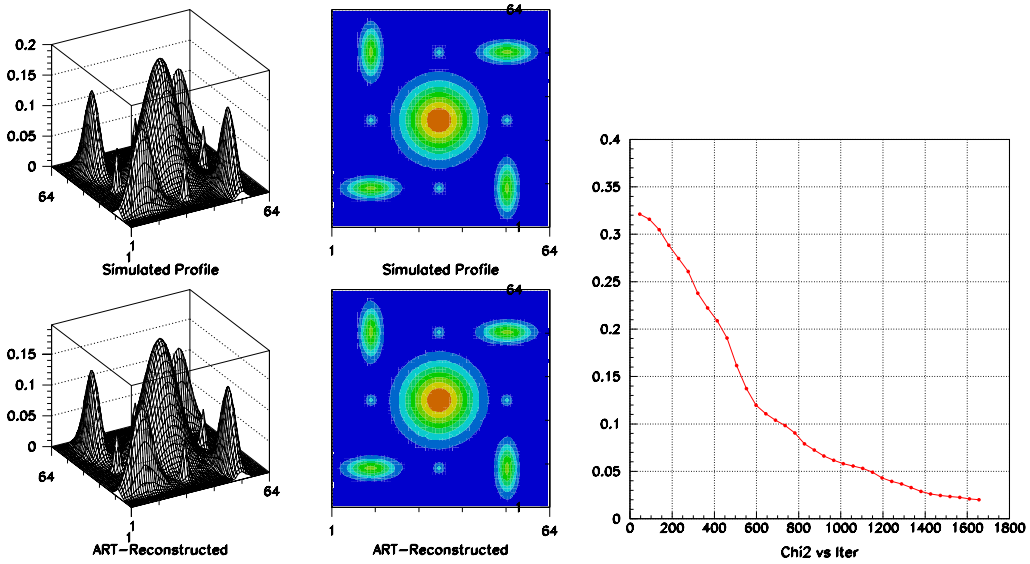

Figure 2: Reconstruction of a software phantom using ART. The original image has a dimension of $N^2 = 64 \times 64$ while the number of projections is $NP = 36$.

2. Artificial Neural Network Reconstruction

2.1. The ANN Technique

In this work we present an alternative approach to the tomographic problem using the Artificial Neural Network (ANN) Technique [3]. A typical neural network consists of the input and output layer (Figure 3). In our discussion the inputs are the experimentally obtained $NP(= M)\times NR$ projections and the outputs are the N^2 elements of the matrix to be reconstructed.

During the training process the weight factors of synapses are varied in order to approximate the desired result. This can be controlled by proper parameters, such as the learning coefficient and the momentum factor. We use the software package JETNET [4] for calculating the synaptic weight factors. It will be shown that the network architecture, and specifically the number of hidden layers, plays a crucial role in our analysis.

If no hidden layer exist and choosing for simplicity reasons $NR = N$, then the number of synapses is proportional to N^3. In the case of one hidden layer this number decreases significantly to N^2. In Figure 4 we demonstrate the reconstruction of a software phantom using ANNs with

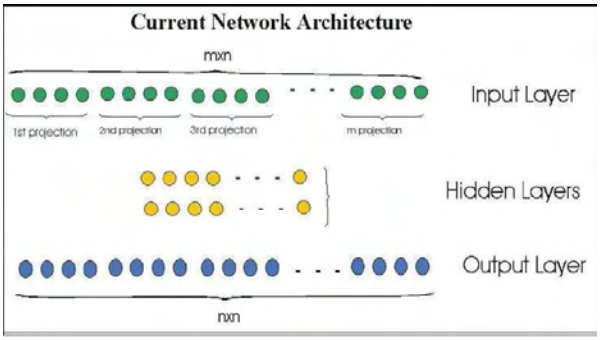

Figure 3: Architecture of the Neural Network used in the tomographic image reconstruction.

different architecture. The number of synapses in the case of no hidden layer is much larger than in the case of one hidden layer. This drastically influences the quality of the reconstructed image.

Image Size $N \times N$	Projections M	INPUT Nodes	HIDDEN Layers	OUTPUT Nodes	Synapses
32×32	18	18×32	0	32×32	589824
32×32	18	18×32	1×64	32×32	102400
32×32	18	18×32	1×32	32×32	51200

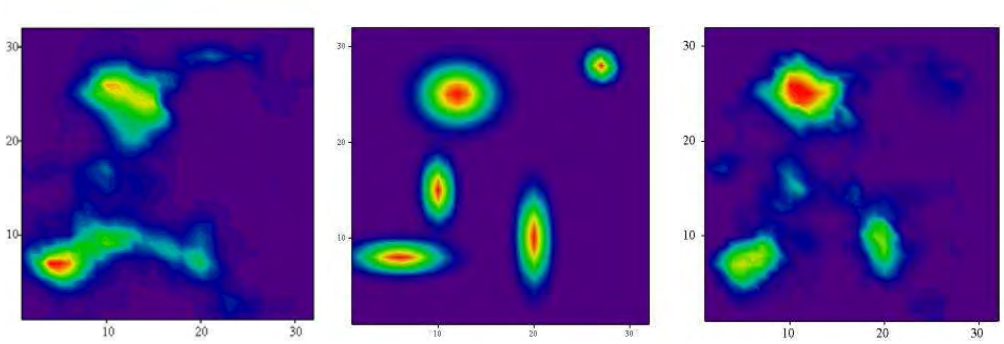

Figure 4: Reconstruction of a 32×32 software phantom (shown in the middle) with the ANN technique and for $M = 18$ projections. *Left:* One hidden layer with 64 nodes is used *Right:* No hidden layer used.

2.2. *The Role of the Pattern Size*

The dependence of the reconstructed image on the size of the geometrical patterns, mainly gaussian ellipsoids and parallelograms, used to construct the software phantom ensemble is discussed here. Three different phantom groups are generated containing geometrical patterns randomly distributed with various widths, which are controlled by the parameter σ and are also randomly distributed between predefined limits. Each of these phantom ensembles is further used as training input for the ANN reconstruction procedure. Data for $N^2 = 64 \times 64$ images are generated with $M = 18$ projections. These image groups trained separately the three different

ANN schemes, each one corresponding to a given pattern size. All three ANN have identical architecture but no hidden layers. The successfully trained networks are finally checked with control images.

Following this procedure, we can tabulate the reconstructed results in a form of a 3×3 matrix for an easier understanding, as shown in the following table. Each row corresponds to a different control image and each column to a specific ANN type, which is trained with a different pattern size. For example, the image A_{ij} is the reconstruction result of the original control image C_i (generated with pattern-width σ_i) produced by the network trained with pattern-width σ_j.

Control Images	Reconstructed Images		
C_1 $(1.0 < \sigma_1 < 3.0)$	A_{11}	A_{12}	A_{13}
C_2 $(3.0 < \sigma_2 < 6.0)$	A_{21}	A_{22}	A_{23}
C_3 $(6.0 < \sigma_3 < 9.0)$	A_{31}	A_{32}	A_{33}

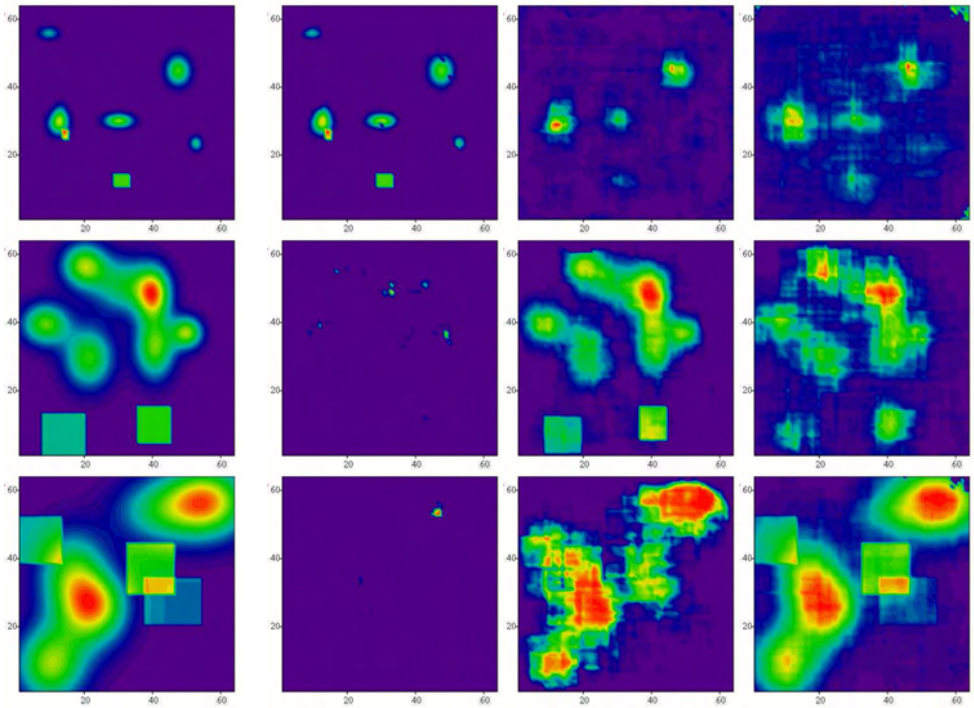

Figure 5: Reconstruction of control images with differently trained ANNs, as explained in the previous table. The original control images are shown on the left panel and the reconstructed ones on the right.

Results of these control images are shown in Figure 5. As expected, the best reconstruction quality is obtained for the diagonal elements of the matrix, that is for the reconstruction by the ANN trained with the same patterns as those of the original control image. On the contrary, the reconstruction result provided by ANN trained with smaller σ-parameters than the control images, fails totally.

3. Concluding Remarks

We have presented a technique based on the Artificial Neural Networks, which is alternative to known analytic and iterative methods (ART). The main disadvantage is the large CPU time and memory requirements during the training process. However, after the training, one can obtain reliable results in a quick and efficient way. It is shown that the network architecture can affect the quality of the reconstructed image. The best results are obtained with no hidden layers. Finally, the reconstruction quality strongly depends on the size of the geometrical patterns used in the training phase. It is preferable to reconstruct images using an ANN trained with patterns of comparable size with the required spatial resolution.

References

[1] T.M. Buzug, *"Computed Tomography"*, Springer-Verlag, Berlin (2008) ISBN: 978-3-540-39407-5.
[2] S. Angeli and E. Stiliaris, *"An Accelerated Algebraic Reconstruction Technique based on the Newton–Raphson Scheme"*, IEEE NSS-MIC (2009) 3382–3387.
[3] P. Paschalis *et al.*, *Tomographic image reconstruction using Artificial Neural Networks*, Nucl. Instr. and Meth. **A 527** (2004) 211–215.
[4] C. Peterson, Th. Rögnvaldsson, L. Lönnblad, *"JETNET 3.0 - A versatile artificial network package*, Comp. Phys. Comm. 81 (1994) 185–220.

^8B and hep solar neutrino detection by terrestrial experiments

G. I. Karathanou [a] V.Tsikoudi [a] T.S. Kosmas [b]

[a] *Division of Astrophysics and Climatology, University of Ioannina, GR 45110 Ioannina, Greece*

[b] *Theoretical Physics Section, University of Ioannina, GR 45110 Ioannina, Greece*

Abstract

Solar neutrino spectra of ^8B and hep neutrinos produced by pp-chain reactions are analysed for various nuclear detectors in current terrestrial experiments. The well known folding method is applied by employing appropriately simulated solar neutrino distributions and using recently calculated total cross section of neutrino-nucleus processes. We focus on the nuclear target of current experiments like MOON and ICARUS as well to other promising nuclear isotopes.

1 Introduction

The main goal of recent experimental and theoretical investigations on phenomena involving neutrinos is to shed light on the open problems to which neutrinos are absolutely crucial. The astrophysical neutrinos play fundamental role in various astrophysical phenomena, therefore, terrestrial experiments detecting astrophysical neutrinos are highly valuable sources of astrophysical information [1].

In the low neutrino-energy region ($E_\nu < 20$ MeV) the solar neutrinos and the lower energy part of the supernova neutrinos are of fundamental interest. The observation of these neutrinos is often based on their interaction with complex nuclei. The study of the corresponding neutrino-nuclear cross section relies on.

In the present work we focus on phenomena related to the standard neutrino-nucleus interaction processes i.e. the neutral- and charged-current reactions of the astrophysical neutrinos with the nuclear detector. In the first case the coherent channel dominates while in the second several channels leading to specific final number excitations are well pronounced. We currently devote

a special e ort on calculating convoluted total cross sections for the coherent channels, using the neutrino-energy distributions of the ^8B and hep solar neutrino sources.

2 Formalism of neutrino-nucleus elastic scattering

In neutral-current neutrino-nucleus processes, considered in the present work, intermediate energy solar neutrinos are elastically scattered o a nucleus (A,Z) via the exchange of neutral Z_0 bosons. This process can be represented by the reaction

$$\nu + (A, Z) \rightarrow \nu' + (A, Z)^* \tag{1}$$

where A, Z the mass and atomic number of the nuclear target.

At low energies, relevant for solar neutrinos, the nuclear detector can be treated as a point scatterer mostly remaining in its ground state (coherent process). In such cases nucleons respond coherently and the expression for the di erential cross section, in a good approximation, reduces to

$$\frac{d\sigma}{d(cos\Phi)} = G^2 \frac{sin^2\theta_w}{2\pi} A^2 E_\nu^2 (1 + cos\Phi) \tag{2}$$

where Φ is the scattering angle, θ_w the Weinberg angle and E_ν the incoming neutrino energy [2].

Integrating over all directions, the total cross section for even-even target nuclei ($J = 0$) having proton number Z equal to the neutron number N (N=Z), is approximately proportional to N^2. i.e.

$$\sigma \approx 4 \times 10^{-43} N^2 E_\nu^2 cm^2 MeV^{-2} \tag{3}$$

The coherence factor A^2 in Eq. (2), or equivalently the factor N^2 in Eq. (3), describes one of the main advantages of using the elastic scattering channel for studying the neutrino-nucleus inetraction. For practical cases, the cross section corresponding the neutrino absorption can be a factor of $10^3 - 10^4$ larger than that of the neutrino-electron scattering process.

In principle, coherent scattering could be used to detect all of the solar neutrino sources in terrestrial experiments. In practice, the ^8B and hep neutrinos (intermediate energy solar neutrinos) which may have energies up to $15 - 18$ MeV, may be easier to detect since both the coherent scattering cross section

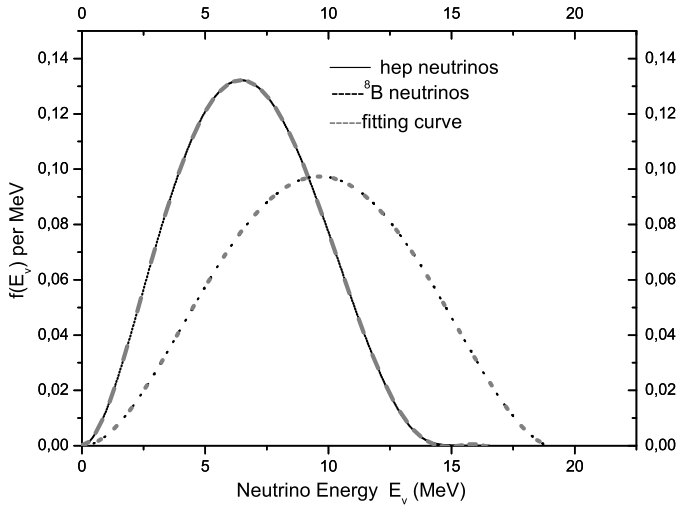

Fig. 1. The solar neutrino energy spectrum for ^8B and hep pp-chain channels.

and the magnitude of the nuclear recoil are proportional to the square of the neutrino energy [3]. While the nuclear models which estimate cross-sections (total or di erential) are not very precise in low energies,$^8B$and hep neutrino energy spectra extends up to 18.8 MeV,which covers the giant resonance region.

In this work we focus on the study of the response of concrete nuclei in the ^8B and hep neutrino energy spectrum. We have chosen a set of four nuclei which are very important from an experiment point of view in ongoing neutrino-detection experiments. Our main goal is to calculate the folded (convoluted) total cross sections of the neutrino spectra of these sources for various reaction channels.

For a specific nuclear detector, the flux averaged cross-section,$\langle\sigma(E_\nu)\rangle$, is expressed as

$$\langle\sigma(E_\nu)\rangle = \int_{E_{thres}}^{\infty} \sigma(E_\nu) f(E_\nu) dE_\nu \tag{4}$$

where E_{thres} is the energy threshold of the neutrino detector.

3 Results and discussion

The energy distributions, $f(E_\nu)$, of ^8B and hep neutrinos predicted by the standard solar model are approximately described by the corresponding curves

Table 1
The coe cients α_κ, of Eq. (6) for the solar neutrino channels ^{8}B- and hep-neutrinos.

Coe cients	^{8}B Neutrinos	hep Neutrinos
α_0	-1.33×10^{-4}	0.00001
α_1	0.0016	-0.00002
α_2	0.01447	0.0042
α_3	-0.0028	-0.00044
α_4	1.78065×10^{-4}	0.00001
α_5	-8.85303×10^{-7}	-2.6641
α_6	-6.11802×10^{-7}	
α_7	4.34285×10^{-8}	
α_8	-1.02536×10^{-9}	

of Fig. 1. These distributions are normalized to unity as

$$\int f(E_\nu) dE_\nu = 1 \tag{5}$$

The analytical polynomial expressions of the form

$$f(E_\nu) = \sum_{\kappa=0}^{8} \alpha_\kappa \, E_\nu^\kappa \,, \tag{6}$$

which fit the above energy distributions shown also in this figure have been estimated by appropriate program. The coe cients α_κ, for each neutrino channel, are listed in Table 1.

Current proposed and ongoing solar neutrino experiments like BOREXINO and SNO+, expect to observe low-rate solar neutrinos as pep and CNO neutrinos significant to study solar physics. Neutrinos will help in understanding the metallicity in the solar core that appears to contrast with recent interpretations of solar surface chemical abundances.

Furthermore, other type of experiments (cryogenic, etc.) are designed with the aim to study coherent neutral-current scattering of neutrinos on nuclei. Such experiments may provide a potential to detect low-energy neutrinos with an excellent energy resolution. Neutrino-induced recoil events may constitute a background to direct dark matter searches [8].

Currently we perform calculations for folded total cross sections of neutrino-nucleus reactions for other interesting neutrino-detection nuclear isotopes such as ^{28}Si and ^{32}S. Such estimations of total cross sections in neutrino-nucleus reactions is of great importance in neutrino detection of existing neutrino detectors and promising nuclear isotopes proposed to be used in future neutrino detection experiments.

References

[1] E. Kolbe and T.S. Kosmas, *Springer Trac. Mod. Phys.* **163**, 199 225 (2000).

[2] A. Drukieer and L. Stodolsky, Phys. Rev. D 30, 2295, (1984).

[3] J. Bahcall, Neutino Astrophysics (Cambridge University, Cambridge) (1989).

[4] W.C. Haxton, P.D. Parker and C.E. Rolfs, nucl-th/0501020v1, (2005).

[5] T.S. Kosmas,*Nucl. Phys. A* **683**, 443 (2001).

[6] G.I.Karathanou, V.Tsikoudi, Th.Liolios and T.S.Kosmas,17^{th} Symposium of The Hellenic Nuclear Physics Society, Ioannina, May, 2008

[7] G.I.Karathanou, V.Tsikoudi, Th.Liolios and T.S.Kosmas, in preparation.

[8] J.D. Vergados and H. Ejiri, 2008, hep-ph/0805.2583v2

Attempted study of the ^{237}Np(n,2n)^{236}Np reaction cross section at 9.5 MeV

M. Diakaki[1], R. Vlastou[1], M. Kokkoris[1], C. T. Papadopoulos[1], A. Tsinganis[1], C. A. Kalfas[2], A. Lagoyannis[2] and G. Provatas[2]

[1]National Technical University of Athens, Department of Physics, Athens, Greece
[2]Institute of Nuclear Physics, NCSR "Demokritos", Aghia Paraskevi, Athens, Greece

Abstract

The cross section measurement of the ^{237}Np(n,2n)^{236}Np reaction has been attempted at an incident neutron energy of 9.5 MeV by means of the activation technique. The neutron beam was produced via the ^{2}H(d,n)^{3}He reaction at the VdG Tandem accelerator of NCSR "Demokritos". It is the second time that this measurement has been tried with a gamma spectroscopy method and the difficulties faced due to the high gamma ray background produced by the sample itself and the fission fragments produced by the irradiation, in combination with the very low intensity of the gamma ray of interest are being reported.

Introduction

The study of neutron threshold reactions on actinide isotopes is of considerable importance for practical applications, especially in reactor physics. The ^{237}Np isotope is a product of the fuel cycle of Uranium in the reactor and so the study of ^{237}Np(n,2n)^{236}Np reaction is of interest for the following reasons: Firstly, it is the major reaction channel in competition with fission that causes the emission of neutrons and, secondly, it leads to the production of the long-lived (80y) ^{232}U (see fig. 1), the decay of which contains a series of short-lived daughter nuclei and emission of 'hard' gamma rays. This explains why the study of this reaction is one of the priorities of the IAEA [1]. Nevertheless, it presents experimental difficulties and very few cross section data exist in literature (see fig. 1). More specifically, only one dataset exists for neutron energies up to 9.5 MeV [2] and a few around 14.5 MeV with large discrepancies among them [3-7]. These datasets are mainly deduced by measuring the α-particles of the ^{236}Pu decay after chemical separation of Pu from Np and using ^{239}Pu/ ^{242}Pu tracers.

The ^{236}Np isotope has two isomers, one short lived, with a half life of 22.5 h, and one long lived, with a half life of 153000 y, but no information exists on which is the ground state [9]. The short lived isomer decays with a probability of 50% to ^{236}U and with a probability of 50% to ^{236}Pu. The long lived isomer decays basically (with a probability of 86.3%) to excited states of ^{236}U (see fig. 2). In the present study, the measurement of the cross section of the production of the short lived isomer was attempted, with use of the activation method, i.e. by bombarding the Np target with the neutron beam and measuring the induced activity off-line with a HPGe detector. The detection of gamma rays from the decay of ^{236}U was chosen, although they have very low intensity: 642.4 and 687.6 keV, with (1.09 ± 0.08)% and (0.30 ± 0.02)%,

respectively [8]. This has already been tried in the past [5], and problems were reported due to the high gamma ray background from the target itself and the fission fragments produced, in combination with the low intensity gamma rays detected. The cross section data that occurred from the gamma ray spectroscopy were ~10% higher than the ones occurred from the measurement of the α-particles of the ^{236}Pu decay.

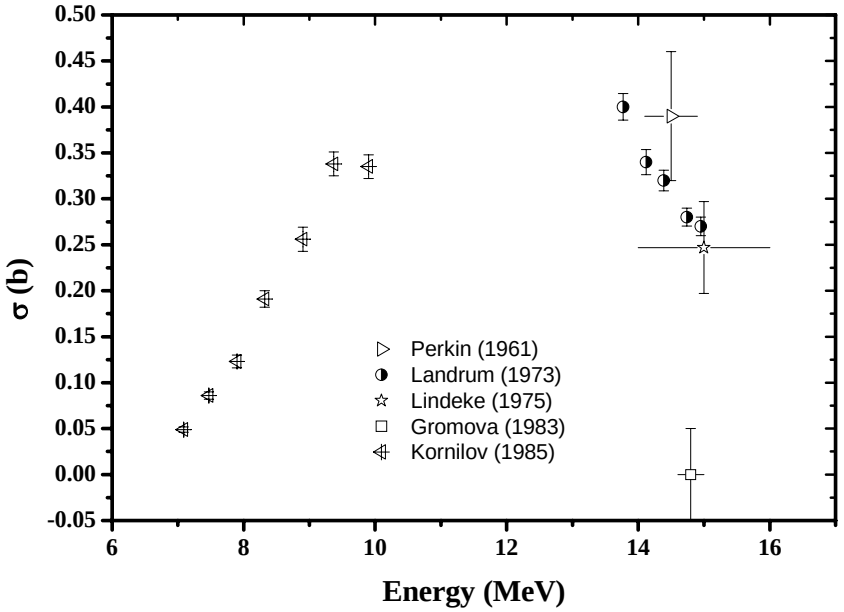

Fig. 1: Existing cross section data for the ^{237}Np(n,2n) reaction (for the production of the short lived isomer) [8].

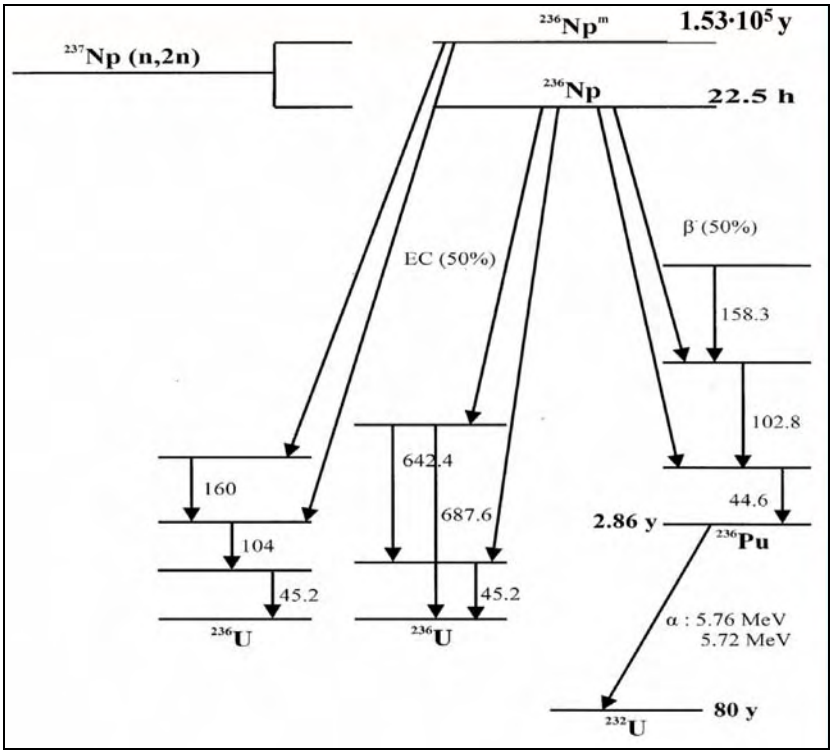

Fig. 2: Decay scheme of the reaction ^{237}Np(n,2n). For the long lived isomer of ^{236}Np only the decay to ^{236}U (the most probable) has been included in the scheme.

Experimental Procedure

The measurement was performed at an incident neutron energy of 9.5 MeV. The quasi-monoenergetic neutron beam was produced via the $^{2}H(d,n)^{3}He$ reaction by bombarding a deuterium gas target with a deuteron beam at currents around 2-2.5 μA. The deuteron beam was provided by the 5.5 MV Tandem Van de Graaff accelerator of the N.C.S.R. "Demokritos". The gas target is fitted with a 5 μm molybdenum entrance foil and a 1 mm Pt beam stop and is constantly cooled with a cold air jet during irradiation to diminish the risk of damage to the Mo foil. The deuterium pressure was set to 1500 mbar. With this setup, the achieved neutron flux was of the order of $\sim 10^{6}$ n/(cm^{2} sec). The absolute flux of the beam was obtained with respect to the $^{27}Al(n,\alpha)^{24}Na$ reference reaction, while its variations during the irradiation were monitored by a BF_3 detector placed at a distance of 3 m from the neutron source.
The sample was 6.892 g of NpO_2 mixed with 40.152 g of S canned in 0.5mm Al and it was provided at the IRMM of Belgium. The nominal radioactivity of the sample was 155MBq. Shielding was considered necessary in order to reduce the high gamma ray background from the target itself and for radioprotection reasons. A mixed Pb-Cd shielding was chosen, thinner at the top and the bottom of the cylindrical sample (1mm Cd - 1mm Pb) and thicker at the side (3mm Cd - 5mm Pb). The shielded sample was placed at a distance of 3 cm from the deuterium gas cell, stacked between two 0.5 mm thick reference Al foils, and was irradiated for ~44 h i.e. for two half lives of the short lived ^{236}Np isomer. The integrated flux, obtained by the front Al foil was $\sim 5 \cdot 10^{10}$ n/cm^{2} (±6%).
The induced activity of the sample and reference foils was measured off line with HPGe detectors of 80% and 56% efficiency respectively.

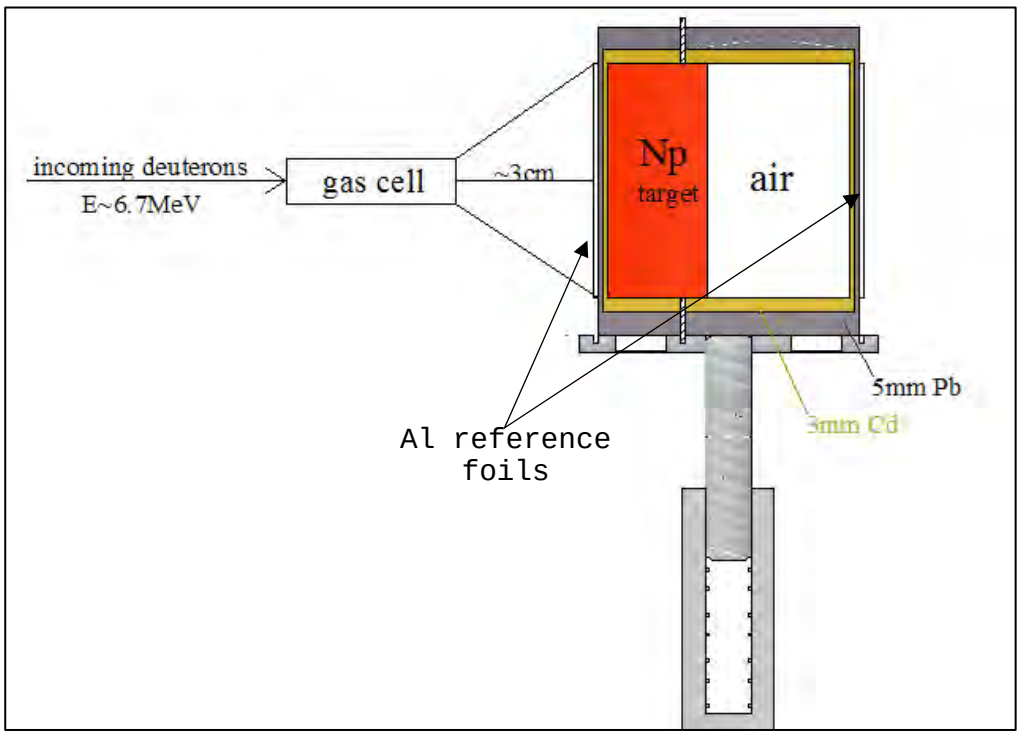

Fig. 3: The setup for the neutron irradiation of the Np target.

Problems faced during the activity measurements

The high radioactivity of the sample itself caused problems during the activity measurements. It was fabricated in 1994, and the reported isotopic purity of ^{237}Np (half -life of $2.14 \cdot 10^6$ years) initially was 99.99%, but at the time of the measurement (2010) the sample was contaminated by the short lived daughter nucleus ^{233}Pa (half -life of 27 d) in secular equilibrium with ^{237}Np, and this caused a severe increase at the already high gamma ray background, even before the irradiation. As a result, additional shielding of the HPGe detector was needed (3mm of Pb absorber was placed in front of the detector) and the sample-to-detector distance was increased to 43 cm. This detection setup caused a severe reduction of the efficiency by 1 order of magnitude for the gamma ray of interest (eff_{642keV}~0.0005) and its attenuation by the shielding which reached ~40% (calculated using gamma ray attenuation data from XCOM [10] and validated with the measurement of the activity of a calibrated ^{152}Eu source with and without the Pb shielding of the detector).

A further problem was the production of additional gamma ray background by the fission fragments in the sample. In figure 4, a calibrated spectrum of the sample before the irradiation is presented, where it becomes clear that the dominant background comes from the ^{233}Pa present in the sample. The gamma ray peaks from the decay of ^{237}Np have energies below ~280 keV and were more efficiently absorbed by the shielding of the sample. In figure 5 a calibrated spectrum of the sample after the irradiation is presented in the energy region above ~450 keV (at lower energies the gamma ray activity of ^{233}Pa prevents the analysis of gamma ray peaks coming from isotopes produced by the irradiation). Most of the peaks are from fission fragments from the fission of ^{237}Np and ^{233}Pa [11,12]. The peak of 642 keV that would occur from ^{237}Np(n,2n)^{236}Np reaction should appear in the position circled on the spectrum. Nevertheless, after a careful analysis of the peak that appears in this position, taking into account the number of counts expected (based on the previous cross section measurements-see fig. 1), the FWHM of the peak in comparison with other neighbor peaks, the background etc., it turned out that it was contaminated.

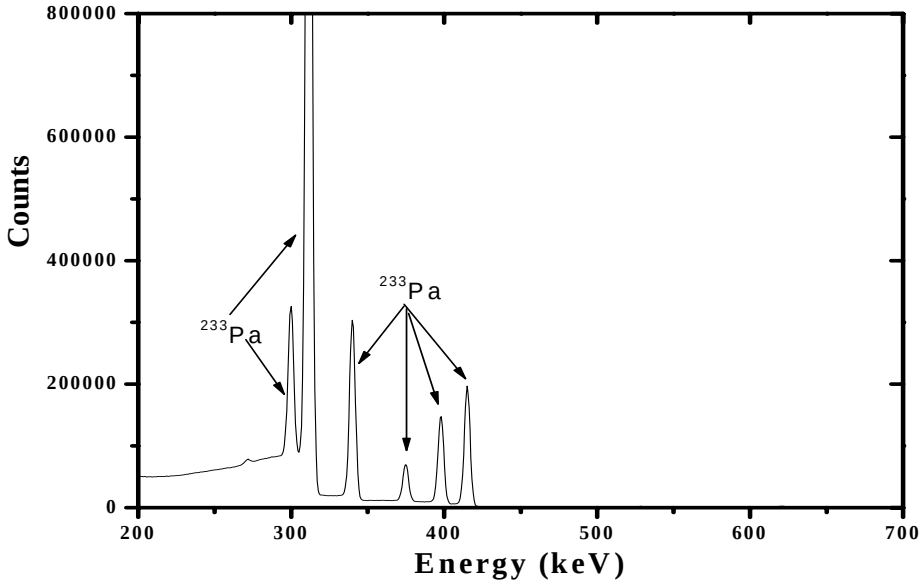

Fig. 4: Calibrated spectrum of the sample before the irradiation.

An effort has been made to check which peak(s) contaminate 642 keV region. The candidate gamma rays mainly were from fission fragments from the actinides in the sample and their daughters as well as isotopes that would occur from other neutron induced reactions in the sample. The selection was made taking into account the decay curves and the intensities of the candidates, and their correlation to other peaks that appear in the spectrum. It turned out that the contamination most probably comes from gamma rays of ^{110}In (possible fission fragment of actinides) and/or from ^{233}Pa(n,γ) ($T_{1/2}$=6.7h) and/or ^{233}Pa(n,2n) ($T_{1/2}$=1.32d) . Other gamma rays from these residual nuclei are also seen in the spectrum. This unfortunate result precludes a conclusion on the accuracy of any possible analysis of the gamma ray peak of interest and thus the extraction of safe results for the cross section measurement has been impossible.

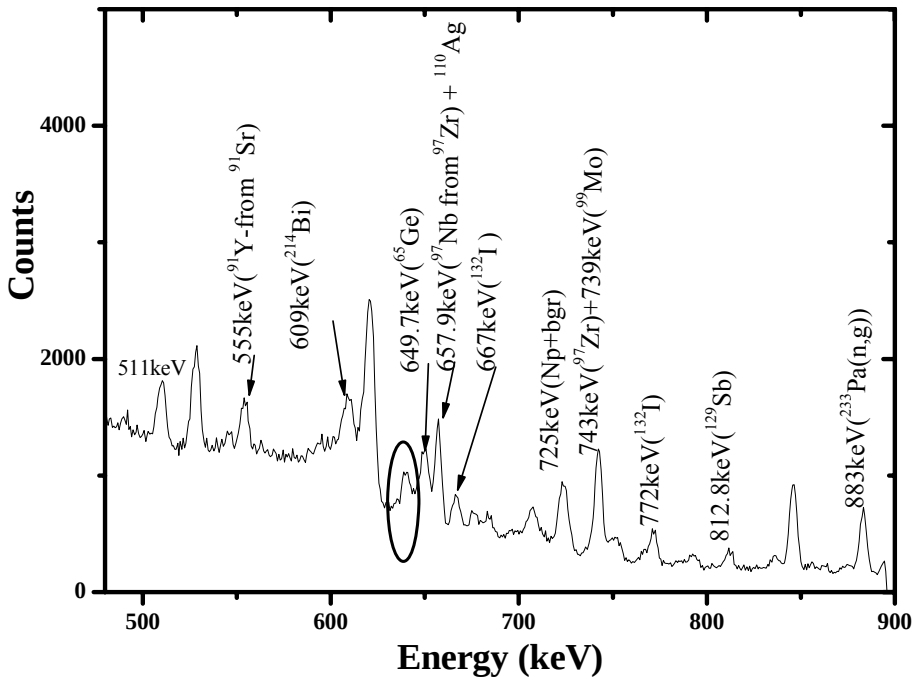

Fig. 5: Calibrated spectrum of the sample after the irradiation ($t_{measurement}$=10h), zoomed in the energy region of interest. The gamma ray energy of interest 642 keV is circled at the spectrum.

Conclusions

The cross section measurement of the ^{237}Np(n,2n)^{236}Np reaction has been attempted at an incident neutron energy of 9.5 MeV by means of the activation technique. The main difficulty faced was the high gamma ray background from the target itself. The main contribution to this background was the gamma rays coming from the short lived daughter nucleus ^{233}Pa which is in secular equilibrium with ^{237}Np. As a result, additional shielding of the detector and increase of the sample-to-detector distance became necessary, which reduced the efficiency of the detector by 1 order of magnitude. Furthermore, contamination of the gamma ray peaks coming from ^{237}Np occurred due to neighboring transitions from the ^{233}Pa content in the target. Thus, chemical separation of ^{233}Pa from ^{237}Np before the irradiation is considered essential

in order to measure cross sections of neutron induced reactions on Np with use of the activation method.

Acknowledgements

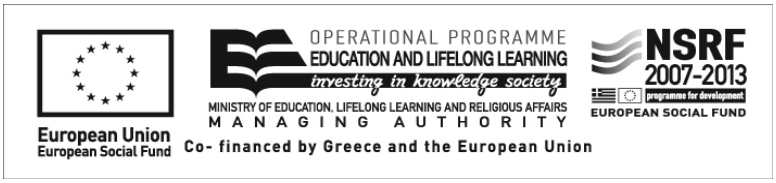

This research has been co-financed by the European Union (European Social Fund – ESF) and Greek national funds through the Operational Program "Education and Lifelong Learning" of the National Strategic Reference Framework (NSRF) - Research Funding Program: Heracleitus II. Investing in knowledge society through the European Social Fund.

References

1. http://www-nds.iaea.org/manread/
2. N.V.Kornilov et al., At.Energ. 58 (1985) 131.
3. J.L.Perkin and R.F.Coleman, Reactor Science and Technology 14 (1961) 69.
4. J.H.Landrum et al., Phys.Rev.C 8 (1973) 1938.
5. K.Lindeke et al., Phys.Rev.C 12 (1975) 507.
6. E. A. Gromova et al., At.Energ. 54 (1983) 108.
7. E. A. Gromova et al., At.Energ. 60 (1986) 68.
8. www.nndc.bnl.gov/**exfor**/
9. K. Wisshak et al., Phys.Rev.C 73, 045807 (2006).
10. www.nist.gov/pml/data/xcom
11. M. N. Namboodiri, N. Ravindran, M. Rajagopalan, M. V. Ramaniah, J. inorg. nucl. Chem. Vol. 30 (1968) 2305-2310.
12. Fission Product Nuclear Data, Vol. I, IAEA-169, Proceedings of a panel on Fission Product Nuclear Data by IAEA, Bologna (1973).

Constraints on the inner edge of neutron star crusts from relativistic nuclear energy density functionals

Ch.C. Moustakidis[1], T. Nikšić[2], G.A. Lalazissis[1], D. Vretenar[2,3], and P. Ring[3]

[1] *Department of Theoretical Physics, Aristotle University of Thessaloniki, 54124 Thessaloniki, Greece*
[2] *Physics Department, Faculty of Science, University of Zagreb, 10000 Zagreb, Croatia*
[3] *Physik-Department der Technischen Universität München, D-85748 Garching, Germany*

Abstract

The transition density n_t and pressure P_t at the inner edge between the liquid core and the solid crust of a neutron star are analyzed using the thermodynamical method and the framework of relativistic nuclear energy density functionals. Starting from a functional that has been carefully adjusted to experimental binding energies of finite nuclei, and varying the density dependence of the corresponding symmetry energy within the limits determined by isovector properties of finite nuclei, we estimate the constraints on the core-crust transition density and pressure of neutron stars: 0.086 fm$^{-3} \leq n_t < 0.090$ fm^{-3} and 0.3 MeV fm$^{-3} < P_t \leq 0.76$ MeV fm^{-3} [1].

Keywords: Nuclear density functional, Equation of state, Neutron star crust.

Neutron stars are extraordinary astronomical laboratories for the physics of dense neutron-rich nuclear matter [2]. They consists of several distinct layers: the atmosphere, the surface, the crust and the core. The latter, divided into the outer core and inner core, has a radius of approximately 10 km and contains most of the star's mass. The crust, of ≈ 1 km thickness and containing only a few percent of the total mass, can also be divided into the outer crust and inner crust. One of the most important prediction of a given equation of state (EOS) is the location of the inner edge of a neutron star crust. The inner crust comprises the region from the density at which neutrons drip-out of nuclei, to the inner edge separating the solid crust from the homogeneous liquid core. At the inner edge, in fact, a phase transition occurs from the high-density homogeneous matter to the inhomogeneous matter at lower densities.

All theoretical studies have shown that the core-crust transition density and pressure are very sensitive to the density dependence of the nuclear matter symmetry energy. In particular, it has been shown that the $E_{sym}(n)$ constrained in the same sub-saturation density range as the neutron star crust by the isospin diffusion data in heavy-ion collisions at intermediate energies [3, 4], limits the

transition density and pressure to 0.040 fm$^{-3} \leq n_t \leq$ 0.065 fm^{-3} and 0.01 MeV fm$^{-3} \leq P_t \leq$ 0.26 MeV fm^{-3}, respectively. In the present work we apply a class of relativistic density functionals in a systematic investigation of the transition density n_t and pressure P_t at the inner edge separating the liquid core from the solid crust of neutron stars by employing the thermodynamical method.

The core-crust interface corresponds to the phase transition between nuclei and uniform nuclear matter. The uniform matter is nearly pure neutron matter, with a proton fraction of just a few percent determined by the condition of beta equilibrium. Weak interactions conserve both baryon number and charge [5], and from the first low of thermodynamics, at temperature $T = 0$:

$$\mathrm{d}u = -P\mathrm{d}v - \hat{\mu}\mathrm{d}q, \tag{1}$$

where u is the internal energy per baryon, P is the total pressure, v is the volume per baryon ($v = 1/n$ where n is the baryon density) and q is the charge fraction ($q = x - Y_e$ where x and Y_e are the proton and electron fraction in baryonic matter respectively). The stability of the uniform phase requires that $u(v, q)$ is a convex function [6]. This condition leads to the following two constraints for the pressure and the chemical potential

$$-\left(\frac{\partial P}{\partial v}\right)_q - \left(\frac{\partial P}{\partial q}\right)_v \left(\frac{\partial q}{\partial v}\right)_{\hat{\mu}} > 0, \tag{2}$$

$$-\left(\frac{\partial \mu}{\partial q}\right)_v > 0. \tag{3}$$

It is assumed that the total internal energy per baryon $u(v, q)$ can be decomposed into baryon (E_N) and electron (E_e) contributions

$$u(v, q) = E_N(v, q) + E_e(v, q). \tag{4}$$

In this work the well know parabolic approximation is used for the baryon energy $E_N(v, q)$

$$E_N(v, q) \simeq V(v) + E_{sym}(v)(1 - 2x)^2 \ . \tag{5}$$

The condition of charge neutrality $q = 0$ requires that $x = Y_e$. This is the case we will consider in the present study. After some algebra, it can be shown that the conditions (2) and (3) are equivalent to

$$\begin{aligned} C_I(n) &= n^2\frac{\mathrm{d}^2V}{\mathrm{d}n^2} + 2n\frac{\mathrm{d}V}{dn} \\ &+ (1-2x)^2\left[n^2\frac{\mathrm{d}^2E_{sym}}{\mathrm{d}n^2} + 2n\frac{\mathrm{d}E_{sym}}{\mathrm{d}n} - 2\frac{1}{E_{sym}}\left(n\frac{\mathrm{d}E_{sym}}{\mathrm{d}n}\right)^2\right] > 0, \end{aligned} \tag{6}$$

$$C_{II}(n) = -\left(\frac{\partial q}{\partial \hat{\mu}}\right)_v = \frac{1}{8E_{sym}} + \frac{3Y_e}{\hat{\mu}} > 0. \tag{7}$$

The second inequality (7) is usually valid. The transition density n_t is determined from the first inequality (7). For a given EOS, the quantity $C_I(n)$ is

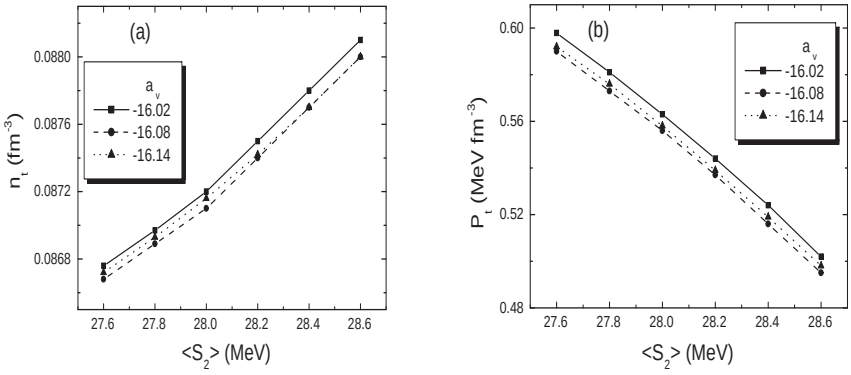

Figure 1: The transition density n_t (a), and the transition pressure P_t (b), as functions of $\langle S_2 \rangle$ for three values of the nuclear matter volume energy coefficient a_v.

plotted as a function of the baryonic density n, and the equation $C_I(n_t) = 0$ defines the transition density n_t.

The framework of nuclear energy density functionals (NEDF) provides, at present, the most complete microscopic approach to the rich variety of structure phenomena in medium-heavy and heavy complex nuclei, including regions of the nuclide chart far from the valley of β-stability. By employing global functionals parameterized by a set of ≈ 10 coupling constants, the current generation of EDF-based models has achieved a high level of accuracy in the description of ground states and properties of excited states, exotic unstable nuclei, and even nuclear systems at the nucleon drip-lines [7]. Starting from the relativistic energy density functional DD-PC1, in this work we examine the sensitivity of the core-crust transition density n_t and pressure P_t of neutron stars, on the density dependence of the corresponding symmetry energy of nucleonic matter.

Fig. 1 displays the values of the transition density n_t (in fm^{-3}) and transition pressure P_t (in Mev fm^{-3}), calculated in the thermodynamical model, as functions of $\langle S_2 \rangle$ for three values of the nuclear matter volume energy coefficient a_v. For a given value of the parameter a_v, the values of n_t rise with increasing $\langle S_2 \rangle$, whereas the opposite is found for the values of P_t. For the considered interval of $\langle S_2 \rangle$, however, the changes are small. An increase of 3.5% in $\langle S_2 \rangle$ leads to an increase of 1.5% in the value of n_t. The transition pressure exhibits a somewhat more pronounced dependence (the corresponding decrease is around $16 - 20\%$). Both n_t and P_t display a negligible dependence on a_v, even though $a_v = -16.02$ MeV and $a_v = -16.14$ MeV lie outside the interval of values for which the absolute deviations between calculated and experimental masses are smaller than 1 MeV.

In Fig. 2 we plot the transition pressure P_t as a function of the transition density n_t for the three sets of nuclear matter EOS and symmetry energy

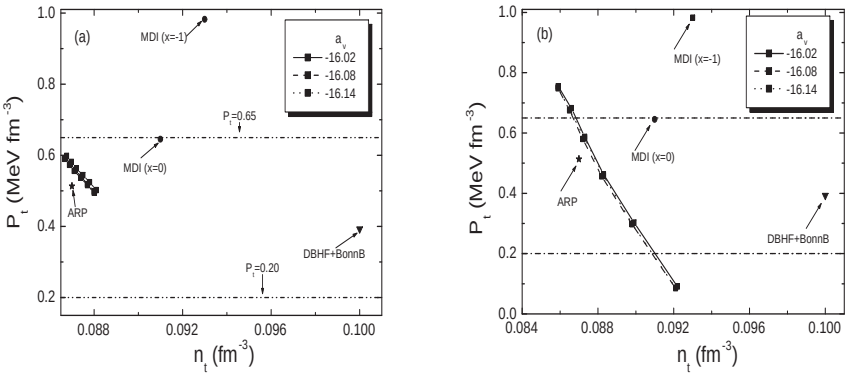

Figure 2: (a) The transition pressure P_t as a function of the transition density n_t. For a fixed value of the symmetry energy at saturation $a_4 = 33$ MeV, and three values of the nuclear matter volume energy coefficient a_v, the parameter $\langle S_2 \rangle$ is varied in the interval between 27.6 MeV and 28.6 MeV. (b) The same but for fixed $\langle S_2 \rangle = 27.8$ MeV, and the symmetry energy at saturation in the interval 30 MeV $\leq a_4 \leq$ 35 MeV.

described above, in comparison with results of recent calculations performed using an isospin and momentum-dependent modified Gogny effective interaction (MDI) [8]. The different values of the parameter x in the MDI model correspond to various choices of the density dependence of the nuclear symmetry energy. In addition to the MDI EOS, in Fig. 2 we also show the result obtained by Akmal et al. [9] with the $A18 + \delta v + UIX^*$ interaction (ARP), and the value obtained in the recent Dirac-Brueckner-Hartree-Fock (DBHF) calculation [10] with the Bonn B One-Boson-Exchange (OBE) potential (DBHF+Bonn B) [11]. We notice that by keeping $\langle S_2 \rangle$ constant and varying a_4 in the interval between 30 MeV and 35 MeV, the density dependence of the symmetry energy can be modified in a controlled way, i.e. the corresponding energy density functionals still reproduce ground-state properties of finite nuclei in fair agreement with data.

In Fig. 3 we display the corresponding values of the transition density n_t (in fm^{-3}) and transition pressure P_t (in Mev fm^{-3}) as functions of a_4 for three values of the nuclear matter volume energy coefficient a_v. The transition pressure P_t as a function of the transition density n_t for the three sets of nuclear matter EOS and symmetry energy is also plotted.

Finally, in Fig. 4 we compare the present prediction for the range of values of the transition density n_t with the results of Horowitz and Piekarewicz who, in Ref. [12], also used the framework of relativistic mean-field effective interactions to study the relationship between the neutron-skin thickness of a heavy nucleus and the properties of neutron star crusts. For the solid crust of a neutron star, the effective RMF interactions were used in a simple RPA calculation of the transition density below which uniform neutron-rich matter becomes unstable

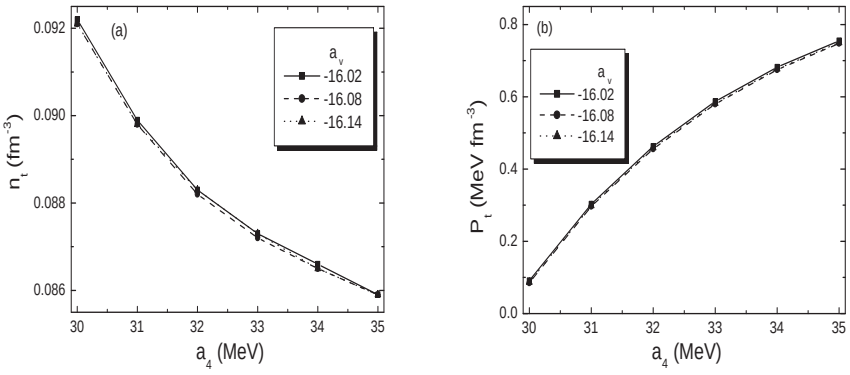

Figure 3: The transition density n_t (a), and the transition pressure P_t (b), as functions of the symmetry energy at saturation density a_4, for three values of the nuclear matter volume energy coefficient a_v.

against small amplitude density fluctuations. The resulting transition densities are plotted in Fig. 4 as a function of the predicted difference between neutron and proton *rms* radii in ^{208}Pb. This inverse correlation was parameterized [12]

$$n_t \approx 0.16 - 0.39(R_n - R_p), \tag{8}$$

with the skin thickness expressed in fm. In the present analysis, using a different type of relativistic effective interactions and varying the density dependence of the symmetry energy by explicitly modifying $\langle S_2 \rangle$ or a_4, we find a much weaker dependence n_t on the neutron-skin thickness of ^{208}Pb.

The framework of relativistic nuclear energy functionals has been employed to analyze and constrain the transition density n_t and pressure P_t at the inner edge between the liquid core and the solid crust of a neutron star, using the thermodynamical method. Starting from a class of energy density functionals carefully adjusted to experimental masses of finite nuclei, we have examined the sensitivity of the core-crust transition density n_t and pressure P_t on the density dependence of corresponding symmetry energy of nucleonic matter. Instead of an unrestricted variation of the parameters of the Taylor expansion of the symmetry energy around the saturation density of nuclear matter, that is the slope parameter and the isovector correction to the compression modulus, we modify the density dependence by varying the value of the nuclear symmetry energy at a point somewhat below the saturation density $\langle S_2 \rangle$ (the symmetry energy at $n = 0.12$ fm^{-3}), and at the saturation density a_4 (the symmetry energy at $n = 0.152$ fm^{-3}, the saturation density for this class of relativistic density functionals). In the former case, for a given value of the volume energy coefficient a_v, $\langle S_2 \rangle$ has been varied in a rather narrow interval of values 27.6 MeV $\leq \langle S_2 \rangle \leq$ 28.6 MeV determined by a fit to the experimental binding

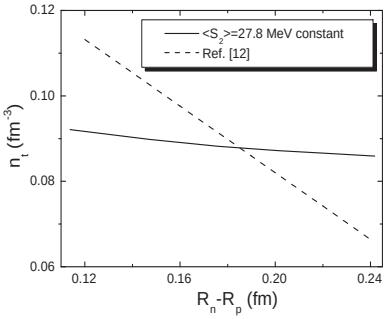

Figure 4: The transition density n_t as function of the neutron-skin thickness $R_n - R_p$ of ^{208}Pb. The values of n_t calculated using the thermodynamical model in the present work (solid), are compared with those of Ref. [12] (see text for description).

energies. Both n_t and P_t display a negligible dependence on a_v. The variation of the parameter a_4 has been in the range of values: 30 MeV $\leq a_4 \leq$ 35 MeV, allowed by the empirical thickness of the neutron-skin and excitation energies of isovector dipole resonances, for a fixed value of $\langle S_2 \rangle$. Again, there is virtually no dependence on a_v, but now both n_t and P_t span much wider intervals.

References

[1] Ch.C. Moustakidis, T. Nikšić, G.A. Lalazissis, D. Vretenar, and P. Ring, Phys. Rev. C **81**, 065803 (2010).

[2] P. Haensel, A.Y. Potekhin, and D.G. Yakovlev, *Neutron Stars 1: Equation of State and Structure* (Springer-Verlag, New York, 2007).

[3] M.B. Tsang et al., Phys. Rev. Lett. **92**, 062701(2004).

[4] L.W. Chen, C.M. Ko, and B.A. Li, Phys. Rev. Lett. **94**, 032701 (2005).

[5] J.M. Lattimer and M. Prakash, Phys. Rep. **442**, 109 (2007).

[6] H.B. Callen, Thermodynamics, Wiley, New York, 1985.

[7] T. Nikšić, D. Vretenar, and P. Ring, Phys. Rev. C **78**, 034318 (2008).

[8] J. Xu, L.W. Chen, B.A. Li, and H.R. Ma, Astrophys. J. **697**, 1549 (2009).

[9] A. Akmal, V.R. Pandharipande, and D.G. Ravenhall, Phys. Rev. C **58**, 1804 (1998).

[10] F. Sammarruca and P. Liu, Phys. Rev. C **79**, 057301 (2009).

[11] R. Machleidt, Adv. Nucl. Phys. **19**, 189 (1989).

[12] C.J. Horowitz and J. Piekarewicz, Phys. Rev. Let. **86**, 5647 (2001).

Application of RBS and NRA for the Investigation of Corrosion Resistance of Nitrogen-Implanted Steel.

F. Noli[1*], P. Misaelides[1], A Lagoyannis[2], J.-P. Rivière[3]

[1] *Department of Chemistry, Aristotle University, GR-54124 Thessaloniki, Greece*
[2] *Tandem Accelerator Laboratory, Nuclear Physics Institute, NCSR Demokritos, GR-15310 Aghia Paraskevi- Attiki,Greece*
[3] *Université de Poitiers, Laboratoire de Physique des Matériaux UMR6630-CNRS, 86960 Chasseneuil, Futuroscope Cedex, France*

Abstract

Austenitic stainless steel AISI 304L was implanted with low energy, high current nitrogen ions at moderate temperatures extracted from a Kaufman type ion source (Extraction voltage: 1.2 keV; Extracted current: 1 mA/cm^2; Ion dose: about 4x10^{19} ions /cm^2). The temperature during the implantation (duration 1 hour) was 400 and 500 ^{o}C respectively for the two series of samples prepared. The characterization of the samples by X-Ray Diffraction, Transmission Electron Microscopy and Scanning Electron Microscopy showed that a metastable fcc solid solution with a high nitrogen content (about wt. 30%) was formed resulting in an increase of its Vickers hardness. Rutherford Backscattering Spectrometry (E_d: 1.75 MeV) was applied in combination with Nuclear Reaction Analysis (NRA) in order to obtain information about the N-, O- and C- depth distribution in the near-surface layers of the samples. The nitrogen depth distribution was determined using the $^{14}N(d,\alpha)^{12}C$ and the $^{14}N(d,p)^{15}N$ nuclear reactions whereas the oxygen and carbon ones by the $^{16}O(d,p)^{17}O$ and $^{12}C(d,p)^{13}C$ (E_d: 1.35 MeV). Investigation of the corrosion behaviour of the samples was performed under strong aggressive conditions (hydrochloric acid 2% at 50 ^{o}C) using electrochemical techniques (potentiodynamic polarization and cyclic voltammetry). The samples implanted at 400 ^{o}C exhibited remarkable resistance to corrosion compared to those implanted at 500 ^{o}C and the untreated material. This could be attributed to the modified surface region and its high nitrogen content.

Keywords: N-implantation; RBS; NRA; corrosion; stainless steel

[*]*Corresponding author: Address: Department of Chemistry, Aristotle University, GR-54124 Thessaloniki, Greece*
Tel.:+30 2310 997997, Fax .:+30 2310 997753, E-mail: noli@chem.auth.gr

1. INTRODUCTION

The high Cr content AISI 304 austenitic stainless steel (Cr 20/Ni 10/Fe) is, due to its excellent corrosion resistance, a material with a wide spectrum of industrial applications. However, it presents poor tribological properties such as hardness and wear resistance. For these reason different techniques have been developed for the

improvement of its surface mechanical properties [1-3]. Nitrogen-ions have widely been used in the past in order to increase the hardness of metallic alloys. However, the austenitic steels are known as materials difficult to be nitrided because the nitridation requires temperatures higher than 450 ^{o}C. At these temperatures CrN precipitation takes place leading to a Cr-depleted surface which is susceptible to corrosion and the material loses its stainless character. On the other hand, recently nitridation treatments performed at moderate temperatures (~400 ^{o}C) were found to be beneficial for improving the mechanical properties of steels simultaneously enhancing their corrosion resistance. These improvements are associated with the formation of a saturated nitrogen solution (N-content about 20 %) and the nitrogen diffusion into the bulk [4-9]. Of special interest among these nitridation processes is the Low Energy-High Flux Nitrogen-Implantation, which has already been successfully applied to the hardness and corrosion resistance improvement of austenitic stainless steels [5,10-14].

The majority of the publications, which appeared in the literature and concern the influence of the nitridation on the corrosion of stainless steels, are related with studies performed in chlorides solutions (especially NaCl). The published data in these cases show an enhancement of the corrosion resistance of the steels after the N-implantation [15-26].

The aim of this work was to investigate the influence of the nitridation temperature of AISI 304 stainless steel (400 and 500 ^{o}C respectively) on its corrosion behavior.

2. EXPERIMENTAL PART

2.1. Sample preparation

The AISI 304L stainless steel (Fe, 18.54 Cr, 10.46 Ni, 1.69 Mn, 0.65 Si, 0.016 C) samples used in this work had the form of disks of 1.6 cm diameter and 1.0 mm thickness. Prior to implantation the surface of the samples was mechanically polished using silicon carbide paper (down to 2400 grid) and diamond paste (down to 1.0 μm) leading to a final roughness of about 0.05 μm. Finally, the samples were ultrasonically degreased in acetone and rinsed in 96% ethanol.

The low-energy high-flux nitrogen implantation was performed using a Kaufmann type ion source. The energy of the extracted nitrogen-ions ($N^{2+,}$ N^{+}) was 1.2 keV and the current density of about 1 mA/cm^2 providing in 1 hour a total dose of 3,5x10^{19} ions/cm^2. The temperature during the implantation, measured by a thermocouple attached on the back of the samples, was 400 and 500^{o}C for the two series of implantations performed.

The corrosion resistance of the implanted samples was investigated by potentiodynamic polarization and cyclic voltammetry in 2% HCl at 50^{o}C using rapid and slow scan measurements. The tests were performed in an AUTOLAB Potentio-Galvanostat (ECO CHEMIE, Netherlands) interfaced to a computer and recorder. The conventional three-electrode cell (EG&G PAR model) used for all measurements, was equipped with a saturated calomel electrode as a reference electrode, a graphite one as an auxiliary electrode and a holder leaving only the one side of the specimen exposed to the corroding medium. Experiments were performed in de-aerated

solution after 5 min stabilisation and scan starting from the open circuit potential in the region -400 up to 1000 mV using the following scan rate; rapid scan rate = 25 mV/sec and slow scan rate = 0.25 mV/sec. In all cases the electrolyte volume was 800 ml and the sample surface in contact with the testing solution 1 cm^2 [27].

2.2 Characterization of the coatings

The phase composition and the structure of the coatings were investigated by X-Ray Diffraction (XRD), Transmission and Scanning Electron Microscopy (TEM, SEM) whereas their Vickers micro-hardness was also determined [5, 14].
Rutherford Backscattering Spectrometry (RBS) at the 5.5 MV Tandem Accelerator of the NCSR Demokritos/ Athens using deuterons of 1.75 MeV energy (scattering angle: 170^o, solid angle: 2.54×10^{-3} sr), was applied in combination with Nuclear Reaction Analysis (NRA) in order to obtain information about the N-, O- and C- depth distribution in the near-surface layers of the samples. The nitrogen depth distribution was determined using the $^{14}N(d,\alpha)^{12}C$ and the $^{14}N(d,p)^{15}N$ nuclear reactions whereas the oxygen and carbon ones by the $^{16}O(d,p)^{17}O$ and $^{12}C(d,p)^{13}C$ reactions respectively (E_d:1.35 MeV, scattering angle: 150^o, solid angle: 0.34×10^{-3} sr). The beam current on the target during the measurements did not exceed 10 nA, while the beam spot size was 1.5×1.5 mm^2. The analysis of the data was performed by means of the SIMNRA simulation code [28] using cross sections from the IBANDL nuclear data library [29]. The overall uncertainty of the determination was estimated to be ca. 8%.

3. RESULTS AND DISCUSSION

The results of the XRD investigation (not presented here) led to the conclusion that in the case of 400°C N-implantation the incorporation of the nitrogen atoms into interstitial positions resulted in the formation of an nitrogen solid solution in the initial austenitic steel matrix so called “expanded austenite” or γ_N phase of fcc crystallographic structure. This induced an expansion of the lattice producing compressive residual stresses and micro-distortions in the N-implanted layer being responsible for the hardness increase. In the 500°C N-implantation CrN and α-FeNi phases were formed because Fe, Cr and Ni atoms were allowed to diffuse. The lattice parameter deduced from the XRD peaks was found to be expanded and the Vickers micro-hardness, compared to that of the non-implanted material, four and five times higher for the two series of samples [5,14].
The oxygen, carbon and nitrogen content in the near-surface layers of the non-implanted and implanted at 400 and 500^o samples was measured by NRA. In the case of the sample implanted at 400 ^{o}C the oxygen peaks were more intense indicating the formation of a surface oxide layer whereas the nitrogen found to be less diffused. Several authors have reported that the oxygen absorbed during nitrogen implantation is considered to act as barrier to nitrogen transfer into the bulk [7-8, 12, 14]. The carbon concentration for all the samples was found to be between 1.2 and 1.5 % with a maximum depth range of ca. 1.0 μm.
The nitrogen distribution obtained by the SIMNRA simulation of the NRA spectrum (s. Fig. 1) also allows an estimation of the thickness of the modified surface layer (ca.

4 and 6 μm for the samples implanted at 400 and 500 ^{o}C respectively). In Fig. 1 the presence of peaks corresponding to particles emitted by the $^{14}N(d,\alpha_1)^{12}C$, $^{14}N(d,p_0)^{15}N$ and the $^{14}N(d,\alpha_0)^{12}C$ nuclear reactions is obvious.

As demonstrated from the polarization measurements the corrosion resistance of the samples implanted at 400 ^{o}C was significantly enhanced. In the case of the samples implanted at 500 ^{o}C a slight improvement of the corrosion resistance was observed compared to that of the non-implanted material.

Figure 2 presents the NRA spectra of the samples implanted at 400 and 500 ^{o}C after the corrosion attack showing increased oxygen- and carbon concentration in the sample implanted at 500^{o}C. This could be attributed to the higher corrosion rate due to the dissolution and oxidation of the main steel constituents especially Fe and Cr. Concerning the nitrogen distribution no differences were observed compared to the spectra of the non-corroded samples.

The increased corrosion tendency, but lower compared to that of the non-implanted steel, exhibited by the sample implanted at 500 ^{o}C can be observed in Fig. 3. The extended corrosion attack in this case is indicated by the missing edge appearing in the region of channels 270 to 330 in the RBS data presented in this figure. No similar effects appeared in the corresponding spectrum of the sample implanted at 400 ^{o}C (s. Fig. 4). This means that the implanted samples at 400 ^{o}C exhibited a remarkable resistance to the corrosive medium.

The SEM micrographs after the corrosion attack showed a long-standing and uniformly corroded surface of the implanted samples at 400 ^{o}C whereas a thick porous corroded zone with large pits was observed on the non-implanted and the sample implanted at 500 ^{o}C. The Cr-concentration was found to be reduced across this layer (about 10%) demonstrating a Cr-depletion in the surface region due to CrN precipitation taking place during the implantation at high temperatures.

The beneficial effect of N-implantation on the corrosion behaviour of stainless steel could be associated to structural effects (e.g. formation of an amorphous layer) and mainly assigned to chemical reasons as reported in the literature [19-20, 22]. Osozawa and Okata suggested that nitrogen reacts with H^{+}-ions in the pits leading to the formation of NH_3 and NH_4^{+}. The reaction causes a decrease of the acidity in the pits and the repassivation is thereby enhanced [26]. The results of this work demonstrated an improvement of the corrosion resistance of the N-implanted steel samples associated with the thick nitrogen-containing modified surface region. Even in the case of the implantation at 500 ^{o}C , despite the CrN precipitation and the Cr-depletion, an improved corrosion resistance, due to the iron nitrides protecting the substrate, was also observed under the testing conditions.

4. Conclusions

The high-dose low-energy nitrogen implantation of AISI 304L steel at 400 ^{o}C significantly increases the surface hardness and the corrosion resistance of the material in 2% HCl solution. These effects can be associated with radiation damage and the segregation of nitrogen at the grain boundaries.

The implantation at 500 ^{o}C leads to a more drastically increased surface hardness of the AISI 304L steel but the Cr-depletion due to the CrN precipitation taking part at

this temperature influences the corrosion resistance of the material which was found to be low but better than that of the non-implanted steel.

5. Acknowledgements

The assistance of the staff of the Tandem Accelerator Laboratory of the Nuclear Physics Institute of the NCSR Demokritos (Athens/GR) is thankfully acknowledged.

6. References

1. G. Dearneley, Nucl. Instr. and Meth. B 50 (1990) 358.
2. R. Wei, P. J. Wilbur, O. Özturk, D.L. Williamson, Nucl. Instr. and Meth. B 59/60 (1991) 731.
3. L.J. Bredell, J.B. Malherbe, Thin Solid Films 228 (1993) 267.
4. T. Bell, J. Phys. D. 25 (1991) 297.
5. S. Picard, J.B. Memet, R. Sabot, J.L. Grosseau-Poussard, J.P. Rivière, R. Meilland, Mater. Sci. Engin. A303 (2001) 163.
6. C.X. Li, T. Bell Corros. Sc. 48 (2006) 2036.
7. S. Parascandola, O. Kruse, W. Möller, Appl. Phys. Lett. 75 (1999) 1851.
8. C.A. Figueroa, F. Alvarez, Surf. Coat. Technol. 200 (2005) 498.
9. T.Christiansen, M.A.J.Somers, Scripta Materiala, 50, (2004) 35.
10. D.L. Williamson,O. Özturk,R. Wei,P.J. Wilbur, Surf. Coat. Technol. 65(1994)15.
11. R. Wei, B. Shogrin, P.J. Wilbur, O. Ozturk, D.L. Williamson, I. Ivanov, E. Metin, J. Tribol. 116 (1994) 870.
12. R. Wei, Surf. Coat. Technol. 83 (1996) 218.
13. G.Abrasonis, J.P.Rivière, C.Templier, A.Declemy, L.Pranevicius, X.Milhet, J. Appl. Phys. 97 (2005), 083531.
14. F. Pedraza, J. L. Grosseau-Poussard, G. Abrasonis, J.P. Rivière, J.F. Dinhut, J. Appl. Phys. 94 12 (2003) 7509.
15. J.P. Hirvonen, D. Ruck, S. Yan, A. Mahiuot, P. Torri, J. Likonen, Surf. Coat. Technol. 74-75 (1995) 760.
16. T. Weber, L.de Wit, F.W. Saris, A. Koniger, B. Rauschenbach, G.K.Wolf, S. Krauss, Mater. Sc. Engin. A199 (1995) 205.
17. J. Flis, J. Mankowski, T. Zakcrozymski, T. Bell, S. Janosi, Z. Kolozswary, B. Narowska, Corros. Sc. 41 (1999) 1257.
18. Lei MK., Zhu X.M., Surf. Coat. Technol. 201 15 (2007) 6865.
19. R.F.A. Jargelius-Petterson, Cor. Sci. 41 (1999) 1639.
20. I. Olefjord, L. Wegrelius, Cor. Sci. 38 7(1996) 1203.
21. H-C. Choe, Surf. Coat. Technol. 112 (1999) 299.
22. X. B. Tian, S.C. Kwork, L.P. Wang, P.k. Chu, Mater. Sc. Engin. A326 (2002) 348.
23. V. Muthukumaran, V. Selladurai, S. Nandhakumar, M. Senthilkumar, Mater. Des. 31 (2010) 2813.
24. C.M. Abrieu, M.J. Cristobal, P. Merino, X.R. Novoa, G. Pena, M.C. Perez, Electrochim. Act. 53 (2008) 6000.
25. J.H. Liang, C.S. Wang, W.F. Tsai, C.F. Ai, Surf. Coat. Technol. 1(2007) 6638.
26. K. Osozava, N. Okato, in:Proc. USA-Japan Seminar:Passivity and its Breakdown on Iron and Iron-Based Alloys, Honolulu, NACE 1976, p.135.

27. Laboratory Corrosion Tests and Standards (Eds. Haynes and Baboian), American Society for Testing and Materials, Philadelphia, 1985.
28. M. Mayer, 'SIMNRA User's Guide 6.0', Max Plank Institut für Plasmaphysik, Garching, Germany, 2006.
29. Ion Beam Analysis Nuclear Data Library, http://amdu1.iaea.org/ibandl/.

Figure captions

Fig.1 NRA spectrum presenting the N-distribution of the sample implanted at 400 ^{o}C.

Fig.2 NRA spectra of the implanted samples at 400 and 500 ^{o}C after the corrosion tests.

Fig.3 RBS-spectra of the implanted samples at 500 ^{o}C, before and after the corrosion treatment.

Fig.4 RBS-spectra of the implanted samples at 400 ^{o}C, before and after the corrosion treatment.

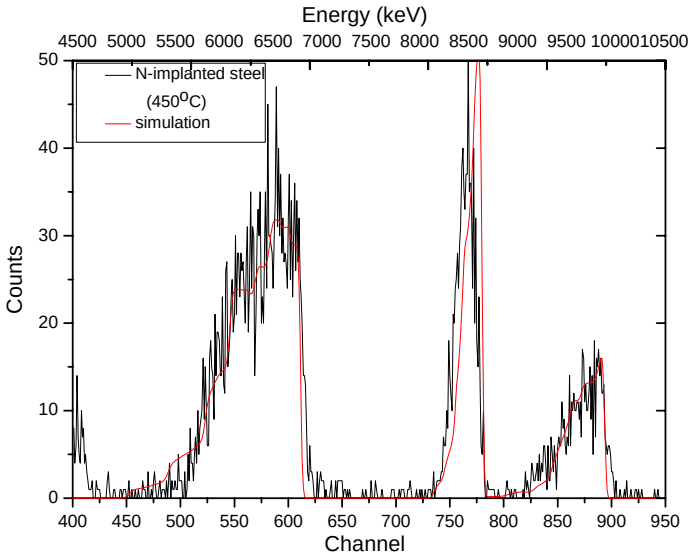
Energy (keV)
4500 5000 5500 6000 6500 7000 7500 8000 8500 9000 9500 1000010500
N-implanted steel
(450°C)
simulation
Counts
Channel
0 10 20 30 40 50
400 450 500 550 600 650 700 750 800 850 900 950

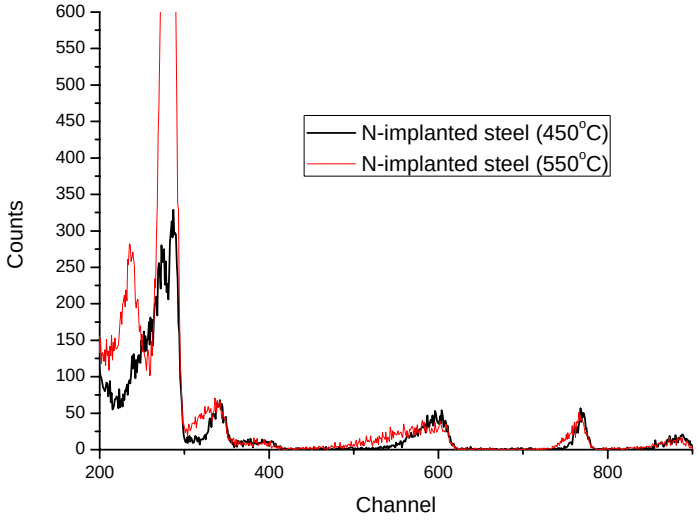
N-implanted steel (450°C)
N-implanted steel (550°C)
Counts
Channel
0 50 100 150 200 250 300 350 400 450 500 550 600
200 400 600 800

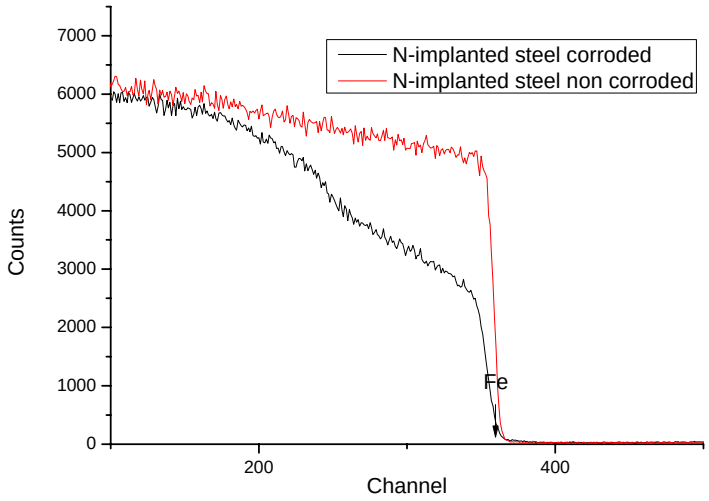
N-implanted steel corroded
N-implanted steel non corroded
Counts
Channel
Fe
0
1000
2000
3000
4000
5000
6000
7000
200
400

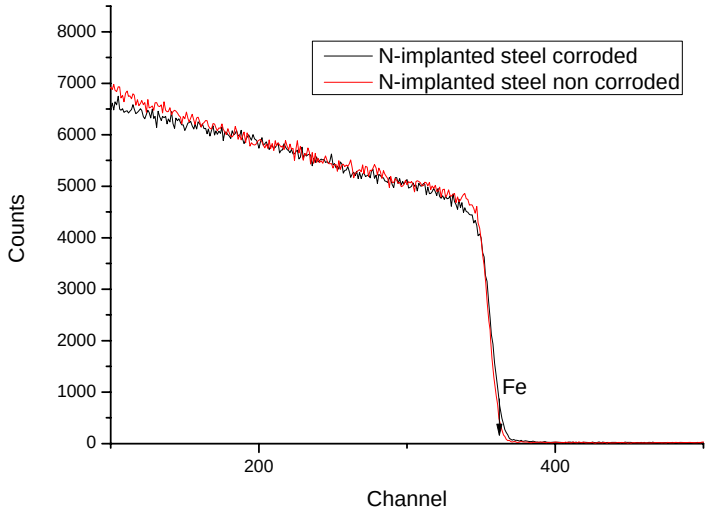
N-implanted steel corroded
N-implanted steel non corroded
Counts
Channel
Fe
0
1000
2000
3000
4000
5000
6000
7000
8000
200
400

Theoretically and under very special applied conditions a nuclear fission reactor may explode as nuclear bomb

Kondylakis J.C.[a]

[a] *Institute of Oceanography, Hellenic Center for Marine Research, 19013 Anavyssos, Greece*

e-mail : joseph@hcmr.gr

Abstract

This article/presentation describes a theoretical and applied research in nuclear fission reactor systems. It concerns with theoretical approaches and in very special applied cases consideration where a common nuclear fission reactor system may be considered to explode as nuclear bomb. This research gives critical impacts to the design, operation, management and philosophy of nuclear fission reactors systems. It also includes a sensitivity analysis of a particular applied problem concerning the core melting of a nuclear reactor and its deposit to the bottom of reactor vessel. Specifically, in a typical nuclear fission power reactor system of about 1000 MWe, the nuclear core material (corium) in certain cases can be melted and it may deposited in the bottom of nuclear reactor vessel. So, the nuclear criticality conditions are evaluated for a particular example case(s). Assuming an example composition of melted corium of 98 tones of U238 , 1 tone of U235 , 1 tone Pu239 and 25 tones Fe56 (supporting material) in a 5 m diameter of a finite cylindrical nuclear reactor vessel it is found that it may result in nuclear criticality above the unit. This condition corresponds to Supercritical Fast Nuclear Fission Reactor case, which may under certain very special applied conditions to nuclear explode as nuclear bomb.

Key words: Nuclear reactor, fission, core meltdown, nuclear accident, human factor, nuclear safety, nuclear bomb, nuclear engineering, corium

1. Introduction

The Nuclear Safety is a vital theme of paramount value for the Humanity and Ecosystems. The Deaths from the Chernobyl Nuclear Accident, USSR ,1986 , until 2009 was estimated from IAEA/WHO to about 4000 [1] and from according to literature [2] to about 1.000.000. Also have been reported from the Associated Press,USA,on Thursday 21-April-2011,that the cost of worst case(Not for our extreme severe case of nuclear explosion as nuclear bomb which is much more worst case) of a severe Nuclear Accident for example in Germany, has estimated to result in a total cost as much as 7.6 Trillions Euro!

The Nuclear Safety has three critical components: a) the nuclear human factor (management, workers, designers, others effecting the Nuclear Safety) [3], [5], [12], [13], [16] and b) the nuclear technological factor [4], [6], [13]and c) the theoretical critical factor [7]. The nuclear human factor has been proven in practice from the nuclear accidents to be the most critical factor [3].

The author goal in this research is to warn the nuclear society for the possibility of extreme severe nuclear accidents in order together with future studies to contribute to minimization or perhaps zero of probabilities for extreme worst nuclear fission accidents to happens in particular nuclear system.

Until now, qualitative simple arguments have propagated the belief that nuclear fission reactor accidents cannot lead to nuclear explosions as nuclear bomb(examples of articles can be found by Internet search). The present scientific research offers the first quantitative research in the question if a nuclear fission reactor (or/and with perhaps similar thinking approach for a nuclear waste storage) can explode as nuclear bomb, and therefore may contribute to open a new direction in research in the nuclear safety of severe nuclear fission accidents (considering the very critical case of extreme worst nuclear fission accidents).

A nuclear fission system can explode with conventional (chemical) explosions from f.e. the ignition of an explosive mixture of hydrogen,etc, or from nuclear explosions of low yield(early dispersion of nuclear fissioning material,common cases in nuclear accidents) or with high power nuclear yield (explosion as a nuclear bomb).

The study of the real cases of Nuclear Fission Reactors System (theoretically, applied or in simulators) demands a system of equations which contains the integral differential NON-linear system of equations of the neutrons flow (considering the system of neutrons transport equation(s)) with nuclear reactivities feedbacks and time-depended transients states (in the dynamic of nuclear fission reactors) with at least 6 to 13 energies groups of delayed neutrons (>6 if we consider and the photo-neutrons f.e. in CANDU nuclear fission reactor types). The study must be made in three spatial dimensions (because of the Non-homogenous flow of neutrons in the core of the nuclear energy reactor) and considering the influences («poisoning», feedbacks, oscillations,etc) of the products of nuclear fissions, the generations of transuranic elements, the burn up considerations, and possible «external» neutron sources. The above must be considered for a finite nuclear reactor system model, in real spatial-time (geometry) dimensions and material (space,time) composition calculations ,and in this nuclear system the description of its nuclear energy states(in a multi energy groups approach model) to be coupled with the system of equations of dynamic thermohydraulic of two phases flow (considering also the possibilities of cases of nucleate boiling,etc) for a compressible and viscous fluid (which can also possible to include turbulence flow cases) ,and also to be coupled with the rest of sybsystems of the Nuclear Plant (f.e turbine(s) behaviours, electrical load behaviour, accidents,etc) . All the above considerations must also be coupled with the Human(s) cognitive intelligence & education & Management knowledge of the nuclear system & its behaviour in (space,time,case) ,and with the plant ergonomics & information fields & Human psychologies of workers ,test cases considerations, etc, which may effect directly or/and indirectly the nuclear plant…

With the considerations in the mathematical models of the mathematical existence of solution(s) and its uniqueness studies with the problems in analytical solutions and numerical algorithms approximations, in convergence and stability of solution(s) thinking, and in simulator sensitivities research and optimization studies considerations.We also recommend the studies of relevant ILL-posed problems that may arise in research and in modelling,etc.

In order to evaluate the possibility of the explosion of a nuclear reactor as a nuclear bomb the following principles are considered:

the physical processes in nuclear reactor meltdown accidents [8] and in the reactor safety study [9], the cases of Uranium and Pu239 nuclear energy reactor core meltdown, the human factor and the conventional explosions that can occur. Considering the literature [10] an initial evaluation has been made using our original model of the above processes. There are uncertainties in applied cases because most of experiments concerning specific system of engineering nature are considered uncertain to be generalize to other systems. It is possible ([10],etc) a «closet» configuration to be formed inside the nuclear reactor vessel, which is similar, in principles, with the first Uranium nuclear bomb configuration (f.e. [17])[at least theoretically a nuclear supercritical fissioning system which can be maintained together for adequate nuclear fission generations can nuclear explode as nuclear bomb...]

This could be a steel «closet» with steel on top, steel on sides and in the bottom, and inside to contain Nuclear Fissioning Mass [NFM] (mostly melted Uranium and Plutonium). So the configurations (geometry, composition, etc) in combination with the expected nuclear and transport phenomena can create supercritical NFM. Any kind of maintaining in the enclosed space «closet» for adequate time the supercritical NFM will create nuclear explosion. The reactor vessel is made from very strong steel (in most common nuclear reactor types) which form the very strong construction of the "closet" of the reactor vessel and thus can increase considerably the probability of a nuclear explosion as nuclear bomb, since it will keep in restricted space a supercritical fissioning mass for long time(many nuclear fission generations in supercriticality).

In Additional to the above mentioned consideration, there may be the worst case where conventional explosions of explosive melt plus water (or more general , two or three phases solid ,liquid and air (usually in the form of bubbles) in a nuclear reactor melted core to interact with cold material in which spontaneous explosions may occur (as melt is falling through water the melt surface temperature fall below the minimum film boiling temperature, causing the vapour film to become unstable and collapse, triggered explosions may occur (when water is forced in contact with melt due to some external event). Thinking on the accidental cases of Spontaneous, Triggered Explosions and the case of the enclosed NFM in «closet», this may be similar in certain specific cases to the case of Plutonium nuclear bomb, since strong implosive compressions may occur.

2. Material and Methods

In this work the evaluation of the criticality of melted corium in f.e. pressurized light water nuclear fission reactors or boiling water fission reactors or other types is studied when all the corium is deposited in the bottom of the nuclear reactor vessel. The following scenario will be examined:

A. The Scenario of Nuclear Fission Reactor Severe Accident, where all the nuclear core material (corium) is melted and go as corium to be deposited in the bottom of the nuclear reactor vessel, and the corium can form a nuclear super critical mass configuration in a steel "closet" situation which may lead to nuclear explosion.

B. Assumptions in our the applied simplified model:

a. Assuming that the nuclear reactor vessel has finite cylindrical shape with internal diameter five (5) meters, into which all the melted corium is deposited in its bottom.

b. Assuming the approximately validity of neutrons diffuse equation and considering one energy group (fast neutrons group).

c. Assuming instantaneous steady-state for the evaluated position of corium inside the bottom of the nuclear reactor vessel.

d. The extrapolated distance, d, from the boundaries of the corium and the nuclear reactor vessel is taken into account.

e. Assuming finite cylindrical shape of the nuclear reactor vessel; therefore the critical Buckling and fluxes are used for a reflected finite cylinder fast nuclear fission reactor.

f. Assuming that the corium to be composed, in first approximation, from homogenous mixture of melted 98 tones U238, 1 tone of U235 , 1 tone Pu239 and 25 tones Fe56.

g. Assuming that the nuclear reactor vessel , initially, holds for certain time the melted corium (which it is separated from the water above it).

h. Assuming in the calculation a fast neutrons nuclear fission reactor case study , to consist the layer of melted corium, in the closet.

g. Assuming neutrons reflection in the fissioning mass' "closet" walls and we approximately calculate its impact to the multiplication factor.

3. The Results

I. Simple Approximation calculation of the problem (the CGS system of units is used in calculations)

The Criticality Coefficient (or the Fissions Multiplication factor) is defined as

$$\mathrm{k} = \frac{\text{Number of fissions in one generation (in nuclear fission(s) chain reaction)}}{\text{Number of fissions in the preceding generation}}$$

and the Critical state of the nuclear chain reaction system is present when k=1, subcritical state when k<1 (reducing nuclear fission power) and Supercritical state when k>1 (increasing nuclear fission power). The calculations were made according to the literature [11]. Considering the relevant assumptions and the approximation is derived in similar way as the equation for k for a homogenous mixture of materials, considering that now in our case the term for the neutron sources, in the approximation of one-energy group (the fast energy neutrons group) neutron diffusion equation for nuclear fission reactor will be:

$$S(sources\,of\ neutron) = \left[\sum_{i=1}^{3} \nu_i \cdot \left[\left(\frac{V_i}{V_{tot}} \right) \cdot N_i \sigma_{f,i} \right] \right] \cdot \Phi\left(vector(\vec{r}, t) \right)$$

where Φ(vector[r],t) is the neutrons flux in the melted corium nuclear reactor system.

Therefore we can write:

$$k = \frac{\nu_{fast(Pu239)} \cdot \sum_{f,fast}(Pu239) + \nu_{fast(U235)} \cdot \sum_{f,fast}(U235) + \nu_{fast(U238)} \cdot \sum_{f,fast}(U238)}{D \cdot B^2 + \Sigma\alpha}$$

Where νfast is the average number of fast neutrons (both prompt and delayed) released per fission event in a fissioning isotope. This number take the values : νfastPu239 , νfastU235 , νfastU238 for the isotopes of Pu239,U235,U238 respectively , for the fast neutrons energy group.

Σf is the macroscopic cross section for fission ,here induced by fast neutrons, Σα the macroscopic cross section of absorption of neutrons, D the diffusion coefficient (which is considered constant) for the diffusion of neutrons approximation of nuclear fission reactor, B^2 the Geometrical Buckling.

Now we consider the very simple approximation of a HOMOGENOUS mixture of nuclear "fuel" consisting from [Pu239 , U235 , U238] for fast neutrons nuclear fission reactor model. In a homogenous mixture the following approximation is used:

$$\Sigma\alpha = \sum_{j=1}^{4} \frac{V_i}{V_{tot}} \cdot N_j \cdot \sigma(a)_j$$

where Vi denote the volume occupied in the corium from the i constituent of corium (i=1,…,4 , for Pu239,U235,U238,Fe56) and Vtot the total volume of corium

Also from equations (5.10) & (5.11) & (5.12) of reference [11] we obtain:

$$D = \frac{1}{3 \cdot \Sigma transport}$$

and by denoting N the Nuclei(or atomic) density in nuclei/cm^3 we can write(for one type of material system) $\Sigma\chi = N.\ \sigma\chi$, for the x-type of nuclear interaction. In order to calculate the Σtranport(Mixture of Materials) the following equation is used (and similar for the calculations of others Σχ macroscopic cross sections, in the homogenous mixture of isotopes in our system) :

$$\Sigma trasport(mixture) = \sum_{i=1}^{4} \left(\frac{V_i}{V_{tot}} \right) \cdot N_i \cdot \sigma_{i,tr}$$

where σi,tr the microscopic transport cross section , Ni the nuclei density ,of element i, per cm^3

Also by considering the case of a FINITE cylindrical geometry Nuclear Fissioning Masss (a Nuclear Fission Reactor type, representing the melted corium) the Geometrical Buckling (from table 6.2 of the book [11]) is given as follows (and considering the extrapolation distance d due to correction from the neutrons transport theory and the reflector saving δ due to neutrons reflections in the thick walls of steel "closed" which is formed from the thick walls of nuclear reactor vessel on the sides and in the bottom and in the upper side the reflection from steel plate reflection.):

$$B^2 = \left[\frac{2.405}{R + d + \delta} \right]^2 + \left[\frac{\pi}{H + 2d + 2\delta} \right]^2$$

where R is the radius in cm and H the height in cm of the Finite cylinder nuclear reactor. Now we do the relevant for the problem numerical calculations using the above system of equations

a. relevant nuclear data

N(Pu) = 0.04938 . 10^{24} (nuclei{atoms] densities per cm^3)
N(U) = 0.04833 . 10^{24}
N(Fe) = 0.08487 . 10^{24}

ρ(Pu239) = 19.816 (mass density in gr/cm^3)
ρ(U238) about equal to ρ(U335) = 19.1
ρ(Fe56) = 7.87

ν-fast (Pu239) = 2.98 (ν for fast(energetic) neutrons)
ν-fast (U235) = 2.6
ν-fast (U238) = 2.6

microscopic cross sections of relevant nuclear interactions (to be multiplied by 10^{-24})

σ[α]fast (Pu239)=2.11 σ[transport]fast(Pu239)=6.8 σ[fission]fast(Pu239) =1.85
σ[α]fast(U235) = 1.65 σ[transport]fast(U235) = 6.8 σ[fission]fast(U235)= 1.40
σ[α]fast(U238) =0.255 σ[transport]fast(U238) = 6.9 σ[fission]fast(U238)=0.095
σ[α]fast(Fe56) =0.006 σ[transport]fast(Fe56) = 2,7 σ[fission]fast(Fe56)= 0

b. We assume a homogenous mixture of melted Corium as fluid , forming a FAST nuclear fission reactor of Finite cylindrical geometry , as following:
0.008 %w Pu239 → 1000 Kgr =106 gr VOL(Pu239)=50464.27 cm^3
0.008 %w U235 → 1000 Kgr=106 gr VOL(U235)=52356.20 cm^3
0.784%w U238 → 98000 Kgr=98 x106 gr VOL(U238)=5 130 000 cm^3
0.20 %w Fe56 → 25000 Kgr=25 x106 gr VOL(Fe56)= 3 176 620 cm^3
TOTAL VOLume= 8 409 440 cm^3

c. Geometry of the Finite Cylinder Nuclear Reactor

Radius =250 cm Height=TotalVolume/BottomSurface=42.90 cm

BottomSurface= π , R^2 = 19.6 x104 cm^2

And using the following equations:

$$d = 2.13 \cdot D_c$$

$$\delta = \frac{D_c}{D_R} \cdot L_R , \quad L_R = \sqrt{\frac{D_R}{\Sigma_{\alpha,R}}}$$

$$D_R = \frac{1}{3 \cdot \Sigma_{tr,R}}$$

Where d is the extrapolation distance , δ the reflection saving (simple approximate calculation), D_C, D_R, the diffusion constants for the core and the reflector areas respectively , and $\Sigma\chi$,R the macroscopic cross section for χ nuclear interaction type in the reflector areas.

d. Using the above mentioned system of equations, the relevant numerical calculations result to the following value of fissions multiplication factor k, (for 2.5 m internal nuclear reactor vessel radius):

$$k = 1.0492 > 1$$

This result may interpreted that the operation of the nuclear fast reactor (fissioning corium) becomes supercritical and thus it may nuclear explode and under certain special conditions(strong tamper effects, very strong steel “closet” formation, etc) may even explode as Nuclear Bomb.

II. Sensitivity Analysis of the main problem

In order to improve the Nuclear Energy Safety, a Sensitivity study is performed on the simplified model used, by considering a nuclear energy reactor with hypothetical from 1.6 m to 6.0 m internal radius of the nuclear reactor vessel and by increasing the vessel radius in steps of 0.2 m we calculated the fissions multiplication factors k , and the results are presented in the graph-1 which is following:

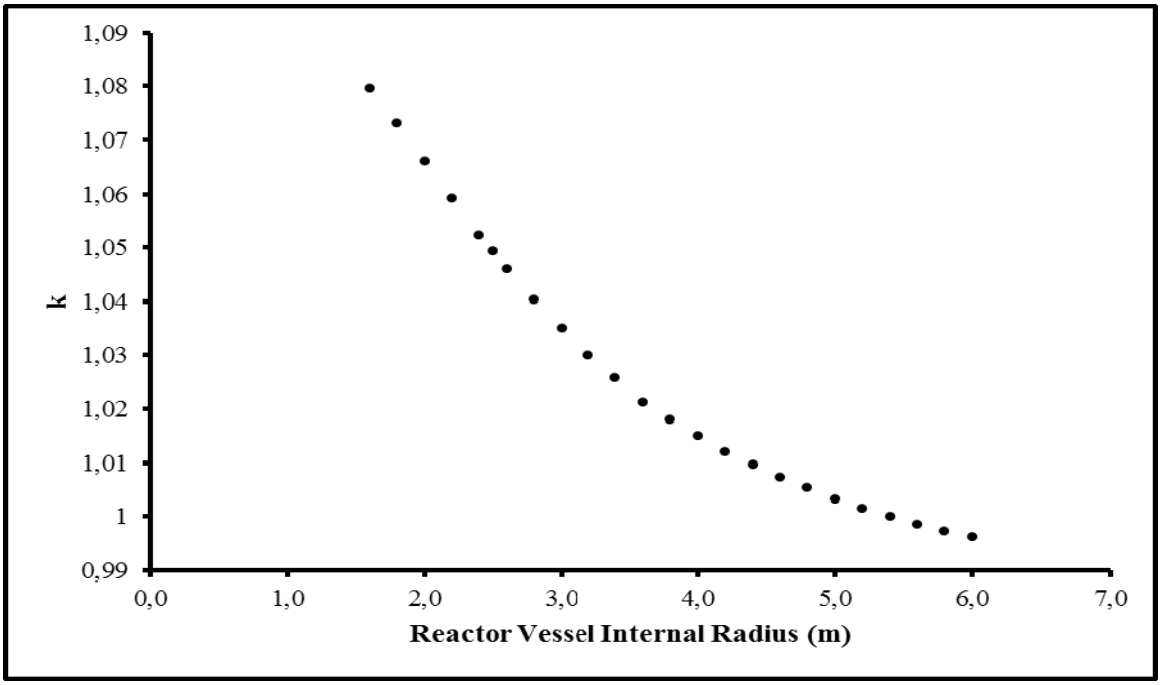

Graph-1. Sensitivity analysis of the nuclear criticality (k factor) as a function of the reactor vessel internal radius.

From the Graph-1 we notice that from internal reactor vessel radius 1.6 m to about 5.5 m , there may be, theoretically, a possibility of nuclear explosion , because in these radius values, the k can be greater to one. These results must motivate further research and to be considered in the designs and operations of nuclear fission reactors.

4. Conclusions

According to this simplified model, it is shown that in a nuclear fission reactor severe accident , it is probable in a nuclear core meltdown to be formed a nuclear configuration of Supercritical mass layer (in form of a closet) in the bottom of the nuclear reactor vessel. Further scientific research is required in order to understand more precisely the phenomena and preventions in nuclear fission reactors severe accidents. This study recommend the following aspects:

a. Further research and studies are required by using more precise models calculations of fission multiplication factor k (nuclear criticality studies) for different (space,time,case) configurations.

b. The development of high advanced scientific nuclear fission reactor types simulators is proposed with spatial and time transients' consideration and sensitivity analyses in many views of hyper-nodes network model[13] and considering our discussion in the introduction of this article which refer to the study of the real cases of Nuclear Fission Reactor Systems….

c. A Mathematical hint, for studying ill posed ,initial and boundary value problems relating to the uniqueness, stability, continuous data dependence and instability of solutions for both linear and non-linear partial integral/differential equations[14] , and also studying stochastic neutron transport cases[15].

d. The multi-factors sensitivity analysis of solutions in the simplified or more advanced model, where the case of Supercriticality of nuclear corium configuration is obtained, recommends new designs of nuclear fission reactors considering the size of cylindrical nuclear reactor vessel of larger diameters, and under the nuclear fission reactor the cavityies to be in such way constructed so to be more "manageable" the possible processes that they may lead to the creation of Super critical configuration of nuclear fissioning mass(NFM).

Here we must stress that , considering the official report by Henry De Wolf Smyth ,1945 and the double importance of the Tamper (neutrons back reflection , delay of the expansion of supercritical mass) and the fact that U238 is an excellent tamper in the design of nuclear bombs,

And that in this article we have Not taken in precise account the tamper effects, which are very serious because of about 98 tones of U238 in the corium , we conclude that the probability of a nuclear fission reactor in a case of meltdown severe nuclear accident to nuclear explode as nuclear bomb may be higher than what we initially thought.Therefore further scientific research in our theme is considered Mandatory and Must be Supported in order to be prepared and to find Preventive ways to increase significantly the Nuclear Safety in Extreme Severe Nuclear Accidents cases…

References

[1] I.A.E.A./W.H.O. Report on Chernobyl Nuclear Accident , September 2005

[2] Alexey V. Yablakov , et all ," Chernobyl: Consequences of the Catastrophe for the People and the Environment " , in Annals of the New York Academy of Sciences,USA, 2009
[3] Joseph-Christos Kondylakis , "Human Management in Nuclear Systems"(Human Factor) , submitted to the 20th Scientific Symposium of the Hellenic Nuclear Physics Society , 2011 , organized by the Technical University of Athens & HCMR , in Athens , Greece
[4] Gianni Petrangeli , "Nuclear Safety" (Technological Factor) , 2006 , Elsevier publisher
[5] J. Misumi , et al (Editors) "Nuclear Safety: A Human Factor Perspective" , 1999 , Taylor Francis publisher
[6] Jacques Libmann , "Elements of Nuclear Safety " , 1996 , Les Edition de Physique (France)
[7] E. E. Lewis , "Nuclear Power Reactor Safety " , 1977 , John Wiley publishers
[8] Report WASH-1400 , NRC , USA
[9] Report NUREG-75/014 , NRC , USA
[10] George A. Greene et al., "Heat transfer to Nuclear Safety" (1997), Academic press
[11] John R. Lamarsh , et al, "Introduction to Nuclear engineering", 3rd edition (2001), Prentice Hall
[12] Joseph-Christos Kondylakis " On the Vital Duty of Responsibility on Nuclear energy systems" 22-May-2010 , sent to Embassies in Greece and to I.A.E.A. and to U.N. and elsewhere (2010).
[13]. Joseph-Christos Kondylakis, "A consideration of some uncommon but Very Critical aspects of Nuclear safety" (my practical experience from working in Nuclear Reactor(s) Power Plants Headquarters in North America), 1983,1997 , last version 2001 , with very good scientific comments from the Prof. Jacques Poirier, Commissariat a l' Energie Atomique (DRN) of France , editor of the journal "Nuclear Engineering and Design" , but other bad interests did not allow the publication of my Original and Critical article in this journal.
[14] A.N. Tikhonov , et al , "Nonlinear ILL-posed problems ", 1998 , Chapman & Hall publishers
[15] Wyatt D. Sharp III , "Development and Implementation of stochastic neutron transport equations and development and analysis of finite difference and Galerkin methods for approximate solution to Volterra's population equation with diffusion and noise " , Ph.D. Thesis in Mathematics , Texas Technical University,USA,1999
[16] Joseph-Christos Kondylakis, My Relevant Law Action to the Prosecutors of the Greek Supreme Criminal Court of Justice with file number 8081/5-11-1998 AND its relevant later information.
[17] Kostas Tsipis "Arsenal : understanding weapons in the nuclear age",1983, Simon & Schuster press

Probing the ^{17}F+p potential by means of elastic scattering at near barrier energies

N. Patronis[a], A. Pakou[a], D. Pierroutsakou[b], A. M. Sanchez-Benitez[c], L. Acosta[c], N. Alamanos[d], A. Boiano[b], G. Inglima[e], D. Filipescu[f], T. Glodariu[f], A. Guglielmetti[g], N. Keeley[h], M. La Commara[i], I. Martel[c], C. Mazzocchi[g], M. Mazzocco[j], P. Molini[j], C. Parascandolo[b], M. Sandoli[i], C. Signorini[j], R. Silvestri[i], F. Soramel[j], E. Stiliaris[k], M. Romoli[b], A. Trzcinska[l], K. Zerva[a], E. Vardaci[i]

[a]*Department of Physics and HINP, The University of Ioannina, 45110 Ioannina, Greece*
[b]*INFN - Sezione di Napoli, via Cinthia, I-80126 Napoli, Italy*
[c] *Dapartamento di Fisica Atomica Molecular y Nuclear, Universidad de Huelva, E-21071 Huelva, Spain*
[d]*CEA-Saclay, DAPNIA-SPhN, Gif-sur-Yvette, France*
[e]*Dipartimento di Scienze Fisiche and INFN Sez. di Napoli, Universitá di Napoli, via Cintia,I-80126, Napoli, Italy*
[f]*"Horia Hulubei" National Institute of Physics and Nuclear Engineering , Romania*
[g]*Universita' degli Studi di Milano and INFN - Sezione di Milano, via Celoria 16, I-20133 Milano, Italy*
[h]*Department of Nuclear Reactions, The Andrzej Sołtan Institute for Nuclear Studies, Hoża 69, 00-681 Warsaw, Poland*
[i]*Dipartimento di Scienze Fisiche and INFN - Sezione di Napoli, via Cinthia, I-80126 Napoli, Italy*
[j]*Dipartimento di Fisica and INFN - Sezione di Padova, via F. Marzolo 8, I-35131 Padova, Italy*
[k]*Institute of Accelerating Systems and Applications and Department of Physics, University of Athens, Greece*
[l]*Heavy Ion Laboratory, University of Warsaw , Pasteura 5a, 02-093 Warsaw, Poland*

Abstract

Results from the first stage of analysis of the recently performed ^{17}F+p experiment are presented. The experiment was performed at the EXOTIC facility of Legnaro National Laboratory (Italy, LNL-INFN), where the ^{17}F radioactive beam is available. The measurement of elastic scattering angular distributions, in a wide angular range (θ_{cm}=20-160 deg) was taken over in order to probe the potential at two near barrier energies, namely: 3.5 AMeV and 4.3 AMeV. The present work, should be considered as the starting point of a general survey along drip line nuclei, aiming to a better understanding and mapping of the nuclear potential at near barrier energies.

Keywords: Radioactive ion beams; Elastic scattering; Nuclear potential

1. Introduction

Proton-nucleus elastic scattering has been traditionally used to probe the nuclear potential. In this respect, extensive studies have been performed and both phenomenological and microscopic potential models have been developed. A large amount of experimental data has been successfully interpreted through such models with at most the adjustment of only a few parameters.

By the advent of radioactive ion beams during the last years, we have the ability to extent our knowledge to regions of the nuclear landscape that previously were unaccessible. The ^{17}F being a proton rich nucleus, with extremely small binding energy of the last proton for the ground (S_p = -600 keV) and the first excited state (S_p=-105.13 keV), is one of the most important drip line nuclei involved in reactions of astrophysical importance. The nuclear reaction sequence ^{14}O(a,p)^{17}F(p,γ)^{18}Ne takes place during x-ray bursts - one of the most violent explosions in the universe. The key role of this reaction sequence comes from the fact that it provides a breakout from the HCNO cycle. Accordingly, the knowledge of the nuclear parameters for those nuclei is important since can set constrains on ignition conditions and the thermonuclear runaway timescale. For these reasons, a number of studies have been performed so far focusing to the understanding of the resonance character of the p+^{17}F interaction [1, 2, 3, 4, 5] by the determination of the energy dependence of proton elastic scattering cross section. The experimental determination of the ^{17}F(p,p) excitation

Email address: npatronis@uoi.gr (N. Patronis)

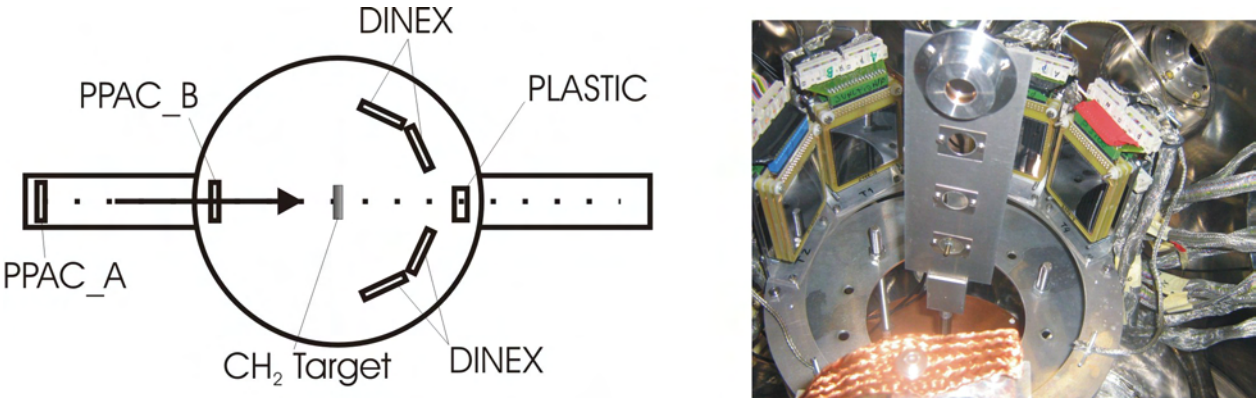

Figure 1: The experimental setup as was realized during the ^{17}F+p experiment. In the photo of the scattering chamber the four DINEX telescopes and the target ladder can be seen.

function at low energies of astrophysical interest is important, but significant is also the role and the knowledge of the p+^{17}F nuclear potential which can only be determined by recording the full center-of-mass (CM) angular distribution. In this way, valuable information can be deduced for any phenomenological or microscopic calculation that includes the p+^{17}F interaction either as incoming and/or outgoing channel.

Into the above context, the measurement of the elastic scattering angular distributions, ^{1}H(^{17}F,p), in a wide angular range (Θ_{cm}=20-160 deg) was taken over [6] as to probe the potential at two near barrier energies, namely: 3.5 AMeV and 4.3 AMeV. In this way the mapping of the nuclear potential will be derived together with the information about the existence or not of halo structure for the ground state of ^{17}F.

2. Secondary Beam

The ^{17}F radioactive beam was produced at the EXOTIC facility [7] at Laboratori Nazionali di Legnaro (LNL-Italy) of the Istituto Nazionale di Fisica Nucleare (INFN) by means of the In-Flight technique and by using the reaction ^{1}H(^{17}O,^{17}F)n. The $^{17}O^{+8}$ primary beam delivered from the LNL-XTU Tandem Van de Graaf accelerator at the energy of 105 MeV and was directed to a 5 cm long gas cell.The double walled gas cell with 2.2 μm-thich Havar foils was filled with H_2 under controlled pressure and temperature conditions. The energy of the secondary beam is defined from the primary beam energy as well as from the pressure of the primary gas target. Additionally, the energy loss of the secondary beam from the different beam line elements on the way to the scattering chamber has to be taken into account. For the first run the energy of the secondary beam was 64 MeV and for the second one was 77 MeV, resulting to 3.5 AeV and 4.3 AMeV at the middle point of the secondary 1mg/cm^2 thick CH_2 target. In both runs the secondary beam energy was chosen as to be outside known resonances and was measured before and after each run by the end-channel Si-detector. The selection, separation and focusing of the secondary beam is achieved by a quadrapole triplet, a 30°-bending magnet, a 1m-long Wien-filter and a second quadrupole triplet. The beam spatial profile was defined by means of four slits and a triple stack of collimators with diameters of 10 mm placed at ~ 264-324 mm upstream the secondary target. Under these conditions the resulted beam intensity at the secondary target position was 10^4-10^5 pps

3. Experimental Setup

The beam profile during the measurement was recorded by means of a parallel plate avalanche counter (PPAC) located 750 mm upstream the secondary target providing the event-by-event position and time information for each beam particle. Each PPAC consists of a cathode plate placed between a double anode frame made by 60 wires at a distance of 1.0 mm in perpendicular orientation. In this way, position resolution for the beam particles with an accuracy of 1 mm was achieved.

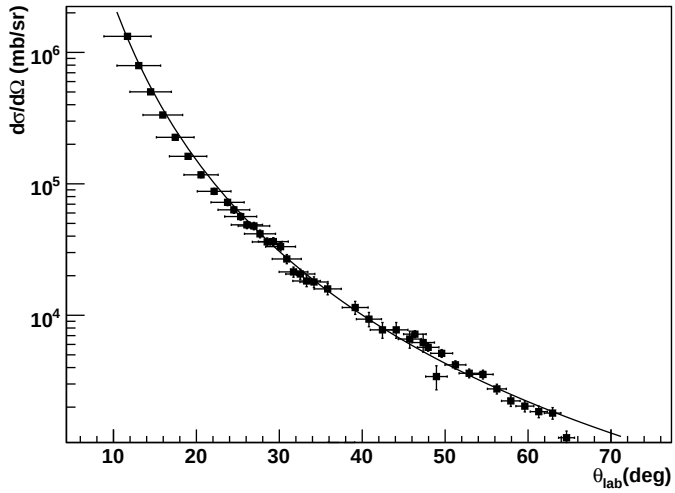

Figure 2: The experimentally deduced angular distribution of the calibration ^{17}F+^{197}Au run together with the expected Rutherford scattering reaction cross section. The experimental points were deduced by taking into account the angular coverage and and solid angle for each strip as deduced from MC calculations.

The elastic scattered protons were detected by means of the DINEX Si-detector array that was coupled into the EXOTIC LNL facility. The DINEX detector array consist of four triple Si telescopes. Each telescope provides three detection stages: a) ΔE1-40μm Double-Sided-Silicon-Strip-Detector (DSSSD), b)ΔE2-500μm PAD detector and c) E-1000μm DSSSD. The four telescopes were placed at 104 mm distance from the target position according to the configuration seen in Fig.1. With this setup the covering detection area of 4×50×50 mm^2 corresponds to an overall solid angle of ∼0.8 sr. Position information for each 16 × 16 striped DSSSD detector was determined from the id-number of each of the x and y strip. Considering just the y strip id an angular resolution of 1.3° - 3.1° can be achieved.

4. Data analysis

The first stage of the data analysis procedure was the determination of the angular coverage and solid angle determination for each strip of the DSSSD detectors. This was done by extensive Geant4 [8] Monte-Carlo (MC) calculations where all the details of the beam profile, of the target and the detection geometry, were taken into account. In a second stage of the analysis procedure, the deduced results from MC calculations were combined with the counting-rate per strip as resulted from the ^{17}F+ ^{198}Au run at the sub-Coulomb-barrier energy of 72 MeV. At this energy a Rutherford angular distribution is expected. This run proved to be very useful for the solid angle as well as for the overall angular calibration of the DINEX-array. The results of the angular calibration procedure as resulted from the combination of the gold calibration-run and MC calculations can be seen in Fig. 2. The excellent agreement of the theoretical angular distribution with the corresponding experimental points visualize the precision of the angular calibration procedure.

Concerning the necessary analysis codes are already built and tested. Different modes of analysis were implemented in a way to reduce as much possible systematic and statistical uncertainties in the deduced proton elastic scattering angular distribution. Preliminary results for both energies at 3.5 AMeV and 4.3 AMeV can be seen in Fig. 3. The analysis is still in progress and is expected to be finalized within 2011.

5. Conclusions and outlook

The analysis of the experimental results for the determination of the angular distribution in a wide angular range of the ^{17}F+p elastic scattering at two near barrier energies is in the final stage. The deduced angular distributions for both

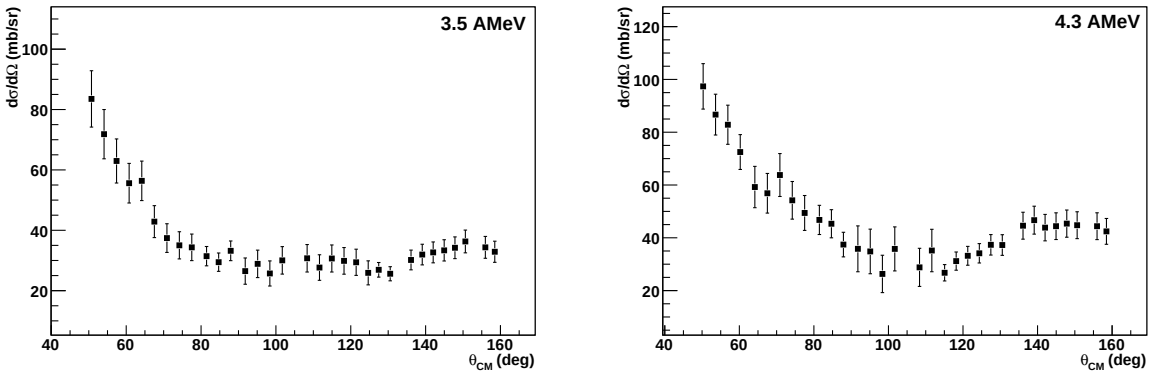

Figure 3: Preliminary results of the deduced angular distribution at two near barrier energies (3.5 AMeV and 4.3 AMeV) for the ^{17}F+p system.

near barrier energies will be compared with phenomenological calculations as well as with microscopic calculations towards to a better understanding and mapping of the nuclear potential. Possible halo-structure of ^{17}F will be revealed through the analysis process by the comparison of the experimentally deduced angular distribution with microscopic JLM calculations [9]. An other indication concerning the existence of halo structure or not can be the comparison of the deduced total reaction cross section from phenomenological calculations with those from Wong's [10] estimates. Final results of the theoretical analysis are expected in close future.

In conclusion, we see that coupling the DINEX silicon detector array with the EXOTIC/LNL facility was successful. A new series of experiments was launched where the flexibility, high-segmentation and high angular coverage of the DINEX array can be efficiently combined with the EXOTIC RIB facility, towards to a better understanding and mapping of the nuclear potential near the proton drip line.

References

[1] B. Harss et al., Phys. Rev. C65, 035803 (2002)
[2] Jin Sun-Jun et al., Chin. Phys. Lett. 27, 032102 (2010)
[3] J.C. Blackmon et al., Nucl. Phys. A 688, 142c-145c (2001)
[4] D.W. Bardayan et al., Phys. Rev. C62, 055804 (2000)
[5] J. Gómez del Campo et al., Phys. Rev. Lett. 86, 43 (2001)
[6] A. Pakou et al., Accepted proposal LNL-PAC, July 2009.
[7] F. Farinon et al., Nucl. Instrum. Methods Phys. Res. B 266, 4097 (2008).
[8] S. Agostinelli et al., Nucl. Instrum. Methods. Phys. Res. A 506, 250 (2003)
[9] J. P. Jeukenne, A. Lejeune, C. Mahaux, Phys. Rev. C 16, 80 (1977).
[10] C.Y. Wong, Phys. Rev. Lett. 31, 766 (1973)

Investigation of the Transient Field at High Velocities by magnetic-moment measurements in ^{74}Ge and ^{70}Zn

T.J. Mertzimekis[a,*], for the LNS-HVTF collaboration

[a] *INP, NCSR "Demokritos", 15310, Aghia Paraskevi, Greece*

Abstract

The advent of radioactive beams at large experimental facilities has motivated extensive research work on the expansion of techniques to accommodate higher ion velocities. The application of the Transient Field technique in measuring magnetic moments of excited states in energetic nuclei is investigated at the INFN-LNS in Catania by means of re-measuring the $g(2_1^+)$ factors in ^{74}Ge and ^{70}Zn. The description of the experiment method and some preliminary angular correlation results are presented.

Keywords: Magnetic moments, Transient Field, HVTF parameterization

1. Introduction and Motivation

Radioactive beams (RIB) are available almost routinely at large experimental facilities around the world. By means of RIB, new phenomena may be studied, providing important input to our understanding of the nuclear landscape. In that framework, tools and techniques are re-visited, updated and expanded to keep up in pace with recent developments.

The Transient Field (TF) technique is an experimental method that has been utilized successfully for magnetic-moment measurements of nuclear states with lifetimes at the picosecond range. In general, the method is well applicable for ion velocities below the K-shell electron velocities $V_K = Zv_o$ [1, 2], with $v_o = c/137$ being the Bohr velocity. With the exception of several light nuclei in the range $6 < Z < 24$ (see Ref.[2] and references therein) the behavior of the TF strength has been studied at velocities $v_{ion} \ll Zv_o$. For that range several studies have been carried out up to $v_{ion} \sim Zv_o$, resulting in the observation of a steady increase of the TF strength, approaching its maximum value at Zv_o [1, 2, 3]. The lack of an analytic expression for TF is overcome by using strength parameterizations as a function of ion velocity and type and magnetization of the ferromagnetic host.

*Present address: Dept. of Physics, Univ. of Athens, 15784, Zografou Campus, Athens, Greece

Exotic nuclei produced as low-intensity radioactive beams are now available as projectiles at high velocities and may be studied at the maximum TF strength, expected to occur at v_K. This type of studies should allow for measurements of very short lived nuclear states and provide critical information on their structure. The application of the technique is based on the utilization of a ferromagnetic target where the TF is observed during the ion's flight through the host. In the low-velocity regime Gd is usually preferred as ferromagnetic layer compared to Fe. Larger precession angles may be achieved since Gd has a lower stopping power.

Older parameterizations do not cover the velocity ranges of ions produced in the modern RIB facilities and new data have to be provided to (a) understand the new physics associated with higher ion energies (b) improve the existing parameterizations, if possible, and (c) use the new information to improve the technique expanding its range of applicability. Such a recent parameterization using newly acquired data on magnetic moments of light ions experiencing the TF in a Fe foil has been established [3]. However, this parameterization needs to be tested further for heavier ions and additional ferromagnetic hosts, such as Gd.

2. Experimental Details

An experiment was carried out at the INFN-Laboratori Nationali del Sud in Catana, Italy. The INFN-LNS K800 Superconducting Cyclotron produced and delivered 0.5 pnA, 40 MeV/u ^{74}Ge and ^{70}Zn beams. The beams impinged a Gd single-layer target which acted both as a Coulomb excitation layer and the ferromagnetic layer which is required for the application of the technique. The interacted target particles traversed the target, which was cooled at 50 K to obtain its ferromagnetic properties, and were detected by a 8-fold segmented plastic scintillator located after the target. The particle detector was designed with cylindrical symmetry and placed coaxially with the beam allowing non-interacted beam to travel all the way to a beam stop located several meters downstream.

The ions that were excited in the target further experienced the influence of the TF for as long as they were crossing the Gd foil. The direction of the TF was adjusted by a ≈600 G external polarizing magnetic field, which was controlled by a specially designed electronic circuit responsible to flip its direction every 5 min, mainly to eliminate any systematic effects.

De-excitation of the beam particles led to photon emission that was detected by eight (8) EXOGAM Clover detectors, located on a plane and positioned at $\pm 30^\circ, \pm 90^\circ, \pm 130^\circ$ and $\pm 150^\circ$ with respect to the beam axis. The left-right segments of the clover detectors were examined separately to double the number of angular data points in search for an improvement in angular correlation pattern. Furthermore, *gamma*-rays were selected in coincidence with the target particles detected in the plastic scintillator.

The analysis of data and extraction of the information has been described extensively in the past (see e.g. [2]). It is currently under progress and the

results presented in the next section are considered preliminary.

3. Results

Angular correlation data were extracted during the experimental run. The angular correlation function is necessary to extract the logarithmic slope, S. Then the slope is used together with the precession effect, ϵ to deduce the precession angle which is directly related to the g factor of the first 2^+ states in ^{74}Ge and ^{70}Zn. See Ref. [2] for further details.

Relativistic corrections due to high velocities were taken into account. The experimental angular correlation data are plotted in Fig. 1.

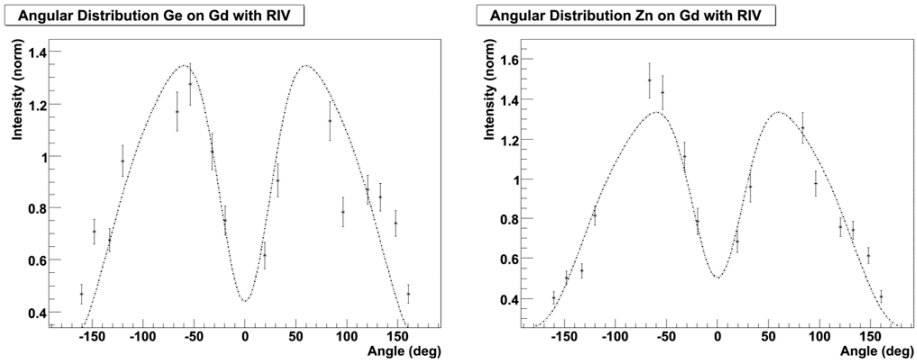

Figure 1: Angular correlation data for ^{74}Ge (left) and ^{70}Zn(right)

The solid lines reflect the best fit to the experimental points of a typical angular correlation function for an E2 transition, $W(\theta)$ of the form:

$$W(\theta) = 1 + a_2 G_2 P_2(\cos\theta) + a_4 G_4 P_4(\cos\theta) \quad (1)$$

where $a_{2,4}$ and $G_{2,4}$ are coefficients needed to be estimated, and $P_{2,4}$ are standard Legendre polynomials. All parameters involved in the kinematics and interactions were taken into account for the best fit estimated by the code GKINT [4] and the current results for ^{74}Ge are:

$$\begin{aligned} a_2^{Ge} &= -0.614 \quad G_2^{Ge} = 0.892 \\ a_4^{Ge} &= -0.211 \quad G_4^{Ge} = 0.639 \end{aligned}$$

while for ^{70}Zn the following values were estimated:

$$\begin{aligned} a_2^{Zn} &= -0.584 \quad G_2^{Zn} = 0.886 \\ a_4^{Zn} &= -0.192 \quad G_4^{Zn} = 0.620 \end{aligned}$$

4. Conclusions

The applicability of the TF parameterization at higher ion velocities reached at RIB factories was studied by means of the angular correlation measurements as a first step in obtaining a reliable parameterization. Previously studied excited states of the ^{74}Ge and ^{70}Zn nuclei, excited by and precessed in Gd foils were used as reference. The experimental results provide well determined values for the angular correlation coefficients needed for the subsequent measurement of the magnetic moments of the excited states in these nuclei. Undergoing analysis [5] is expected to provide the required first excited 2^+ state g factor data to optimize the HVTF calibration for ions traversing ferromagnetic Gd foils at RIB velocities.

Acknowledgements

The author would like to acknowledge partial financial support from the LIBRA project (FP7/REGPOT-230123).

References

[1] N. Benczer-Koller *et al.*, Ann. Rev. Nucl. Part. Sci. 30, 53 (1980)

[2] K.-H. Speidel *et al.*, Prog. Part. Nucl. Phys. 49, 91 (2002)

[3] A.E. Stuchbery *et al.*, Phys. Lett. B 611, 81 (2005)

[4] A.E. Stuchbery, unpublished (2003)

[5] E. Fiori, Ph.D. thesis, (2010) - in preparation

Isoscaling of mass $A \simeq 40$ reconstructed quasiprojectiles from collisions in the Fermi energy regime

S. Galanopoulos, G.A. Souliotis, A.L. Keksis, M. Veselsky, Z. Kohley, L.W. May, D.V. Shetty, S.N. Soisson, B.C. Stein, S. Wuenschel, S.J. Yennello

Cyclotron Institute, Texas A&M University, College Station, TX 77843, USA

Abstract

Isoscaling studies of fragments with Z=1-8 from reconstructed quasiprojectiles of mass $A \simeq$40 from the ^{40}Ca + ^{112,124}Sn and ^{40}Ar + ^{112,124}Sn reactions at beam energy of 45 MeV/nucleon were performed. After initial efforts to obtain isoscaling using pairs of systems differing in their neutron-to-proton ratio N/Z, "intra-system" isoscaling for each of these four systems was obtained using fragment sources restricted in two narrow N/Z zones, one neutron rich and one neutron poor. The observed isoscaling behaviour was excellent and the isoscaling parameter α was found to decrease as the excitation energy increases. Corrections due to undetected neutrons were also taken into account in the source N/Z determination by using the theoretical models DIT (Deep Inelastic Transfer) and SMM (Statistical Multifragmentation Model) along with a software replica of the experimental setup. The reduced isoscaling parameter α/Δ was found to decrease as the excitation energy of the quasiprojectile source increases, in good agreement with recent work on reconstructed mass $A \simeq 80$ quasiprojectiles. This decrease of α/Δ may point to a decrease of the symmetry energy coefficient with increasing excitation energy.

Keywords: Heavy-ion reactions; Isoscaling; reconstructed quasi-projectiles;

1. Inroduction

The nuclear equation of state (EOS) determines the relationship between energy, temperature, density and isospin asymmetry for a nuclear system and is divided into an isospin symmetric contribution ($N \approx Z$) and a symmetry energy part, quadratically dependent on isospin asymmetry [1]. The symmetry energy expressing the energy difference between symmetric nuclear matter and pure neutron matter is not adequately constrained away from the normal nuclear density. The symmetry energy is important in a number of astrophysical topics like the structure and cooling of neutron stars and the dynamics of supernova explosions, as well as in nuclear physics issues like the structure of nuclei away from the the valley of stability. Information on the symmetry energy has been

extracted from the neutron skin, elastic scattering of neutron rich nuclei and from heavy ion collisions [2]. One observable sensitive to the symmetry energy is fragment isotopic compotition investigated in the isoscaling approach [2, 3]. In the isoscaling, which refers to an exponential relation between the yields of a given fragment from two similar reactions which differ only in their isospin asymmetry (N/Z), the effects of the nuclear symmetry energy are isolated in the fragment yield ratios, allowing access of the symmetry energy coefficient during the formation of hot fragments [3].

2. Experiment, analysis and results

The experimental work was performed at the Cyclotron Institute of Texas A&M University. Beams of ^{40}Ar and ^{40}Ca ions of 45 MeV/nucleon were delivered by the K500 superconducting cyclotron and interacted with isotopically enriched ^{112}Sn and ^{124}Sn targets. Fragments produced in peripheral and semi-peripheral collisions were detected by the FAUST multi-detector array. Details on the experimental setup can be found in Ref. [4].

The event-by-event particles detection providing the opportunity to isotopically and kinematically reconstruct the primary fragments. Since FAUST is a charged particle detector, neutrons cannot be detected. As a result, the reconstructed events may have the right atomic number but smaller than the actual mass number, due to the inability of neutron loss. To ensure selection of fragments coming from the decay of quasiprojectiles, the parallel velocity component (with respect to the beam direction) of each individual fragment was required to be greater than the velocity of the c.m. of the projectile-target system. The main criterion for QPs selection was that the total Z of the reconstructed event be close to the Z of the projectile. For the ^{40}Ar+^{124,112}Sn systems the Z range chosen was Z_{QP}=12-21, whereas for the ^{40}Ca+^{124,112}Sn, the corresponding range was Z_{QP}=14-23. Due to limitations in the number of pages of this article, only the ^{40}Ar+^{124}Sn and ^{40}Ca+^{124}Sn systems will be presented. In the upper parts of each panel in Fig. 1, the velocity vs Z_{event} distributions for the reconstructed events are presented, along with the boxes which indicate the Z ranges of the QPs. The lower parts of each panel show the Z_{event} distributions. The intense peaks appear at Z_{event}=5-7 are due to incomplete reconstruction of the selected QPs. The yield ratio $R_{21}(N,Z)$ of a given fragment produced in two similar reactions that differ in the isospin content can exhibit isoscaling which has been observed experimentally [2] and obtained in theoretical studies [3]. Isoscaling occurring when the two reactions take place at the same temperature and differ only in their in the isospin asymmetry according to the relation

$$R_{21}(N,Z) \equiv \frac{Y_2(N,Z)}{Y_1(N,Z)} = C\exp(\alpha N + \beta Z)\ , \qquad (1)$$

where $Y_2(N,Z)$, $Y_1(N,Z)$ are the fragment yields from the neutron rich and the neutron deficient source respectively, α and β are the scaling parameters and C is an overall normalization factor. It is common to consider reaction 2 as the

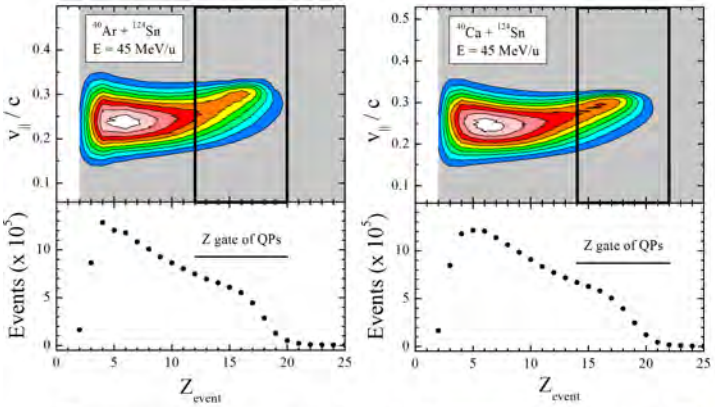

Figure 1: (Color online). Distributions of $v_{||}/c$ versus Z_{event} in the upper part of each panel and Z_{event} distributions in the lower part of each panel, (see text).

neutron rich source, while reaction 1 as the neutron deficient one. The isoscaling parameter α is related to the symmetry energy coefficient C_{sym} of the nuclear binding energy through the relation [5],

$$\alpha = \frac{4C_{sym}}{T}\left[\left(\frac{Z}{A}\right)_1^2 - \left(\frac{Z}{A}\right)_2^2\right] \equiv \frac{4C_{sym}}{T}\ \Delta\ , \qquad (2)$$

where, (Z_1,A_1) and (Z_2,A_2) are the charge and mass numbers from the two systems respectively and T their common temperature. This relation provides the link between the measurable quantities and the nuclear symmetry energy coefficient. It should be pointed out that the parameter α refers to the hot primary fragments which undergo sequential decay into cold secondary fragments, while the parameter Δ represents the difference in the neutron-to-proton composition of the two sources considered in the isoscaling approach.

In this work, we investigated the isoscaling behavior of fragments with Z=1-8. The isoscaling approach of using pairs of systems differing in their N/Z ratio was not good (for details see [6]). In order to improve the isoscaling behavior, our approach was to perform the isoscaling for each system separately using as sources a neutron-rich and a neutron-poor N/Z zone with sufficient statistics. The $(N/Z)_{QP}$ zones for the ^{40}Ar+^{124}Sn reaction were 1.05-1.09 (neutron-rich) and 0.91-0.95 (neutron-poor), while for the ^{40}Ca+^{124}Sn were 1.04-1.08 and 0.92-0.96 respectively, as can be seen in Fig. 2 From the mean N/Z values of the two N/Z zones for each system, the values of the Z/A of the sources were calculated, along with the difference Δ in equation (2). Employing the yields of the fragments from the two QPs sources for each system, the "intra-system" isoscaling behavior was studied in detail. At first, the yield ratios of the fragments from the above mentioned neutron rich and neutron poor QPs sources were investigated for all systems under study. It was found that the yield ratios of the fragments of of the same element as a function of the neutron number can

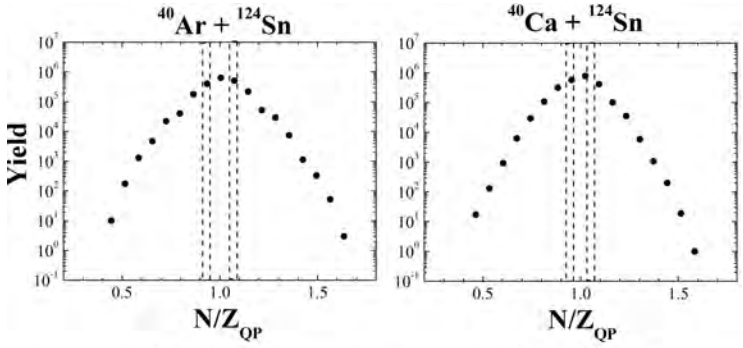

Figure 2: (Color online). Distributions of N/Z of the reconstructed QPs for ^{40}Ar+^{124}Sn and ^{40}Ca+^{124}Sn reaction systems. In each panel, the dashed lines indicate the two narrow $(N/Z)_{QP}$ zones employed in the isoscaling procedure (see text).

be fit by a straight line the slope of which gives the isoscaling parameter α, see Eq. (1). As a next step, the isoscaling for each reaction system was performed at eight excitation energy bins from 1.5 to 8.5 MeV/nucleon with a step of 1 MeV. At each excitation energy bin, the yield ratios of the fragments of the same element were fitted by straight lines whose slopes provide the isoscaling parameter α. As can be seen in Fig. 3, the fit lines are parallel and equidistant in the semilogarithmic plots, indicating an excellent isoscaling behavior. In the upper panel of Fig. 3, the isoscaling of the corresponding reactions is presented without excitation energy cuts.

The isoscaling parameter α is related to the symmetry energy coefficient C_{sym} through (2), which is now written in the form $\alpha/\Delta = 4C_{sym}/T$, where α/Δ is the reduced isoscaling parameter. The α/Δ parameter was determined for each reaction under study. However, the neutrons produced in the reactions could not be detected by the experimental setup. For this reason, Δ has to be corrected for neutron loss. The correction in Δ was performed employing the theoretical models DIT (Deep Inelastic Transfer) and SMM (Statistical Multifragmentation Model), along with the Faust filter software which takes into account the geometry of the setup and the energy thresholds of the detectors used in the experiment.

Using the corrected Δ values along with the isoscaling parameters α, the corrected reduced isoscaling parameter α/Δ was determined at each excitation energy bin. The values of α/Δ as a function of the quasiprojectile excitation energy for each system are shown in Fig. 4 As we see in the left panel of Fig.4, the values of the corrected α/Δ decrease as the excitation energy of the QPs increases for all reaction systems studied in this work. Also, the values of α/Δ obtained in our recent work on mass $A \simeq 80$ show the same trend in good agreement with the results of the present work. We note that the N/Z correction procedure followed was based on measured neutron multiplicities, whereras in this work was performed via the DIT/SMM/filter simulation procedure.

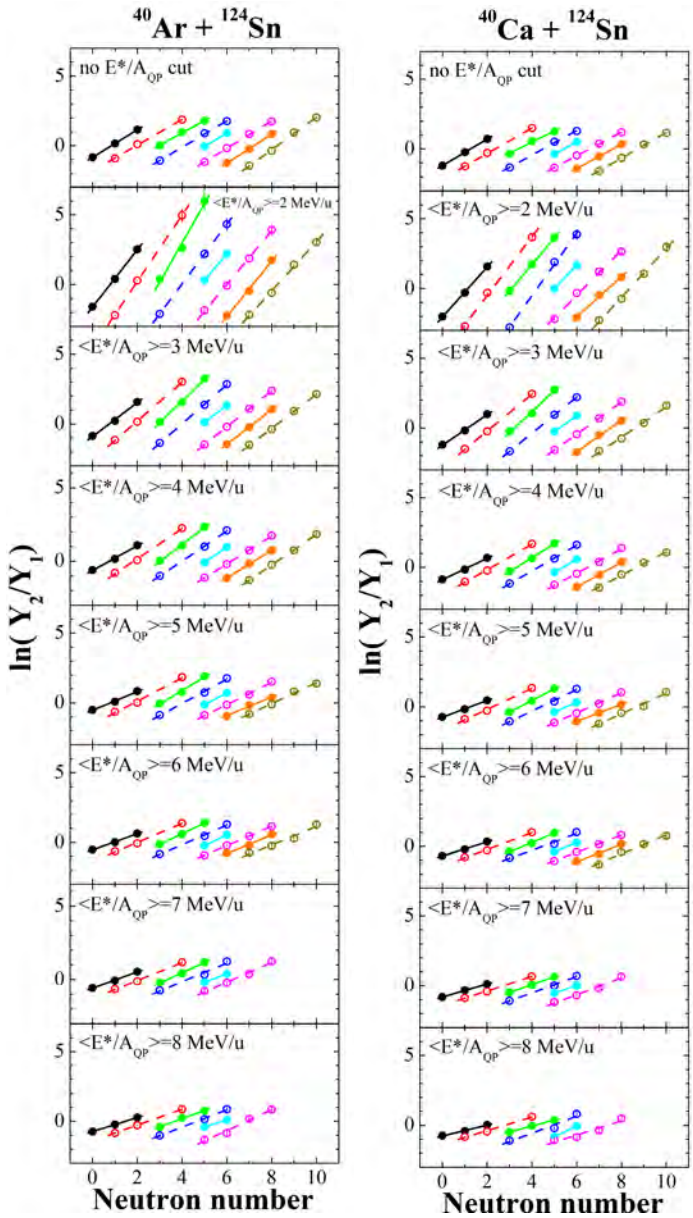

Figure 3: (Color online). Isotopic yield ratios of fragments from reconstructed sources (quasiprojectiles) for the ^{40}Ar+^{124}Sn and ^{40}Ca+^{124}Sn reactions at 45 MeV/nucleon. The isoscaling was performed using fragments from the neutron-rich and neutron-deficient N/Z bins for 8 excitation energy bins (see text). In the upper panels, the isoscaling without the excitation energy cuts is presented for comparison.

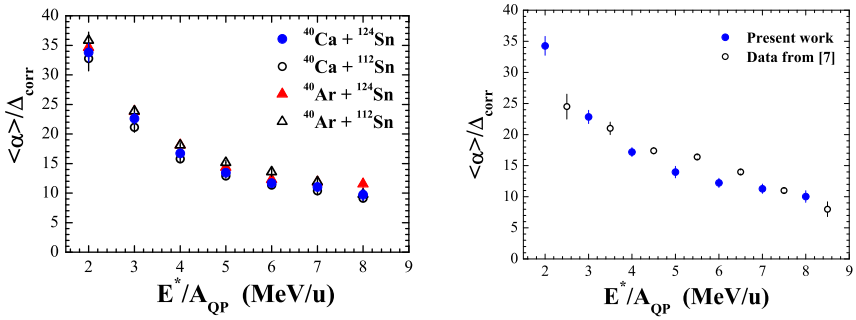

Figure 4: (Color online). Left panel: Reduced isoscaling parameter α/Δ as a function of the excitation energy of the fragmenting sources for the four systems studied in this work. Right panel: Comparison of the averaged value of α/Δ parameter obtained from data of this work with corresponding data from [7].

3. Summary

In this work, a systematic study of fragment isoscaling in reconstructed QPs of mass $A \simeq 40$ obtained in peripheral collisions of ^{40}Ca + ^{124,112}Sn and ^{40}Ar + ^{124,112}Sn reactions at 45 MeV/nucleon. Intra-system isoscaling for each reaction system was performed using as QPs sources two narrow N/Z regions (one neutron-rich and one neutron-poor). The isoscaling behavior was excellent and the isoscaling parameter α was found to decrease with increasing excitation energy. Correction for neutron loss of the N/Z of the sources was performed and was applied to the determination of the parameter Δ. The reduced isoscaling parameter α/Δ was found to decrease with increasing the excitation energy of the QPs source, in good agreement with the recent work on reconstructed mass $A \simeq 80$ QPs [7]. This consistent decrease of α/Δ may indicate a possible decrease of the symmetry energy coefficient with increasing excitation energy.

References

[1] B.A. Li, L.W. Chen and C.M. Ko, Phys. Rep. **464** (2008) 113.

[2] D.V. Shetty, et al., Phys. Rev. C **76** (2007) 024606.

[3] M.B. Tsang et al., Phys. Rev. Lett. **86** (2001) 5023.

[4] F. Gimeno-Nogues et al. , Nucl. Instr. Meth. A **399** (1997) 94.

[5] A.S. Botvina, et al., Phys. Rev. C **65** (2002) 044610.

[6] S. Galanopoulos et al., Nucl. Phys. **A837** (2010) 145.

[7] S. Wuenschel et al., Phys. Rev. C **79** (2009) 786.

High sensitive depleted MOSFET-based neutron dosimetry

M. Fragopoulou[1], Konstantakos V.[1], M Zamani[1], S. Siskos[1], T. Laopoulos[1]and G. Sarrabayrouse[2,3]

[1]*Aristotle University of Thessaloniki, Physics Department, 54124 Thessaloniki, Greece*

[2]*CNRS; LAAS; 7 avenue du colonel Roche, F-31077 Toulouse, France*

[3]*Université de Toulouse; UPS, INSA, INP, ISAE; LAAS; F-31077 Toulouse, France*

Abstract

A new dosemeter based on a depleted Metal-Oxide-Semiconductor field effect transistor, sensitive to both neutrons and gamma radiation was manufactured at LAAS-CNRS Laboratory, Toulouse France. In order to be used for neutron dosimetry a thin film of lithium fluoride was deposited on the surface of the gate of the device. The characteristics of the dosemeter such as its response to neutron dose were investigated. The response in thermal neutrons was found to be high. In fast neutrons the response was lower than that of thermal neutrons but higher than the one presented in literature.

1. Introduction

Metal-Oxide-Semiconductor Field Effect Transistor (MOSFET) dosemeters have numerous advantages such as: low cost, small size and weight, robustness, accuracy of measurement, real-time or delayed direct read-out, information retention with small fading, possibility of integration with other sensors and/or circuitry. In addition they can be used without power supply during irradiation i.e as passive dosemeters for dose measurements of large ranges, which is very important for a dosemeter. These advantages prove that MOSFET's can be successfully applied in dosimetry. They have been used in several application fields [1,2] especially in gamma and neutron dosimetry. It was found that this kind of dosemeters are not significantly influenced by neutrons [3] and the response, if any, is mainly due to the interaction of neutrons with the packaging [4, 5]. However they can be used as a neutron dosemeter when an appropriate converter is applied [6-8]. In addition, by

using two dosemeters, with and without LiF converter, gamma rays can easily be discriminated by neutrons.

In literature thermal neutron doses measured by MOSFETs are rarely presented. The published data show that the response to fast neutrons is very low (of the order of 0.01 mV/mGy) due to the large distance between the converter and the detector [5, 8]. In addition, the lower detectable dose of these dosemeters is very high, about 1mSv. Especially for personal dosimetry the lower detectable dose is a very important parameter as it is required to be as low as possible for practical applications. Therefore, the study of the characteristics of MOSFET's have to be continued, even for lower doses, in order to be applied in gamma and neutron dosimetry.

In the current study in order to increase the MOSFETs sensitivity in neutron dosimetry LAAS have create a new set of MOSFETs and covered by a layer of LiF. These MOSFETs are of depletion type – their chanel is pre-fabricated – presenting a positive threshold voltage and they have a thick gate insulator. They can be used for both thermal and intermediate-fast neutron dosimetry. The effect of neutron irradiation on the threshold voltage of these new transistors was studied in order to determine their sensitivity.

2. Experimentals

The p-type depleted MOSFETs with 1.6 μm thick gate insulator studied in the present work were developed at LAAS-CNRS, Toulouse. As it is known from previous studies in the literature thick SiO_2 p-MOSFETs present a high negative threshold voltage of the order of several Volts [9]. The p-MOSFETs used in the present study were fabricated following a process designed for improving both sensitivity to radiation dose and stability and operate with a positive threshold voltage. A 3 μm thick LiF converter was deposited on the surface of the MOS gate in order to be able for neutron dose measurements. With this converter neutron doses of thermal up to fast neutrons can be determined, from the charge collection of the alpha particles' emitted via the $^{6}Li(n,\alpha)^{3}H$ reaction. The alpha particles cause electron-hole pairs in the insulator. Recombination of the generated pairs takes place and those holes which escape recombination are trapped close to the oxide-silicon interface. As a result, the positive charges which are stored in the gate oxide lead to a shift of the

transistor threshold voltage V_T. The threshold voltage shift, ΔV_T, which is the measured quantity, depends upon the incident particle type and energy, the ionizing particle penetration into the oxide, the absorbed dose, the gate bias during irradiation, the gate insulator thickness, the temperature during measurement and processing parameters. Irradiations were performed at different positions inside the subcritical reactor of the Nuclear Physics Laboratory of the Physics Department/Aristotle University of Thessaloniki, Greece. In order to measure thermal neutrons and intermediate-fast neutrons, 2 dosemeters were irradiated at the same position inside the sub-critical reactor. The first sensors were in contact with LiF converter, while the second was additionally covered by 1mm thick Cd layer. The Cd covered detector was used to measure the response of the dosemeters to intermediate-fast neutrons. The response of the dosemeters to thermal neutrons can be obtained by subtracting the shift of V_T of Cd covered from Cd un-covered detector.

An automated instrumentation configuration based on a small microcontroller was used to collect data from multiple measurements [10]. During measurement the MOSFETs were diode connected (gate and drain grounded) while the source was fed by a constant current of 100 μA. The difference ΔV_{out} between output voltages, taken from the source terminal, before and after irradiation corresponds directly to the threshold voltage increment and can be connected to the dose absorbed by the device in the time interval between the two measurements.

3. Results and Discussion

The response of a MOSFET dosemeter can be influent by applying a voltage to the gate of the transistor during the radiation exposure. In personal dosimetry an unbiased dosemeter is preferable and for that reason in these experiments the irradiated dosemeters were chosen to be unbiased. For this exposure mode, usually called zero bias mode, the expected response of the voltage shift ΔV_T follows a power-law [5,11]:

$$\Delta V_T = \alpha D^b \qquad (1)$$

Parameters a and b were experimentally determined. Parameter b was found to be close to the unity then the response of the MOSFETs can be expressed by parameter a.

In order to detect neutrons, the p-MOSFETs with LiF converter were irradiated by thermal and intermediate-fast neutrons in calibrated neutron mixed fields. For the conversion of neutron fluence to ambient dose equivalent, appropriate conversion coefficients neutrons to *H*(10)*, for thermal and intermediate-fast neutrons, was used [12]. The threshold voltage shift, of the MOSFET dosemeters with LiF converter was measured. The corresponding component to gamma rays was subtracted from the total MOSFETs response.

In each position of irradiation the calibrated neutron field contains an almost equivalent number of intermediate-fast and thermal neutrons. The LiF converter mainly was used for thermal neutron detection, because of the high Li (n, a) reaction cross section in thermal neutrons (about 10^3 barns for ^{6}Li). However the same converter can also be applied for the detection of intermediate-fast neutrons although the reaction cross section is much lower than the corresponding to thermal neutrons, but not negligible, of the order of 1 barn. Therefore two MOSFET dosemeters with LiF layer were irradiated in each position. The one of them was additionally shielded with Cd layer of 1 mm in thickness, which absorbs the 90% of thermal neutrons. By this detector arrangement it is possible to take information about the response of the dosemeters to intermediate-fast neutrons. While from the subtraction of the voltage shift of the Cd covered dosemeter from the Cd un-covered one the response to thermal neutrons can be deduced. The threshold voltage shift as a function of neutron dose, for both thermal and intermediate-fast neutron components, is presented in Figs 1.a and 1.b respectively. A power function fitted the response curve and the results are presented in table 1. Parameter b for thermal neutrons was found to be close to 1, (1.13 ± 0.001), indicating the linear behavior of the threshold voltage variation with neutron dose. In the case of fast neutrons the fitting of the response curve was performed after the subtraction of gamma ray contribution. Parameter b was found to be around 1, (0.97 ± 0.002) which was very close to the behavior of irradiated MOSFETs by gamma rays.

The response of the dosemeters to thermal neutrons was found by the same practice as in the previous experiments [11]. Its value was found to be 1.58 mV/mSv (8.13 mV/mGy), much higher than their response to intermediate-fast neutrons which is 0.017 mV/mSv (0.22 mV/mGy). These values show that the response of the MOSFETs was improved compared to the response obtained in previous studies in which LiF powder was deposited on the gate surface [13]. This response is also higher

than previously reported in the literature with different neutron converters such as Gd in which the sensitivity to thermal neutrons was found to be 1.5-.1.6 mV/mGy [7]. Although pin diodes are not of the same construction their response presented lower than that of the MOSFETs studied in this work (40 kΩ.cm, 5 V/Gy especially for thermal neutrons) [14].

The almost linear behavior of the MOSFETs response curve to intermediate-fast neutrons can be shown in fig. 1b. The sensitivity resulted by the estimated parameter a, was found to be 0.0165 ± 0.001 mV/mSv. This value was clearly lower than that obtained for thermal neutron, Table 1. The effect can be attributed to the lower ^{6}Li (n, a) reaction cross section at intermediate-fast neutrons. The new p-MOSFETs are operating in depletion mode compared to the enhancement mode ones studied in previous experiments and they present a response lower than the one reported for fast neutrons using a polyethylene converter (0.01 V/Gy) [5].

Conclusion

p-MOSFETs are promising devices for their use in radiation dosimetry. In order to improve their characteristics and prolonged their use in neutron dosimetry new p-MOSFETs were fabricated at LAAS-CNRS Toulouse, France. They had 1.6 μm thick gate oxide and positive threshold voltage. To enhance the sensitivity to neutrons a layer of 3 μm LiF was evaporated on the surface of the transistors gate. These dosemeters working in the unbiased mode present high response to thermal neutrons, which is about two orders of magnitude higher than the measured one for intermediate-fast neutrons.

An important result deduced from this study is the almost linear response of the new p-MOSFETs observed. This behavior is valid for a wide neutron dose range, from μSv up to Sv giving good flexibility to use p-MOSFETs in personal dosimetry as well as for environmental monitoring. Further study dedicated to the lower detection limits has to be done in order to be used for personal dosimetry.

References

[1] G. Sarrabayrouse, S. Siskos, 1998. IEEE Instr. Measur. Magaz.1(3) (1998) 26.
[2] I. K. Kwan, et. al., Rad. Measurments 43 (2008) 929.
[3] F. Vettesse, C. Donishak, P. Bourgeault and G. Sarrabayrouse, IEEE Trans. Nucl. Sci., 43, 3, part 1(1996) 991.

[4] A. B. Rosenfeld, M. G. Carolan, G. I. Kaplan, B. J. Allen and V. I. Khivrich, IEEE Trans. Nucl. Sci. 42, No. 6 (1995)1870.
[5] F. Ravotti, M. Glaser, M. Moll, Ch. Ilgner, B. Camanzi, and A.G. Holmes-Siedle, IEEE Tran. Nuc. Sci. 52, No 4 (2005) 959.
[6] S. Kronenberg, and G.J. Bruker, IEEE Tran. Nuc. Sci. 42, No 1 (1995) 20.
[7] N. H. Lee, S. H. Kim, G.U. Youk, I.J. Park , Y.M. Kim, Rad. Prot. Dos. 110 (2004) 277.
[8] R.A. Price, C. Benson, M.J. Joyce, D.J. Kestell, J. Silvie, Rad. Prot. Dos. 110 (2004) 283.
[9]http://www.tyndall.ie/projects/radfets/ds1000.html
[10] P. Tsardaklis, Th. Laopoulos, S. Siskos, G. Sarrabayrouse, Instrumentation and easurement Technology Conference (IMTC 2006), Sorrento, Italy 24-27 April 2006.
[11] M. Fragopoulou V. Konstantakos, M. Zamani, S. Siskos, T. Laopoulos, G. Sarrabayrouse, Nuclear Inst. and Methods in Physics Research A 621 (2010) 611-614
[12] G. Leuthold, V. Mares, and H. Schraube,Rad. Prot. Dos. 40 (1992) 77.
[13] M. Fragopoulou, S. Siskos, M. Manolopoulou, M. Zamani and G. Sarrabayrouse, Rad. Measurements 44 (2009) 1006-1008
[14] A. Rosenfeld et. al. Rad. Prot. Dos 84, 1-4 (1999) 349.

Table 1.

Characteristics of the new depleted MOSFET dosemeters

Type of radiation	*Applied current*	*Response (mV/mSv)*	*Response (mV/mGy)*	*b parameter*
Thermal neutrons (up to 1eV)	100 μA	1.580 ± 0.002	8.13 ± 0.01	1.13 ± 0.001
Intermediate-fast neutrons (above 1 eV)	100 μA	0.017 ± 0.001	0.22± 0.13	0.97 ± 0.002

Figure Captions

FIG 1a. The response of the depleted p- MOSFET dosemeters to thermal neutrons.

FIG 2b. The response of the depleted p- MOSFET dosemeters to intermediate-fast neutrons

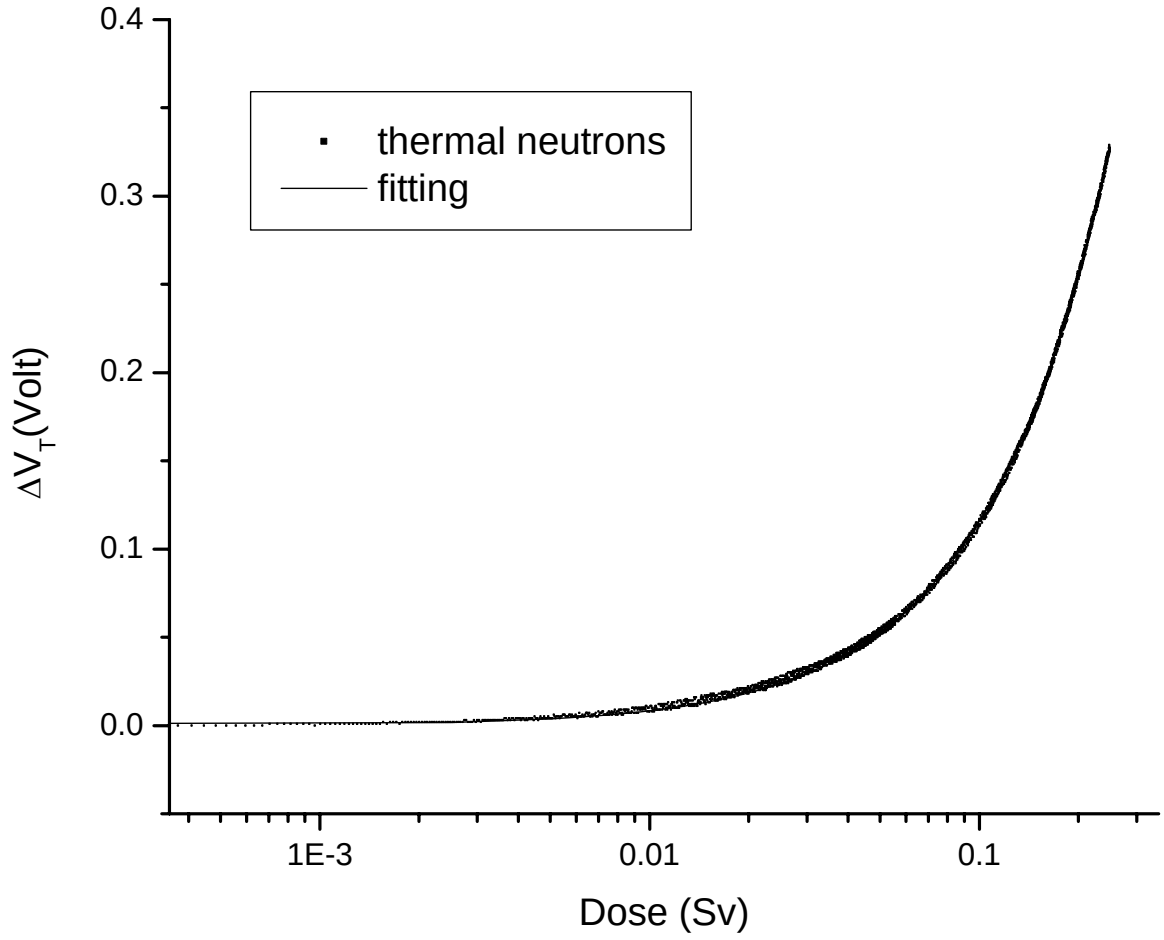
0.4
0.3
0.2
0.1
0.0
ΔV_T(Volt)
thermal neutrons
fitting
1E-3
0.01
0.1
Dose (Sv)

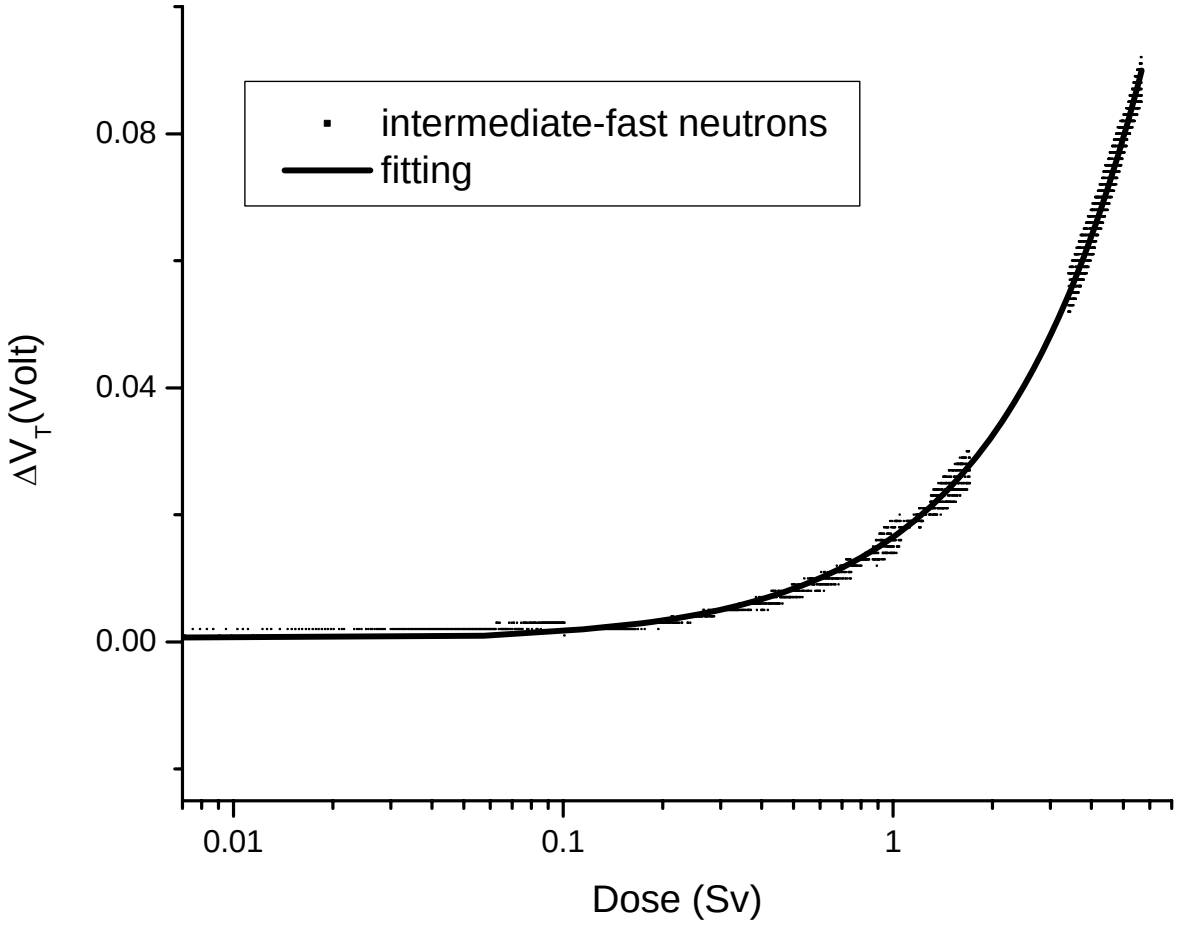
intermediate-fast neutrons
fitting
0.08
0.04
0.00
ΔV_T(Volt)
0.01
0.1
1
Dose (Sv)

Gamma spectrometry technique for the determination of residence time in Submarine Groundwater Discharges

G. Eleftheriou[a,b*], C. Tsabaris[a], D. Patiris[a], E. Androulakaki[b],M. Kokkoris[b], R. Vlastou[b]

[a]*Hellenic Centre for Marine Research, Institute of Oceanography, 19013 Anavyssos, Greece*

[b]*National Technical University of Athens, Dep. of Applied Mathematics and Physics, 15780 Zografou, Greece*

Abstract

The evaluation of time period that meteoric water remains in the ground (residence time) before exiting in the open sea can be a valuable information for the submarine groundwater discharges (SGD) in the costal zones. Coastal waters contain elevated dissolved activities of radium isotopes compared to the open ocean, where excess activities are zero. Lately it has been shown by Moore et al., that residence time can be estimated by a model based on radium radioisotopes ratio reduction throughout the coast. However the standard methods for the estimation of radium isotopes concentration in the water are sophisticated, time consuming or require big amount of sample. Hereby, a method based on the direct gamma ray spectrometry of untreated water samples from coastal areas is applied to determine the residence time of the SGD. Efficiency calibration of the spectrometry set up has been performed for two different volumetric sample geometries, using ^{152}Eu/^{154}Eu solution as reference source. In order to ensure the reliability of the method, the background courting rate magnitude and variance through time have been defined for the radioisotopes of interest. Additionally, the minimum detectible activity (MDA) of the measuring system was determined, in Becquerel per cubic meter, as a function of energy in water samples. The developed method was applied and validated for water samples from the submarine spring in Stoupa Bay, southwestern Peloponnesus. The defined residence time varies from 3 to 6 days, being in good agreement with the results of the standard geological pigment-tracer method.

Keywords: residence time; SGD; gamma ray spectrometry; HPGe; ^{224}Ra /^{228}Ra AR ; MDA; Stupa Bay

* Corresponding author.
Tel.: +30 -210- 772- 3783; *Fax*: +30 -210- 772- 3025; *E-mail address*: gelefthe@central.ntua.gr (G.Eleftheriou).

1. Introduction

The last decades it has been clarified that Submarine Groundwater Discharges (SGD) are a phenomenon of crucial importance for coastal – inland hydrology and responsible for many oceanic and environmental processes. Only recently the use of radiotracers for the investigation of SGD has been established as a very effective scientific tool. Among the natural radiotracers, Radium isotopes can be considered as the most suitable, with various applications in oceanic, costal and estuary environmental studies [1, 2].

The time that groundwater remains underground before it exits at the costal seabed is a parameter of great interest, not only for understanding the local hydrology in regional scale, but the water cycle budget in wider scales. However, the quantitative approximation of this magnitude is rather complicated and not yet well established. Among many definitions, residence (or flushing) time of groundwater has been widely used in many field studies, where it can be derived through the ratio calculation of radium isotopes in water samples [3]. In specific, measurements of the radium radiotracers ^{224}Ra and ^{228}Ra with vast decay rate variance - 3.66 days and 5.7 years respectively - at the groundwater input coastal zone (Flux) and at the mixing/decay balance intermediate zone (Inventory) provide the ^{224}Ra /^{228}Ra activity ratio (AR) for samples isolated from fresh inputs of Ra. Residence time can then be calculated from the equation:

$$T_w = \frac{\left[F\left({}^{224}\mathrm{Ra}/{}^{228}\mathrm{Ra} \right) - I\left({}^{224}\mathrm{Ra}/{}^{228}\mathrm{Ra} \right) \right]}{I\left({}^{224}\mathrm{Ra}/{}^{228}\mathrm{Ra} \right)\lambda_{224}} \quad (1)$$

where λ_{224} is the is the decay constant of ^{224}Ra (0.19 d^{-1}). The model is based on the fact that both isotopes are lost from the system by mixing, but only ^{224}Ra is lost by radioactive decay, as well as the assumption that the system is in steady state so the mixing and decay terms along with fresh Ra inputs are incorporated into the residence time equation.

The standard techniques for the Ra isotopes concentration measurement are using water samples pre-concentration and/or infiltration in Ra-absorption filters, using α, β and, lately, γ spectrometry [4-6]. Although the above methods are steady and reliable, they are also time consuming, expensive and present sampling difficulties. In this work we investigate the possibility of indirect determination of the radium radioisotopes concentration in water, throw the direct measurement of natural water samples with high resolution HPGe detector. Assuming radioactive equilibrium, ^{224}Ra and ^{228}Ra ratio can be indirectly calculated by the gamma radioactive daughters ^{208}Tl and ^{228}Ac, respectively. Subsequently, residence time can be estimated from the equation (1), replacing the ^{224}Ra /^{228}Ra ratio by the ^{208}Tl/ ^{228}Ac ratio.

2. Materials and method

Two different volumetric containers of 0.615 L and 2.265 L, from high pressure toughness pyrex-glass, where used for the water samples collection. The samples where measured placed vertically on the window of a coaxial p-type high purity Ge detector (GEM-FX8530P4, Ortec®).

The detector was shielded surround by a lead layer with 23 mm height and 31 mm width. The energy and efficiency calibrations for the two geometries were performed using ^{152}Eu/^{154}Eu solution reference source [7]. Proportion of the source was dissolved in deionized water filling the two containers and the solutions were homogenized mechanically before they were measured for 1 h. The contribution of the ambient background radiation in the experimental spectrums was determined using phantom samples containing only deionized water, while measurements for various measuring times during 7 months period were analyzed (Fig. 2).

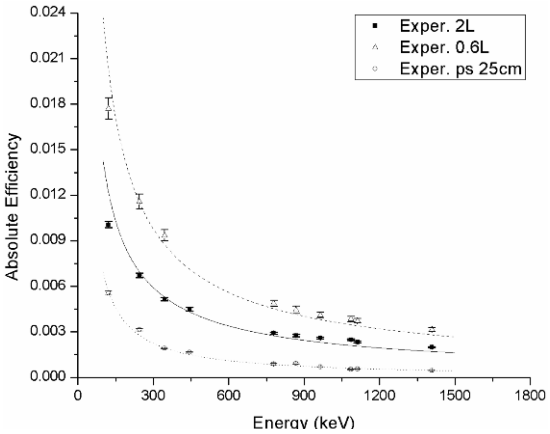

Fig. 1. Experimental efficiency curves of the detection system for point source in 25 cm distance from the detector and for extended volumetric sources (0.615 and 2.265 L) in contact with the detector's window.

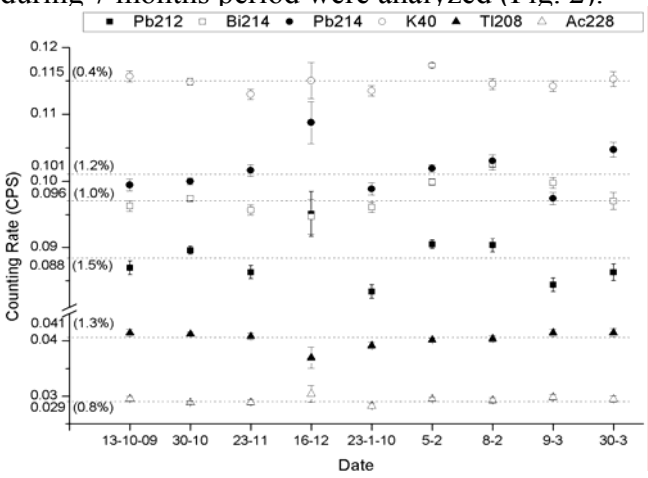

Fig. 2. Time variance estimation of the main background radioisotopes influence in the spectrum from their stronger photopeak.

The estimation of the residence time according the equation (1) demands the calculation of the ^{224}Ra /^{228}Ra ratio in one water sample from the SGD flux point and in another sample, from a typical inventory point. Taking into account that there is not any physical reason for selective enrichment of a particular isotope consequent ^{224}Ra and ^{228}Ra natural radioisotopes series it can be assumed radioactive equilibrium between the Ra isotopes and their progenies at the instant of the samples collection. The concentrations of ^{224}Ra and ^{228}Ra are then proportional to the concentrations of ^{208}Tl and ^{228}Ac, respectively, as well as and their ratios. ^{208}Tl and ^{228}Ac concentrations in the water samples can be derived from gamma ray spectrometry, namely from the counting rate of their more intense photopeaks – at 583.19 keV and 911.16 keV respectively – having subtracted the background spectral contribution in these energies. The ^{224}Ra /^{228}Ra ratio in each sample is then equal to the deviation of these two counting rates (e.g. $(^{208}\mathrm{Tl})_{cpd}$/ $(^{228}\mathrm{Ac})_{cpd}$ for counts per day) multiplied with a constant that includes the photopeaks intensities and efficiencies. Finally, after of the deletion of this constant factor, the equation (1) becomes:

$$T_w = \frac{\left[F\left(\left(^{208}Tl\right)_{cpd}\Big/\left(^{228}Ac\right)_{cpd}\right) - I\left(\left(^{208}Tl\right)_{cpd}\Big/\left(^{228}Ac\right)_{cpd}\right)\right]}{I\left(\left(^{208}Tl\right)_{cpd}\Big/\left(^{228}Ac\right)_{cpd}\right)\lambda_{^{224}Ra}} \qquad (2)$$

where λ_{224} is the is the decay constant of ^{224}Ra (0.19 d^{-1}).

For the residence time estimation two water samples from the flux and the inventory regions of the examined SGD were measured, along with background radiation correction. Because of the small Ra concentration in the environmental samples and in order to prevent the short lived ^{224}Ra loss, the measurements were performed in less than 5 days period from the samplings. Decay correction of the ^{208}Tl counting rate was also performed, taking into account the time between sampling and measurement, as long as the measuring time itself.

3. Study area

The aforementioned method was implied and tested at a submarine spring in the Bay of Stoupa, located in southwestern Peloponnese, in Messinia prefecture (Fig. 1). Many locations of submarine groundwater discharge are easily visible on the sea surface around the bay, while the largest groundwater source is located about 100 m offshore with a strong SGD emanating from fissures in the bedrock at roughly 25 m depth. The submarine spring was first reported in 1975, although local inhabitants claim that the spring have never stopped emanating water during, at least, the past 60 years. The study area is easily reached by a small boat and divers were recruited to grab water samples throughout one year period (2009 - 10). In each campaign, two water samples were collected directly from the spring exit (Flux) and from a random point of the water accumulation/mixing area (Inventory), at 25 and 10 m depth respectively.

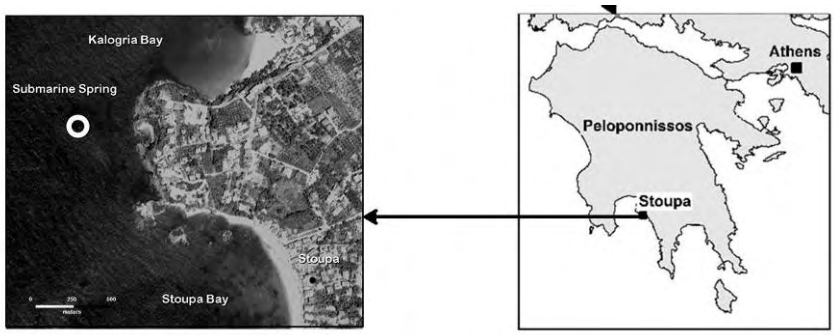

Fig. 3. The location of the studied costal submarine spring of Stupa Bay in southwestern Peloponnesus.

4. Results

The developed method was carried out in order to provide an alternative and effective way for the estimation of the residence time in costal SGD. The method's possibilities and limitations were examined by the determination of the minimum detectible activity (MDA) of the detection system. A comparison with a standard geological method was also performed for the estimation of the groundwater residence time of a submarine spring in Stoupa.

4.1. Minimum detectible activity

According to the analysis of the background radiation (Fig. 2), the variation of the counting rate for all important radioisotopes does not exhibit 1.5 %, for both extended geometries. However, the capability of the measuring system to detect additional radiation is also depend

on the detector efficiency for the specific set up and the sample magnitude. Mathematically, based on the Currie formula [8], the minimum detectible activity (MDA) of volumetric water samples in Bq/m^3 is given by the equation [9]:

$$\mathrm{MDA} = \frac{L_D}{\varepsilon \cdot V \cdot I_\gamma \cdot T} \tag{3}$$

where L_D is the detection limit (in counts), T is the acquisition time (in sec), I_γ the emission probability of the detected γ-ray, V the volume of the sample (m^3) and ε is the absolute efficiency.

The mean MDAs have been calculated for the dominant ambient radioisotopes, by appling equation (3) to the data from the systematic analysis of the background spectrums for the two sample geometries, (Fig 4a). Additionally, the dependence of MDA from the time was also examined, by measuring deionized water samples for acquisition time varying from same hours to few days (Fig. 4b). From the results of the study it is shown that one day measurement of water samples placed in the big container are the more suitable set up form the needs of the developed method, achieving a ~2.5 Bq/L lower Ra concentration threshold.

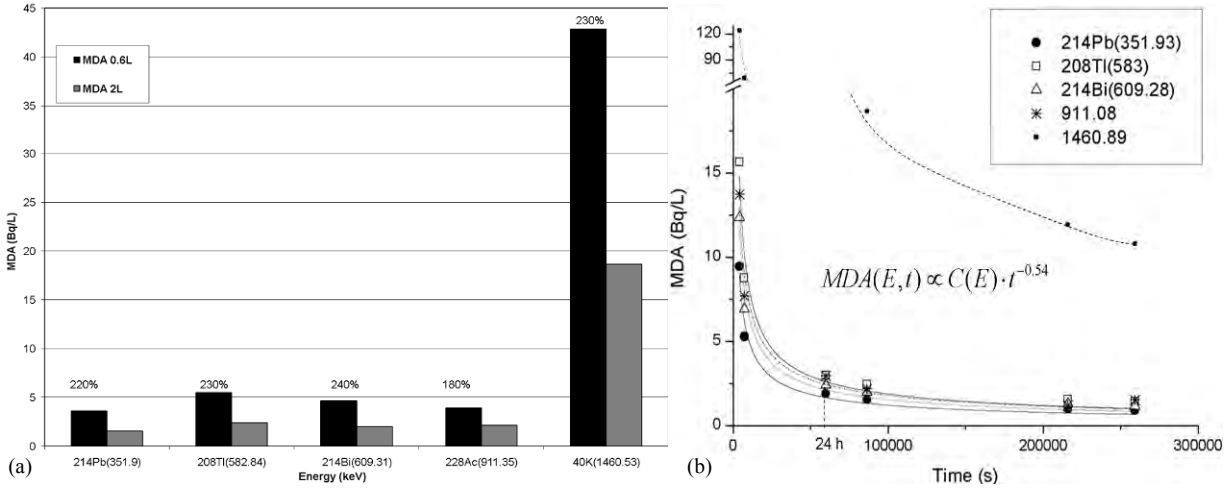

Fig. 4. MDA of some isotopes of interest calculated from their main photopeaks: a) comparison between measurement set up of the two water sample containers and b) dependence from the measuring time.

4.2. Models comparison

Samples from the submarine spring in Stoupa, from the flux and the inventory region were measured according the developed technique and the residence time was calculated (Table 1).

Table 1

Residence time estimation according the developed method (equation 2) of the submarine spring in Stoupa, for different sampling period.

Sampling date	8-Oct-2009	13-Nov-2009	18-Jan-2010	3-Mar-2010	23-Mar-2010	12-May-2010	12-May-2010
Residence time (d)	4.5 ± 2.4	5.7 ± 2.9	3.4 ± 2.0	4.8 ± 2.2	2.7 ± 1.8	3.8 ± 1.6	3.8 ± 1.6

The residence time varies from 3 to 6 days, while the mean value was found 4.6 ± 1.7 d for the period from Oct. 2009 to May 2010. The relative error of the estimation was approximately 50%, due to the low Ra activities in the water samples.

Experimental estimation of the residence time was also performed, using the standard geological pigment-tracer method. Namely, large quantity (~ 4 kg) of fluorescent substance (pigment) was shed at the nearest mountainous karst opening, where terrestrial flowing water sinks underground. Later on, samples from terrestrial costal springs were collected on regular base for several days, in which the concentration of the fluorescent substance was determined. The average residence time was calculated from the exponential decrease of the pigment concentration in the samples; and found to be approximately 5.5 d.

5. Conclusions and discussion

The developed method for the estimation of residence time in SGD described here is based on the direct gamma spectrometry of untreated water samples. The method is reliable for quantitative analysis of radium rich waters (> 2.5 Bq/L). For small concentrations the statistical errors rise up to 50%, though it can provide the upper threshold of the ^{224}Ra and ^{228}Ra activity. The comparison between the two different volumetric geometries shows that measurements of water samples with 2 L container are having reduced detection efficiency in all the gamma rays energy range than with the 0.6 L container, but they provide a MDA improvement by a factor of two for the radium isotopes. The application of the method in the Stoupa Bay submarine spring concluded with a annual mean residence time of 4.6 ± 1.7 d, being in very good agreement with the pigment-tracer method.

The main advantage of the described method is that it is straightforward, quick and economic, as requires a small amount of water samples and no chemical or physical samples treatment. From the other hand, it is strongly dependent from the sampling technique and point selection, as well as demands elevated radium concentration. Consequently, it can be said that the method is suitable and robust for point source SGD with nitense flux. The method is expected to be improved for further shielded detection system, while other geometries (e.g. Marinelli) can be tested in order to extend its applicability in more diffusive SGD cases.

Acknowledgments

The research work described in this paper took place in the framework of the "*Integrated marine and terrestrial study for the quantitative and qualitative characterization of the submarine groundwater spring in Stoupa, Lefktro Municipality, Messinia Prefecture*" project of the Hellenic Centre for Marine Research (HCMR). The authors would like to acknowledge the researcher Dr. K. Kalfa for providing the Europium reference source and the Professor G.

Migiro for his collaboration in the comparison of the developed method with the standard geological pigment-tracer method.

References

[1] W.S. Moore, Mar. Chem. 65 (2000) 75.
[2] W.C. Burnett, P.K. Aggarwal, A. Aureli, H. Bokuniewicz, J.E. Cable,,(...), J.V. Turner, Sci. Tot. Environ. 367 (2006) 498.
[3] W.S. Moore, J.O. Blanton, S.B. Joye, J. Geoph. Res. 111 (2006) C09006.
[4] W.S. Moore, Mar Chem.109 (2008)188.
[5] M. Baskaran, G.H. Hong, P.H. Santschi, in: O. Wurl (Ed.), Practical guidelines for the analysis of seawater, Taylor & Francis, New York, 2009, Ch 13.
[6] M. Condomines, S. Rihs, E. Lloret, J.L. Seidel, Appl. Rad. and Isot. 68 (2010) 384.
[7] K. Kalfas, personal communication, 2010.
[8] L.A. Currie, Anal. Chem. 40 (1968) 586.
[9] C. Bagatelas, C. Tsabaris, M. Kokkoris, C.T. Papadopoulos, R. Vlastou, Env. Monit. Assess. 165 (2009) 59.

Application of Information and Complexity Measures to Neutron Stars Structure

K.Ch. Chatzisavvas[1,2], V.P. Psonis[1], C.P. Panos[1], and Ch.C. Moustakidis[1]

[1] *Department of Theoretical Physics, Aristotle University of Thessaloniki, 54124 Thessaloniki, Greece*
[2] *Department of Informatics and Telecommunications Engineering, University of Western Macedonia, 50100 Kozani, Greece*

Abstract

We apply several information and statistical complexity measures to neutron stars structure. Neutron stars is a classical example where the gravitational field and quantum behaviour are combined and produce a macroscopic dense object. We concentrate our study on the connection between complexity and neutron star properties, like maximum mass and the corresponding radius, applying a specific set of realistic equation of states. Moreover, the effect of the strength of the gravitational field on the neutron star structure and consequently on the complexity measure is also investigated. It is seen that neutron stars, consistent with astronomical observations so far, are ordered systems (low complexity), which cannot grow in complexity as their mass increases. This is a result of the interplay of gravity, the short-range nuclear force and the very short-range weak interaction.

Keywords: Shannon Entropy, Disequilibrium, Statistical Complexity, Self-Organisation, Equation of State, Neutron Stars.

1. Information and Complexity Measures

The Shannon information entropy S for a continuous probability distribution $\rho(\mathbf{r})$, denoting a measure of the amount of uncertainty associated with a probability distribution, is defined as

$$S = -\int \rho(\mathbf{r})\, \ln \rho(\mathbf{r})\, \mathrm{d}\mathbf{r}, \tag{1}$$

while the disequilibrium D, being a quadratic distance from equiprobability, is defined as

$$D = \int \rho^2(\mathbf{r})\, \mathrm{d}\mathbf{r}, \tag{2}$$

with dimension of inverse volume [1].

In order to study the statistical complexity defined by López-Ruiz, Mancini and Calbet (LMC), we use a slightly modified definition

$$C = H \cdot D, \tag{3}$$

where $H = \mathrm{e}^S$ is the information content of the system, while the exponential functional preserves the positivity of C [2].

The aforementioned definitions of information entropy and disequilibrium in the case of neutron stars are modified as follows:

$$S = -b_0 \int \bar{\epsilon}(r)\, \ln \bar{\epsilon}(r)\, \mathrm{d}\mathbf{r}, \quad \text{and} \quad D = b_0 \int \bar{\epsilon}(r)^2\, \mathrm{d}\mathbf{r}, \tag{4}$$

where $b_0 = 8.9 \times 10^{-7}$ Km^{-3} is a proper constant satisfying the condition that both information entropy S and disequilibrium should be dimensionless quantities, while $\bar{\epsilon}(r)$ is the dimensionless energy density of the system. It is equivalent to the density mass $\rho(r)$, obtained by solving the structure equations characterising the system [3].

2. Neutron Star Structure Equations and Nuclear Equation of State

In order to calculate the gross properties of a neutron star, we assume that the star has a spherically symmetric distribution of mass in hydrostatic equilibrium and is extremely cold ($T = 0$). Effects of rotations and magnetic fields are neglected and the equilibrium configurations are obtained by solving the Tolman-Oppenheimer-Volkoff (TOV) equations

$$\begin{aligned} \frac{\mathrm{d}P(r)}{\mathrm{d}r} &= -\frac{GM(r)\rho(r)}{r^2}\left(1+\frac{P(r)}{c^2\rho(r)}\right)\left(1+\frac{4\pi r^3 P(r)}{c^2 M(r)}\right)\left(1-\frac{2GM(r)}{c^2 r}\right)^{-1}, \\ \frac{\mathrm{d}M(r)}{\mathrm{d}r} &= 4\pi r^2 \rho(r) = \frac{4\pi r^2 \epsilon(r)}{c^2}, \end{aligned} \tag{5}$$

where $P(r)$ and $M(r)$ are the pressure and the mass functions of the star respectively, The radius R and the total mass of the star, $M \equiv M(R)$, depend on the value of P_c. Also, we have to know the energy density $\epsilon(r)$ (or the density mass $\rho(r)$) in terms of the pressure $P(r)$. This relationship is the equation of state (EOS) for neutron star matter and here, has been calculated applying a phenomenological nuclear model.

In general, the energy per baryon of neutron-rich matter may be written to a very good approximation as

$$\frac{E(n,x)}{A} = \frac{E(n,\frac{1}{2})}{A} + (1-2x)^2 E_{\mathrm{sym}}(n) \tag{6}$$

where n is the baryon density ($n = n_n + n_p$) and x is the proton fraction ($x = n_p/n$). The symmetry energy $E_{\mathrm{sym}}(n)$ can be expressed in terms of the difference of the energy per baryon between neutron ($x = 0$) and symmetrical ($x = 1/2$) matter.

The density dependent potential $V(u)$ of the symmetric nuclear matter is parameterised as follows

$$V(u) = \frac{1}{2}\,Au + \frac{Bu^{\sigma}}{1+B'u^{\sigma-1}} + 3\sum_{i=1,2} C_i \left(\frac{\Lambda_i}{p_F^0}\right)^3 \left(\frac{p_F}{\Lambda_i} - \arctan\frac{p_F}{\Lambda_i}\right), \qquad (7)$$

where p_F is the Fermi momentum, related to p_F^0 by $p_F = p_F^0 u^{1/3}$. The parameters Λ_1 and Λ_2 parameterise the finite-range forces between nucleons, while the parameters A, B, B', σ, C_1 and C_2 are determined using the constraints provided by the empirical properties of symmetric nuclear matter and the saturation density n_0 [4].

To a very good approximation, the nuclear symmetry energy $E_{\rm sym}$ can be parameterised as

$$E_{\rm sym}(u) \simeq 13\,u^{2/3} + 17\,F(u), \qquad (8)$$

where the first term of the right-hand side part of Eq. (8) is the contribution of the kinetic energy and the second term comes from the interaction energy (function $F(u)$ parametrises the interaction part of the symmetry energy).

Now the total energy and total pressure of charge neutral and chemically equilibrium nuclear matter are

$$\epsilon_{tot} = \epsilon_b + \sum_{l=e^-,\mu^-} \epsilon_l, \quad \text{and} \quad P_{tot} = P_b + \sum_{l=e^-,\mu^-} P_l\ . \qquad (9)$$

From equations (9) we can construct the equation of state in the form $\epsilon = \epsilon(P)$. In order to calculate the global properties of the neutron star, i.e. the radius and mass, we solved numerically the TOV equations (5) with the given equations of state constructed employing the present model.

The model of our study, both in the sense of the information and statistical complexity measures, and the neutron star structure equations and nuclear equation of state, along with extensive bibliography, is presented in [3].

3. Results

In Fig. 1(a), we plot the nuclear symmetry energy $E_{\rm sym}$, in Fig. 1(b) the corresponding equations of state and in Fig. 1(c) the mass-radius diagrams for each of the three cases. Actually every pair (R, M) in a mass-radius diagram is the outcome of the structure equations for an arbitrary chosen initial value of the pressure P_c in the center of the star. Thus, varying the value of P_c in a reasonable range, we can have a picture of the behaviour of those substantial structure characteristics. We have to note here that the region where $\mathrm{d}M/\mathrm{d}R < 0$ corresponds to a stable neutron star, while $\mathrm{d}M/\mathrm{d}R > 0$ to an unstable one. Another important feature of a neutron star is the value of $M_{\rm max}$ corresponding to the maximum mass for which the star can exist for the specific equation of state. As displayed in Fig. 1(c), $M_{\rm max}$ is strongly dependent on the equation of state, while a stiffer equation leads to larger $M_{\rm max}$. Note that we vary the parameter

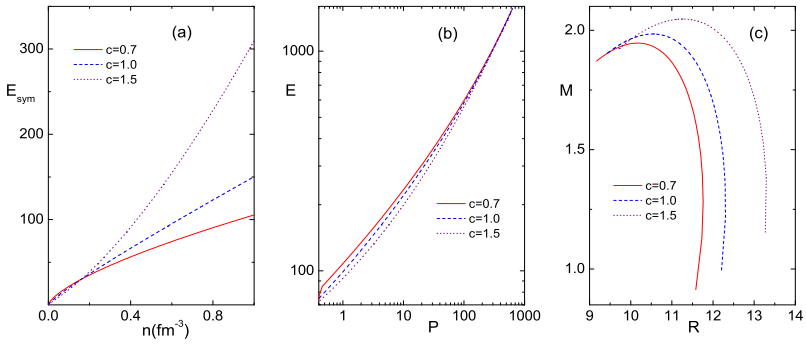

Figure 1: (a) Symmetry Energy vs Baryon Density n, (b) Energy vs Pressure, and (c) Mass vs Radius.

c, which characterises the density dependence of the nuclear symmetry energy, from $c = 0.7$ (soft equation of state) and $c = 1.0$, to $c = 1.5$ (stiff equation of state).

In Fig. 2(a), we present the information entropy S, as a function of the mass M. We find that S is a decreasing function of M in the region denoting a stable neutron star, while in the unstable region S increases with M, as expected intuitively (in Fig. 2(b) we present $H(M)$). In Fig. 2(c) we display the disequilibrium $D(M)$. Increasing M corresponds to greater concentration of the density distribution, its energy density becomes more localised, resulting to a monotonically increasing D. Complexity C, is plotted in Fig. 2(d). C is a monotonically decreasing function of the star mass M. In the unstable region, where $M > M_{\rm max}$, C increases with M, as indicated in the detailed (inset) figure, but this refers to a case with no physical meaning. The most interesting result in this figure is that a neutron star can not grow in complexity as its mass increases towards the limit of $M_{\rm max}$.

This result becomes more striking in the following set of figures, Fig. 3, where we plot in three-dimensions information and complexity measures, as functions of both M and R, taking advantage of the fact that each choice of initial values in the equation of state provides a different pair (R, M), reflecting the competition between the gravitational and degenerate gas pressures. The fact that the most probable radii of a neutron star are close to 10 Km, together with the aforementioned comment on the most likely masses, lead us to the conclusion that a neutron star is in general, a system of minimum complexity. Furthermore, it can not grow in complexity as mass or radius increase inside the regions imposed and commented above. The neutron star is an ordered system.

Finally in Fig. 4, we present the direct dependence of complexity C on the parameters c and G. It is seen from Fig. 4(a) that complexity for a given $M_{\rm max}$, is a decreasing function of the equation of state parameter c, while it increases exponentially with the parameter of the gravitational field Fig. 4(b).

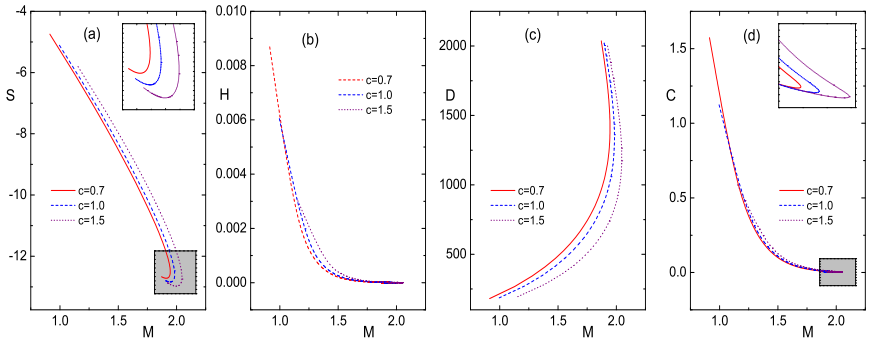

Figure 2: (a) Entropy $S(M)$, (b) Information Content $H(M) = \mathrm{e}^S$, (c) Disequilibrium $D(M)$, and (d) Complexity $C(M)$.

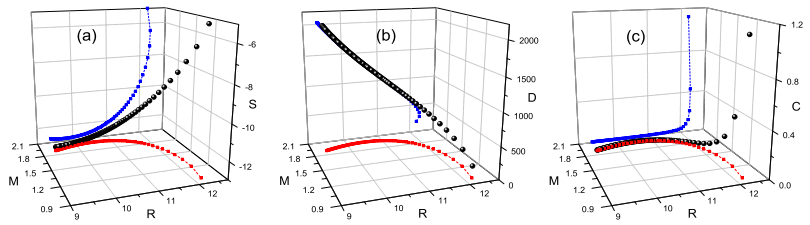

Figure 3: Three-dimensional display of (a) Entropy $S(R, M)$, (b) Disequilibrium $D(R, M)$, and (c) Complexity $C(R, M)$, projected for each case on two planes: (a) $R - M$ and $S - R$, (b) $R - M$ and $D - R$, (c) $R - M$ and $C - R$.

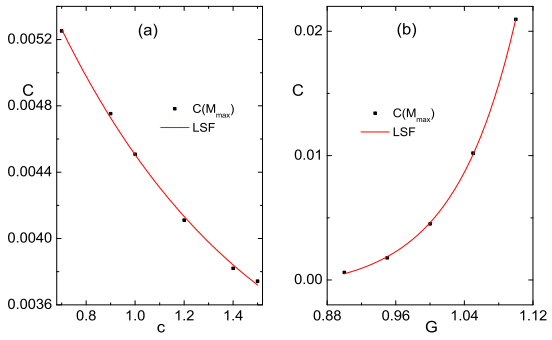

Figure 4: (a) Complexity vs the equation of state parameter c, and (b) Complexity vs the gravitational parameter G, for a given $M = M_{\mathrm{max}} = 1.5\ \mathrm{M}_{\odot}$.

4. Summary

We present a study of neutron stars from the point of view of information and complexity theories [3], continuing a recent application to white dwarfs structure [5]. It is shown that the measures of information entropy S and disequilibrium D can serve as indices of structure of a neutron star. More specifically, S is a decreasing function of the mass of the star, while it is an increasing one of its radius. The result is consistent with the fact that as a neutron star's mass increases, its radius decreases resulting to more localised energy and mass densities. The disequilibrium D shows an inverse behaviour. It is an increasing function of the mass and a decreasing one of its radius. More localised energy and mass densities correspond to a distribution far from equiprobability and as a result the disequilibrium of the system is higher.

The complexity C of a neutron star is a decreasing function of its mass. It almost vanishes for a vast set of pairs of values (R, M), while it increases rapidly for masses less than $1.5M_{\odot}$ and radii greater than 12 km, a not so favourable case for a neutron star (present astronomical observations). The favourable case, for masses larger than $1.5M_{\odot}$ and radii less than 12 km, corresponds to almost vanishing complexity, supporting the conclusion that a neutron star is an ordered system, which cannot grow in complexity as its mass increases.

Furthermore, we investigate the impact of the equation of state parameter c and the gravitational parameter G on S and C. The behaviour of information and complexity measures is equivalent in both cases. Complexity decreases exponentially with the mass, while it increases linearly with the radius. In direct calculations, complexity decreases exponentially with the equation of state parameter c, while it increases exponentially with the gravitational parameter G.

Acknowledgements

K.Ch. Chatzisavvas has been supported by a Post-Doctoral Research Fellowship of the Hellenic State Institute of Scholarships (IKY).

Bibliography

[1] K.Ch. Chatzisavvas, Ch.C. Moustakidis, C.P. Panos, J. Chem. Phys. 123 (2005) 174111.

[2] López-Ruiz, H.L. Mancini, X. Calbet, Phys. Lett. A 209 (1995) 321; R.G. Catalán, J. Garay and R. López-Ruiz, Phys. Rev. E 66 (2002) 011102.

[3] K.Ch. Chatzisavvas, V.P. Psonis, C.P. Panos, Ch.C. Moustakidis, Phys. Lett. A 373, (2009) 3901; and references therein.

[4] V.P. Psonis, Ch.C. Moustakidis, S.E. Massen, Mod. Phys. Lett. A 22 (2007) 1233.

[5] J. Sañudo, A.F. Pacheco, Phys. Lett. A 373 (2009) 807.

Search for $E(5)$ Symmetry in ^{102}Pd

S. F. Ashley[a], S. Harissopulos[a], T. Konstantinopoulos[a], G. de Angelis[c], A. Dewald[b], A. Fitzler[b], N. Marginean[c], M. Axiotis[a], D. L. Balabanski[f], D. Bazzacco[d], E. Farnea[d], A. Linnemann[b], R. Julin[g], G. Kalyva[a], D. R. Napoli[c], C. Rusu[c], B. Saha[b], A. Spyrou[a], C. Ur[d], R. Vlastou[e]

[a]*Institute of Nuclear Physics, Tandem Accelerator Laboratory, NCSR "Demokritos", Aghia Paraskevi, Athens Gr.-153.10, Greece*
[b]*Institut für Kernphysik, Universität zu Köln, Zulpicherstr. 77, Köln, Germany*
[c]*INFN, Laboratori Nazionali di Legnaro, Legnaro, Italy*
[d]*Dipartimento di Fisica dell' Universita and INFN Sezione di Padova, Padova, Italy*
[e]*National Technical University of Athens, Zographou Campus, 157.80 Athens, Greece*
[f]*INRNE, Bulgarian Academy of Sciences, Sofia, Bulgaria*
[g]*Department of Physics, University of Jyväskylä, Jyväskylä, Finland*

Abstract

Lifetimes of the excited states in the yrast band of ^{102}Pd have been determined using the Recoil-Distance Doppler Shift experiment at INFN, Laboratori Nazionali di Legnaro. Excited states in ^{102}Pd were populated by the ^{92}Zr(^{13}C,3n)^{102}Pd fusion-evaporation reaction. Lifetimes were deduced using the Differential Decay Curve method and the corresponding $B(E2)$ values were compared to the $E(5)$ critical-point symmetry, and also the $U(5)$ and $O(6)$ limits of the Interacting Boson Model-1. It is evident that ^{102}Pd agrees poorly with the predicted $E(5)$ symmetry but has a very good (and somewhat surprising) agreement with the $O(6)$ limit.

1. Introduction

Within the classical limit of the Interacting Boson Model, two shape-phase transitions have been predicted. Firstly, between the spherical vibrator and γ-soft rotor limits (referred to as the $E(5)$ symmetry [1]). Secondly, between the spherical vibrator and rigid rotor limits (referred to as $X(5)$ symmetry [2]). These "dynamical" symmetries both occur when the spherical and deformed potentials coexist at the same depth, and both symmetries are modelled around infinite square-wells. In the case of $X(5)$ symmetry,

numerous nuclei show good agreement, both in terms of level energies and $B(E2)$ values, to level scheme predicted in Ref. [2] (see for example [3–5]). A survey for potential $E(5)$ candidates has been performed [6], and with the exception of ^{134}Ba [7], information is lacking on the $B(E2)$ values of the yrast-band transitions in the majority of the candidate nuclei. This paper focusses on the determination of lifetimes in ^{102}Pd, a candidate for $E(5)$ symmetry [6, 8], such that $B(E2)$ values could be extracted and a more inclusive comparison to $E(5)$ symmetry can be made.

2. Experimental Technique and Data Analysis

Intrinsic state lifetimes of various excited states in ^{102}Pd were determined by a Recoil Distance Doppler-Shift experiment that was performed at INFN, Laboratori Nazionali di Legnaro (LNL). Excited states in ^{102}Pd were populated using the ^{92}Zr(^{13}C,3n)^{102}Pd fusion-evaporation reaction, with E(^{13}C) = 48 MeV. An enriched ^{92}Zr target foil, of ≈ 1 mg/cm^2, was mounted inside the Cologne plunger along with a separate 4 mg/cm^2 Au stopper foil. The average recoil velocity of the evaporation residues was $\sim 0.8\%$ c. Measurements involving twenty-four different target-to-stopper distances were performed, with this distance being regulated by a piezoelectric feedback loop housed in the plunger. Reaction γ rays were detected using the GASP array [9] (in configuration "I"), which consisted of forty, large-volume, Compton-suppressed HPGe detectors coupled to a BGO inner ball. Valid events, which were recorded for offline analysis, consisted of coincident γ rays being detected in (at least) two different HPGe detectors. The HPGe detectors were grouped such that there were seven "rings" at angles of 34.5°, 59.4°, 72.0°, 90.0°, 108.0°, 120.6° and 145.4°, with respect to the beam axis. These valid events were then sorted offline into γ-ray energy vs. γ-ray energy matrices for all ring permutations and for each individual distance.

Lifetimes were extracted using the Differential Decay Curve Method [10, 11]. In a nutshell, by placing a gate on the shifted component of a transition feeding the state of interest, the lifetime can be extracted by Equation 1:

$$\tau = \frac{I_U^{out}(x)}{v \cdot dI_S^{out}(x)/dx} \tag{1}$$

where $I_U^{out}(x)$ is intensity of the unshifted component depopulating the state, v is the recoil velocity and $dI_S^{out}(x)/dx$ is the rate of change of the shifted component as a function of target-stopper distance. In the case of indirect

Table 1: Lifetimes and corresponding $B(E2)$ values of excited states populated in the ^{92}Zr(^{13}C,3n)^{102}Pd RDDS experiment.

I_i^π	E_x (keV)	τ (ps)	$I_i^\pi \rightarrow I_f^\pi$	E_γ (keV)	$B(E2)$ (W.u.)
2_1^+	556.4	17.5 (6)	$2_1^+ \rightarrow 0_1^+$	556.4	30.8 (10)
4_1^+	1275.9	3.7 (3)	$4_1^+ \rightarrow 2_1^+$	719.4	40.7 (29)
6_1^+	2111.4	1.93 (8)	$6_1^+ \rightarrow 4_1^+$	835.5	36.8 (16)
8_1^+	3013.1	1.78 (15)	$8_1^+ \rightarrow 6_1^+$	901.7	27.3 (23)

feeding, one has to account for the feeding into the excited state of interest, as shown in Equation 2:

$$\tau = \frac{I_U^{out}(x) - I_U^{in}(x)}{v \cdot dI_S^{out}(x)/dx} \cdot \frac{[I_U^{out}(x) + I_S^{out}(x)]}{[I_U^{in}(x) + I_S^{in}(x)]} \quad (2)$$

where $I_U^{in}(x)$ and $I_S^{in}(x)$) are the unshifted and shifted components feeding the state. Gaussian peaks were fitted to the shifted and unshifted peaks to ascertain their intensities (using the program TV [12]) and a series of second-order polynomials were fitted to the intensities of both the unshifted and shifted peaks (using the program NAPATAU [13]). From these fits, the lifetime of the excited state was extracted. In this work, numerous direct and indirect gates were placed on yrast-band transitions, the weighted average of these results yielded the final lifetimes. The corresponding $B(E2)$ values were compared to $E(5)$ symmetry, and also the $U(5)$ and $O(6)$ limits of the IBM-1.

3. Results

Figure 1 shows the total projection spectrum seen in the detectors at 34.5° with respect to the beam-axis, where the target and stopper are in contact. The transitions labelled in Figure 1 are the yrast-band transitions of ^{102}Pd populated in this experiment. An example of a complete set of gated-projection spectra is shown in Figure 2, which shows the 556-keV $I^\pi = 2_1^+ \rightarrow 0_1^+$ transition (seen in the detectors at 140.6°), from a gate placed on the forward-shifted component of the 719-keV, $I^\pi = 4_1^+ \rightarrow 2_1^+$ transition (seen in the detectors at 34.5°). The results for the yrast-band transitions are tabulated in Table 1.

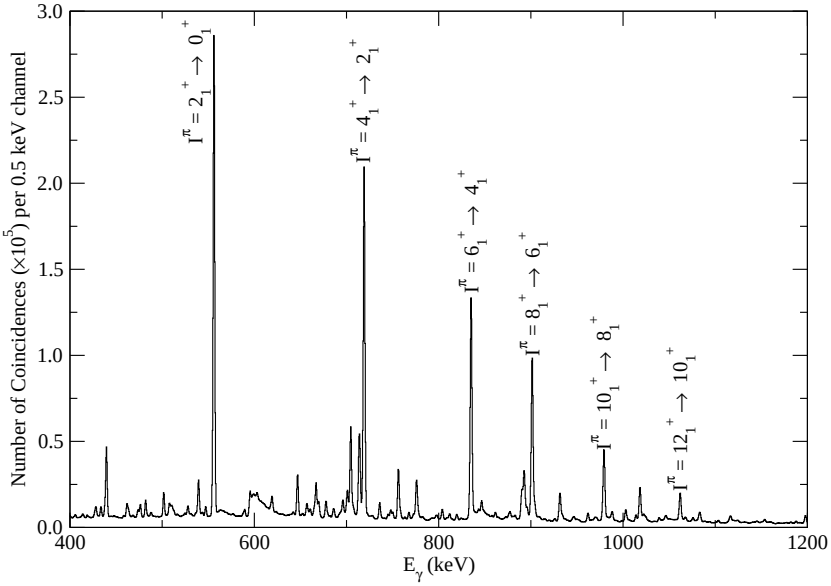

Figure 1: Total projection spectrum of the γ rays observed at 34.5° from the ^{92}Zr(^{13}C,3n)^{102}Pd reaction.

4. Discussion

The ratios of measured $B(E2)$ values to those predicted for a harmonic vibrator, γ-soft rotor, $E(5)$ limit [14], the $U(5)$ limit (see Eqn. 4 in Ref. [15]) and $O(6)$ limit (see Eqn. 5.14 in Ref. [16]) both with $N = 5$ bosons are shown in Figure 3. It is evident that a very good agreement is observed between the experimentally deduced $B(E2)$ values and the $O(6)$ limit. Furthermore, in the $O(6)$ limit, the $B(E2; 0_2^+ \rightarrow 2_1^+) = 0$, this compares to an upper limit of 0.004 [17]. IBA calculations to show the nature of the excited level scheme and for all inter- and intraband transitions are currently being performed.

5. Conclusion

Lifetimes of the yrast-band states in ^{102}Pd have been determined using the Recoil-Distance Doppler Shift technique. Significant deviations from the $E(5)$ symmetry are noted and it is apparent that from the yrast-band transitions, ^{102}Pd is a good candidate for $O(6)$ symmetry. A fuller account of this work is being prepared for publication [18] and will also be found in the Ph.D. thesis of T. Konstantinopoulos [19].

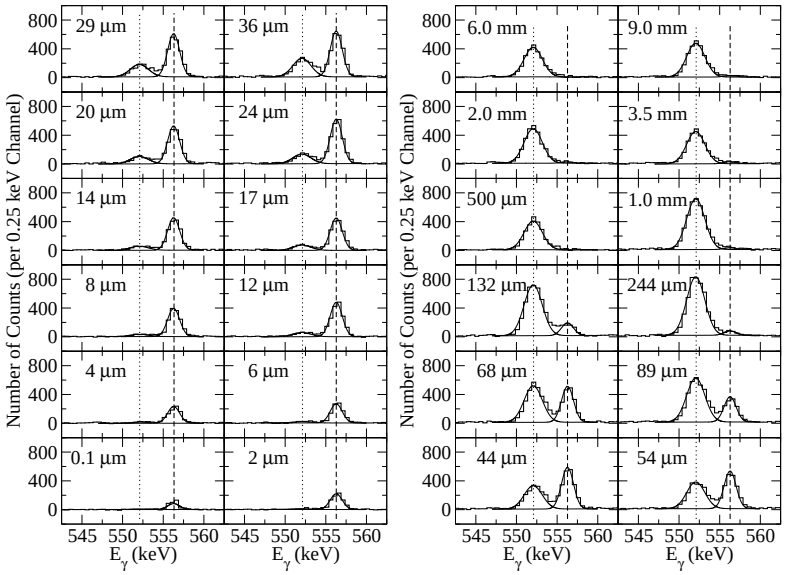

Figure 2: Deconvoluted spectra for all separate target-stopper distances of the stopped and backward-shifted component of the 556-keV, $I^\pi = 2_1^+ \rightarrow 0_1^+$ transition, from a gate placed on the forward-shifted component of the 719-keV, $I^\pi = 4_1^+ \rightarrow 2_1^+$ transition. The centroids of the stopped and backward-shifted peaks are shown by the dashed and dotted lines respectively.

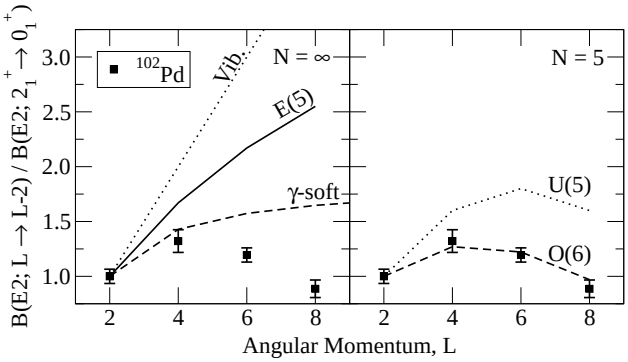

Figure 3: Left: Comparison of the experimentally deduced $B(E2; L \rightarrow L-2)/B(E2; 2_1^+ \rightarrow 0_1^+)$ ratios of the yrast-band transitions in ^{102}Pd to the classical harmonic vibrator, γ-soft rotor and $E(5)$ limit. Right: Comparison of the experimentally deduced $B(E2; L \rightarrow L-2)/B(E2; 2_1^+ \rightarrow 0_1^+)$ ratios of the yrast-band transitions in ^{102}Pd to the $U(5)$ and $O(6)$ limits with $N = 5$ bosons.

[1] F. Iachello, Phys. Rev. Lett. **85**, 3580 (2000).

[2] F. Iachello, Phys. Rev. Lett. **87**, 052502 (2001).

[3] R. F. Casten and N. V. Zamfir, Phys. Rev. Lett. **87**, 052503 (2001).

[4] R. Krücken *et al.*, Phys. Rev. Lett. **88**, 232501 (2002).

[5] D. Tonev *et al.*, Phys. Rev. C **69**, 034334 (2004).

[6] R. M. Clark *et al.*, Phys. Rev. C **69**, 064322 (2004).

[7] R. F. Casten and N. V. Zamfir, Phys. Rev. Lett. **85**, 3584 (2000).

[8] V. Zamfir *et al.*, Phys. Rev. C **65**, 044325 (2002).

[9] D. Bazzacco, AECL Report **10613**, 376 (1992).

[10] A. Dewald *et al.*, Zeitschrift für Physik A **364**, 163 (1989).

[11] G. Böhm *et al.*, Nucl. Instr. Meth. in Phys. Res. **A329**, 248 (1993).

[12] J. Theuerkauf *et al.*, Computer Program "TV", unpublished: http://www.ikp.uni-koeln.de/∼fitz (1993).

[13] B. Saha, Computer Program "NAPATAU", unpublished: http://www.ikp.uni-koeln.de.

[14] M. A. Caprio and F. Iachello, Nucl. Phys. **A781**, 26 (2007).

[15] J. Kern, P. E. Garrett, J. Jolie and H. Lehmann, Nucl. Phys. **A593**, 21 (1995).

[16] A. Arima and F. Iachello, Ann. Phys. **123**, 468 (1979).

[17] M. Luontama *et al.*, Zeitschrift für Physik A **324**, 317 (1986).

[18] T. Konstantinopoulos *et al.*, Phys. Rev. C, (In Preparation).

[19] T. Konstantinopoulos, Ph.D. thesis, NCSR "Demokritos" (In Preparation).

Detailed calculations for muon capture rates within the quasi-particle RPA

I.S. Kardaras [a],V.N. Stavrou [b],I.G. Tsoulos [c] and T.S. Kosmas [a]

[a] *Theoretical Physics Section, University of Ioannina, GR 45110 Ioannina, Greece*

[b] *Theoretical Physics Section, University of Ioannina, GR 45110 Ioannina, Greece, Division of Academic Studies, Hellenic Navy NCO School, GR 12400*

[c] *Department of Computer Science, University of Ioannina, GR 45110 Ioannina, Greece*

Abstract

Detailed calculations for bound muon capture in complex nuclei are performed by employing the quasi particle random phase approximation (QRPA). The required bound muon wavefunctions for the large and the small components of the Dirac muon wavefunctions are obtained by using the genetic algorithm approach. We obtained contributions for 2p muon orbit; that is to say wavefunctions for atomic excited state of the muonic atoms in nucleus ^{28}Si. As a byproduct the above method give the corresponding energies to these wavefunctions which are compared with those of other methods. Our goal is to use the method developed recently by Laganke, Zinner and Vogel and our advantageous numerical approach to obtain state by state calculations of the muon capture rates within the QRPA.

1 Introduction.

A bound muon in a muonic atom could be captured either from 1s or from 2p state. In order to calculate this capture rate the wavefunctions for both states are required. In the present work we calculated these wavefunctions for 2p state using Genetic Algorithms(GAs). In the past, numerical methods which have been used for solving the Schrödinger and Dirac equations are the Artificial Neural Networks (ANN)[1–3]. Even though there are no big differences between the two methods, Genetic Algorithms is the most realistic one because it chooses the first point randomly. The main advantage of this new technique is that it produces precise analytic solutions for these wave equations expressed as linear combinations of sigmoid functions.

Preprint submitted to Elsevier *1 May 2011*

2 The genetic algorithms.

GAs are modelled loosely on the principles of the evolution via natural selection, employing a population of individuals that undergo selection in the presence of variation-inducing operators such as mutation and recombination (crossover) [5].

(1) Generate an initial random population N(0) of chromosomes
(2) Evaluate and save the fitness function f(n) that is used to evaluate chromosomes, and their reproductive success in the current population
(3) Define selection probabilities p(n) for each individual n. p(n) is proportional to f(n)
(4) Generate new population of chromosomes via genetic operators and replace the worst chromosomes
(5) Repeat step 2 until a solution that is satisfying is obtained.

In this article a modified version [6] of the standard genetic algorithm is used. The modified version utilizes three modifications namely: a) a new stopping rule, b) a new mutation scheme and c) a periodical application of a local search procedure.

3 Solving the Dirac equation for the excited state (2p) with the Genetic Algoritmhs method

The solution of the Dirac equation in the case of the potential $V(\mathbf{r})$ related to the extended nuclear Coulomb field, for example the one originating from the point-nucleon charge distribution $\rho(r)$ which is given by

$$V(\mathbf{r}) = -\mathbf{e^2} \int_{-\infty}^{\infty} \frac{\rho(\mathbf{r'})}{|\mathbf{r} - \mathbf{r'}|} \mathbf{d^3 r'} \tag{1}$$

requires numerical integration by using the appropriate algorithm.The nuclear charge density $\rho(r)$ can be estimated using the two parameter Fermi model [7]:

$$\rho(r) = \frac{\rho(r_0)}{1 + e^{\frac{r-c}{z}}} \tag{2}$$

The Dirac Equation in a central force system is described by the following equation

$$E\psi = [-i\gamma_5\sigma_r(\frac{\partial}{\partial r} + \frac{1}{r} - \frac{\beta}{dr}K) + V(r) + m_i\beta]\psi \tag{3}$$

We use the following parametrized solutions for the small and large component of the Dirac equation

$$f(r) = re^{-\beta r}N(r, \mathbf{u_f}, \mathbf{v_f}, \mathbf{w_f}) \ ; \ g(r) = re^{-\beta r}N(r, \mathbf{u_g}, \mathbf{v_g}, \mathbf{w_g}) \tag{4}$$

In order to evaluate wavefunctions of excited muon states we attempted to implement the solution of the Dirac equation for the 2p state. The energy for this state(2p) is:

$$E = \frac{\int_0^\infty (m_\mu[g^2(r) + f^2(r)] + V(r)[g^2(r) - f^2(r)] - \frac{2}{r}f(r)g(r))dr}{\int_0^\infty [g^2(r) - f^2(r)]} \tag{5}$$

The error function that has to be minimized in order to evaluate the binding energy:

$$\frac{1}{\int_0^\infty [g^2(r) + f^2(r)]dr} \sum_{i=1}^{n} \Bigg\{ [\frac{df(r_i)}{dr} - [m_\mu - E + V(r_i)]g(r_i)]^2 + \sum_{i=1}^{n} [\frac{dg(r_i)}{dr} - \frac{2g(r_i)}{r_i} - [m_\mu - E + V(r_i)]f(r_i)]^2 \Bigg\} = 0 \tag{6}$$

4 Results

The goal of this work is to use the exact muon wave functions in the evaluation of the muon capture rate and especially focus on the contributions coming from the 2p, 3p etc low-lying orbits of a bound muon. To this aim, we have constructed an advantageous and very efficient numerical approach providing us with these wave functions by solving the Dirac equation. By exploiting the aforementioned computational tools and the (rather complicated) formalism of the muon capture rate (see Eq. below [8], [14]) we are going to study systematically and throughout the chart of nuclides the muon capture process.

$$\mathcal{H} = \frac{2G_F \cos\theta_c N^*}{\sqrt{2}} \times [\sum_{J=0}^{\infty} \sqrt{4\pi}[J](-i)^J [i\delta_{m,-1/2}[M^{'}_{J,0} - \mathcal{L}^{'}_{J,0}]$$
$$+a(J-1,J,m+1/2)\mathcal{T}_1(J-1,J,m+\frac{1}{2})$$
$$+a(J+1,J,m+\frac{1}{2})\mathcal{T}_1(J+1,J,m+1/2)$$
$$-i\beta_+(J,J,m)\mathcal{T}_2(J,J,m+\frac{1}{2})$$
$$-i\beta_+(J+1,J,m)\mathcal{T}_2(J+1,J,m+\frac{1}{2})$$
$$-i\beta_+(J+1,J+2,m)\mathcal{T}_2(J+1,J+2,m+\frac{1}{2})$$
$$-i\beta_-(J-1,J-2,m)\mathcal{T}_3(J-1,J-2,m+\frac{1}{2})$$
$$-i\beta_-(J-1,J,m)\mathcal{T}_3(J+1,J,m+\frac{1}{2})$$
$$-i\beta_-(J,J,m)\mathcal{T}_3(J,J,m+\frac{1}{2})]$$
$$+\sum_{J=0}^{\infty} \sqrt{4\pi}[J](-i)^J [i\delta_{m,-1/2}[\mathcal{T}^{'el}_{J,1} - \mathcal{T}^{'mag}_{J,1}]$$
$$-\delta(J-1,J-1,m)\mathcal{T}_4(J-1,J-1,m+\frac{1}{2})$$
$$-\delta(J-1,J-1,m)\mathcal{T}_4(J-1,J-1,m+1/2)$$
$$-\delta(J,J,m)\mathcal{T}_4(J,J,m+1/2)$$
$$-\delta(J,J+1,m)\mathcal{T}_4(J,J+1,m+1/2)$$
$$-\delta(J+1,J+1,m)\mathcal{T}_4(J+1,J+1,m+1/2)$$
$$+i\eta_+(J,J,m)\mathcal{T}_2(J,J,m+1/2)$$
$$+i\eta_+(J+1,J,m)\mathcal{T}_2(J+1,J,m+1/2)$$
$$+i\eta_+(J+1,J+2,m)\mathcal{T}_2(J+1,J+2,m+1/2)$$
$$-i\eta_-(J-1,J,m)\mathcal{T}_3(J-1,J,m+1/2)$$
$$-i\eta_-(J,J,m)\mathcal{T}_3(J,J,m+1/2)$$
$$-i\eta_-(J-1,J-2,m)\mathcal{T}_3(J-1,J-2,m+1/2)]]$$

Where the tensors operators in the nuclear Hilbert space is:

$$\mathcal{M}^{'}_{J,M} = \int d^3\vec{x} g(r) Y_{00} j_J(kx) Y_{JM} J_0$$
$$\mathcal{L}^{'}_{J,M} = \frac{i}{k} \int d^3\vec{x} g(r) Y_{00} \nabla (j_J(kx) Y_{JM}) J_0$$
$$\mathcal{J}^{'mag}_{J,M} = \int d^3\vec{x} g(r) Y_{00} j_J(kx) \vec{\mathcal{Y}}^M_{J,J,1} \vec{J}$$
$$\mathcal{J}^{'el}_{J,M} = \frac{1}{k} \int d^3\vec{x} g(r) Y_{00} \nabla \wedge (j_J(kx) \vec{\mathcal{Y}}^M_{J,J,1}) \vec{J}$$

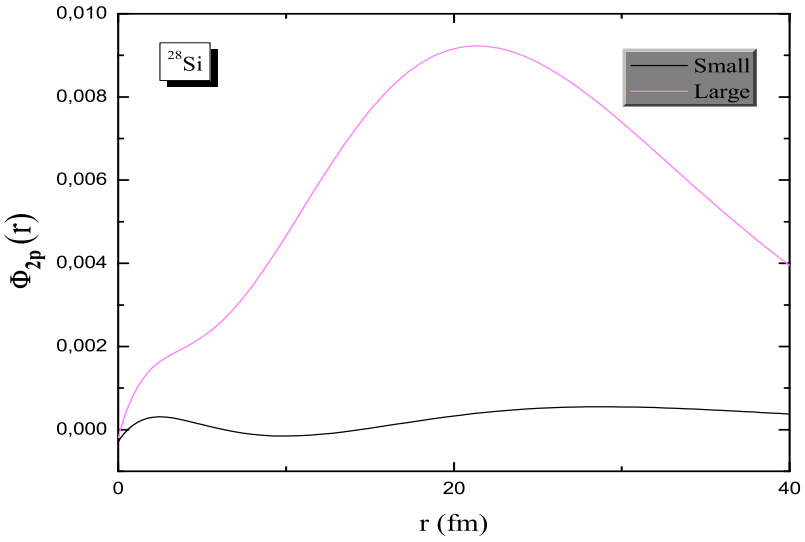

Fig. 1. The two components of Dirac spinor for the 2p state of a muon bound in ^{28}Si

$$\mathcal{T}_1(\gamma,\rho,\mu) = \int d^3\vec{x} f(r) j_\rho(kx) Y_{\gamma,\mu} J_0$$
$$\mathcal{T}_2(\gamma,\rho,J,\mu) = \int d^3\vec{x} f(r) j_{J+1}(kx) \vec{\mathcal{Y}}^{\mu}_{\gamma,\rho,1} \vec{J}$$
$$\mathcal{T}_3(\gamma,\rho,J,\mu) = \int d^3\vec{x} f(r) j_{J-1}(kx) \vec{\mathcal{Y}}^{\mu}_{\gamma,\rho,} \vec{J}$$
$$\mathcal{T}_4(\gamma,\rho,J,\mu) = \int d^3\vec{x} f(r) j_{J}(kx) \vec{\mathcal{Y}}^{\mu}_{\gamma,\rho,1} \vec{J}$$

where Υ are the spherical harmonics and $\vec{\Upsilon}$ are the vector harmonics.

In this work we calculated the muon wavefunction (see Fig. 1) and the corresponding binding energy of the μ^- in a ^{28}Si muonic atom by solving Dirac's equation. We concluded that the estimated binding energy and the bound muon wavefunctions (small and large component for the $2p$ state) for the ^{28}Si nucleus are in very good agreement with that expected from other theoretical models. In the future we will calculate such partial muon capture rates for other shells(p,d,f). These calculations have already been estimated with a different method of ours [13].

5 ACKNOWLEDGMENTS

The authors would like to thank Prof I.E. Lagaris for valuable discussions.

References

[1] I.E. Lagaris, A. Likas and D.I. Fotiadis, Comput. Phys. Commun. **104** (1997) 1-14.

[2] I.E. Lagaris, A. Likas and D.I. Fotiadis, Comput. Phys. Commun. **103** (1997) 112.

[3] T.S. Kosmas and I.E. Lagaris, J. Phys. G 28 (2002) 2907.

[4] H. Primakoff, Rev. Mod.Phys. **31** 802 (1959).

[5] D. Whitley, T. Starkweather, C. Bogart, Genetic algorithms and neural networks: Optimizing connections and connectivity, Parallel Computing **14**, pp. 347-361, 1990.

[6] I.G. Tsoulos, Modifications of real code genetic algorithm for global optimization, Applied Mathematics and Computation 203, pp. 598-607, 2008.

[7] H. de Vries, C.W. de Jager and C. de Vries, At. Data and Nucl. Data Tables **36**, (1987) 495.

[8] N.T. Zinner, K. Langanke and P. Vogel, Phys. Rev. C **74** 024326 (2006).

[9] R. Kitano, M. Koike and Y. Okada Phys. Rev. D **66** 096002 (2002).

[10] D.F.Measday Phys. Rep. 354 (2001) 243-409.

[11] V.C. Chasioti, T.S. Kosmas, *Nucl. Phys. A* **829** 234-252 (2009).

[12] I.S. Kardaras, V.N. Stavrou, T.S. Kosmas, and I.G. Tsoulos, submitted to AIP Conf. Proc., (2009).

[13] N.T.Zinner, K.Laganke, P.Vogel Phys. Rev. C74 024326 (2006)

[14] J. D. Walecka, in Muon Physics II, edited by V. W. Hughes and C. S. Wu (Academic Press, NY, 1975), p. 113.

Towards applications of graded Paraparticle algebras

Konstantinos Kanakoglou[a,b], Alfredo Herrera-Aguilar[a]

[a] *Instituto de Física y Matemáticas (*Ifm*), Universidad Michoacana de San Nicolás de Hidalgo (*Umsnh*), Edificio C-3, Cd. Univ., CP 58040, Morelia, Michoacán,* Mexico
[b] *School of Physics, Nuclear and Elementary Particle Physics Department, Aristotle University of Thessaloniki (*Auth*), CP 54124, Thessaloniki,* Greece

Abstract

An outline is sketched, of applications of the ideas and the mathematical methods presented at the 19^{th} symposium of the Hnps in Thessaloniki, May 2010

Keywords: Relative Paraparticle algebras, general linear superalgebra, multiple-level system

1. Introduction

In [2, 4] we have studied algebraic properties of the Relative Parabose algebra P_{bf} and the Relative Parafermi algebra P_{fb} such as their gradings, braided group structures, θ-colored Lie structures, their subalgebras etc. These algebras, constitute paraparticle systems defined in terms of (parabosonic and parafermionic) generators [1] and (trilinear) relations. We have then proceeded in building realizations of an arbitrary Lie superalgebra $L = L_0 \oplus L_1$ (of either fin or infin dimension) in terms of these mixed paraparticle algebras. Utilizing a given (graded), fin. dim., matrix representation of L, we have actually constructed maps of the form $\mathbb{J} : L \to gl(m/n) \subset \begin{matrix} P_{bf} \\ P_{fb} \end{matrix}$ from the LS L to an isomorphic copy of the general linear superalgebra $gl(m/n)$ embedded into either P_{bf} or into P_{fb}. These maps have been shown to be graded Hopf algebra homomorphisms or more generally braided group isomorphisms. From the pure mathematics viewpoint, such maps may be

[1] or: interacting parabosonic and parafermionic degrees of freedom, in a language more suitable for physicists

considered as generalizations of the Ado-Iwasawa theorems [2] for Lie and super-Lie algebras or even of the Cayley theorem [3] of group theory. From the viewpoint of mathematical physics, these maps generalize -in various aspects- the usual bosonic-fermionic Jordan-Scwinger realizations of Quantum mechanics. In [1, 3], we have further proceeded in building and studying a class of irreducible representations [4] for the simplest case of the $P_{bf}^{(1,1)}$ algebra in a single parabosonic and a single parafermionic degree of freedom (a 4-generator algebra).

2. Prospects-Research objectives

The carrier spaces of the Fock–like representations of $P_{BF}^{(1,1)}$ constitute a family parametrized by the values of a positive integer p. They have the general form $\bigoplus_{n=0}^{p}\bigoplus_{m=0}^{\infty}\mathcal{V}_{m,n}$ where p is an arbitrary (but fixed) positive integer. The subspaces $\mathcal{V}_{m,n}$ are 2–dim except for the cases $m=0$, $n=0,p$ i.e. except the subspaces $\mathcal{V}_{0,n}$, $\mathcal{V}_{m,0}$, $\mathcal{V}_{m,p}$ which are 1–dim for all values of m and n. These subspaces can be visualized as

$$\begin{array}{ccccccccc}
\mathcal{V}_{0,0} & \mathcal{V}_{0,1} & \dots & \mathcal{V}_{0,n} & \dots & \dots & \mathcal{V}_{0,p-1} & \mathcal{V}_{0,p} \\
\mathcal{V}_{1,0} & \mathcal{V}_{1,1} & \dots & \mathcal{V}_{1,n} & \dots & \dots & \mathcal{V}_{1,p-1} & \mathcal{V}_{1,p} \\
\vdots & \vdots & \dots & \vdots & \dots & \dots & \vdots & \vdots \\
\mathcal{V}_{m,0} & \mathcal{V}_{m,1} & \dots & \mathcal{V}_{m,n} & \mathcal{V}_{m,n+1} & \dots & \dots & \mathcal{V}_{m,p} \\
\vdots & \vdots & \dots & \mathcal{V}_{m+1,n} & \dots & \dots & \vdots & \vdots \\
\vdots & \vdots & \dots & \vdots & \dots & \dots & \vdots & \vdots
\end{array}$$

Our research will focus on both aspects of Pure Mathematics (developing or generalizing techniques for building new representations and studying their properties i.e. computing characters, eigenvalues of Casimirs, formulae for the action of the generators, irreducibility, ... etc.) and aspects of applying these representations in constructing a realistic model for the interaction of monochromatic radiation with a multiple level system:

[2] which roughly state that any f.d. Lie (or super-Lie) algebra is actually isomorphic to a matrix subalgebra of $gl(n)$ (or a graded matrix subalgebra of $gl(m/n)$)

[3] that any fin. group is isomorphic to some subgroup of the permutation group S_n

[4] we have used in [1, 3] the terminology "Fock-like reprs." because these reprs. apparently generalize the well known boson-fermion Fock spaces of Quantum Field theory

2.1. Representation-theoretical aspects:

Our first objective is to study representation theoretic implications and applications of the above mentioned constructions: We intend to present an abstraction of the Fock representations methodology, in such a way that it can be applicable to an arbitrary algebra given in terms of generators and relations. This work has already begun [6]. Our next task, will be apply the method in order to extend the results of [1] to the case of the $P_{fb}^{(1,1)}$ algebra as well and then to proceed in studying the general cases of arbitrary degrees of freedom for either P_{bf} or P_{fb}. Combining this study with the results of [2, 4] we will "translate" the constructed paraparticle representations in terms of an arbitrary Lie superalgebra. Finally, we will proceed in studying and computing properties of the constructed Lie Superalgebra representations such as computation of characters, explicit formulae for the action of the generators, eigenvalues for the Casimirs, reduction in reducible modules, classification of the cyclic irreducible modules etc. This work has also already begun, by considering the simplest case of $P_{bf}^{(1,1)}$: In [5] we are building Lie superalgebra representations starting from an arbitrary Lie Superalgebra (LS) possessing a 2-dim. graded matrix representation.

2.2. Towards the construction of a realistic model for the interaction of monochromatic radiation with a multiple level system:

Our second objective has to do with a potential physical application of the of the paraparticle and LS Fock-like representations discussed above, in the extension of the study of a well-known model of quantum optics: the Jaynes-Cummings model [7] is a fully quantized -and yet analytically solvable- model describing (in its initial form) the interaction of a monochromatic electromagnetic field with a two-level atom. Using the Fock-like modules described above, we will attempt to proceed in a generalization of the above model in the study of the interaction of a monochromatic parabosonic field with a $(p+1)$-level system. The Hamiltonian for such a system might be of the form

$$\begin{aligned} \mathcal{H} = \mathcal{H}_b + \mathcal{H}_f + \mathcal{H}_{interact} = \omega_b N_b + \omega_f N_f + \lambda(Q^+ + Q^-) = \\ = \tfrac{\omega_b}{2}\{b^+, b^-\} + \tfrac{\omega_f}{2}[f^+, f^-] + \tfrac{(\omega_f - \omega_b)p}{2} + \tfrac{\lambda}{2}(\{b^-, f^+\} + \{b^+, f^-\}) \end{aligned} \tag{1}$$

or more generally:

$$\mathcal{H} = \mathcal{H}_b + \mathcal{H}_f + \mathcal{H}'_{interact} = \omega_b N_b + \omega_f N_f + \lambda(Q^+ + Q^-) =$$

$$= \tfrac{\omega_b}{2}\{b^+, b^-\} + \tfrac{\omega_f}{2}[f^+, f^-] + \tfrac{(\omega_f - \omega_b)p}{2} + \lambda_1 b^- f^+ + \lambda_2 f^+ b^- + \lambda_3 b^+ f^- + \lambda_4 f^- b^+ \quad (2)$$

where ω_b stands for the energy of any paraboson field quanta (this generalizes the photon, represented by the Weyl algebra part of the usual JC-model), ω_f for the energy gap between the subspaces $\mathcal{V}_{m,n}$ and $\mathcal{V}_{m,n+1}$ (this generalizes the two-level atom, represented by the $su(2)$ generators of the usual JC-model) [5] and λ or λ_i, $(i = 1, .., 4)$ suitably chosen coupling constants. The $\mathcal{H}_b + \mathcal{H}_f$ part of the above Hamiltonian represents the "field" and the "atom" respectively, while the $\mathcal{H}_{interact} = \lambda(Q^+ + Q^-)$, $\mathcal{H}'_{interact} = \lambda_1 b^- f^+ + \lambda_2 f^+ b^- + \lambda_3 b^+ f^- + \lambda_4 f^- b^+$ terms represent the "field-atom" interactions causing transitions from any $\mathcal{V}_{m,n}$ subspace to the subspace $\mathcal{V}_{m-1,n+1} \oplus \mathcal{V}_{m+1,n-1}$ (absorptions and emissions of radiation). The Fock-like representations, the formulas for the action of the generators and the corresponding carrier spaces, will provide a full arsenal for performing actual computations in the above conjectured Hamiltonian and for deriving expected and mean values for desired physical quantities. A preliminary version of these ideas, for the simplest case of $P_{bf}^{(1,1)}$ has already appeared (see Section 5 of [1]). The spectrum generating algebra of $\mathcal{H}$ may be considered to be either $P_{bf}^{(1,1)}$ or $P_{fb}^{(1,1)}$ or more generally any other mixed paraparticle algebra whose representations can be directly deduced (see [6] for details) from those of $P_{bf}^{(1,1)}$ or $P_{fb}^{(1,1)}$. In this way, we will actually construct a family of exactly solvable, quantum mechanical models, whose properties will be studied quantitatively (computation of energy levels, eigenfunctions, rates of transitions between states, etc) and directly compared with theoretical and experimental results. Last, but not least, it is expected that the study of such models will provide us with deep inside into the process of Quantization itself: We will be able to proceed in direct comparison between mainstream quantization methods of Quantum Mechanics and the idea of Algebraic (or Statistical) Quantization (using Hamiltonians which contain no explicit dynamical interaction terms but including the interaction implicitly into the relations of the spectrum generating algebra itself) as this is outlined in works such as [8].

[5] actually ω_b and ω_f might be some functions of m or n or both.

3. Acknowledgements

KK would like to thank the whole staff of IFM, UMSNH for providing a challenging and stimulating atmosphere while preparing this article. His work was supported by the research project CONACYT/No. J60060. AHA was supported by CIC 4.16 and CONACYT/No. J60060; he is also grateful to SNI.

References

[1] K.Kanakoglou, A.Herrera-Aguilar, "*Ladder Operators, Fock Spaces, Irreducibility and Group-Gradings for the Relative Parabose Set algebra*", Intern. J. of Algebra, v.**5**, 9, 2011, p.413-428

[2] K. Kanakoglou, C. Daskaloyannis, A. Herrera-Aguilar, "*Super-Hopf realizations of Lie superalgebras: Braided Paraparticle extensions of the Jordan-Schwinger map*", AIP Conf. Proc., v.**1256**, 2010, p.193-200

[3] K.Kanakoglou, A.Herrera-Aguilar, "*Graded Fock-like representations for a system of algebraically interacting paraparticles*", submitted at J. of Physics Conf. Ser. (for the Proceedings of the XIV Mexican School on Particles and Fields, Morelia, MEXICO, 04-12 November 2010)

[4] K. Kanakoglou, C. Daskaloyannis, A. Herrera-Aguilar, "*Mixed Paraparticles, Colors, Braidings and a class of Realizations for Lie superalgebras*", arXiv:0912.1070v1 [math-ph]

[5] K. Kanakoglou, A. Herrera-Aguilar, "*On a class of Fock-like representations for Lie superalgebras*", arXiv:1104.0696v1 [math.RT]

[6] K. Kanakoglou, A. Herrera-Aguilar, "*Fock-type modules for algebras defined in terms of generators and relations*", under preparation

[7] E.T. Jaynes, F.W. Cummings, "*Comparison of quantum and semiclassical radiation theories with application to the beamer-maser*", Proc. IEEE, **51**, 1963, p.89-109

[8] T.D. Palev, "*SL(3/N) Wigner quantum oscillators: examples of ferromagnetic-like oscillators with noncommutative, square-commutative geometry*", arXiv:hep-th/0601201v2, 30 Jan 2006

Nuclear response to supernova neutrino spectra

V. Tsakstara [a] T.S. Kosmas [a] and J. Sinatkas [b]

[a] *Theoretical Physics Section, University of Ioannina, GR 45110 Ioannina, Greece*

[b] *Department of Informatics and Computer Technology, TEI of Western Macedonia, GR-52100 Kastoria, Greece*

Abstract

In current probes searching for rare event processes, appropriate nuclear targets are employed (in the COBRA double-beta decay detector the CdZnTe semiconductor is used). In this work the response of such detectors to various low-energy neutrino spectra is explored starting from state-by-state calculations of the neutrino-nucleus reactions cross sections obtained by using the quasi particle random phase approximation (QRPA) based on realistic two-body residual interactions. As a concrete example, we examine the response of ^{64}Zn isotope to low energy supernova neutrinos.

Key words: Neutrino-nucleus reactions, Supernovae.
PACS: 23.20.Js, 23.40.-s, 25.30.-c, 24.10.-i.

1 Introduction

In general, nuclear responses to neutrinos are crucial for low-energy neutrino detection but also for nuclear structure studies because of the presence of both the vector and the axial-vector weak interactions. Accordingly, the nuclear responses connected to the charged current neutrino-nucleus interactions are nuclear isospin and spin isospin responses, which reflect the spin isospin structures. Such responses in nuclear medium are modifed much by strong nuclear spin and isospin interactions [1,2]. Isospin and spin isospin giant resonances, which absorb most of isospin and spin isospin strengths, are located at the excitation region of E_{ex} = 10-25 MeV.

Thus, nuclei show large responses for neutrinos in that energy region. In the case of the neutral current neutrino-nucleus reactions, in addition to the other

neutrino-induced nuclear excitations, the coherent channel (gs $\rightarrow$ gs transitions) is also possible and, this is the dominant channel for low-energy neutrinos.

In the present work, we study nuclear responses to supernova neutrino spectra using the convolution method and the neutrino energy distributions described in Section 2.

2 Nuclear detector response to low-energy neutrino sources

In order to estimate the response of a nucleus to a specific source of neutrinos, the calculated differential cross sections of neutrino-nucleus induced reactions must be folded with the neutrino energy distribution of the source in question [3,4].

For the double differential cross sections, $d^2\sigma(\varepsilon_\nu,\theta,\omega)/d\Omega d\omega$, of neutrino-nucleus reactions, the folding is defined by the expression

$$\left[\frac{d^2\sigma(\theta,\omega)}{d\Omega d\omega}\right]_{folded} = \int_{\omega}^{\infty} \frac{d^2\sigma(\varepsilon_\nu,\theta,\omega)}{d\Omega d\omega}\eta(\varepsilon_\nu)d\varepsilon_\nu\,, \tag{1}$$

where $\eta(\varepsilon_\nu)$ represents the energy distribution of SN-neutrinos (traditionally a Fermi-Dirac or Power-Law distributions are utilized) [5,6].

If we introduce the chemical potential n_{dg}, the Fermi-Dirac energy distribution reads

$$\eta_{FD}[\varepsilon_\nu,T,n_{dg}] = F(n_{dg})\,\frac{1}{T^3}\frac{\varepsilon_\nu^2}{1+e^{(\varepsilon_\nu/T-n_{dg})}}\,, \tag{2}$$

In this case the width of the spectrum is reduced compared to the corresponding thermal spectrum (for this reason the parameter n_{dg} is also called pinching parameter). (in MeV) is the neutrino temperature. The degeneracy parameter n_{dg}, is the ratio of the chemical potential divided by the temperature. The factor $F_2(n_{dg})$, is the normalization constant of the distribution determined so that

$$\int_0^{\infty} n_{FD}[\varepsilon_\nu,T,n_{dg}]d\varepsilon_\nu = 1\,. \tag{3}$$

This means that the normalization constant $F(n_{dg})$ depends on the degeneracy

parameter n_{dg} and it is given by the relation

$$\frac{1}{F(n_{dg})} \equiv \int_0^\infty \frac{x^2}{e^{x-n_{dg}}+1} dx \,. \tag{4}$$

The mean energy, $\langle \varepsilon_\nu \rangle$, of the neutrino is written as a function of temperature as [7]

$$\langle \varepsilon_\nu \rangle = (3.1515 + 0.125\ n_{dg} + 0.0249\ {n_{dg}}^2 + ...)T \,. \tag{5}$$

We can easily prove that, for $n_{dg} = 0$, $F(0) = \frac{7\pi^4}{120} \sim 5.68$. Also, inserting Eq. (4) into Eq. (2), we take

$$\eta_{FD}[\varepsilon_\nu, T, n_{dg}] = \left[\int_0^\infty \frac{x^2}{e^{x-n_{dg}}+1} dx \right]^{-1} \frac{(\varepsilon_\nu^2/T^3)}{1+e^{(\varepsilon_\nu/T - n_{dg})}} \,. \tag{6}$$

After processing the later equation is written as

$$\eta_{FD}[\varepsilon_\nu, T, n_{dg}] = \frac{1}{\int_0^\infty \frac{x^2}{e^x + e^{n_{dg}}} dx} \frac{(\varepsilon_\nu^2/T^3)}{e^{(\varepsilon_\nu/T)} + e^{n_\alpha}} \,. \tag{7}$$

From the later equation it is clear that, for $n_{dg} = -\infty$ we finally take

$$\begin{aligned} \eta_{FD}[\varepsilon_\nu, T, n_{dg} = -\infty] &= (\varepsilon_\nu^2/T^3) e^{-(\varepsilon_\nu/T)} \left[\int_0^\infty x^2 e^{-x} dx \right]^{-1} \\ &= \frac{1}{2} (\varepsilon_\nu^2/T^3) e^{-(\varepsilon_\nu/T)} \,. \end{aligned} \tag{8}$$

It had been found that [5], the SN-neutrino energy spectra can be fitted by using a Power-Law energy distribution of the form:

$$\eta_{PL}[\langle \varepsilon_\nu \rangle, \alpha] = C \left(\frac{\varepsilon_\nu}{\langle \varepsilon_\nu \rangle} \right)^\alpha e^{-(\alpha+1)(\varepsilon_\nu/\langle \varepsilon_\nu \rangle)} \,, \tag{9}$$

where $\langle \varepsilon_\nu \rangle$ is the neutrino mean energy and the parameter α adjusts the width of the spectrum. The normalization factor C, is calculated by the equation

$$\int_0^\infty \eta_{PL}[\langle \varepsilon_\nu \rangle, \alpha] d\varepsilon_\nu = C \int_0^\infty \left(\frac{\varepsilon_\nu}{\langle \varepsilon_\nu \rangle} \right)^\alpha e^{-(\alpha+1)(\varepsilon_\nu/\langle \varepsilon_\nu \rangle)} d\varepsilon_\nu \ = 1 \,. \tag{10}$$

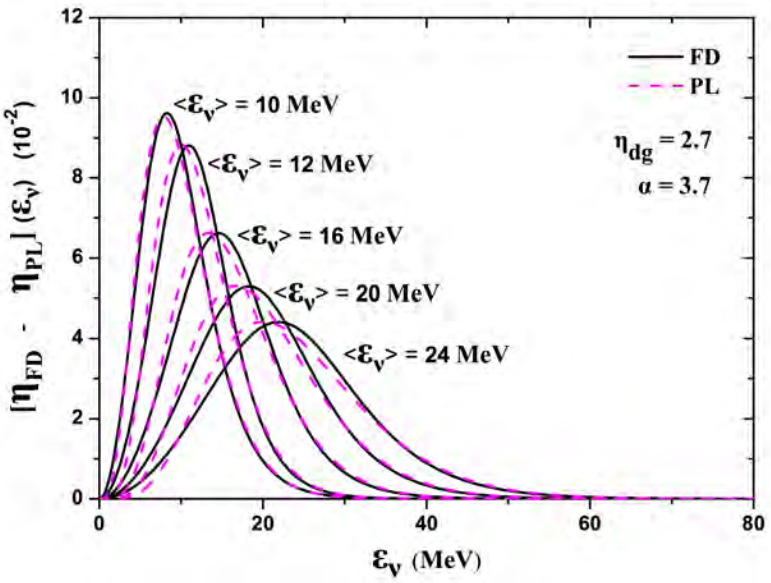

Fig. 1. Comparison between Fermi-Dirac and Power-law energy distributions for various values of their parameters.

From the later equation we find

$$C = \frac{(\alpha+1)^{\alpha+1}}{\Gamma(\alpha+1)\langle\varepsilon_\nu\rangle}\,, \tag{11}$$

therefore, Eq. (9) becomes

$$\eta_{PL}[\langle\varepsilon_\nu\rangle,\alpha] = \frac{(\alpha+1)^{\alpha+1}}{\Gamma(\alpha+1)}\,\frac{\varepsilon_\nu^\alpha}{\langle E\rangle^{\alpha+1}} e^{-(\alpha+1)(\varepsilon_\nu/\langle\varepsilon_\nu\rangle)}\,. \tag{12}$$

For $\alpha = 2$, Eq. (12) gives

$$\eta_{PL}[\langle\varepsilon_\nu\rangle,\alpha=2] = \frac{27}{2}\,\frac{\varepsilon_\nu^2}{\langle\varepsilon_\nu\rangle^3} e^{-3\varepsilon_\nu/\langle\varepsilon_\nu\rangle}\,. \tag{13}$$

By comparing Eqs. (9) and (13), we conclude that, the equality (equivalent spectra) applies when the temperature of the neutrinosphere and its mean energy $\langle\varepsilon_\nu\rangle$, related via the expression

$$T = \frac{\langle\varepsilon_\nu\rangle}{3}. \tag{14}$$

We note that, for non-degenerate particles $\langle\varepsilon_\nu\rangle = 3$, which means that, the above equality between the distributions applies when we consider the neutrinos non-degenerate [5,6].

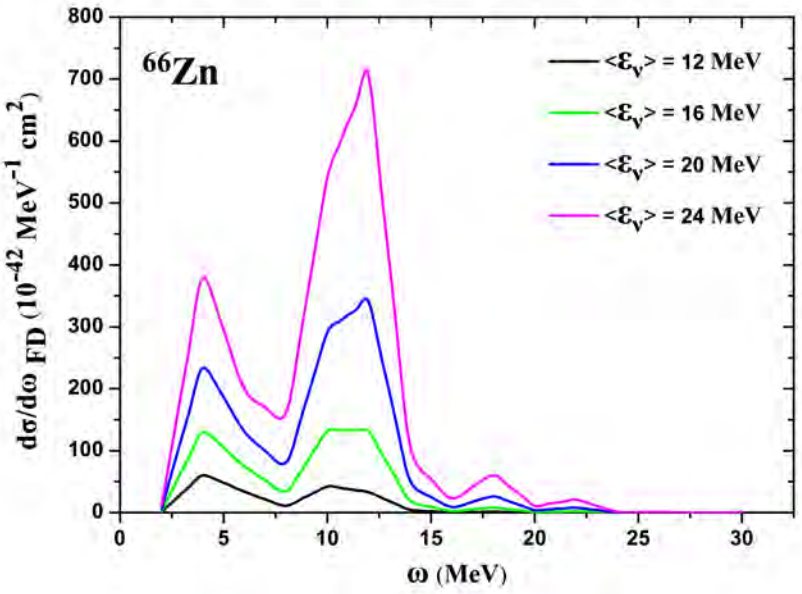

Fig. 2. Differential cross section for the reaction $^{66}Zn(\nu,\nu')^{66}Zn^*$, averaged over neutrinos and antineutrinos and over a Fermi- Dirac distribution with mean energies $\langle\varepsilon_\nu\rangle$=12, 16, 20 and 24 MeV.

3 Results and discussion

The folded results for ^{66}Zn are illustrated in Fig. 2. These results have been obtained by folding the original cross sections with a Fermi-Dirac distribution. More specifically, Fig. 2 shows the mean energy dependence of the folded differential cross section $[d\sigma(\omega)/d\omega]_{fold}$ for η_{dg}=2.7 (the mean energy values used are $\langle\varepsilon_\nu\rangle$=12, 16, 20 and 24 MeV).

We see that, the folded differential cross sections increase appreciably with the mean energy (or the temperature) $\langle\varepsilon_\nu\rangle$. This increase is depended also on the detector's excitation energy ω. In the case of the ^{64}Zn, our results show a pronounced response in the excitation region $\omega = 10 - 15$ MeV. This means that signals of supernova neutrinos of the type ν_x and $\widetilde{\nu}_x$, $x = \mu, \tau$ (high mean energies), cause much stronger response in this range of excitations of the detector [8–10].

4 Summary and Conclusions

As can be seen, there is a rich response, not only in the particle-unbound energy region, but also in the particle bound energy region of the discrete spectrum. Obviously, the folded cross section is strongly dependent on the mean energy $\langle\varepsilon_\nu\rangle$. Also there is a clear temperature (T) increase of the folded

cross section.

5 Acknowledgments

This research was supported by the ΠΕΝΕΔ No 03EΔ807 project of the General Secretariat for Research and Technology of the Hellenic Ministry of Development.

References

[1] H. Ejiri, J. Engel, R. Hazama, P. Krastev, N. Kudomi, and R.G.H. Robertson, *Phys. Rev. Lett.* **85** (2000), 2917.

[2] K. Zuber, *Phys. Lett. B* **519** (2001), 1–7; *Prog. Part. Nucl. Phys.* **57** (2006), 235–240.

[3] V. Tsakstara, T.S. Kosmas, P.C. Divari, and J. Sinatkas, *AIP Conf. Proc.* **1180** (2009), 61.

[4] T.S. Kosmas and V. Tsakstara, *J. Phys. Conf. Ser.* **203** (2010), 012090.

[5] M.T. Keil, G.G. Raffelt, and H.T. Janka, *Astrophys. J.* **590** (2003), 971.

[6] N. Jachowicz and G.C. McLaughlin, *Phys. Rev. Lett.* **96** (2006), 172301.

[7] V. Tsakstara, T.S. Kosmas, V.C. Chasioti, and J. Sinatkas, *AIP Conf. Proc.* **972** (2008), 562.

[8] V. Tsakstara and T.S. Kosmas, *Prog. Part. Nucl. Phys.* **64** (2010), 407.

[9] V. Tsakstara, T.S. Kosmas, and J. Sinatkas, *Prog. Part. Nucl. Phys.* **66** (2011), 430-435.

[10] V. Tsakstara and T.S. Kosmas *Phys. Rev. C* (2011), in press.

Studying supernova neutrinos through nuclear structure calculations

V. Tsakstara [a] T.S. Kosmas [a] and J. Sinatkas [b]

[a] *Theoretical Physics Section, University of Ioannina, GR 45110 Ioannina, Greece*

[b] *Department of Informatics and Computer Technology, TEI of Western Macedonia, GR-52100 Kastoria, Greece*

Abstract

Differential and integrated cross section calculations are performed in the context of the quasi particle random phase approximation (QRPA) by utilizing realistic two-nucleon forces, for the ^{64,66}Zn isotopes, contents of the COBRA double beta decay detector. For these isotopes the response to supernova neutrinos is of current interest. The response of the ^{66}Zn isotope to the energy-spectra of supernova neutrinos is also explored by convoluting the original results for the differential cross sections by employing: (i) a two-parameter Fermi-Dirac (FD) and (ii) a Power-Law (PL) neutrino energy distribution. Such folded cross sections are useful in low-energy astrophysical-neutrino detection in underground terrestrial experiments.

Key words: Neutrino-nucleus reactions, Supernovae.
PACS: 23.20.Js, 23.40.-s, 25.30.-c, 24.10.-i.

1 Introduction

Terrestrial neutrino experiments and telescopes provide crucial information about the weak processes taking place in the interior of stars thanks to the fact that neutrinos are extremely sensitive probes for studying stellar evolution and astro-nuclear processes. They provide the main signal from distant stars since electromagnetic signals fail to reach the detectors. Recent measurements of solar neutrinos (KAMLAND, Borexino, etc.) have been used to test the standard solar model (SSM) while recent probes at SNO (SNO+ experiment) aim to measure low-flux solar neutrinos (pep and CNO-cycle neutrinos) to check the abundances of the solar core and clarify if the metallicity in the Sun is homogeneous [1,2].

Among the promising double beta decay detectors, the semiconductor detectors CdTe and CdZnTe, and also the TeO_2 are used in the COBRA and CUORE experiments at Gran Sasso [2,3]. In these materials, the Zn isotopes have large portion and an investigation of their potential use in low-energy neutrino detection (or neutrino cross sections measurements) has not yet been addressed. We mention that, the most abundant Te isotopes, ^{128,130}Te, of these experiments have been investigated in detail in Ref. [3]. It is the purpose of the present work to study the response of ^{64,66}Zn isotopes (which have big abundances on the natural Zn) to the low-energy neutrino spectra through detailed state-by-state cross-section calculations of their neutral current reactions with neutrinos and anti-neutrinos.

It is worth mentioning that the COBRA experiment has recently been funded and an investigation of the response of its isotopes as supernova neutrino detectors but also, in general, as detectors of low-energy astrophysical and laboratory neutrinos is of current interest. In this work we study the nuclear response of the COBRA detector isotopes to the supernova neutrino energy spectra. We focus on the ^{64,66}Zn isotopes which have big abundances on the natural Zn of the matter of the CdZnTe detector [2].

2 The Structure of the $^{64,66}Zn$ isotopes

In the present paper, we present only original results for the cross sections of (anti)neutrino reactions with the isotopes ^{64}Zn and ^{66}Zn obtained within the context of the quasi-particle RPA of pp-nn type. We study the neutral current neutrino-nucleus reactions

$$\nu_l + {}^{64,66}Zn \rightarrow {}^{64,66}Zn^* + \nu_l{}' \,, \tag{1}$$

$$\widetilde{\nu}_l + {}^{64,66}Zn \rightarrow {}^{64,66}Zn^* + \widetilde{\nu}_l' \,, \tag{2}$$

where $\ell = e, \mu, \tau$ [4]. In the first stage, we determine the model parameters describing the nuclear structure of ^{64}Zn and ^{66}Zn as follows.

2.1 Determination of the model parameters

The final wavefunctions $|J_f^\pi\rangle$ of the nuclei ^{64}Zn or ^{66}Zn entering the description of the interactions of Eqs. (1) and (2), are very important for the cross section calculations. Their reliability has been cheched by the reproduction of the low-lying excitation spectrum ($\omega \preceq 4$ MeV) of the isotopes $^{64,66}Zn$ which is induced by the neutrinos(antineutrinos) of the reaction. We used as model

Table 1
Parameters determining the pairing interaction for protons, g^p_{pair}, and neutrons g^n_{pair}. They reproduce rather well the corresponding (for each isotope) empirical energy gaps $\Delta^{exp}_{p,n}$ listed also in this table (the values of the harmonic oscillator size parameter b used for $^{64,66}Zn$ isotopes are also shown).

	b (fm)	g^n_{pair}	g^p_{pair}	S_n	S_p	Δ^{exp}_p	Δ^{th}_p	Δ^{exp}_n	Δ^{th}_n
^{64}Zn	2.034	0.933	0.823	11.862	7.713	1.372	1.368	1.658	1.668
^{66}Zn	2.043	0.964	0.839	11.059	8.925	1.282	1.288	1.772	1.772

Table 2
Renormalization parameters for the particle-hole, g_{ph}, and particle-particle, g_{pp}, channel of the residual interaction for ^{64}Zn and ^{66}Zn isotopes (different for each multipolarity). They have been determined so as the low-lying excitation spectrum of each isotope ($\omega \preceq 4$ MeV) to be reproduced.

	^{64}Zn		^{66}Zn			^{64}Zn		^{66}Zn	
J^+	g_{pp}	g_{ph}	g_{pp}	g_{ph}	J^-	g_{pp}	g_{ph}	g_{pp}	g_{ph}
0^+	0.765	0.369	0.765	0.354	0^-	0.940	1.123	1.000	1.000
1^+	1.260	1.287	0.880	1.120	1^-	0.810	0.390	0.510	0.440
2^+	1.026	0.483	1.026	0.480	2^-	1.220	1.190	1.250	1.300
3^+	1.170	1.170	1.000	1.000	3^-	0.910	0.620	0.829	0.700
4^+	1.010	0.610	0.900	0.610	4^-	1.150	1.250	1.000	1.000
5^+	1.180	0.400	1.000	1.000	5^-	0.980	1.020	0.941	0.900
6^+	1.030	1.000	1.200	1.003	6^-	1.220	1.230	0.890	0.900
7^+	1.080	1.060	0.950	0.950	7^-	1.070	1.090	0.950	0.950
8^+	0.895	0.880	0.950	0.950	8^-	1.230	1.220	0.900	0.900

space the 14 lower energy levels up to $N = 4\hbar\omega$ with core the ^{16}O, the major shells with 2, 3, 4 ($\hbar\omega$).

In Tables 1 and 2, we tabulate the values of the parameters used for the construction of the nuclear states of the isotopes $^{64,66}Zn$: the initial (ground) state, which has been constructed by the BCS method and the final excited states which have been constructed within the QRPA method [4,5].

The nuclear ground state of each isotope has been constructed by solving the BCS equations using as single particle energies those determined by a Coulomb corrected Woods-Saxon potential which incudes also spin-orbit part and it is given by the equation

$$V(r) = V_{central}(r) - V_{so} r_0^2 \frac{1}{r} \frac{\partial V_{central}(r)}{\partial r} (\overrightarrow{L} \cdot \overrightarrow{S}) + \frac{1+\tau_3}{2} V_C(r)\,, \qquad (3)$$

as effective field. The pairing interaction of a Bonn-C two-body potential, was also utilized at the BCS level.

As central potential, $V_{central}(r)$, as usually, we used the Woods-Saxon potential, which is given by the expression

$$V_{central}(r) = -\frac{V_0}{1 + exp[\frac{r-R}{\alpha}]}\,. \tag{4}$$

The correction Coulomb for protons is produced by an homogeneously charged sphere of radius R_c, given as

$$V_C \;=\; \begin{cases} \frac{(Z-1)e^2}{2R_0}\left[3 - \left(\frac{r}{R_c}\right)\right], & for \quad r \preceq R_c \\ \frac{(Z-1)e^2}{2r}, & for \quad r > R_c \end{cases} \tag{5}$$

The pairing strength parameters for proton pairs, g^p_{pair}, and neutron pairs g^n_{pair} have been adjusted so as the semi-empirical pairing gaps denoted as $\Delta^{exp}_{p,n}$, to be reproduced. From Table 1 it is obvious that, there is a very good agreement between the empirical energy gaps for neutrons, Δ^{exp}_n, and for protons, Δ^{exp}_p, with the corresponding theoretical lowest quasiparticle energy which had been determined by the separation energies for protons, S_p, and for neutrons, S_n, by using the equations (known as three point semi-empirical formulae)

$$\Delta^{exp}_n = -\frac{1}{4}\{S_n[(N-1),Z)] - 2S_n[(N,Z)] + S_n[(N+1),Z)]\}\,, \tag{6}$$

$$\Delta^{exp}_p = -\frac{1}{4}\{S_p[(N,Z-1)] - 2S_p[(N,Z)] + S_p[(N,Z+1)]\}\,. \tag{7}$$

In Table 2, we tabulate the values of the parameters used in the context of the QRPA for the determination of the wave function and energies of the final nuclear states $|J^\pi\rangle$ ($J^\pi \preceq 8^\pm$, for the isotopes ^{64}Zn and ^{66}Zn. Specifically, for the construction of the QRPA matrices $\mathcal{A}$ and $\mathcal{B}$, the renormalization parameters for the particle-hole, g_{ph}, and particle-particle, g_{pp}, channel of the residual interaction for ^{64}Zn and ^{66}Zn isotopes, have been determined seperately for each multipole $|J^\pi_m\rangle$, so as the low-lying QRPA excitations ($E_\delta \preceq 4$ MeV) to fit the corresponding experimental spectrum.

After the determination of the the pairing parameters, g^p_{pair}, and neutrons g^n_{pair} and the parameters particle-hole, g_{ph}, and particle-particle, g_{pp}, the resulting energy spectrum is compared with the corresponding experimental of ^{66}Zn, in Fig. 1. As can been seen, with a few exceptions the agreement is good.

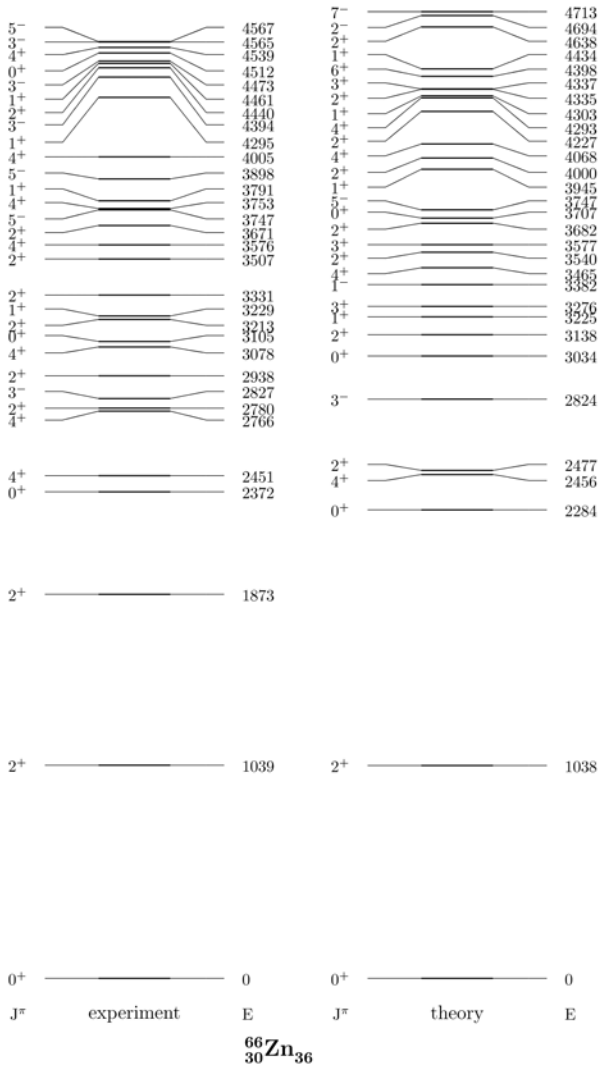

Fig. 1. Experimental and theoretical spectrum of the ^{66}Zn isotope.

3 Results and discussion

The calculational procedure of this work was carried out with the following steps. In the first step, the original results for the double differential cross section $d^2\sigma/d\Omega d\epsilon_f$ [3,4], were obtained for both nuclear isotopes, ^{64,66}Zn. Figure 2, shows the double differential cross section as a function of the excitation energy ω of the nucleus and the scattering angle θ of the outgoing lepton, for ^{66}Zn. For all the excitation energies ω in the range $0 < \omega < 25 - 30$ MeV, the cross section is clearly backward peaked ($\theta \approx 180$), a result that comes from the contribution of the transverse term of the operator which describes the interaction of the neutrino-^{64,66}Zn. This behavior was also found the ^{128,130}Te for neutral-current reactions in this energy range [3].

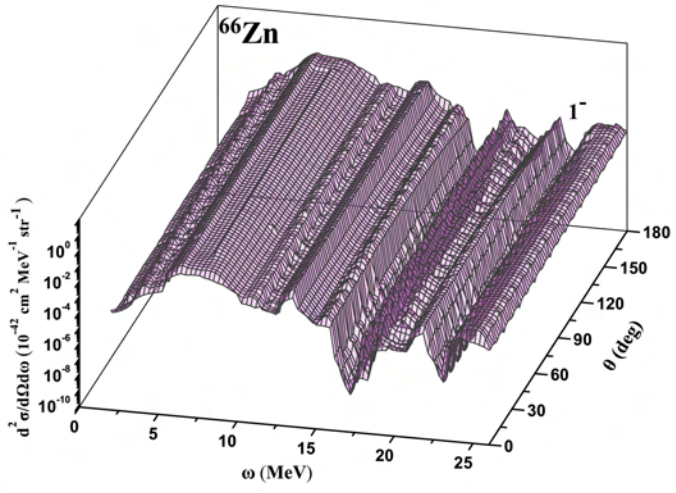

Fig. 2. The double differential cross section, $d^2\sigma/d\Omega d\omega$ as function of the excitation energy ω of the nucleus and the scattering angle θ of the outgoing lepton, for ^{66}Zn . The incoming neutrino energy is ε_ν= 40 MeV. The curves correspond to the principal multipolarity $J^\pi = 1^-$.

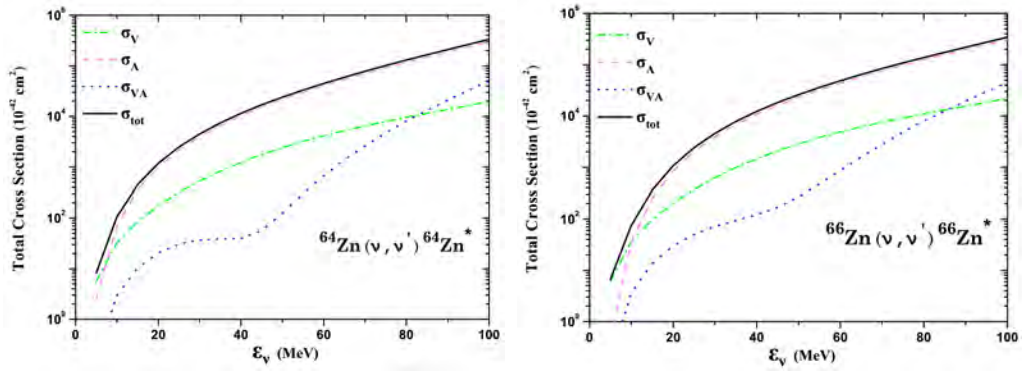

Fig. 3. Total cross sections σ_{tot} for the reaction $^{64}Zn(\nu,\nu')^{64}Zn^*$ (left) and for $^{66}Zn(\nu,\nu')^{66}Zn^*$ (right), respectively. The individual contributions of the polar-vector σ_V, axial-vector σ_A and of the interference term σ_{VA} are also illustrated.

In the final step of our calculations we studied total cross sections for the reactions of Eqs. (1) and (2). In Fig. 3, we plot the total cross section σ_{tot} (in logarithmic and linear scale) of the reactions $^{64,66}Zn(\nu,\nu')^{64,66}Zn^*$ as a function of the incoming neutrino energy ε_ν. For each reaction, the individual polar-vector, σ_V, and axial-vector, σ_A, parts as well as the interference term σ_{VA} are also illustrated.

By comparing the corresponding curves in the two Zn isotopes, we see that, there is a qualitative and quantitative similarity of the cross sections for ^{64}Zn and ^{66}Zn in all plots of Fig. 3, except a slight quantitative difference between the curves of the interference term σ_{VA}. For neutrino energies $\varepsilon_\nu \preceq 5-8$ MeV, the polar-vector contribution σ_V dominates, while for large energies the axial-vector cross section σ_A is approximately equal to the total cross section

σ_{tot} [4,5].

4 Summary and Conclusions

In the present work, we used the microscopic approach of the pp-nn quasiparticle QRPA to evaluate cross sections for the neutral current reactions $^{64}Zn(\nu,\nu')^{64}Zn^*$ and $^{66}Zn(\tilde{\nu},\tilde{\nu}')^{66}Zn^*$. The Zn isotopes are main contents of the materials of the COBRA double-beta decay detector.

We started from double differential cross sections $d^2\sigma/d\Omega d\omega$, calculated (state-by-state) with the QRPA and, subsequently we obtained integrated $d\sigma/d\omega(\omega)$ and total σ_{tot} ones. These cross sections may be folded with the neutrino-energy distributions of specific neutrino sources to which the nuclear response is of current interest. The present results show that ^{64,66}Zn present rich responses in the excitation energy range $\omega \preccurlyeq 20$ MeV (including transitions to bound states), relevant for solar neutrinos and geo-neutrinos but also for the low- and intermediate-energy supernova neutrinos. These inelastic neutrino-nucleus cross sections are suitable for use in astrophysical neutrino (including supernova neutrinos) simulations utilized in order to interpret neutrino oscillations, neutrino properties and supernova explosion mechanisms.

5 Acknowledgments

This research was supported by the ΠΕΝΕΔ No 03EΔ807 project of the General Secretariat for Research and Technology of the Hellenic Ministry of Development.

References

[1] H. Ejiri, J. Engel, R. Hazama, P. Krastev, N. Kudomi, and R.G.H. Robertson, *Phys. Rev. Lett.* **85** (2000), 2917.

[2] K. Zuber, *Phys. Lett. B* **519** (2001), 1–7; *Prog. Part. Nucl. Phys.* **57** (2006), 235–240.

[3] V. Tsakstara and T.S. Kosmas, *Phys. Rev. C* (2011), in press.

[4] V. Tsakstara, T.S. Kosmas, and J. Sinatkas, *Prog. Part. Nucl. Phys.* (2011), in press.

[5] V.C. Chasioti and T.S. Kosmas, *Nucl.Phys. A* **829** (2009), 234–252.

Elastic backscattering measurments for ^{6,7}Li+^{58}Ni, ^{6,7}Li+^{116,120}Sn, ^{6,7}Li+^{208}Pb at near barrier energies

K. Zerva[a], A. Pakou[a], N. Patronis[a], P. Figuera[b], A. Musumarra[b], A. Di Pietro[b], M. Fisichella[b], T. Glodariu[c], M. La Commara[d], T. Glodariu[b], M. Mazzocco[e], M. G. Pellegriti[b], D. Pierroutsakou[d], A. Sanchez Benitez[f], V. Scuderi[b], E. Strano[b]

[a]*Department of Physics and HINP, The University of Ioannina, 45110 Ioannina, Greece*
[b]*INFN-LNS and University of Catania, Italy*
[c]*Horia Hulubei" National Institute of Physics and Nuclear Engineering, Romania*
[d]*INFN Sezione di Napoli, I-80125, Napoli, Italy*
[e]*Dipartimento di Fisica, INFN, I35131 Padova, Italy*
[f]*Dapartamento di Fisica Atomica Molecular y Nuclear, Universidad de Huelva, E-21071 Huelva, Spain*

Abstract

We have performed, elastic backscattering measurements for the weakly bound nuclei ^{6,7}Li on the medium and heavy mass targets ^{58}Ni, ^{116,120}Sn, ^{208}Pb at sub- and near-barrier energies (0.6 to 1.3 $E_{C.b.}$). Excitation functions of elastic scattering cross sections have been measured at 160^O and 170^O and the corresponding ratios to Rutherford scattering and relevant barrier distributions have been extracted. These measurements will complement recent work on a ^{28}Si target for probing the potential at sub- and near barrier energies and relevant reaction mechanisms.

1. Introduction

As it is well known in heavy ion reactions, approaching the vicinity of the Coulomb barrier, couplings between various channels increase in importance. Describing elastic scattering, either these couplings have to be taken into account through coupled channel theories, or the energy dependence of the various optical model parameters has to be considered explicitly. In well bound nuclei, the term "threshold anomaly" was invoked to describe a rapid variation of such model parameters appeared as a sudden increase of the real part of the potential approaching the barrier, which is connected via dispersion relations with a decrease of the imaginary part. Moving to weakly bound nuclei the situation becomes more complicated due to the influence of breakup and/or transfer effects leading to a new type of anomaly [1-5]. In principle, the lack of sensitivity for obtaining the energy dependence of optical potential parameters, at energies below and near the coulomb barrier, leads occasionally to vague conclusions. Therefore, to improve our understanding on the energy dependence of the optical potential especially at sub-barrier energies and the relevant processes involved in the threshold anomaly, other complementary means should be adopted. We have shown in [6] that a very promising method to probe the potential and relevant reaction mechanisms is that of elastic backscattering. Into this context we will describe below our measurements on ^{6,7}Li+^{58}Ni, ^{6,7}Li+^{116,120}Sn, ^{6,7}Li+^{208}Pb.

2. Experimental details and results

Beams of ^{6,7}Li ions were delivered by the SMP Tandem accelerator of LNS Catania at 0.5 energy steps in the energy range 0.6 to 1.3 $E_{C.b.}$. Beam currents were of the order of 5 to 20 nA depending on energy. The beams impinged on 200 μg/cm2 thick self-supporting ^{58}Ni, ^{116,120}Sn, ^{208}Pb targets with the target frame fixed perpendicular to the beam direction. Excitation functions of (Quasi)-elastic backscattering events were recorded in four telescopes consisting of 10 μm and 2000 μm silicon detectors, set at 160 and 170 degrees. The beam flux was estimated via a measurement of the Rutherford scattering in two silicon detectors set at 20 degrees. Cross sections were extracted via the relation

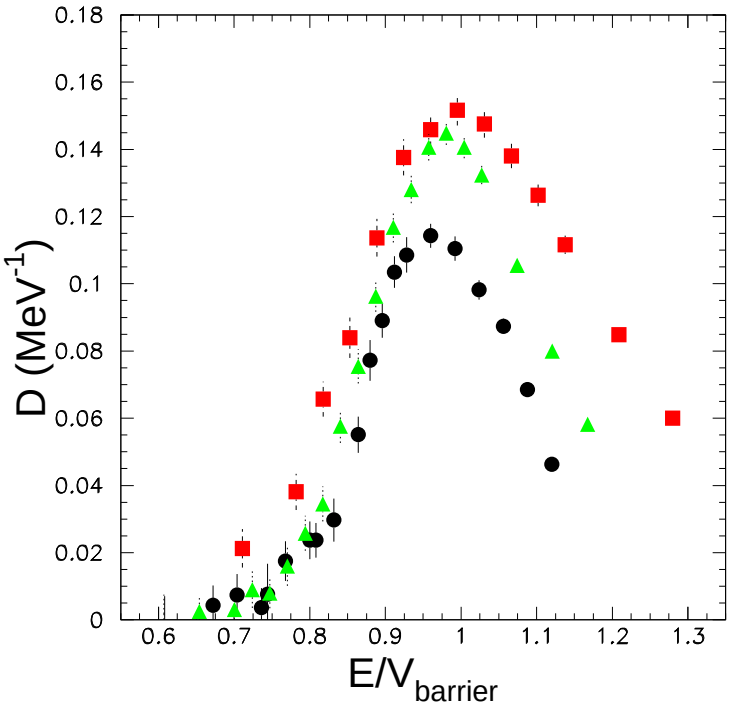

Figure 1: Barrier distributions for ^{6}Li on ^{208}Pb (solid circles) ^{120}Sn (triangles) and ^{58}Ni (solid boxes).

$$\sigma_{q170} = \frac{N_2}{N_1}\frac{\Omega_1}{\Omega_2}\sigma_{R30} \tag{1}$$

where N_2 and N_1 are the yield on the backward and forward detectors respectively while Ω_1 and Ω_2 are the solid angles of the forward and backward detectors respectively. The ratio of the solid angles was determined from the data at the lowest energies where the scattering is Rutherford for both forward and backward detectors eliminating most of the assigned error in the above relation. Barrier distributions were formed by using the relation for elastic scattering[7]

$$D(E) = \frac{d}{dE}\left[\sqrt{\frac{d\sigma_{el}}{d\sigma_{ruth}}(E)}\right] \tag{2}$$

Preliminary results of barrier distributions are compared for ^{6}Li on the the three targets ^{58}Ni, ^{120}Sn, ^{208}Pb in Figure 1, while for ^{7}Li on the four targets ^{58}Ni, ^{116,120}Sn, ^{208}Pb in Figure 2. From the above systematic it is seen that the barrier heights are larger for the lower mass targets than for the heavier ones and this variation is more obvious for the ^{6}Li projectile. Additionally to that the barrier distribution widths and heights are larger for the lighter targets and larger for the ^{6}Li projectile than the ^{7}Li one. Another interesting result is that there is no isotopic target dependence as sought for ^{7}Li+^{116,120}Sn, since the barrier distributions are almost identical for the two targets. The above results will be further explored in the future via theoretical calculations in order to probe any relation with the reaction mechanisms involved. Also theoretical anlysis is under way to probe and map till very low energies the optical potential.

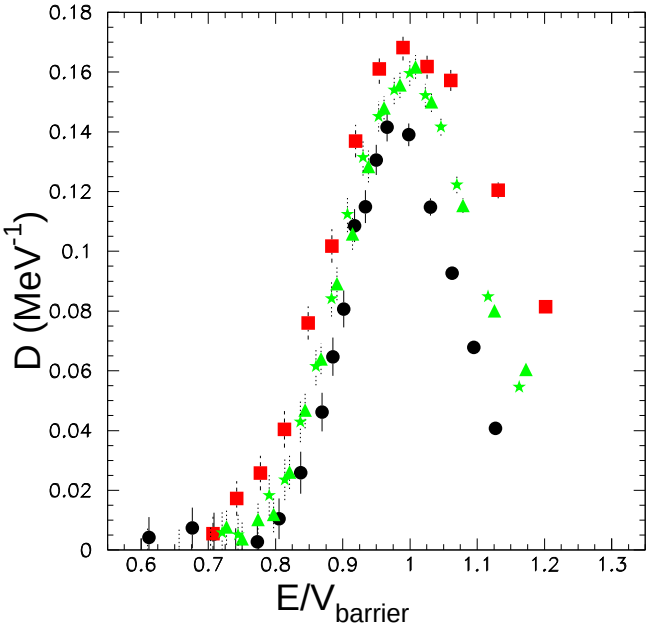

Figure 2: Barrier distributions for ^{7}Li on ^{208}Pb (solid circles), ^{116}Sn (stars), ^{120}Sn (triangles) and ^{58}Ni (solidboxes).

References

[1] N. Keeley et al., Nucl. Phys. A 571 (1994)326.
[2] A. Pakou et al., Phys. Lett. B556(2003)21.
[3] A. Pakou et al., Phys. Rev. C 69 (2004) 054602.
[4] M.S.Hussein et al., Phys. Rev. C 76 (2007) 019901.
[5] J. M. Figueira et al., Phys. Rev. 75 (2007) 017602.
[6] K. Zerva et al., Phys. Rev. C 80, (2009) 01760.
[7] N. Rowley et al., Phys. Lett. B 373 (1996)23

Electron fluence determination per Monitor Unit of a linear accelerator used for radiation therapy

A. Makridou[a], C. Tziaka[a], M. Fragopoulou[b], S. Stoulos[b] and M. Zamani[b]

[a]*Radiotheraphy section, "Theageneio" Hospital, Thessaloniki 54007 ,Greece*
[b]*Aristotle University of Thessaloniki, School of Physics, Thessaloniki 54124, Greece*

Abstract

About 20% of patients in Greece undergoing radiotherapy were irradiated by electron beams with energies ranged between 4 to 20 MeV. The correct determination of electron beam, leads to the proper treatment planning. In this study electron fluence at the isocenter was determined for a linear accelerator ELECTA SL 20 for nominal electron energy of 20 MeV. Two methods have been applied using (a) an ionization chamber in the frame of monthly quality assurance and activation detector (^{238}U). The experimental estimated electron flux, which was in good agreement with the applied calculations using the data of irradiation procedure, ranged between 3.5 up to 4.3 x 10^8 electrons per cm ^{2} per sec or 6.1 ±0.7 x 10^7 e. cm $^{-2}$ per MU.

1. Introduction

Cancer is a leading cause of death worldwide, accounting for 7.6 million deaths (around 13% of all deaths) in 2008 [1]. According to the National Statistical Service, Greece presents an upward trend in deaths from cancer in both males and females during the last 20 years; only the last five years, 148.712 people died from cancer. These figures drive to improve treatment techniques used today. In Greece, 60% of cancer patients undergoing radiotherapy and 20% of them undergoing radiotherapy with electron beams.

The fast electron beam radiotherapy has been used since 1950, initially by Van de Graff generator and after 1970 by linear accelerators. The clinical features of the electron beam are also associated with the type of accelerator producing them. The electron beam is suitable for treating superficial tumours up to five to six cm from the surface of the skin, because unlike photons, the percent depth dose (PDD) decreases rapidly with distance from the skin surface. Both the maximum absorbed dose and its distribution in the tissue varied depending on the initial energy of electrons. In the figure 1 the difference in depth dose distribution of photons at 4 MV and 12 MeV electron beam is shown. Because electrons scatter in the air, the irradiation field should be located close to the skin of the patient. For this reason,

secondary collimators or specific cones (electron applicators) are used. Electron applicators operate in the linear accelerator head and create square field's size from 2 × 2 cm^2 to 25 × 25 cm^2.

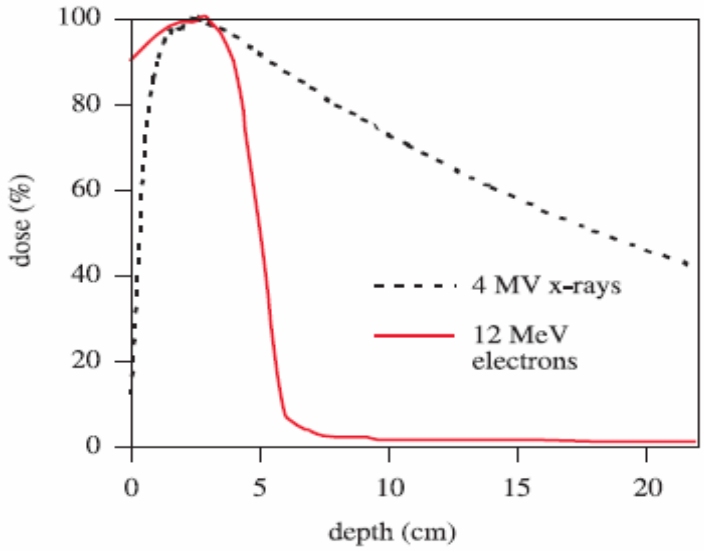

Figure 1: Depth dose curves for a 4 MV photon and 12 MeV electron beam.

In the present study the electron flux from an electron linear accelerator ELECTA SL 20 was determined for nominal electron energy 20 MeV and field size 4x4 cm^2. The fluence was determined experimentally by using an ionization chamber, in the frame of monthly quality assurance and activation detector (^{238}U). The experimental results were compared to nominal data of the irradiation system.

2. Experimental

The specifications of ELECTA SL 20 linear accelerator are: maximum nominal electron energy 20 MeV; target W; primary collimator W; y-backup collimator W; x collimator W/Pb; flattening filter Fe and leaves W/Pb. For electron beam measurements, plane parallel ionization chamber was used (Markus type 23 343 - PTW). The Model N23343 plane-parallel ionization chamber is designed specifically for electron measurements with energy above 100keV, according to the Bragg-Gray principle. The ionization chamber was connected to a MULTIDOS electrometer with high measuring accuracy and good long-term stability (Fig. 2).

Figure 2: Markus ionization chamber – MULTIDOS electrometer

Electron fluence was also determined using passive methods; sample of depleted U ($^{235}U/^{238}U$ = 0.18 ±0.01%) with thickness 0.75 μm were irradiated. The U radiator is used as activation detector, following the reaction $^{238}U(e,n)\rightarrow{}^{237}U\xrightarrow{(\beta-,6.75d)}{}^{237}Np$..... . The counting rate of ^{237}U was determined using the two most intense γ-rays: 59.5 keV (Iγ=34.5 ±0.8%) and 208 keV (Iγ=21.2 ±0.3%). Measurements took place on a LEGe planar detector with 0.7 keV resolutions at 122 keV photons, shielded by iron and lead blocks.

3. Results and Discussion

The ionization chamber was placed in contact to the electron applicator for a cylindrical area Ø 4 cm ^{2} and irradiated with nominal electron energy and rate of 20 MeV and 400MU/min. The measurement was repeated three times and the results were corrected taken into account the beam quality (K_q = 0.899) and the correction factor for pressure and temperature ($K_{T,\,P}$ = 0.999). The estimated absorbed dose corresponds to an equal amount of effective dose equivalent since the weighted factor for electrons is unity. Taken into account the fluence-to-effective dose conversion factor H'(0.07) 270 ±0.05 pSv .cm^2 [2-4] an electron fluence 3.8 ± 0.3 x 10^8 electrons per cm ^{2} per sec was estimated.

The passive detector was placed at the same position and irradiated in the same conditions as in the case of active detector – ionisation chamber. The number of electron per cm^2 and per sec was derived from the γ-spectrometry measurements (C,cps) using the following equation: $\Phi = \frac{C}{f_{decay} \cdot f_{beam} \cdot \varepsilon \cdot I_\gamma \cdot \sigma_{eff} \cdot N}$, where

$f_{decay} = (1 - e^{-\lambda t_m}) \cdot e^{-\lambda t_a}$ corresponds to the decay process during the measurement (t_m) and the waiting time (t_a) between the end of irradiation and the begging of the measurement, λ is the decay constant. The $f_{beam} = \frac{1 - e^{-\lambda t_{ir}}}{\lambda t_{ir}}$ correction factor corresponds to the decay process during the irradiation time (t_{ir}) for the monitoring isotope, which has a half-life much longer than the beam breaks. The factors ε is the counting efficiency; Iγ is the γ-ray fraction corrected for summation effect, σ_{eff} the experimental effective cross section and N the foil nuclei. Using the effective cross section for electron-plus-photon disintegration as it is reported in the bibliography [5], for the actual electron beam energy (18.3 MeV) a mean flux value of 4.3 ± 0.4 x 10^8 electrons per cm^2 and per sec was estimated.

During irradiation of ^{238}U target, the software of linear accelerator recorded average dose rate of 3.85 ±0.05 Gy/min. Taken into account the above mentioned fluence-to-effective dose conversion factors an electron flux 3.5 ±0.3 x 10^8 electrons per cm^2 per sec was calculated.

4. CONCLUSIONS

Regarding to verify the electron flux of a linear medical accelerator determined during monthly quality assurance procedure using a plane-parallel ionization chamber, the activation technique was also involved to the specific measurements. The electron flux determined in the present work was ranged between 3.5 up to 4.3 x 10^8 electrons per cm^2 per sec. The experimental results as well as the calculations applied to the nominal data of the irradiation system were presented to be in good agreement within the measurement uncertainties. According to the results each Monitor Unit delivered by the accelerator corresponds to a fluence of 6.1 ±0.7 $e.cm^{-2}$.

References

[1]http://globocan.iarc.fr/factsheets/populations/factsheet.asp?uno=900
[2] ICRU 47, Measurement of Dose Equivalents from External Photon and Electron Radiations (1992)
[3] A. Ferrari and M. Pelliccioni, Rad.Prot.Dos. 55 (1994) 207.
[4] A. Ferrari, M. Pelliccioni and M. Pillon, Rad.Prot.Dos. 69 (1997) 97
[5] F. Gerad and M.N. Martins, Phys.Rev. C 48 (1993) 105.